DISTRIBUTION OF FUNCTIONAL ACCEPTORS FOR DENDROTOXIN AND β-BUNGAROTOXIN IN THE CENTRAL NERVOUS SYSTEM

Annegret Pelchen-Matthews

A thesis submitted for the degree of
Doctor of Philosophy of the University of London
and for the Diploma of Imperial College

Department of Biochemistry
Imperial College of Science and Technology
London SW7

March 1988

ABSTRACT

The distributions in the rat and chick central nervous systems of specific neuronal acceptors for two potent snake venom toxins, β-bungarotoxin and dendrotoxin, have been mapped using radioiodinated derivatives of the toxins. These have been shown to bind saturably and with high affinity to brain cryostat sections.

Quantitative sheet film autoradiography revealed a unique distribution of ^{125}I-β-bungarotoxin acceptors in cerebral cortex, the basal ganglia, diencephalon and brainstem. In particular synapse-rich areas such as the cerebellum molecular layer, the strata oriens and radiatum of the hippocampus and the stratum moleculare of the dentate gyrus were strongly labelled.

^{125}I-Dendrotoxin acceptors showed an overlapping but much wider distribution. The toxin labelled the same brain areas as ^{125}I-β-bungarotoxin but to a greater extent and, in addition, bound extensively to myelinated tracts such as the corpus callosum, anterior commissure or the deep white matter bundles of the cerebellum. Sheet film autoradiography also revealed heterogeneity among the dendrotoxin acceptors. Whilst all ^{125}I-β-bungarotoxin binding could be blocked by excess dendrotoxin, β-bungarotoxin reduced ^{125}I-dendrotoxin binding only in grey matter areas; myelinated tracts remained prominently labelled by ^{125}I-dendrotoxin even in the presence of a large excess of β-bungarotoxin. Furthermore, when rat cerebellum sections were incubated in a range of ^{125}I-dendrotoxin concentrations high affinity toxin acceptors in the granule cell layer could be distinguished from lower affinity binding sites in the molecular layer and white matter laminae.

To define the distribution of the toxin acceptors further, brain slices from chick or rat cerebellum and rat hippocampus were incubated with ^{125}I-β-bungarotoxin or ^{125}I-dendrotoxin and processed for electron microscope autoradiography. This revealed that both β-bungarotoxin and dendrotoxin acceptors occur predominantly on neuronal plasma membranes, particularly on synaptic bouton membranes and presynaptic unmyelinated axons. In addition dendrotoxin acceptors are located on myelinated axons and, possibly, also on cell soma membranes.

These results are discussed with regard to recent reports that both dendrotoxin and β-bungarotoxin attenuate certain rapidly activating potassium currents in various neurones.

CONTENTS

Abstract 2

Table of Contents 3

List of Tables 9

List of Figures 11

Abbreviations 14

Acknowledgements 15

CHAPTER 1:

General Introduction

1.1. The nervous system 17

1.1.1. The brain 17

1.1.2. Structure of nerve cells 19

1.2. The neuronal membrane 20

1.2.1. Transmission of electrical signals 20

1.2.2. Study of neuronal membrane proteins 22

1.3. Beta-Bungarotoxin 23

1.3.1. Isolation, structure and enzyme activity of β-bungarotoxin 23

1.3.2. Effects of β-bungarotoxin at the neuromuscular junction 25

1.3.2.1. Electrophysiological studies 25

1.3.2.2. Ultrastructural changes 28

1.3.3. Specificity of β-bungarotoxin in the peripheral nervous system 30

1.3.4. Effects of β-bungarotoxin in the central nervous system 31

1.3.5. Identification of specific acceptors for β-bungarotoxin 34

1.4. Dendrotoxin and facilitatory neurotoxins 35

1.4.1. Isolation and structure of dendrotoxin and its homologues 35

1.4.2. Effects of facilitatory neurotoxins on neuro-transmission 37

1.4.3. Specific inhibition of potassium currents by dendrotoxin and toxin I 39

1.4.4. Functional neuronal acceptors for dendrotoxin 40

1.5. Interactions between the facilitatory neurotoxins and β-bungarotoxin 42

1.6. Conclusions 44

CHAPTER 2:

Identification of Acceptors for Dendrotoxin and β-Bungarotoxin on Cryostat Sections

2.1. Introduction 45

2.2. Materials 46

2.3. Methods 46

2.3.1. Preparation of synaptosomes 46

2.3.2. Fixation of synaptosomes in formaldehyde 47

2.3.3. Measurement of the binding of ^{125}I-DTX to synaptosomes 47

2.3.4. Preparation of cryostat sections 47

2.3.5. *In vitro* binding of radiolabelled toxins to brain sections 48

2.3.6. Quantitation of radioiodinated toxins bound to brain sections 49

2.4. Results 49

2.4.1. ^{125}I-DTX binding to specific acceptors 49

2.4.1.1. Effect of formaldehyde fixation on ^{125}I-DTX acceptors in rat brain synaptosomes and cryostat sections 49

2.4.1.2. Equilibrium binding of ^{125}I-DTX to cryostat sections 53

2.4.1.3. Kinetics of the binding of ^{125}I-DTX to rat brain cryostat sections 56

2.4.1.4. Inhibition of the binding of ^{125}I-DTX to cryostat sections by unlabelled DTX and β-BuTX 59

2.4.2. ^{125}I-β-BuTX binding to specific acceptors 63

2.5. Discussion 70

2.5.1. Binding of ligands to cryostat sections 71

2.5.2. Acceptors for DTX and β-BuTX in chick brain 74

2.5.3. Characterization of the acceptors for DTX and β-BuTX in rat brain cryostat sections 75

2.5.4. Interactions of β-BuTX and DTX 76

CHAPTER 3:

Distribution of Acceptors for β-Bungarotoxin in the Central Nervous System

3.1. Introduction 78

3.2. Materials 79

3.3. Methods 80

3.3.1. Preparation of cryostat sections and incubation with radiolabelled β-BuTX 80

3.3.2. Ultrofilm autoradiography 80

3.3.3. ^{125}I-labelled brain paste standards 80

3.3.4. Densitometric analysis of autoradiograms 81
3.4. Results 83
3.4.1. β-BuTX acceptors can be localized by *in vitro* autoradiography 83
3.4.2. Response of ^{3}H-sensitive Ultrofilm to iodine-125 . 85
3.4.3. Concentration-dependent binding of ^{125}I-β-BuTX to rat brain cryostat sections 88
3.4.4. Detailed analysis of the location of β-BuTX acceptors in various brain regions 91
3.4.4.1. The telencephalon 95
3.4.4.2. The diencephalon 99
3.4.4.3. Cerebellum and brainstem 99
3.4.4.4. White matter tracts 101
3.4.4.5. Spinal cord 101
3.4.5. Distribution of β-BuTX acceptors in chick brain .. 103
3.5. Discussion 103
3.5.1. Quantitative autoradiography using iodine-125 103
3.5.2. Analysis of autoradiograms by laser densitometry . 107
3.5.3. Distribution of β-BuTX acceptors in rat brain 108
3.5.4. Predominantly synaptic location of β-BuTX acceptors 109
3.5.5. β-BuTX acceptors in chick brain 110

CHAPTER 4:

Distribution of Dendrotoxin Acceptors in the Central Nervous System

4.1. Introduction 112
4.2. Materials and methods 112
4.3. Results 113
4.3.1. Distribution of DTX acceptors in the rat central nervous system 113
4.3.1.1. The telencephalon 113
4.3.1.2. The diencephalon 120
4.3.1.3. The pituitary 122
4.3.1.4. The mesencephalon 122
4.3.1.5. Cerebellum and brainstem 122
4.3.1.6. White matter tracts 125
4.3.1.7. The spinal cord 125
4.3.2. Evidence for heterogeneity of DTX binding sites in rat brain 127
4.3.2.1. β-BuTX distinguishes two types of ^{125}I-DTX binding sites 127

4.3.2.2. Inhibition of ^{125}I-DTX binding by various concentrations of unlabelled β-BuTX 133

4.3.2.3. Concentration-dependence of ^{125}I-DTX binding in the cerebellum 137

4.3.3. Distribution of DTX acceptors in chick brain 140

4.3.3.1. Inhibition of ^{125}I-DTX binding by β-BuTX 143

4.3.3.2. Concentration dependent binding of ^{125}I-DTX to chick cerebellum sections 144

4.4. Discussion 144

4.4.1. Distribution of DTX acceptors in the rat central nervous system 144

4.4.2. Interaction of β-BuTX with DTX binding sites suggests heterogeneity among DTX acceptors 146

4.4.3. Concentration-dependence of the interaction of ^{125}I-DTX with its acceptors 148

4.4.4. DTX acceptors in chick brain 148

4.4.5. DTX acceptors and K^+ channels 149

4.4.6. Distribution of ion channels in the rat central nervous system 151

CHAPTER 5:

A High Resolution Study of the Distribution of Acceptors for β-Bungarotoxin and Dendrotoxin

5.1. Introduction 154

5.1.1. Electron microscope autoradiography 154

5.1.1.1. Resolution of electron microscope autoradiography 154

5.1.1.2. Iodine-125 as a tracer in electron microscope autoradiography 156

5.1.1.3. Analysis of autoradiograms 157

5.1.2. Study of the distribution of acceptors for β-BuTX and DTX 158

5.2. Materials 158

5.3. Methods 158

5.3.1. Preparation of brain slices 158

5.3.2. Incubation of brain slices with radiolabelled toxins 159

5.3.3. Fixation and embedding of brain slices 159

5.3.4. Sectioning 159

5.3.5. Autoradiography 160

5.3.5.1. Exposure: Coating sections with Ilford L4 emulsion 160

5.3.5.2. Development 160

5.3.6. Electon microscope observations 161

5.3.7. Preparation of ^{125}I-labelled radioactive line sources for resolution studies 161

5.3.8. Analysis of silver grain distributions 162

5.3.8.1. Random sampling of tissue by photography 162

5.3.8.2. Analysis of silver grain distributions 162

5.4. Results 163

5.4.1. Preliminary studies to define a suitable tissue preparation for localization experiments 163

5.4.2. Resolution of the electron microscope autoradiography method 164

5.4.3. Localization of β-BuTX acceptors in chick cerebellum 165

5.4.3.1. Light microscope autoradiography of semithin survey sections 167

5.4.3.2. Electron microscope autoradiography of ^{125}I-β-BuTX binding in chick cerebellum 167

5.4.3.3. Analysis of the distribution of ^{125}I-β-BuTX binding in the molecular layer of chick cerebellum 170

5.4.3.4. Analysis of the distribution of ^{125}I-β-BuTX binding in the granule cell layer and white matter regions of chick cerebellum 173

5.4.4. Localization of DTX acceptors in chick cerebellum 180

5.4.4.1. Analysis of the distribution of ^{125}I-DTX binding in the molecular layer of chick cerebellum 180

5.4.4.2. Analysis of the distribution of ^{125}I-DTX binding in the granule cell layer and white matter regions 183

5.4.5. Distribution of DTX acceptors in rat cerebellum .. 187

5.4.6. Distribution of DTX acceptors in rat hippocampus . 191

5.5. Discussion 198

5.5.1. Ultrastructural localization of acceptors for β-BuTX and DTX in the central nervous system: comparison with the peripheral nervous system 198

5.5.2. Electron microscope autoradiography of toxin acceptors on brain slices 200

5.5.3. Ultrastructural distribution of β-BuTX acceptors in the central nervous system 202

5.5.4. Distribution of DTX acceptors in the central nervous system 203

5.5.5. Toxin acceptors and K^+ channels 205

CHAPTER 6:

General Discussion

6.1. Dendrotoxin and β-bungarotoxin bind to neuronal K^+ channels 207

6.2. Localization of K^+ channels by autoradiography and other methods 209

6.3. Heterogeneity of DTX acceptors and K^+ channel variants 210

6.4. Possible structure of rapidly activating voltage sensitive K^+ channels 213

6.4.1. Sequences of K^+ channel subunits in *Drosophila* ... 213

6.4.2. Structure of K^+ channels 215

6.5. Conclusions 217

APPENDIX A.1:

Purification and Radiolabelling of ß-Bungarotoxin

A.1.1. Purification of ß-BuTX from *Bungarus multicinctus* venom 219

A.1.2. Labelling of ß-BuTX with ^3H-N-succinimidyl propionate 220

A.1.3. Labelling of ß-BuTX with iodine-125 222

APPENDIX A.2:

Analysis of Ligand-Acceptor Interaction:

Formulae and Definitions

A.2.1. The Scatchard Equation 223

A.2.2. The Hill Equation 224

A.2.3. Kinetic Studies 224

A.2.4. Competition Studies Using Unlabelled Ligands 225

A.2.5. Complex Binding Situations and Multiple Acceptor Sites 226

References 227

LIST OF TABLES

Table:

2.1. Effect of formaldehyde fixation on the synaptosome binding of ^{125}I-DTX 51

2.2. Saturable binding of ^{125}I-DTX to cryostat sections from rat and chick brain 55

2.3. Inhibition of the binding of ^{125}I-DTX to cryostat sections by unlabelled DTX and β-BuTX 64

2.4. Saturable binding of ^{125}I-β-BuTX to cryostat sections from rat and chick brain 68

2.5. Binding of ^{125}I-β-BuTX and ^{125}I-DTX to acceptors in the rat central nervous system: Equilibrium and kinetic constants for cryostat section and sub-cellular fractions 72

3.1. Binding constants obtained from measuring the saturable binding of ^{125}I-β-BuTX to regions of rat brain 90

3.2. Divalent cation dependence of ^{125}I-β-BuTX binding in rat brain 92

3.3. Distribution of ^{125}I-β-BuTX acceptors in the central nervous system of the rat 93

3.4. Distribution of ^{125}I-β-BuTX binding in chick brain 105

4.1. Distribution of ^{125}I-DTX acceptors in the rat central nervous system 115

4.2. Distribution of ^{125}I-DTX binding in the presence of excess unlabelled β-BuTX 132

4.3. Distribution of ^{125}I-DTX binding in chick brain .. 142

5.1. ^{125}I-β-BuTX binding in chick cerebellum molecular layer: Distribution of silver grains and relative grain densities over various tissue elements 174

5.2. ^{125}I-β-BuTX binding in chick cerebellum granule cell layer: Distribution of silver grains and relative grain densities over various tissue elements 178

5.3. ^{125}I-DTX binding in chick cerebellum molecular layer: Distribution of silver grains and relative grain densities over various tissue elements 182

5.4. ^{125}I-DTX binding in chick cerebellum granule cell layer: Distribution of silver grains and relative grain densities 185

5.5. ^{125}I-DTX binding in rat cerebellum molecular layer: Distribution of silver grains and relative grain densities 189

5.6. ^{125}I-DTX binding in rat hippocampus stratum radiatum: Distribution of silver grains and relative grain densities 195

Table:

5.7. ^{125}I-DTX binding to rat hippocampus pyramidal cells: Distribution of silver grains and relative grain densities 196

6.1. Variants of rapidly activating voltage dependent K^+ currents and their sensitivity to facilitatory neurotoxins 212

LIST OF FIGURES

Figure:

1.1. Diagram of the rat bain, viewed approximately mid-sagitally 18

1.2. Structures of DTX and its homologues 36

2.1. Saturable binding of ^{125}I-DTX to unfixed and formaldehyde-treated rat brain synaptosomes 51

2.2. Effect of fixation with formaldehyde on the ability of β-BuTX to block ^{125}I-DTX binding to synaptosomes 52

2.3. Concentration dependence of ^{125}I-DTX binding to cryostat sections of rat forebrain 54

2.4. Time course of the association of ^{125}I-DTX with its acceptors on rat brain cryostat sections 57

2.5. Dissociation of ^{125}I-DTX from its acceptors on rat brain cryostat sections 58

2.6. First order plots of the dissociation of ^{125}I-DTX from its acceptors on rat brain cryostat sections under various conditions 60

2.7. Binding of ^{125}I-DTX to cryostat sections of different thickness 61

2.8. Inhibition by unlabelled DTX and β-BuTX of the binding of ^{125}I-DTX to cryostat sections of rat and chick brain 62

2.9. Dependence of ^{125}I-DTX binding, and its inhibition by β-BuTX, on divalent cations 65

2.10. Concentration dependence of ^{125}I-β-BuTX binding to cryostat sections of rat forebrain 67

2.11. Divalent cation dependence of ^{125}I-β-BuTX binding to cryostat sections 69

3.1. Densitometric analysis of autoradiograms 82

3.2. Distribution of β-BuTX acceptors in rat brain 84

3.3. Localization of acceptors for ^{3}H-β-BuTX 86

3.4. Response of ^{3}H-sensitive Ultrofilm to ^{125}-labelled brain paste standards 87

3.5 Autoradiographic determination of ^{125}I-β-BuTX binding to rat brain cryostat sections 89

3.6. Distribution of ^{125}I-β-BuTX acceptors in rat forebrain at the level of the striatum 96

3.7. Distribution of ^{125}I-β-BuTX acceptors in rat forebrain at the level of the hippocampus 97

3.8. Location of ^{125}I-β-BuTX acceptors in the hippocampus 98

3.9. Distribution of ^{125}I-β-BuTX acceptors in the cerebellum and brainstem 100

Figure:

3.10. Distribution of ^{125}I-β-BuTX acceptors in the spinal cord 102

3.11. Distribution of β-BuTX acceptors in chick brain .. 104

4.1. Distribution of DTX acceptors in rat brain 114

4.2. Distribution of ^{125}I-DTX acceptors in rat forebrain 119

4.3. Distribution of ^{125}I-DTX acceptors in the hippocampus 121

4.4. Distribution of ^{125}I-DTX acceptors in the pituitary 123

4.5. Distribution of ^{125}I-DTX acceptors in the mesencephalon 123

4.6. Distribution of ^{125}I-DTX acceptors in the cerebellum and brainstem 124

4.7. Distribution of ^{125}I-DTX acceptors in the spinal cord 126

4.8. Distribution of ^{125}I-DTX binding in the presence of excess unlabelled β-BuTX 129

4.9. Distribution of ^{125}I-DTX binding in rat forebrain in the presence of excess unlabelled β-BuTX 130

4.10. Distribution of ^{125}I-DTX binding in the cerebellum and brainstem in the presence of excess β-BuTX ... 131

4.11. Autoradiographic determination of the competition by unlabelled DTX and β-BuTX of ^{125}I-DTX binding: Rat forebrain areas 134

4.12. Autoradiographic determination of the competition by unlabelled DTX and β-BuTX of ^{125}I-DTX binding: Rat cerebellum sections 135

4.13. Concentration-dependence of ^{125}I-DTX binding to rat cerebellum cryostat sections 138

4.14. Quantitative Analysis of the concentration-dependence of ^{125}I-DTX binding to discrete areas of rat cerebellum 139

4.15. Distribution of ^{125}I-DTX acceptors in one-day-old chick brain 140

4.16. Concentration-dependence of ^{125}I-DTX binding to chick cerebellum cryostat sections 145

5.1. Specimen-emulsion geometry in electron microscope autoradiography 155

5.2. Distribution of silver grains about a ^{125}I-labelled radioactive line source 166

5.3. Survey of ^{125}I-β-BuTX binding on chick cerebellum slices 168

5.4. Localization of ^{125}I-β-BuTX binding in chick cerebellum molecular layer 169

5.5. Localization of ^{125}I-β-BuTX binding in chick cerebellum molecular and Purkinje cell layers 171

Figure:

5.6. ^{125}I-β-BuTX binding in chick cerebellum molecular layer in Sr^{2+} Ringer 172

5.7. Distribution of silver grains about the presynaptic membrane 175

5.8. Localization of ^{125}I-β-BuTX binding in chick cerebellum granule cell layer 176

5.9. Localization of ^{125}I-β-BuTX binding in chick cerebellum white matter regions 179

5.10. Localization of ^{125}I-DTX binding in chick cerebellum molecular layer 181

5.11. Localization of ^{125}I-DTX binding in chick cerebellum granule cell layer 184

5.12. Localization of ^{125}I-DTX binding in chick cerebellum white matter regions 186

5.13. Localization of ^{125}I-DTX binding in rat cerebellum molecular layer 188

5.14. Localization of ^{125}I-DTX binding in rat cerebellum granule cell layer and white matter regions 190

5.15. Localization of ^{125}I-DTX binding in 14-day-old rat cerebellum molecular layer 192

5.16. Localization of ^{125}I-DTX binding in rat hippocampus 194

5.17. Localization of ^{125}I-DTX binding in the hippocampus of 14-day-old rat brain 197

6.1. Structure of *Drosophila Shaker* K^+ channel protein subunits 214

A.1. Chromatofocusing of fraction V of *B. multicinctus* venom 221

ABBREVIATIONS USED

4-AP	4-Aminopyridine
BPTI	Bovine pancreatic trypsin inhibitor
BSA	Bovine serum albumin
β-BuTX	β-Bungarotoxin
cDNA	Complementary DNA
DTX	Dendrotoxin
DV-14	A toxin from *Dendroaspis viridis*
ED_{50}	The dose producing 50% of the maximal effect
EDTA	Ethylenediaminetetraacetic acid
EGTA	Ethylene glycol bis(2-aminoethyl ether)-N,N,N',N'-tetraacetic acid
e.p.p.	Endplate potential
GABA	γ-Aminobutyric acid
HD	Half-distance
HR	Half-radius
^{3}H-β-BuTX	Tritium-labelled β-bungarotoxin
I_A	The A-current
^{125}I-β-BuTX	^{125}I-labelled β-bungarotoxin
^{125}I-DTX	^{125}I-labelled dendrotoxin
m.e.p.p.	Miniature endplate potential
pBPB	para-Bromophenacyl bromide
TTX	Tetrodotoxin

ACKNOWLEDGEMENTS

I would like to thank my supervisor, Dr. J. Oliver Dolly for his help and guidance during this work, and for the opportunity to carry out this project in his laboratory. I also thank Dr. Steve Bunn for advice on various aspects of quantitative autoradiography, and Dr. Graham Wilkin, John Cavanagh and Dr. Jennifer Black for help and instruction in electron microscopy. Thanks are further due to Dr. Adrian Black, Alexander Breeze and David Parcej for purifying and radiolabelling some of the snake venom toxins, and to Glyn Millhouse for expert photography. I am very grateful to my lab-mate, Nandita Ray and other fellow students for their friendship thoughout my time at Imperial College, and, last, but not least, to my husband, Derek, for his unfailing support and encouragement.

This thesis is dedicated to my father,
Hermann Pelchen, who stimulated my curiosity and encouraged
my interest in the natural sciences, and who generously
supported me throughout my undergraduate studies
at Imperial College.

CHAPTER 1

General Introduction

1.1. The Nervous System

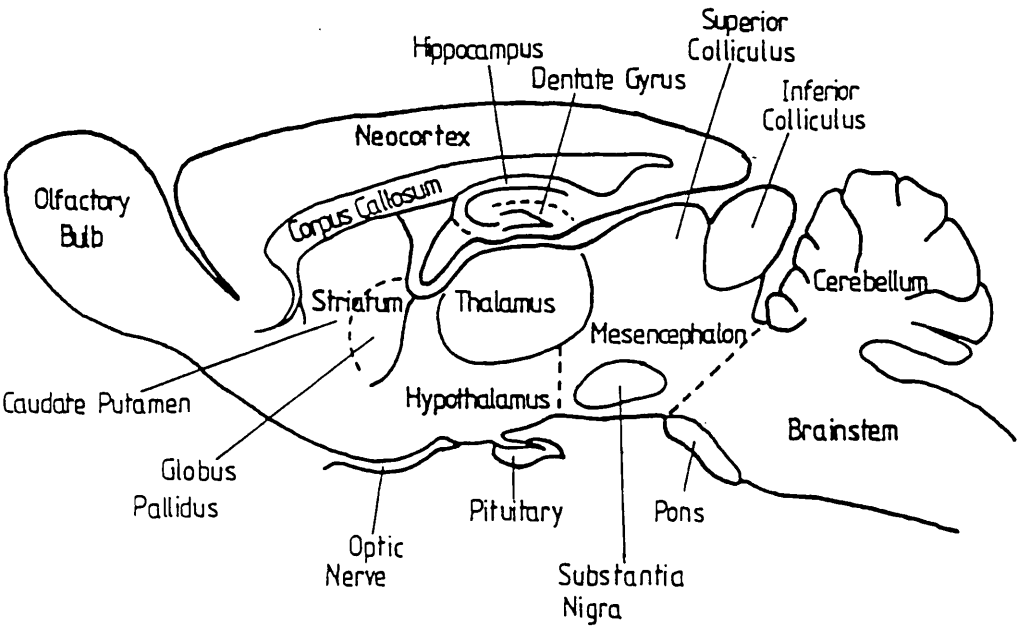
This is the central control system in higher animals, coordinating the functions of other tissues and organ systems so that they act harmoniously as a unit. Thus, an organism is able to react to changes in its environment, maintaining homeostasis and responding to outside stimuli by short term reflexes and long term behavioural changes. In higher animals and in man the nervous system furthermore mediates emotions, conscious thought, memory and learning. Because of these complex functions, the nervous system has long been a popular subject for physiological and biochemical investigation.

1.1.1. The Brain

Most neurones are located together in the central organ of the nervous system, the brain, as a highly ordered and frequently inter-connected network of excitable cells. Structurally the brain may be subdivided into an number of areas as illustrated in Figure 1.1. Many of the connections between brain areas have been traced, and some functions have been assigned to specific areas (for details on neuroanatomy and general neurobiology, see Shepherd, 1983; and Nauta and Feirtag, 1986).

Among the brain areas, the neocortex is the most recently developed evolutionarily. It has reached considerable complexity in higher vertebrates and is most extensive in man, where it

Figure 1.1. Diagram of the rat brain, viewed approximately mid-sagitally



contains ≈70% of all central neurones. Specialized cortical areas receive all sensory impulses from the peripheral nervous system or the special sense organs. For example, somatic sensory impulses from receptor cells in the skin, muscles or visceral organs enter the central nervous system through the spinal cord and are transmitted along ascending fibres through relay centres in the brainstem reticular formation and in the thalamus (ventral nucleus) to the somatic sensory cortex. Auditory stimuli from the inner ear reach the auditory cortex via the cochlear nuclei, inferior colliculi and medial geniculate nuclei. Visual information from the retinae is transmitted along the optic nerve, crossing at the optic chiasma and ascending along the optic tracts to integrating centres in the superior colliculi and thalamus (lateroposterior nucleus), or to the lateral geniculate bodies, before entering the visual cortex. Fibres from the nasal mucosa reach the olfactory cortex via the olfactory bulb. Sensory information is processed in each of these relay centres, as well as in the cortical receptive fields and in cortical association areas. It may also be further transmitted to the hippocampus and amygdala, areas which have been

implicated in memory and learning.

In addition the neocortex controls both motor and visceral responses. Voluntary movement is initiated from motor areas of the cortex. Some fibres from this area pass directly to the motoneurones in the spinal cord. Other motor stimuli are first processed in the caudate putamen, which also receives an input from the substantia nigra, and in the globus pallidus. A further information channel connects the motor cortex to the pons and the cerebellum. Impulses then pass through the reticular formation to synapse with motoneurones in the spinal cord. Further signals from the neocortex pass through the hippocampus and amygdala to the hypothalamus. This area controls inputs to the ganglia of the autonomic nervous system innervating the smooth muscles and glands of visceral organs.

The above brief description serves to illustrate some of the complex functions of the brain, although it is necessarily an oversimplification. Feedback loops and branches from all major fibre tracts cross-connect many areas. Integration is possible at each relay station, thus enabling the fine-tuning of all nervous processes.

1.1.2. Structure of Nerve Cells

The excitable cells of the nervous system are the nerve cells or neurones. These are supported by a much larger number of glial cells, which regulate the nutrient and ionic environment of neurones, provide insulating myelin sheaths and may guide neuronal development. Neurones exhibit a very wide variety of shapes and sizes. However they all share a similar basic structure. The cell body or soma contains the nucleus of the cell, the protein synthetic apparatus (ribosomes and endoplasmic reticulum) and Golgi bodies. From the soma extend many intricately branched dendrites, which form the receptive field of the neurone. Usually a single axon also emerges from the soma to transmit electrical impulses to other cells. In its terminal fields the axon branches extensively, forming many synapses with other neurones or effector cells (for a detailed description of neurone structure, see Peters *et al.*, 1976).

1.2. The Neuronal Membrane

The excitability of neurones, their capacity to transmit electrical signals and their ability to stimulate other cells depend critically on the properties of the neuronal membrane. In particular, the nature of the membrane proteins and their distribution are important in neuronal function. These membrane proteins may be transport proteins such as channels, which permit the diffusion of ions down their concentration gradient, or pumps involved in active transport. Other proteins have recognition functions. Thus receptors bind specific transmitter or neuromodulator molecules and as a result cause ionic currents to flow or second messenger systems to be activated. Membrane proteins may also be involved in regulating cell growth and cell-cell recognition or cell-cell adhesion fuctions (e.g. the neuronal cell adhesion molecules, n-CAMs, reviewed by Edelman, 1984). Membrane-bound enzymes facilitate chemical reactions at the cell surface, while structural proteins are required to maintain subcellular organization.

1.2.1. Transmission of Electrical Signals

The importance of membrane proteins in neuronal function may be illustrated by tracing an electrical signal along a neurone. The following description is necessarily brief and simplified. Further details may be found for example in Kuffler *et al.* (1984).

Nerve signalling depends on changes in the membrane potential as a result of movements of ions through channel proteins. Ion flow is powered by an asymmetric distribution of ions on either side of the plasma membrane (the cytoplasm is enriched in K^+, but relatively depleted of Na^+, Ca^{2+} and Cl^-). This distribution of ions is created and maintained by the Na^+/K^+ ATPase pump (Skou and Nørby, 1979; see also Cantley, 1986). A slow and selective leakage of K^+ out of the cell results in a depletion of positive charge, creating a resting membrane potential of about -70 mV.

Potential changes may be generated by ligand-gated ion channels (receptors) in the postsynaptic membrane of a dendrite or soma. The neurotransmitter acetylcholine, for example, may bind to receptors similar to the nicotinic receptors at the neuromuscular junction. Ligand binding increases the probability of opening of the receptor channels, which are permeable to both Na^+ and K^+ ions. The movement of these ions down their concentration gradients thus leads to a local depolarization of the cell membrane. In a similar

fashion the transmitters γ-aminobutyric acid (GABA) and glycine open Cl^- channels, permitting Cl^- to enter the neurone and cause a local hyperpolarization. Because of the cable properties of the neuronal membrane, such local postsynaptic potentials spread passively along the dendrites, although ion leakage through the membrane diminishes their amplitude with distance. The graded potentials reach the cell soma, whose membrane potential, as a result, will reflect the sum of the potential fluctuations arriving there from the dendrites and the postsynaptic potentials created by synapses directly onto the soma.

In contrast to most dendritic membranes, the cell soma membrane near the axon hillock is highly enriched in voltage-gated Na^+ channels. These channels open in response to local depolarisations built up as a result of the graded potentials described above. The resulting Na^+ influx further depolarizes the membrane close to the reversal potential for Na^+ (40-50 mV). Adjacent voltage-sensitive Na^+ channels open, and an action potential is transmitted along the axon. The cell membrane repolarizes as the Na^+ channels inactivate and voltage-sensitive K^+ channels are opened. Fine control of action potential firing frequency and cell excitability is achieved by the presence of other channels such as various voltage-sensitive Ca^{2+} channels (see, e.g. Carbone and Lux, 1984; Nowycky *et al.*, 1985), rapidly-activating K^+ channels (mediating the A-current, Gustafsson *et al.*, 1982; Rogawski, 1985) or Ca^{2+}-dependent K^+ channels (Meech, 1978; Petersen and Maruyama, 1984) on the cell somas (see also Crill and Schwindt, 1983).

When the action potential reaches a synaptic bouton at the end of the axon the depolarization opens voltage-sensitive Ca^{2+} channels located there. The resulting influx of Ca^{2+} into the nerve terminal releases neurotransmitter from synaptic vesicles (reviewed by Augustine *et al.*, 1987). The released neurotransmitter may trigger postsynaptic potentials (as above), before it is eliminated by enzymic degradation or selective uptake into neurones or glial cells.

This brief description demonstrates the importance of ion channels in neuronal excitability. At the molecular level, a large number of channels may be present to finely control the ion fluxes in the membrane. For example, seven different K^+ channel types have been identified on the soma of mouse dorsal root ganglion neurones (Simonneau *et al.*, 1987). Furthermore, channel properties

may be regulated by second messenger systems acting, for example, through phosphorylation by cyclic-AMP dependent protein kinases (e.g. Costa and Catterall, 1984; Armstrong and Eckert, 1987) or protein kinase C (reviewed by Miller, 1986) or through interactions with GTP-binding proteins (reviewed by Dunlap *et al.*, 1987).

1.2.2. Study of Neuronal Membrane Proteins

Ion fluxes can be studied by extracellular recording techiques. The electrical properties of larger elements such as somata may also be studied by voltage- or current clamp methods. Recently the development of patch clamp analysis methods (Sigworth and Neher, 1980) has made possible the study of the properties of single channels.

Biochemical studies of membrane proteins require their solubilization, purification and structure determination. These studies are not possible without specific probes for these molecules so that they can be assayed in broken cell preparations. Ligands, agonists, antagonists, channel blockers or other drugs may be used for this purpose, or specific antibodies may be raised to the protein to be studied. In addition the venoms of many animals contain specific toxins, which bind with high specificity and affinity to neuronal components. For example, postsynaptic neurotoxins like α-bungarotoxin, from the venom of *Bungarus multicinctus*, specifically block the nicotinic acetylcholine receptor (Lee, 1972). These toxins have been used to localize, purify and determine the structure of the nicotinic acetylcholine receptor (reviewed by Dolly and Barnard, 1984). Similarly, a number of toxins like tetrodotoxin from puffer fish and toxins from scorpion venoms interact with the voltage-sensitive Na^+ channel (Catterall, 1980) and have made possible the purification and structure determination of this protein (Catterall, 1984; 1986). Toxins have also been used in the study of Ca^{2+} channels (Fox *et al.*, 1987) and of one type of Ca^{2+}-dependent K^+ channel (Romey *et al.*, 1984).

Other toxins from snake venoms also cause pronounced electrophysiological responses when applied to neurones, although their site of action is not yet known precisely. In the present work, two such toxins with potent effects on neurotransmitter release, ß-bungarotoxin and dendrotoxin, have been used to study specific neuronal components.

1.3. Beta-Bungarotoxin

β-Bungarotoxin (β-BuTX) is one of a group of presynaptic neurotoxins exhibiting phospholipase A_2 activity (see reviews by Lee and Ho, 1980; Howard and Gundersen, 1980; Chang, 1985). Although these toxins vary widely in structure, containing either an acidic, neutral or basic phospholipase enzyme subunit as a monomer or polymer, or linked with other subunits (Chang, 1985), they all block neurotransmitter release in a complex two- or three-step sequence. β-BuTX appears to be one of the more potent of these presynaptic toxins, and since it is also the most specific, being totally devoid of the postsynaptic, myotoxic or haemolytic activities expressed by other phospholipase A_2 toxins (Harris *et al.*, 1980; Ho *et al.*, 1986), it has been the most widely studied.

1.3.1. Isolation, Structure and Enzyme Activity of β-Bungarotoxin

The venom of the Formosan banded krait, *Bungarus multicinctus*, can be separated by starch zone electrophoresis into four components (Chang and Lee, 1963), three of which are neurotoxic. α-Bungarotoxin acts postsynaptically, binding specifically to the nicotinic acetylcholine receptor (see above), while β- and γ-bungarotoxin block neurotransmitter release presynaptically. More powerful ion exchange chromatography fractionation methods have allowed the separation of the venom into 6-15 peaks (for details see Appendix A.1) containing postsynaptic neurotoxins, various enzymes (Lee *et al.*, 1972; Hanley *et al.*, 1977), a cardiotoxin (Wu *et al.*, 1982), nerve growth factor (Furukawa and Hayashi, 1978) and several species of presynaptic neurotoxins. In the classification of these toxins the term γ-BuTX has now been abandoned, while β-BuTX, the most abundant, has also been identified as β_1-BuTX by Kondo *et al.* (1978a,b) or β_3-BuTX by Abe *et al.* (1977a). A single-chain presynaptic neurotoxin of M_r =11,000d, apparently similar to notexin, has also been isolated from *B. multicinctus* venom (Tobias *et al.*, 1978; Livengood *et al.*, 1978; cf. Hanley *et al.*, 1977).

β-BuTX is a basic polypeptide of M_r =21,000d, pI =9.9, consisting of two covalently linked subunits (Kelly and Brown, 1974; Abe *et al.*, 1977a; Hanley *et al.*, 1977; Kondo *et al.*, 1978a). The larger A-chain (M_r =13,500d) contains 120 amino acid residues and is homologous to pancreatic or snake venom phospholipase A_2 enzymes (Kondo *et al.*, 1978b; 1982b), while the smaller B-chain (M_r =7,000d) of 60 amino acid residues resembles bovine pancreatic

trypsin inhibitor (BPTI: Kondo *et al.*, 1982a). The other presynaptic toxins present in *B. multicinctus* venom share this structure: Five isotoxins have been isolated and shown to be composed of one of three possible A-chains (A_1, A_2 or A_3) and one of two B-chains (B_1 or B_2; for details of the sequences, see Kondo *et al.*, 1982a,b). A large number of intrachain disulphide bridges makes β-BuTX resistant to non-reducing denaturants, heat and acid treatment, and some proteases. However, the toxin is labile in alkaline solution (Hanley *et al.*, 1977; Howard and Truog, 1977; Ikeda and Hayashi, 1983).

As predicted from the amino acid sequence of the A-chain of β-BuTX, the toxin exhibits weak phospholipase A_2 activity (phosphatide acylhydrolase, EC 3.1.1.4., Kelly *et al.*, 1975; Strong *et al.*, 1976; 1977; Abe *et al.*, 1977a; Howard and Truog, 1977; Kondo *et al.*, 1978c). This enzyme activity is dependent on Ca^{2+}, which binds to the toxin ($K_d \approx 0.1$-0.2 mM, Abe *et al.*, 1977a; Ikeda and Hayashi, 1983). No other divalent cations (Sr^{2+}, Mg^{2+} or Ba^{2+}) can activate the phospholipase. The active site of the β-BuTX phospholipase A_2 subunit is similar to that of pancreatic phospholipase A_2, and the essential catalytic residue (A-chain histidine-48 in β-BuTX) can be blocked by modification with p-bromophenacylbromide (pBPB, Abe *et al.*, 1977a; Kondo *et al.*, 1978c,d). β-BuTX hydrolyses phospholipids such as phosphatidylcholine, phosphatidylethanolamine or phosphatidylserine containing fatty acids of various chain lengths (Abe *et al.*, 1977a; Strong and Kelly, 1977; Howard and Truog, 1977; Ng and Howard, 1978), being most potent at the phase transition temperature of the lipid (Strong and Kelly, 1977). At other temperatures, the detergent deoxycholate is required for phospholipolysis (Abe *et al.*, 1977a; Howard and Truog, 1977; Kelly *et al.*, 1975); the presence of proteins in natural membranes or, for example, in high- or low-density lipoprotein particles may also create phase boundaries, thus dispersing the phospholipids into a suitable physical state for hydrolysis (cf. the phospholipase assays of Howard and Truog, 1977; or Noël and Strong, 1982). Cholesterol inhibits the rate of phospholipolysis by β-BuTX (Strong and Kelly, 1977).

The phospholipase A_2 activity of β-BuTX appears to be important in its toxicity: Agents which modify the toxin so as to reduce its enzyme activity also, and to a similar extent, reduce its lethality (Strong *et al.*, 1977; Abe *et al.*, 1977a; Howard and

Truog, 1977). Furthermore, the toxicities of the β-BuTX-isotoxins appear to be related to the phospholipase activity of the different A-chains present (Kondo *et al.*, 1982b). However, other phospholipase enzymes which exhibit much greater phospholipase activity (e.g. bee venom phospholipase A, or the fraction IV phospholipase A of *B. multicinctus*, which is highly homologous and antigenically similar to the A-chain of β-BuTX, Kondo *et al.*, 1981), are not toxic. The phospholipase activity can, therefore, only account for one aspect of the action of β-BuTX.

1.3.2. Effects of β-Bungarotoxin at the Neuromuscular Junction

β-BuTX is toxic to mice with an LD_{50} (after intraperitoneal administration) of 0.01-0.02 μg/g body weight (Abe *et al.*, 1977a; Spokes and Dolly, 1980; Kondo *et al.*, 1982a). After a latent period of at least 60-80 min (Kelly and Brown, 1974; Eterovic *et al.*, 1975) the toxin causes hyperactivity and hyperexcitability (Chang and Lee, 1963; Eterovic *et al.*, 1975). Death occurs by respiratory failure as a result of neuromuscular blockade (Chang and Lee, 1963).

1.3.2.1. *Electrophysiological studies*

β-BuTX irreversibly inhibits muscle contraction as a result of nerve stimulation without affecting the responses elicited either by application of acetylcholine or carbachol (Chang and Lee, 1963; Dryden *et al.*, 1974), or by direct stimulation of the muscle (Kelly and Brown, 1974). The resting membrane potential and the action potential of the muscle, as well as the conduction properties of the nerve, are not affected (Chang *et al.*, 1973; Kelly and Brown, 1974; Abe *et al.*, 1976), indicating that the action of the toxin is confined to presynaptic nerve terminals. Although β-BuTX binds rapidly to its target sites, with the neuromuscular blockade proceeding even if the muscle is washed after only 15-20 min of incubation, the action of the toxin on rodent phrenic nerve-diaphragm preparations is characterized by a delayed onset of blockade, no matter how high the concentration of toxin used (Chang and Lee, 1963; Chang *et al.*, 1973; Kelly and Brown, 1974). The duration of the latent period is reduced when the nerve is stimulated, being shorter at higher stimulation frequencies (Chang *et al.*, 1973; Kelly and Brown, 1974).

β-BuTX exerts a triphasic effect on spontaneous neuro-

transmitter release as demonstrated in studies of the frequency of miniature endplate potentials (m.e.p.p.s; Abe *et al.*, 1976; Oberg and Kelly, 1976; Chang *et al.*, 1977b; MacDermot *et al.*, 1978; Alderdice and Volle, 1978; 1981): Shortly after application of the toxin the m.e.p.p. frequency is reduced to very low levels (phase 1). This inhibition is followed by a several-fold increase in m.e.p.p. frequency, or a period during which bursts of m.e.p.p.s may be observed (phase 2). M.e.p.p. frequency then slowly declines (phase 3), until neurotransmitter release is completely blocked. The amplitude of the m.e.p.p.s remains unchanged (Chang *et al.*, 1973; Alderdice and Volle, 1978). However, studies of the amplitude distribution of the m.e.p.p.s have shown β-BuTX to exert the three phases of its action preferentially on the main population of m.e.p.p.s, which are larger and show an overall bell-shaped frequency distribution, than on the smaller skew-distribution m.e.p.p.s (Llados *et al.*, 1980; see also MacDermot *et al.*, 1978).

β-BuTX similarly has a triphasic effect on evoked release, studied by measuring endplate potential (e.p.p.) amplitude, which is also transiently depressed and then increased (spontaneous twitching may be observed during phase 2, Abe *et al.*, 1976; Abe and Miledi, 1978) prior to blockade (Chang *et al.*, 1973; Abe *et al.*, 1976; Alderdice and Volle, 1981). Since the m.e.p.p. amplitude is not affected by β-BuTX (see above), the quantal content of neurotransmitter release also initially declines, prior to being transiently increased by the toxin (Chang *et al.*, 1973; Kelly *et al.*, 1975; Oberg and Kelly, 1976; Alderdice and Volle, 1981). Delayed release, the increase of m.e.p.p. frequency following an e.p.p. and believed to be caused by the transiently raised Ca^{2+} concentration in the nerve terminal, is similarly affected by β-BuTX (Kelly *et al.*, 1975; Oberg and Kelly, 1976)

These complex effects of β-BuTX are believed to be due to two distinct steps in its action (Kelly *et al.*, 1975; 1979; Abe *et al.*, 1976; Abe and Miledi, 1978; Caratsch *et al.*, 1981): The toxin initially binds to specific acceptors on nerve terminals. The phospholipase enzyme then attacks the phospholipids near the acceptors, perturbing the membrane properties and control of neurotransmitter release and eventually causing blockade of transmitter release.

Phase 1 of β-BuTX action, the initial decrease in m.e.p.p. frequency or e.p.p. amplitude, appears to be due to toxin binding

to the nerve terminal. This inhibition can still be observed under conditions in which the toxin's phospholipase activity has been inactivated, for example by (i) substituting the Ca^{2+} required for enzyme activity (Section 1.3.1 above) with Sr^{2+}, which can support neurotransmitter release (Abe and Miledi, 1978; Caratsch *et al.*, 1981; Chang *et al.*, 1977a; Kelly *et al.*, 1979); (ii) lowering the temperature (Caratsch *et al.*, 1981; Su and Chang, 1984); or (iii) chemically modifying the toxin with pBPB (Abe *et al.*, 1977b; Chang and Su, 1980; 1982; Kelly *et al.*, 1979). The toxin binding step requires divalent cations, with an apparent potency of $Ca^{2+} > Mg^{2+} > Sr^{2+} \simeq Co^{2+} > Mn^{2+}$ (Caratsch *et al.*, 1985), very different from the potency of these ions in promoting phospholipase activity. Furthermore, a non-specific phospholipase enzyme from bee venom does not mimic the initial depression of neurotransmitter release by β-BuTX, although it is capable of stimulating and blocking neurotransmitter release at high concentrations (Abe and Miledi, 1978).

The involvement of phospholipase activity in phase 2 of β-BuTX action is not clear. Under conditions where the phospholipase activity is inhibited (experiments in Sr^{2+} buffer, at reduced temperature, or using pBPB-modified β-BuTX) a transient initial decrease in e.p.p. amplitude may be observed, implying that both phases 1 and 2 still occur (Kelly *et al.*, 1979; Chang *et al.*, 1977a; Chang and Su, 1982; Su and Chang, 1984). However, the slow recovery (phase 2) reported could be due to residual phospholipase activity under the conditions cited, since none of the modifications described above reduce phospholipase activity by more than ≈90-95%. Furthermore, bee venom phospholipase A_2 at high doses also facilitates and eventually blocks neurotransmitter release (Abe and Miledi, 1978). Early work by Kelly *et al.* (1975) suggested that the time courses of the actions of β-BuTX on spontaneous, evoked and delayed release were similar. However, while the initial depression (phase 1) of both m.e.p.p. frequency and e.p.p. amplitude occur simultaneously, other authors report that the toxin's effects on e.p.p. amplitude (phases 2 and 3) are considerably faster than those on m.e.p.p. frequency (Alderdice and Volle, 1981), with m.e.p.p.s still being recorded at a time when e.p.p.s are completely blocked (Chang and Lee, 1963; Chang *et al.*, 1973; Abe *et al.*, 1976). Furthermore Chang *et al.* (1977b) find that for evoked release the first two phases, depression and facilitation,

are possible without latency, and suggest therefore that these effects are not due to the enzyme activity. It is possible that the facilitation of evoked release differs from the increase in spontaneous release in its dependence on the toxin's phospholipase activity. It is clear that at the time when m.e.p.p. frequencies are increased, the terminal membrane becomes permeable to a variety of inorganic cations (Masukawa and Livengood, 1982). This effect on membrane permeability may be responsible for the interference of β-BuTX with intraterminal Ca^{2+} metabolism: β-BuTX has been suggested to cause an accumulation of Ca^{2+} inside nerve terminals (Kelly and Brown, 1974; Oberg and Kelly, 1976; Abe *et al.*, 1976), possibly by inhibiting Ca^{2+} uptake by mitochondria (Wernicke *et al.*, 1975; Howard, 1975; see also Section 1.3.4).

The final irreversible blockade of neurotransmitter release is due to the enzyme activity of the toxin (Abe and Miledi, 1978; Caratsch *et al.*, 1981; Chang and Su, 1982; Su and Chang, 1984). Phospholipolysis can alter membrane properties, such as the ability of synaptic vesicles to fuse with the plasma membrane, or the properties of ion channels (cf. Okamoto, 1980; Reed, 1981; Hinzen and Tauc, 1977). Ng and Howard (1980) and Howard (1982) have suggested that β-BuTX may affect synaptic ion channels, possibly by binding directly to a channel protein and then hydrolysing the nearby annular phospholipids which may be essential for channel activity (see also Strong and Kelly, 1977). The final blockade does not appear to be due to depletion of available neurotransmitter stores, as suggested by Chen and Lee (1970). In fact Chang *et al.* (1973) reported that the acetylcholine content of the muscle was unchanged at a time when transmitter release was completely blocked, while Gundersen and Jenden (1981) found that the acetylcholine content of rat diaphragm was temporarily increased after β-BuTX treatment. The final cessation of neurotransmitter release could, alternatively, be due to a depletion of nerve terminal energy stores (see Section 1.3.4).

1.3.2.2. *Ultrastructural changes*

Electron microscopy studies of β-BuTX-intoxicated neuromuscular junctions confirm the presynaptic specificity of the toxin: Nerve terminals are progressively damaged, while muscle fibres, fibrocytes, endothelial cells and perineural Schwann cells appear normal (Chen and Lee, 1970; Abe *et al.*, 1976; Strong *et al.*,

1977). β-BuTX initially causes a decrease in the number of synaptic vesicles and an increase in the number of coated vesicles and of Ω-shaped profiles of open vesicles fused with the plasmalemma (Chen and Lee, 1970; Strong *et al.*, 1977; Landon *et al.*, 1980). The synaptic vesicle population appears to recover to near normal levels following presynaptic blockade (Landon *et al.*, 1980). Severe intoxication (exposure to 20-100 μg/ml β-BuTX for several hours) causes clumping of synaptic vesicles and swelling and vacuolization of mitochondria (Chen and Lee, 1970; Abe *et al.*, 1976; Strong *et al.*, 1977), until eventually nerve terminals disintegrate completely and are engulfed by Schwann cells (Abe *et al.*, 1976; Strong *et al.*, 1977). In fact, β-BuTX can be used as a selective denervating agent, producing effects similar to surgical denervation (Hofman and Thesleff, 1972; Chang *et al.*, 1975). Other presynaptic phospholipase neurotoxins have been shown to cause similar ultrastructural changes at peripheral nerve terminals (cf. Cull-Candy *et al.*, 1976; Gopalakrishnakone and Hawgood, 1984; Lee *et al.*, 1984).

Despite the similar ultrastructural effects of the presynaptic neurotoxins, and their similar triphasic actions at peripheral neuromuscular junctions (cf. Chang, 1985), which suggest that they all act by binding to nerve terminals and then alter the presynaptic plasma membrane by phospholipid hydrolysis, it should be noted that these toxins do not share a presynaptic target site. At high concentrations pBPB-modified β-BuTX can protect nerve terminals against the effects of β-BuTX (Abe *et al.*, 1977a; Chang and Su, 1980; Kelly *et al.*, 1979), while it enhances the potencies of taipoxin, crotoxin and notexin (Chang and Su, 1980). Moreover, simultaneous application of any two toxins (from β-BuTX, crotoxin and taipoxin) results in a mutual facilitation of their presynaptic effects (Chang and Su, 1980). The phospholipase neurotoxins also differ in their interaction with the facilitatory neurotoxins (see Section 1.5 below). It is likely, therefore, that these toxins bind to different molecular sites on the nerve terminal membrane and hydrolyse phospholipids at discrete but close sites, resulting in more rapid impairment of the transmitter release mechanism.

1.3.3. Specificity of β-Bungarotoxin in the Peripheral Nervous System

Although β-BuTX blocks neuromuscular transmission in amphibians, birds and mammals, its potency, like that of all phospholipase neurotoxins, differs widely in different species (Chang *et al.*, 1977b; Chang, 1985). Birds are very sensitive to β-BuTX, which is much more potent on the chick biventer cervicis nerve-muscle preparation than on rodent diaphragms (Lee and Tseng, 1969; Chang *et al.*, 1973, 1977b). Ultrastructural studies have shown that the action of β-BuTX is more rapid, and denervation is more complete at frog neuromuscular junctions than on rat muscle (Abe *et al.*, 1976). Among mammals, guinea-pigs are more sensitive to β-BuTX than mice and rats, respectively (Miura *et al.*, 1981), while neonatal rats appear less sensitive than adults (Gundersen, 1981).

In addition to its effects on skeletal muscle neuromuscular transmission, β-BuTX blocks nicotinic cholinergic transmission from preganglionic nerves in both the parasympathetic and sympathetic autonomic nervous system, while postganglionic (muscarinic or adrenergic) responses are not affected (cf. Kato *et al.*, 1977). Again, the potency of the toxin varies with the species examined. Thus β-BuTX blocks transmission in the avian ciliary ganglion (Chiappinelli *et al.*, 1981), and the response to vagal stimulation in the guinea-pig stomach (Miura *et al.*, 1981) and guinea-pig atrium (Muramatsu *et al.*, 1980), while mouse, rat and rabbit atria are not affected by the toxin (Miura *et al.*, 1981). Transmitter release from the postganglionic nerves to the guinea-pig or rat ileum (Chang and Lee, 1963; Kato *et al.*, 1977; Miura *et al.*, 1981) or from the nerve supply to the smooth muscle of canine airways (Hyatt and Russel, 1981) is not affected by the toxin. Likewise in the sympathetic nervous system, the preganglionic transmission across cat superior cervical ganglion is blocked by β-BuTX (Kato *et al.*, 1977), while the release of noradrenaline from the nerve terminals in the cat nictitating membrane preparation, and the adrenergic responses of the atrial preparation, are not affected (Kato *et al.*, 1977; Muramatsu *et al.*, 1980).

Chronic application of β-BuTX to avian, rat or amphibian embryos retards their development (Olek, 1980; Creazzo and Sohal, 1981; Tümmers *et al.*, 1986). The nicotinic cholinergic innervation to skeletal muscle is selectively killed, and the motoneurone cell bodies disappear from the ventral horn of the spinal cord

(Hirokawa, 1978; Pittman *et al.*, 1978; Olek, 1980; Harris, 1981). As a result muscle fibres become disorganized in structure, while a major amount of the muscle tissue is replaced by fat deposits or connective tissue (Mao Chen *et al.*, 1978; Hirokawa, 1978; Harris, 1981). The innervation to the heart and the structure of heart muscle appear normal (Hirokawa, 1978). Similarly, the innervation to the adrenal glands is removed (Tümmers *et al.*, 1986), but the chromaffin cells develop normally (Hirokawa, 1978; Tümmers *et al.*, 1986). The autonomic fibres around blood vessels, and Auerbach's and Meissner's ganglia, are not affected by the toxin (Harris, 1981; Hirokawa, 1978). However, there is a great depletion of neurones in the sensory ganglia (e.g. spinal ganglia, spiral ganglia and olfactory epithelium innervation; Hirokawa, 1977; 1978; Pittman *et al.*, 1978).

In invertebrates, β-BuTX blocks transmission to the body wall muscle of the earthworm, *Lumbricus terrestris* (Hassoni *et al.*, 1985), while the glutamatergic transmission in locust muscles (see Abe *et al.*, 1977a; Tse *et al.*, 1980) and the motor nerve neuromuscular junctions of *Drosophila* larvae (Antonov *et al.*, 1979) are resistant to the toxin. Likewise, β-BuTX does not block transmitter release from the squid giant synapse (Abe *et al.*, 1977a).

1.3.4. Effects of β-Bungarotoxin in the Central Nervous System

Although β-BuTX does not cross the blood-brain barrier when injected peripherally (Lee and Tseng, 1966), its toxicity is increased at least 1,000× to 50 ng/g body weight when administered stereotaxically into rat brain (Hanley and Emson, 1979; Othman *et al.*, 1982). β-BuTX has been shown to block synaptic transmission in rat olfactory cortex and hippocampus slices (Dolly *et al.*, 1980; Halliwell *et al.*, 1982; Halliwell and Dolly, 1982). The primary effect of the toxin is an irreversible inhibition of neurotransmitter release; thus β-BuTX blocks synaptically evoked transmission at a time when axonal conduction, or the cell's responses to direct current injections or bath applied glutamate or aspartate are unaffected (Halliwell and Dolly, 1982). On prolonged exposure to the toxin presynaptic action potentials are decreased and cells become less excitable. While β-BuTX binds when applied in Ca^{2+}-free Sr^{2+} buffer, the presence of Ca^{2+}, and hence the toxin's phospholipase A_2, is required for full activity. This was also confirmed in studies using pBPB-modified β-BuTX (Halliwell *et al.*, 1982). Thus,

again the toxin appears to act by initially binding to specific acceptors on the presynaptic membrane, and then causing generalised membrane damage through phospholipase A_2 activity.

β-BuTX affects a large number of neurones in the central nervous system. In embryos treated with the toxin the brains, cerebella and spinal cords are reduced in size, while neuronal cell groups are destroyed or disorganized (Hirokawa, 1978; 1979; Creazzo and Sohal, 1981; Zilles *et al.*, 1981). In the retina, the ganglion cells and some neurones in the inner nuclear layer are killed (Hirokawa, 1978; see also Rehm *et al.*, 1982); this selective toxicity of β-BuTX has been exploited in the preparation of pure photoreceptor cell cultures (Politi and Adler, 1986). Toxicity again appears to require the phospholipase activity (cf. Creazzo and Sohal, 1981). In adult animals intracerebral injections of sublethal doses of β-BuTX cause pronounced focal degeneration of the nervous tissue and widespread neuronal cell death (Hanley and Emson, 1979; Gulya *et al.*, 1984).

In contrast to the peripheral nervous system, where β-BuTX is only active at nicotinic cholinergic synapses (Section 1.3.3), there is an apparent lack of neurotransmitter specificity in the toxin's central action. Intracerebral injections of β-BuTX produce both short- and long-term changes in the acetylcholine and choline content of various brain areas (Newton *et al.*, 1983; Gulya *et al.* 1984). In the chick retina, treatment with β-BuTX causes a selective decrease in the content of the cholinergic and GABAergic markers, choline acetyl transferase and glutamate decarboxylase, respectively (Rehm *et al.*, 1982). These markers are also decreased after intracerebral injections of the toxin (Hanley and Emson, 1979; Gulya *et al.*, 1984). The electrophysiological studies of Halliwell *et al.* (1982) and Halliwell and Dolly (1982) have shown that transmission to glutamate- and aspartate-sensitive neurones is blocked by β-BuTX. Furthermore, β-BuTX inhibits the uptake and increases the basal release of acetylcholine (Wernicke *et al.*, 1974; Sen *et al.*, 1976; Dolly *et al.*, 1980; Fletcher and Middlebrook, 1986), glutamate (Tse *et al.*, 1980; Smith *et al.*, 1980), aspartate (Smith *et al.*, 1980), GABA (Wernicke *et al.*, 1974; Ng and Howard, 1978; Tse *et al.*, 1980; Smith *et al.*, 1980), serotonin (Wernicke *et al.*, 1974) and catecholamines (Wernicke *et al.*, 1974; Fletcher and Middlebrook, 1986) from brain minces, homogenates, synaptosomes or synaptosome-enriched brain fractions. The release

of neurotransmitters is accompanied by an efflux of the cytoplasmic marker enzyme lactate dehydrogenase (Wernicke *et al.*, 1974; Tse *et al.*, 1980; Halliwell *et al.*, 1982); this efflux is strictly Ca^{2+}-dependent and does not occur in Sr^{2+}-containing buffers (Wernicke *et al.*, 1975; Dolly *et al.*, 1980; Tse *et al.*, 1980; Rugolo *et al.*, 1986). Modification of β-BuTX with pBPB also reduces the releasing potency of the toxin (Halliwell *et al.*, 1982). Thus, it appears that the phospholipase A_2 enzyme activity of β-BuTX makes synaptosomes permeable or leaky to these compounds. In accordance with this suggestion, a number of non-toxic phospholipase A_2 enzymes from various sources have been shown to mimic the neurotransmitter releasing activity of β-BuTX, although these enzymes are less potent than the presynaptic toxin (Wernicke *et al.*, 1974; Ng and Howard, 1978; Sen and Cooper, 1978; Dolly *et al.*, 1980; Fletcher and Middlebrook, 1986). Even fatty acids can release some neurotransmitters from synaptosomes (Wernicke *et al.*, 1975; Sen and Cooper, 1978). However, low concentrations of β-BuTX (up to 1μM) do not cause any gross damage to synaptosomes as revealed by electron microscopy (Wernicke *et al.*, 1974; Sen *et al.*, 1976; Tse *et al.*, 1980).

Other studies on synaptosome and brain slice preparations have revealed that β-BuTX depolarizes synaptosomes (Sen and Cooper, 1978; Ng and Howard, 1978; Nicholls *et al.*, 1985; Rugolo *et al.*, 1986), thereby causing an increase in synaptosomal respiration rates (Wernicke *et al.*, 1975; Smith *et al.*, 1980; Tse *et al.*, 1980), a decrease in ATP and creatine phosphate levels (Wernicke *et al.*, 1975; Swanson, 1977) and K^+ content (Swanson, 1977; Smith *et al.*, 1980), and an uncoupling of mitochondria, thus interfering with their ability to buffer synaptosomal Ca^{2+} levels (Wagner *et al.*, 1974; Kelly *et al.*, 1975; Wernicke *et al.*, 1975; Howard, 1975; Ng and Howard, 1980). All these effects appear to be due to two distinct phospholipase A_2-dependent actions of the toxin (for details, see Nicholls *et al.*, 1985; Rugolo *et al.*, 1986):

1) Upon binding to acceptors on synaptosomes (see below), β-BuTX initially depolarizes synaptosomes by directly permeabilizing the plasma membrane. As specific binding is a pre-requisite for this step it is only weakly mimicked by non-toxic phospholipase enzymes.

2) Continued phospholipase activity produces fatty acids, which uncouple mitochondria, thus interfering with synaptosomal

respiration, ATP stores, Ca^{2+} metabolism and neurotransmitter uptake. This step is common to β-BuTX and non-toxic phospholipase enzymes, and is prevented when bovine serum albumin (BSA), which binds the fatty acids released, is included in the incubation media. A similar indirect action via fatty acids probably accounts for the reported uncoupling of sarcoplasmic reticulum membranes (Lau *et al.*, 1974) and purified synaptic vesicles (Anderson and Parsons, 1986) by β-BuTX.

1.3.5. Identification of Specific Acceptors for β-Bungarotoxin

It is clear from the studies described above that β-BuTX exerts its effects on neurones by binding to specific acceptor sites and subsequently hydrolysing nearby membrane phospholipids (see Sections 1.3.2 and 1.3.4). Direct evidence for the existence of toxin acceptors has been obtained from binding studies using both ^{3}H- and ^{125}I-labelled biologically active derivatives of the toxin (Othman *et al.*, 1982; Rehm and Betz, 1982; Dolly *et al.*, 1987). Specific high affinity acceptors for β-BuTX have thus been identified on synaptosomes from both chick and rat brain (K_d = 0.2-0.6 nM, B_{max} =50 and 300 fmol/mg protein in synaptosomes from chick and rat brains, respectively, Rehm and Betz, 1982; Dolly *et al.*, 1987). Under certain condition (e.g. incubations in imidazole buffer), a second, lower affinity binding site for ^{125}I-β-BuTX can also sometimes be detected (Dolly *et al.*, 1987; Section 1.5). Protease treatment of synaptosomes substantially decreases the specific toxin binding, indicating that the acceptors are proteinaceous (Othman *et al.*, 1982). The binding is dependent on divalent cations (Ca^{2+} or Sr^{2+}, Rehm and Betz, 1982). Only unlabelled β-BuTX can potently displace the binding of radiolabelled β-BuTX, while other phospholipase enzymes and presynaptic phospholipase A_2 toxins cause only a weak inhibition, possibly by interfering with specific phospholipids required for the binding (Othman *et al.*, 1982; Rehm and Betz, 1982).

When radiolabelled β-BuTX is cross-linked to synaptosomes prior to analysis of the synaptosomal proteins by sodium dodecyl sulphate polyacrylamide gel electrophoresis and autoradiography, a polypeptide of M_r =95,000d is specifically labelled (Rehm and Betz, 1983). The β-BuTX acceptor protein has been successfully solubilized in an active form using Triton X-100 (Rehm and Betz, 1984); it has an estimated molecular weight of ≈430,000d and, thus, would

obviously include the 95,000d peptide identified by cross-linking.

One of the most important findings from the studies with radiolabelled β-BuTX was the observation that the binding of the toxin could be specifically inhibited by the mamba venom polypeptides toxin I (Othman *et al.*, 1982) and dendrotoxin (Othman 1983). These facilitatory toxins also have potent effects on neurotransmission, but are devoid of phospholipase activity (see below), and have therefore proved very useful in the study of nervous mechanisms and the action of β-BuTX (see also Section 1.5).

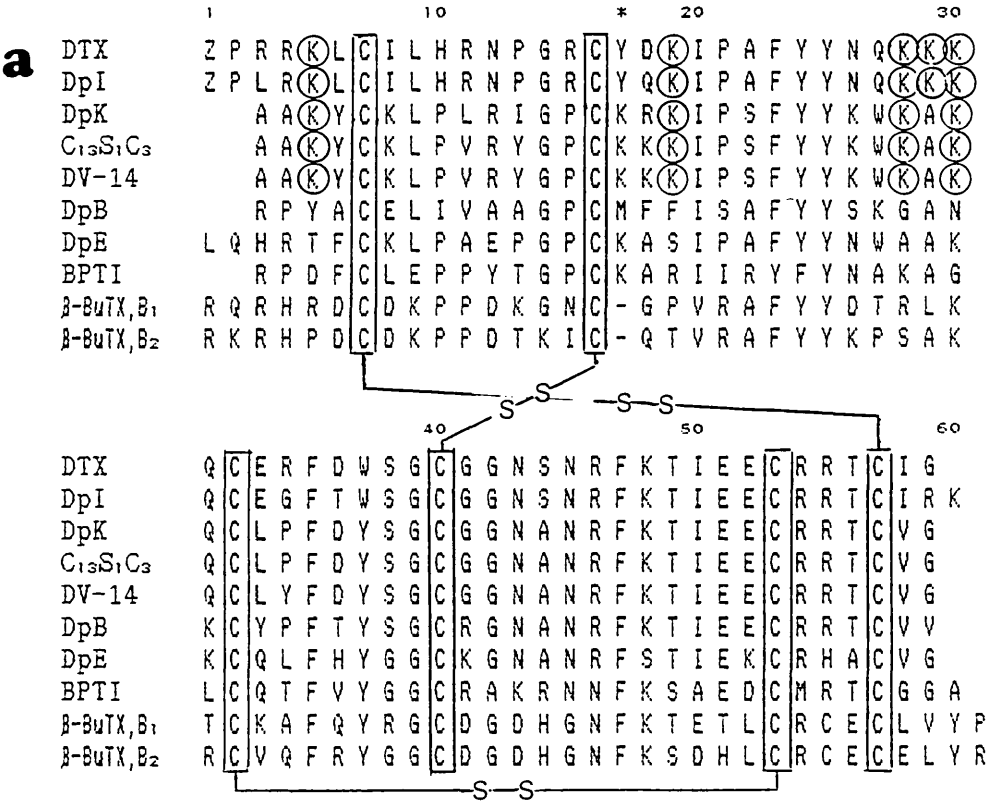
1.4. Dendrotoxin and Facilitatory Neurotoxins

1.4.1. Isolation and Structure of Dendrotoxin and its Homologues

The venom of the Eastern green mamba, *Dendroaspis angusticeps*, has been shown to facilitate neuromuscular transmission (Barret and Harvey, 1979). A protein which appears to be responsible for most of this facilitatory action has been isolated (Harvey and Karlsson, 1980) and called dendrotoxin, DTX.

DTX is a highly basic, single chain polypeptide of 59 amino acid residues (formula molecular weight =7,053d) cross-linked internally by three disulphide bridges (Harvey and Karlsson, 1980). Its amino acid sequence ($C_{13}S_2C_3$, Joubert and Taljaard, 1980) is very similar to that of BPTI (Figure 1.2a). In fact, DTX is a member of a family of BPTI homologues found in various mamba venoms. This includes $C_{13}S_1C_3$ which is also found in *D. angusticeps* venom (Joubert and Taljaard, 1980) and four polypeptides from the black mamba, *D. polylepis* (proteins B and E, and toxins I and K, see legend to Figure 1.2). A further toxin, DV-14, is found in the venom of the Western green mamba, *D. viridis* (R. Shipolini, unpublished; sequence cited in Mehraban *et al.*, 1986). Despite the sequence homologies, only protein E has measurable antiprotease activity (Strydom, 1976; Dufton, 1985). Five of the homologous proteins (DTX and $C_{13}S_1C_3$, toxins I and K, and DV-14), out of a large number of protease inhibitors and homologues tested, have been shown to potentiate neuromuscular transmission (Harvey, 1982; Harvey and Karlsson, 1982; Harvey *et al.*, 1984a). Figure 1.2a shows that these presynaptically active proteins share four conserved lysine residues at positions 5, 19, 28 and 30 (Harvey and Anderson, 1985; for further comparisons of the sequences, see Dufton, 1985). Protein B exhibits neither anti-protease nor pre-

Figure 1.2. Structures of DTX and its homologues



(a) The amino acid sequences of DTX and its homologues. The sequences are taken from: DTX (=$C_{13}S_2C_3$) and $C_{13}S_1C_3$, Joubert and Taljaard (1980). Toxins I and K from *D. polylepis* (DpI and DpK), Strydom (1973) and Strydom (1977). DV-14 from *D. viridis*, cf. Mehraban *et al.* (1986). Proteins B and E from *D. polylepis* (DpB and DpE), Strydom and Joubert (1981) and Joubert and Strydom (1978), respectively. BPTI, Kassel *et al.* (1965). β-BuTX B-chains (B_1 and B_2), Kondo *et al.* (1978b; 1982a). Disulphide bridges are indicated, and the conserved lysine residues (K) in the neuroactive homologues are circled. The one-letter code for amino acids has been used (see *Eur. J. Biochem.*, *5*, 151-153); Z represents pyroglutamic acid.
(b) The proposed α carbon skeleton of DTX, adapted from Dufton (1985). The conserved lysine residues are shown as ●, while lysine-29 in DTX and toxin I is shown as ○.

synaptic facilitatory activity (Harvey *et al.*, 1984a).

In agreement with the sequence homologies, the disulphide bridge structure and the protein folding/unfolding pathways are conserved between BPTI and the protease inhibitor homologues (Hollecker and Creighton, 1983). Furthermore, the structures of various DTX homologues in solution have been shown to be similar to that of BPTI using both nuclear magnetic resonance (Arseniev *et al.*, 1982; Keller *et al.*, 1983; Pardi *et al.*, 1983) and circular dichroism (Hollecker *et al.*, 1981) techniques. The conformation of DTX may, therefore, be assumed to be similar to the three-dimensional structure of BPTI as determined by X-ray crystallography (Huber *et al.*, 1971; Deisenhofer and Steigemann, 1975; see Figure 1.2b). On this basis DTX would appear to be a stable pear-shaped molecule, with two short α-helical regions at the N- and C-termini, separated by two loops of the peptide backbone, which form an extended anti-parallel double-stranded β-pleated sheet. The amino acid residues unique to the facilitatory toxins (see above) are highlighted in Figure 1.2b. Three of these (lysines 5, 28 and 30) are located in the same region of the molecule, forming (together with lysine 29 in DTX and toxin I) a highly charged domain. It has been suggested that this region of the molecule may be involved in the binding of DTX to its target sites (Harvey *et al.*, 1984a,b).

1.4.2. Effects of Facilitatory Neurotoxins on Neurotransmission

DTX (Harvey and Karlsson, 1980), toxins I (Harvey, 1982; Harvey and Karlsson, 1982) and K (Harvey and Karlsson, 1982), and toxin $C_{13}S_1C_3$ from *D. angusticeps* (Harvey *et al.*, 1984a) facilitate neurotransmitter release at motor nerve endplates. In the chick biventer cervicis preparation DTX increases the response of the muscle to indirect stimulation by 200-250%, without affecting its sensitivity to exogenous acetylcholine, carbachol, or high external K^+ concentrations (Harvey and Karlsson, 1980); thus the toxin must be exerting its effect presynaptically. Toxins I and K show similar activity (Harvey and Karlsson, 1982). Although the binding of the toxins is rapid (i.e. within 15 min), and independent of the presence of Ca^{2+} in the incubation medium, nerve stimulation (Harvey *et al.*, 1984a) or temperature (Harvey and Anderson, 1985), their effect on neuromuscular transmission is slow to develop, apparently irreversible, and suppressed at low temperatures (e.g.

at room temperature compared to 37°C, Harvey and Anderson, 1985). In the mouse phrenic nerve-hemidiaphragm, DTX and toxin I increase the quantal content of acetylcholine release, while, on prolonged exposure, the toxins cause stimulation by single pulses to result in multiple e.p.p.s; spontaneously occurring e.p.p.s are also observed (Anderson and Harvey, 1985). Similar effects have been described in studies with DTX on toad sciatic nerve-sartorius muscle (Harvey and Gage, 1981) and when using toxin I on frog cutaneous pectoris nerve muscle preparations (Anderson *et al.*, 1987).

The toxins also potentiate neurotransmitter release in the autonomic nervous system (Harvey *et al.*, 1984a; Anderson, 1985), where the onset of toxin action is apparently faster than at neuromuscular junctions, and the effects are readily reversed by washing (Harvey *et al.*, 1984a). In the predominantly sympathetically innervated rodent vas deferens preparation, both toxin I and DTX immediately increase the amplitude of neurally evoked twitches (Anderson, 1985). In chick oesophagus, which is largely parasympathetically innervated, toxin I (Harvey *et al.*, 1984a) and DTX produce a gradual increase in the amplitude of neurally evoked twitches and, on prolonged exposure, induce multiple contractures or rhythmic contractions (Anderson, 1985). When the mechanism of augmentation of the neurally evoked responses was investigated using a variety of drugs, it could be inferred that the toxins act directly on the presynaptic nerves in these preparations (Anderson, 1985).

Although DTX is not very toxic when administered peripherally (LD_{50} in mice ≈23 μg/g body weight, Joubert and Taljaard, 1980), its lethality is increased 10,000× on intra-cerebroventricular injection into rats: DTX causes severe convulsions within minutes of administration (Mehraban *et al.*, 1986); the minimal lethal doses of DTX and toxin I are 2.5 and 0.5 ng/g body weight, respectively (Othman, 1983; Mehraban *et al.*, 1985). Electrophysiological studies using transverse hippocampal slices from rat or guinea-pig have shown that DTX causes a general potentiation of neurotransmitter release and an increase in cell excitability (Docherty *et al.*, 1983). Spontaneous or regenerative synaptic activity is common, individual neurones frequently showing bursts of action potentials (Dolly *et al.*, 1984). The level of inhibitory activity is also increased, apparently by DTX facilitating the excitatory input to inhibitory neurones, or potentiating the output

of an inhibitory neurotransmitter, most probably GABA (Dolly *et al.*, 1984; 1986).

1.4.3. Specific Inhibition of Potassium Currents by Dendrotoxin and Toxin I

In order to pinpoint the primary action of DTX in hippocampal slices (see Section 1.4.2 above) cells were synaptically uncoupled by blocking Na^+ currents with tetrodotoxin and examined by current- and voltage-clamp techniques (Dolly *et al.*, 1984; 1986; Halliwell *et al.*, 1986). These studies revealed for the first time that DTX reduces a variant of the rapidly activating transient outward K^+ current known as I_A (the A-current, Gustafsson *et al.*, 1982; Rogawski, 1985), without any effect on Ca^{2+} currents or other K^+ currents present in this preparation (Dolly *et al.*, 1984; Halliwell *et al.*, 1986). In this respect the toxin's action is similar to that of 4-aminopyridine (4-AP); however DTX is far more specific in its action and ≈2,000× more potent, 50-300 nM DTX reducing I_A by 60-75% after 1 hr of incubation. Toxin I, at a concentration as low as 10 nM, reduces I_A by 40% in only 30 min (Halliwell *et al.*, 1986).

Another DTX-sensitive K^+ current can be detected in the A-cells of rat nodose ganglia (Stansfeld *et al.*, 1986; Dolly *et al.*, 1987). Although the fast activation time of this current is similar to that of I_A, it differs from I_A in showing only slow and incomplete inactivation ($t_{½}$ of current decay at 30°C =15-24 s, compared with 50-100 ms for the hippocampal I_A, Dolly *et al.*, 1987), and in being much more sensitive than I_A to blockade by both 4-AP (1-30 μM) and DTX (3-10 nM, ED_{50} =2.1 nM; Dolly *et al.*, 1987). Inhibition of this slowly inactivating current by DTX and 4-AP suppresses spike adaptation and leads to repetitive firing in the normally quiescent A-cells (Stansfeld *et al.*, 1986). A similar fast activating, non-inactivating current which is highly sensitive to DTX (0.14-1.4 nM) exists in guinea-pig dorsal root ganglion neurones (Penner *et al.*, 1986). The transient and very rapidly inactivating variant of I_A found in other cells in the nodose or dorsal root ganglia, however, is insensitive to DTX at concentrations up to 800 nM, and even 1-5 mM 4-AP produces only a sub-total blockade (Penner *et al.*, 1986; Stansfeld *et al.*, 1987)

DTX and toxin I also affect K^+ currents on motor nerves. At the frog node of Ranvier, DTX (0.1-30 nM) reduces the amplitude

and prolongs the duration of action potentials (Weller *et al.*, 1985). Voltage-clamp studies have revealed that this is due to the specific blockade of a proportion of the K^+ current by DTX. In the same preparation toxin I similarly reduces the global K^+ current, blocking with high efficacy (ED_{50} =0.4 nM) only one of the three characteristic components of the nodal K^+ current (Benoit and Dubois, 1986; cf. Dubois, 1981). This current, I_{Kf1}, inactivates very slowly and is sensitive to externally applied 4-AP (≃10 μM, Dubois, 1981). Presumably a current similar to I_{Kf1} also occurs at the frog neuromuscular junction, where recordings from extracellular electrodes placed on the perineural sheath have revealed that a proportion of the wave corresponding to the K^+ current is reduced by toxin I (Anderson *et al.*, 1987).

Thus DTX and toxin I appear to be able to inhibit a family of defined rapidly activating and 4-AP sensitive K^+ conductances, being apparently most potent on the slowly inactivating currents and least effective toward the rapidly inactivating K^+ conductance variants (Dolly *et al.*, 1987). The blockade of certain K^+ currents by DTX and toxin I can explain their effects on neurotransmission (Section 1.4.2). The toxins increase the excitability of the target cells and frequently evoke spontaneous or repetitive firing, indicating that the K^+ channels blocked are important in controlling repolarization and excitation thresholds of neurones.

1.4.4. Functional Neuronal Acceptors for Dendrotoxin

DTX can be radioiodinated to high specific activities (200-400 Ci/mmol) without loss of biological activity (Black *et al.*, 1986). The ^{125}I-labelled DTX (^{125}I-DTX) binds saturably and with high affinity (K_d =0.3-0.4 nM) to acceptors on rat cerebrocortical or hippocampal synaptosomes (B_{max} =1-1.2 pmol/mg protein; Mehraban *et al.*, 1984; Black *et al.*, 1986), or synaptic plasma membranes (B_{max} =1.4-1.7 pmol/mg of protein; Black *et al.*, 1986). This binding is highly sensitive to treatment of the synaptosomes with trypsin or chymotrypsin, and abolished by their acidification or heating, indicating that the acceptors are proteinaceous (Black *et al.*, 1986). The specificity of the ^{125}I-DTX-acceptor interaction is evident from the lack of its inhibition by a number of other neurotoxins (crotoxin or its subunits, apamin, and, in Ca^{2+}-free media, taipoxin), Ca^{2+} channel antagonists (D600, nifedipine, nimodipine) or selective K^+ channel blockers (tetraethylammonium

chloride, 4-AP, thienylcyclopiperidine; Black *et al.*, 1986). In Ca^{2+}-containing buffers, taipoxin and bee venom phospholipase A, but not the phospholipase from *Naja melanoleuca*, inhibit ^{125}I-DTX bindig with low potency, suggesting that the interaction of the toxin with its acceptors may depend on conformational stabilization by certain membrane phospholipids. Only the facilitatory mamba neurotoxins efficiently inhibit ^{125}I-DTX binding to synaptosomes, their relative potencies (toxin I > DTX ≃ DV-14 > protein E >> protein B) being related to their toxicities on intra-cerebroventricular injection into rat brain (Mehraban *et al.*, 1985; Black *et al.*, 1986); thus it appears that the DTX acceptors mediate the convulsive symptoms (Mehraban *et al.*, 1986) and toxicity of DTX *in vivo*.

In contrast to these observations on rat brain synaptic membranes, both equilibrium and kinetic measurements of ^{125}I-DTX binding on chick brain synaptic membranes demonstrate the existence of two populations of membraneous acceptors with different affinities for the toxin (K_d ≃0.5 and 15 nM; B_{max} ≃90 and 400 fmol/mg protein, respectively; Black and Dolly, 1986a). The facilitatory homologues of DTX antagonise ^{125}I-DTX binding to both acceptor subtypes in proportion to their central neurotoxicities, while no inhibition of ^{125}I-DTX binding can be observed with various other toxins (e.g. crotoxin or apamin), trypsin inhibitors and lectins (Black and Dolly, 1986a).

When bound ^{125}I-DTX is cross-linked to its acceptors on rat brain synaptosomes using dimethylsuberimidate or dimethylpimilimidate prior to solubilization and analysis by sodium dodecyl sulphate polyacrylamide gel electrophoresis, exposure of the gel to X-ray film identifies a single labelled polypeptide of M_r =65,000d (Mehraban *et al.*, 1984). Likewise cross-linking of the radiolabelled toxin to chick synaptic membranes reveals a polypeptide with M_r =75,000d, together with a minor component of 69,000d (Black and Dolly, 1986a). These polypeptides are likely to be part of a larger oligomeric protein(s), as radiation inactivation of the DTX binding component in rat synaptosomal membranes reveals an apparent acceptor size of >200,000d (Dolly *et al.*, 1984; Black, 1986). Successful solubilization of this component in active form has been achieved using detergents such as Triton X-100, deoxycholate or lubrol (Mehraban *et al.*, 1985; Black *et al.*, 1988). The solubilized protein binds ^{125}I-DTX with high affinity, is sensitive to

trypsin treatment or heating and has an estimated M_r =405,000-465,000d.

1.5. Interactions Between the Facilitatory Neurotoxins and β-Bungarotoxin

The amino acid sequence of the B-chain of β-BuTX (Kondo *et al.*, 1978b) shows considerable homology to that of Kunitz-type protease inhibitors such as BPTI and the facilitatory neurotoxins (Kondo *et al.*, 1982a; see Section 1.3.1 and Figure 1.2). Accordingly, both DTX and toxin I prolong the survival time of mice injected intra-peritoneally with β-BuTX (Othman, 1983). In the indirectly stimulated chick biventer cervicis preparation, pre-incubation with DTX, toxin I or K significantly reduces the presynaptic blocking activity of β-BuTX (Harvey, 1982; Harvey and Karlsson, 1982). Likewise, DTX does not cause any twitch augmentation in muscles pre-incubated in 50 nM β-BuTX (in Sr^{2+}-containing buffer to inhibit the phospholipase activity; the action of DTX is not changed in this buffer). On returning the preparation to Ca^{2+}-containing medium, a slow blockade of neurotransmission, characteristic of β-BuTX, is observed, indicating that this toxin remains bound to its target sites. No similar antagonism has been observed between DTX and other phospholipase neurotoxins (crotoxin, notexin or taipoxin), although crotoxin and notexin can augment the actions of DTX (Harvey and Karlsson, 1982). These results indicate that β-BuTX and the facilitatory neurotoxins may interact at a common or related site in the presynaptic terminal membrane. The toxins may have a similar mechanism for their facilitatory actions as β-BuTX, like DTX and toxin I, has recently been shown to reduce a non-inactivating K^+ current in guinea-pig dorsal root ganglion neurones (Petersen *et al.*, 1986), and to decrease the K^+ current wave observed in extracellular recording at the frog neuromuscular junction (Anderson *et al.*, 1987).

Similarly β-BuTX and DTX appear to interact at their target sites in the central nervous system. Thus DTX blocks the β-BuTX-induced depolarization of guinea-pig synaptosomes (Nicholls *et al.*, 1985; Rugolo *et al.* , 1986). Furthermore both toxin I and DTX completely inhibit the high affinity binding of ^{3}H-β-BuTX or ^{125}I-β-BuTX to rat or chick brain synaptosomes/synaptosomal membranes or to the solubilized β-BuTX acceptor from chick brain (Othman

et al., 1982; Othman, 1983; Dolly *et al.*, 1987; Rehm and Betz, 1984). In agreement with this interaction, β-BuTX has been shown to inhibit completely and with high efficacy the ^{125}I-DTX binding at the high affinity DTX acceptor sub-type in chick brain membranes (Black and Dolly, 1986a), while ^{125}I-DTX binding at the other site remains unaffected.

The interaction of the two toxins on rat brain synaptosomes or synaptic plasma membranes is more complicated. As indicated in Sections 1.3.5 and 1.4.4, both ^{125}I-β-BuTX and ^{125}I-DTX bind saturably and with high affinity to synaptosomes suspended in Krebs Ringer or Tris/HCl buffer; however, the acceptor site content of ^{125}I-DTX binding is much higher than that of ^{125}I-β-BuTX (the ratio of B_{max} for ^{125}I-DTX ÷ B_{max} for ^{125}I-β-BuTX ≃3). Consistent with this disparate stoichiometry, β-BuTX competes with ^{125}I-DTX binding with low efficacy (K_I >400 nM), and the inhibition is incomplete even when high concentrations (μM) of β-BuTX are used (Dolly *et al.*, 1984; 1987; Black *et al.*, 1986). Furthermore, while the binding of radiolabelled β-BuTX is always dependent on Ca^{2+} or Sr^{2+} (as is the inhibition by β-BuTX of ^{125}I-DTX binding in chick membranes, see above), the weak competition of β-BuTX with ^{125}I-DTX binding on rat brain synaptosomes appears to be independent of the divalent cation concentration (Black *et al.*, 1986; Dolly *et al.*, 1987). In similar binding studies, when an imidazole buffer is used instead of Krebs Ringer, the properties of ^{125}I-DTX binding on synaptosomes/synaptosomal plasma membranes remain unchanged, while the levels of non-specific binding observed with the ^{125}I-β-BuTX preparations are reduced. In addition, two ^{125}I-β-BuTX binding sites with different affinities may be distinguished, although the low affinity site is not yet well characterized (Dolly *et al.*, 1987). β-BuTX also shows an improved efficacy in inhibiting ^{125}I-DTX binding in this buffer, and its competition with ^{125}I-DTX becomes Ca^{2+} dependent (A.L. Breeze, personal communication). Thus, the change in the buffer used unmasks a second Ca^{2+} dependent lower affinity binding site for β-BuTX, which can be detected both in direct binding studies with this toxin and in its competition with ^{125}I-DTX. β-BuTX also competes with ^{125}I-DTX binding to solubilized DTX acceptors. When the assay conditions are optimized, β-BuTX can completely inhibit the binding of ^{125}I-DTX with an average K_I =9 nM (Black *et al.*, 1988). Thus, while the rat brain DTX acceptors appear homogeneous with regard to their interaction

with ^{125}I-DTX and their solubilized molecular weight, they show some heterogeneity in their interactions with β-BuTX.

1.6. Conclusions

This introduction has demonstrated the importance of membrane proteins in neuronal function. Furthermore two potent neurotoxins have been identified: β-BuTX and DTX perturb neuronal processes by interacting with specific membrane-bound acceptor proteins. Electrophysiological studies have indicated that the primary effect of these toxins is an attenuation of certain rapidly activating K^+ currents. K^+ Channels are very important in action potential conduction, the regulation of neuronal excitability and the control of neurotransmitter release. These channels have been extensively studied electrophysiologically but have not been characterized biochemically, unlike Na^+ or Ca^{2+} channels, because until now no specific ligands, which could be used as probes in their isolation, have been available. Only recently have probes for K^+ channels been discovered. For example, noxiustoxin from *Centruroides noxius* has been shown to block the rectifying K^+ current, I_K, in squid neurones (Carbone *et al.*, 1982), and the red pepper toxin capsaicin has been demonstrated to affect part of the fast K^+ current, I_{Kf2}, of the frog node of Ranvier (Dubois, 1982). DTX, however, appears to be more potent and specific for a distinct family of K^+ currents than either of these other toxins, suggesting that it interacts directly with K^+ channel proteins.

In the present study, autoradiography methods have been used to study the distribution of the acceptors for β-BuTX and DTX in the central nervous system. In Chapter 2 the binding properties of radioiodinated derivatives of the toxins on cryostat sections will be described. These studies defined optimal labelling conditions for the quantitative sheet film autoradiography studies with ^{125}I-β-BuTX and ^{125}I-DTX, detailed in Chapters 3 and 4, respectively. High resolution localization of the acceptors by electron microscope autoradiography has also been attempted (Chapter 5).

CHAPTER 2

Identification of Acceptors for Dendrotoxin and β-Bungarotoxin on Cryostat Sections

2.1. Introduction

The potent actions in the central nervous system of β-BuTX (Section 1.3.4) and DTX (Section 1.4.2), and the demonstration that both toxins bind specifically and with high affinity to rat brain synaptosomes (Sections 1.3.5 and 1.4.4) raise the question of where precisely the toxin acceptors are located. Details of the anatomical distribution of these acceptors in various brain regions would be particularly interesting in view of the demonstrated blockade of rapidly activating K^+ currents by these toxins, and may clarify the relationship between the acceptors for β-BuTX and DTX (see Section 1.5). With the availability of biologically active radiolabelled derivatives of β-BuTX and DTX, autoradiographic localization studies have become feasible. Cryostat sections from various areas of rat brain can be incubated with the radiolabelled toxins, which may then be visualized by exposure to photographic film or emulsion.

To ensure that relevant acceptors are being localized, autoradiography should be preceeded by binding studies on cryostat sections. Such sections represent a whole-brain preparation, containing synapses, axons, cell bodies and dendrites of various types of neurones, together with glial cells and myelin, and occasional blood vessels. A mixture of anatomical areas may also be present. Thus binding studies with whole brain cryostat sections are equivalent to experiments on crude brain homogenates, and may usefully

complement the information already available for the toxin acceptors on purified cerebrocortical synaptosomes. Furthermore, since the anatomical structure of the tissue remains intact, the localization of bound toxins in various brain areas should be possible.

In this Chapter, the binding of ^{125}I-labelled DTX and β-BuTX to lightly-fixed cryostat sections has been studied by γ-counting and compared to the binding of the toxins on synaptosomes and synaptosomal plasma membranes. These studies were also used to define optimal incubation protocols for use in acceptor mapping by autoradiography (see Chapters 3 and 4).

2.2. Materials

DTX was purified, and ^{125}I-DTX (specific radioactivity of 200-400 Ci/mmol) prepared in this laboratory as described by Black *et al.*, (1986). β-BuTX was purified as described in Appendix A.1 and radioiodinated by A. Breeze to specific activities of 400-800 Ci/mmol using chloramine-T (cf. Appendix A.1) or the lactoperoxidase method (Rehm and Betz, 1982). Bovine serum albumin (BSA) grade V was purchased from Sigma, Poole, Dorset, and paraformaldehyde, dinonyl phthalate and Dow-Corning MS-550 silicone fluid from BDH, Poole, Dorset. All other chemicals and reagents were of analytical grade.

2.3. Methods

2.3.1. Preparation of Synaptosomes

Rat cerebrocortical synaptosomes were prepared by a modification of the method of Gray and Whittaker (1962), as described by de Belleroche and Bradford (1977). Briefly, dissected rat cerebral cortices were homogenized in 0.32 M sucrose. Nuclei and cell debris were removed from the homogenates by centrifugation at 1,000 g for 10 min prior to collection of a crude synaptosomal and mitochondrial pellet at 20,000 g for 20 min. This pellet was fractionated on a discontinuous sucrose gradient by centrifugation at 76,000 g for 1 hr. The synaptic fraction was collected from the 0.8 M/1.2 M sucrose interface, sedimented at 54,000 g for 20 min, resuspended in 10 mM sodium phosphate buffer, pH 7.3. containing 0.9% NaCl, and stored frozen at -20°C.

2.3.2. Fixation of Synaptosomes in Formaldehyde

A 20% formaldehyde stock solution was freshly prepared by heating solid para-formaldehyde in distilled water to ≈60°C and clearing the mixture by dropwise addition of concentrated sodium hydroxide solution.

Synaptosomes were thawed, and 0.5 ml of synaptosome suspension were added to 0.5 ml of formaldehyde fixative in 10 mM sodium phosphate buffer, 0.9% NaCl, pH 7.3, giving final formaldehyde concentrations of 0.1-1%. A control sample of synaptosomes was treated with phosphate buffer alone. After incubation at ≈22°C for 30 min the synaptosomes were collected by centrifugation for 5 min in an Eppendorf microcentrifuge. The pellets were washed twice by resuspension in phosphate/NaCl buffer (above) and re-centrifugation, and finally suspended in 1 ml Krebs phosphate medium (124 mM NaCl, 5 mM KCl, 20 mM Na_2HPO_4, 1.2 mM KH_2PO_4, 1.3 mM $MgSO_4$, 0.75 mM $CaCl_2$ and 10 mM D-glucose, pH 7.4). Aliquots of the synaptosome suspensions were withdrawn, pelleted, dissolved in 0.45 M NaOH and assayed for protein by the method of Lowry *et al.* (1951), using BSA as a standard.

2.3.3. Measurement of the Binding of ^{125}I-DTX to Synaptosomes

Aliquots of synaptosomes, equivalent to ~0.2 mg protein, and fixed as above, were incubated at ≈22°C in a final volume of 250 µl of 0.2, 0.5, 1 or 2.5 nM ^{125}I-DTX in Krebs phosphate medium (see Section 2.3.2) containing 1 mg/ml BSA; for determination of the non-specific binding 200 nM unlabelled DTX was included in control samples. After 30 min, 200 µl of each incubate was layered onto 200 µl of a 1:1 mixture of dinonyl phthalate and Dow-Corning MS-550 silicone fluid in a centrifuge tube and centrifuged for 2 min in an Eppendorf microcentrifuge, thus separating the bound toxin on the pelleted synaptosomes from the free radiolabel in the incubation buffer which remained above the oil (Black *et al.*, 1986). Aliquots of the aqueous supernatant were removed before the oil surface and walls of the tube were washed with 1 ml of 1 M NaCl. The amount of ^{125}I-DTX in the pellets and aliquots of the aqueous phase was determined by γ-counting.

2.3.4. Preparation of Cryostat Sections

Adult Sprague-Dawley rats (200-250 g) were stunned and killed by cervical dislocation or, more often, anaesthetized with

1 ml of Sagatal (60 mg sodium pentobarbitone) administered intraperitoneally, and perfused intra-cardially over 20-25 min with 200-250 ml 0.1% formaldehyde in 10 mM sodium phosphate buffer, pH 7.3, containing 0.9% NaCl. This gentle fixation improves the cutting properties and preservation of the tissue. Slabs of brain tissue were dissected as required, frozen in iso-pentane cooled with solid CO_2 to ≈-60°C and mounted on microtome chucks. Cryostat sections (usually 10 µm thick) were cut at -20°C on a Bright Cryostat microtome or on a Reichert-Jung Cryocut E, thaw-mounted onto subbed slides (dipped in a solution of 0.5% gelatine and 0.05% chromic potassium sulphate) and dried at room temperature for at least 1 hr. The sections were stored over silica gel at -20°C for up to three months. In most binding experiments coronal forebrain cryostat sections cut at the level of the caudate putamen (bregma 1.7 to 0.3mm; interaural 10.7 to 8.7 mm according to Paxinos and Watson, 1982) or at the hippocampus (bregma -2.3 to -4.8 mm, interaural 6.7 to 4.2 mm) were used. Cryostat sections (10 µm) were similarly cut from the cerebellum of 1-day-old leghorn chicks killed by decapitation.

2.3.5. *In Vitro* Binding of Radiolabelled Toxins to Brain Sections

Cryostat sections were routinely incubated by placing 50-200 µl of incubation solution (Krebs phosphate medium, see Section 2.3.2, containing 1 mg/ml BSA and ^{125}I-DTX or ^{125}I-β-BuTX together with unlabelled toxins as required) over each section on the slides, which were kept in sealed boxes at constant humidity. Occasionally this incubation was preceeded by a pre-incubation for 5-30 min in Krebs phosphate/BSA medium or in buffer containing 0.01% Triton X-100. After incubating for 30-45 min at 22°C, the solution was drained from the slides and the sections were washed by immersion in three changes (5 min each) of a large volume (40 ml/3 slides) of Krebs phosphate medium at 4°C, rinsed briefly in distilled water and dried quickly in a stream of cold air.

For examination of the concentration dependence of binding, 0.05-10 nM ^{125}I-DTX or 0.1-10 nM ^{125}I-β-BuTX were used as above. Non-specific binding was determined in the presence of 0.5 or 1 µM unlabelled toxin. After 40 min of incubation, aliquots from the solution over the sections were withdrawn for determination of the "free" toxin concentration by γ-counting. In the kinetic studies, 2.5 nM ^{125}I-DTX was used. The association of ^{125}I-DTX

with its acceptor in cryostat sections was measured by incubating sections for 15 s to 60 min as above and washing in three changes (2 s each) of Krebs medium at 4°C. Dissociation of the ^{125}I-DTX-acceptor complex was studied by labelling the sections with ^{125}I-DTX for 30 min, and then either washing in a single volume of Krebs medium containing 1 mg/ml BSA for 5 s to 5 hr, or rinsing the sections once for 2 s in Krebs medium and then incubating in 500 µl Krebs medium containing 1 mg/ml BSA and 0.5µM unlabelled DTX (per slide) for 5 s to 2 hr. For competition assays, 1 or 3 nM ^{125}I-DTX, or 2.5 nM ^{125}I-β-BuTX were used in the presence of 1 nM to 10 µM unlabelled toxin. In studies on the divalent cation dependence of the binding of β-BuTX or ^{125}I-β-BuTX a Ringer devoid of $CaCl_2$ but containing 5 mM EDTA was used, or $CaCl_2$ was substituted with 2.5 mM $SrCl_2$ in the presence of 1 mM EGTA to chelate any residual Ca^{2+}.

2.3.6. Quantitation of Radioiodinated Toxins Bound to Brain Sections

Dried, toxin-labelled, cryostat sections were wiped from the slides using damped 2.5 cm Whatman GF/C glass microfibre filter discs. The discs were dried under an infra-red heat lamp and the content of ^{125}I-DTX or ^{125}I-β-BuTX was measured using a γ-counter. After dissolving the sections from each disc in 0.45 M sodium hydroxide for at least 24 hr, glass fibre material was sedimented by briefly centrifuging in an Eppendorf microcentrifuge, and the supernatants were assayed for protein by the method of Lowry *et al.* (1951). The amounts of ^{125}I-DTX or ^{125}I-β-BuTX bound to the cryostat sections were calculated in pmoles per mg of protein.

2.4. Results

2.4.1. ^{125}I-DTX Binding to Specific Acceptors

2.4.1.1. *Effect of formaldehyde fixation on ^{125}I-DTX acceptors in rat brain synaptosomes and cryostat sections*

When rat brain tissue is lightly fixed *in situ* by intracardiac perfusion with 0.1% formaldehyde, its sectioning properties are greatly improved, and the resulting cryostat sections show superior preservation. Such gentle fixation is, therefore, widely used when preparing tissue for *in vitro* labelling autoradiography experiments (e.g. Young and Kuhar, 1979; Palacios *et al.*, 1980).

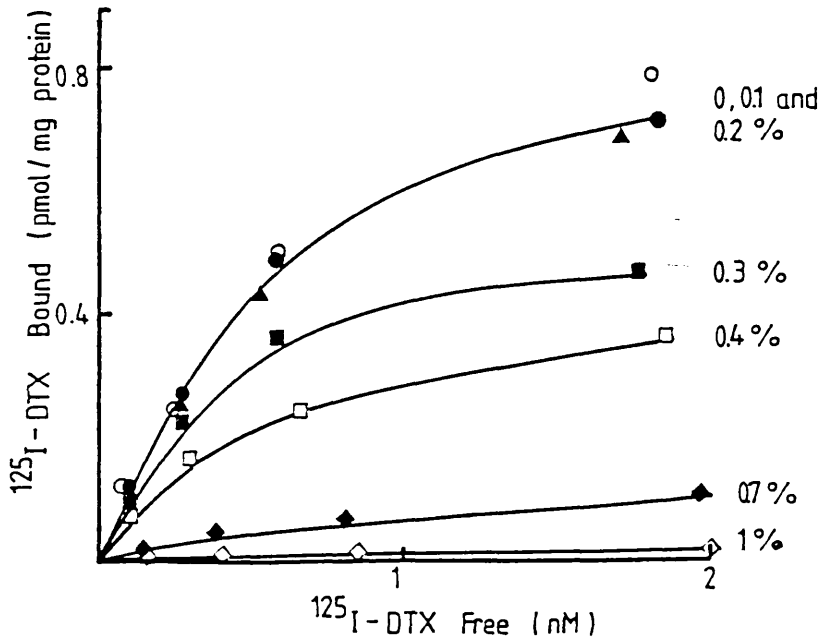
It is important to show, however, that the fixation does not affect the properties of the receptors or binding sites of interest.

The effect of formaldehyde fixation on DTX acceptors was studied on rat brain synaptosomes (Figure 2.1, Table 2.1). ^{125}I-DTX bound saturably to unfixed synaptosomes, with an affinity (K_d) =0.64 nM and site content (B_{max}) =0.94 pmol/mg protein; these values are in reasonable agreement with those reported previously (Mehraban *et al.*, 1984; Black *et al.*, 1986), although only four toxin concentrations were used in the measurements. Identical binding curves and similar binding constants were observed for ^{125}I-DTX binding to synaptosomes treated with 0.1 or 0.2% formaldehyde. When synaptosomes were fixed at higher concentrations of formaldehyde, the K_d values did not vary significantly, but the acceptor content (B_{max}) declined rapidly. Synaptosomes fixed in 0.3 and 0.4% formaldehyde contained only ≈80% and ≈42%, respectively, of the acceptor sites originally present on unfixed synaptosomes. All specific binding was destroyed by fixation in 1% formaldehyde.

As β-BuTX is known to block ^{125}I-DTX binding to a proportion of its acceptor sites (Dolly *et al.*, 1984, 1987; Black *et al.*, 1986), the effect of formaldehyde fixation on the ability of β-BuTX to block ^{125}I-DTX binding to synaptosomes was examined as shown in Figure 2.2. ^{125}I-DTX binding in the presence of 1 μM β-BuTX declined in parallel to the total ^{125}I-DTX binding, its level remaining unchanged in synaptosomes fixed in up to 0.2% formaldehyde, but decreasing at higher concentrations. Figure 2.2 also shows that the non-specific binding was higher on the more strongly fixed samples.

^{125}I-DTX binding to cryostat sections from fresh or perfusion-fixed (0.1% formaldehyde) tissue was also studied. No difference was observed in the concentration dependence of ^{125}I-DTX binding (see Section 2.4.1.2, Table 2.2) or in a competition binding experiment (Section 2.4.1.4), identical binding curves being obtained for fixed or unfixed cryostat sections. Autoradiograms from unfixed sections showed inferior preservation, but the observed ^{125}I-DTX acceptor distribution was identical for both fixed and unfixed sections (data not shown). Thus the gentle fixation in 0.1% formaldehyde does not affect the properties of the ^{125}I-DTX acceptors, and consequently cryostat sections from perfusion-fixed tissue were used in all remaining experiments,

Figure 2.1. Saturable binding of ^{125}I-DTX to unfixed and formaldehyde-treated rat brain synaptosomes



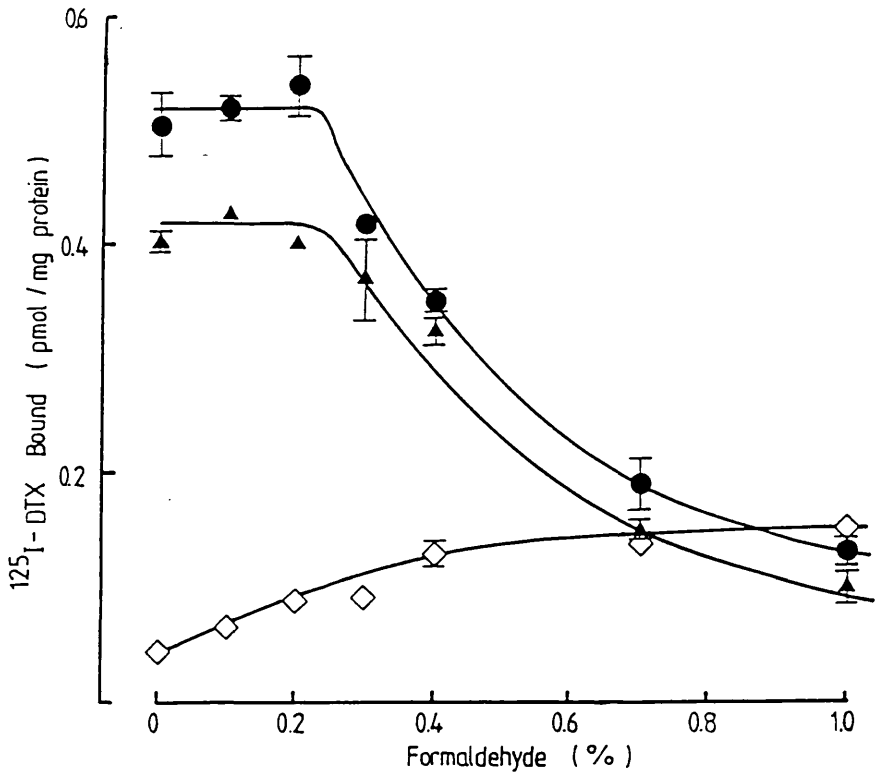
Specific binding of ^{125}I-DTX to unfixed synaptosomes (▲), or synaptosomes fixed in 0.1% (●), 0.2% (○), 0.3% (■), 0.4% (□), 0.7% (◆), or 1% (◇) formaldehyde. For all the values shown, non-specific binding, determined in the presence of 200 nM unlabelled DTX, has been subtracted from the total binding of ^{125}I-DTX alone. All points are averages from duplicate samples which differed by ≤5%. For further details see Section 2.3.1-2.3.3.

Table 2.1. Effect of formaldehyde fixation on the synaptosome binding of ^{125}I-DTX

Concentration of formaldehyde (%)	Apparent K_d (nM)	B_{max} (pmol/mg protein)
0	0.64	0.94
0.1	0.52	0.92
0.2	0.70	1.10
0.3	0.59	0.75
0.4	0.38	0.39
0.7	1.52	0.14
1.0	0.89	0.04

Unfixed rat brain synaptosomes, or synaptosomes fixed in 0.1-1% formaldehyde were incubated in 0.2, 0.5, 1 or 2.5 nM ^{125}I-DTX; non-specific binding was measured in the presence of 200 nM unlabelled DTX (see Section 2.3.3. for details of the binding assay). Approximate K_d and B_{max} values were determined from Scatchard graphs (Appendix A.2).

Figure 3.2. Effect of fixation with formaldehyde on the ability of β-BuTX to block ^{125}I-DTX binding to synaptosomes



Unfixed rat brain synaptosomes, or synaptosomes fixed in 0.1-1% formaldehyde were incubated in Krebs phosphate medium with 1 nM ^{125}I-DTX alone (●) or in the presence of 1 μM unlabelled β-BuTX (▲) or 200 nM unlabelled DTX (◇). Binding was determined as described in Section 2.3.3. Error bars represent standard errors from duplicate samples and have been omitted where smaller than the symbols.

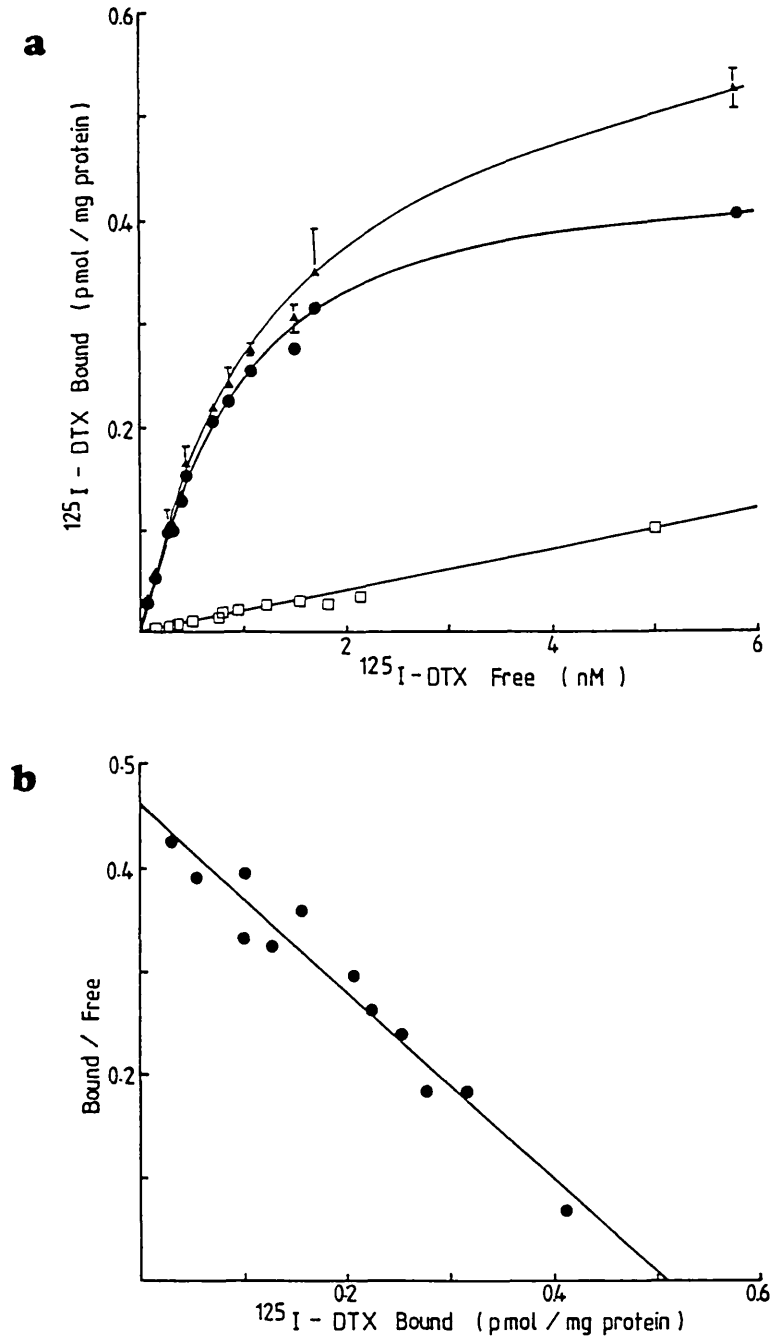
except where stated.

2.4.1.2. *Equilibrium binding of ^{125}I-DTX to cryostat sections*

^{125}I-DTX bound saturably to rat brain cryostat sections. Results from a typical concentration dependent binding experiment are shown in Figure 2.3a. Non-specific binding to the sections was always low, usually comprising less than 10% of the total binding with 2-2.5 nM ^{125}I-DTX, concentrations at which the specific binding was reaching saturation. A Scatchard plot of the data (Figure 2.3b) fitted to a straight line, suggesting that ^{125}I-DTX bound to an apparently homogeneous and non-interacting set of acceptor sites with a K_d =1.1nM and B_{max} =0.51 pmol/mg protein. These values were based on protein contents of the sections assayed after the incubation. Approximately 40% of the section protein (compared to freshly cut cryostat sections) was lost during the incubation and washes; hence the true B_{max} was 0.31 pmol/mg of total (initial) section protein. The binding of ^{125}I-DTX to cryostat sections was not affected by pre-incubation for up to 30 min in Krebs phosphate medium containing 1 mg/ml BSA or 0.01% Triton X-100: In most experiments, therefore, sections were not pre-incubated for convenience.

The results from several saturation binding experiments are summarised in Table 2.2. Throughout rat forebrain, ^{125}I-DTX bound to its acceptors in the sections with K_d ≈1.2 nM. ^{125}I-DTX binding to cerebellum sections had a somewhat lower affinity (K_d =2.3 nM for sagital sections, or 1.7 nM in coronal sections including medulla), but the Scatchard plots could still be fitted to straight lines. However, autoradiography of such sections (see Chapter 4) suggested that there are at least two populations of ^{125}I-DTX binding sites with different affinities for the toxin in the cerebellum. Such multiple sites may not be resolved in Scatchard analysis unless their relative affinities differ substantially and their site contents are near equal (Bürgisser, 1984); thus the linear Scatchard graphs do not exclude the possible existence of several acceptor sites. The differences in the overall K_d observed in sagital and coronal sections were presumably due to different proportions of these acceptor sites in cerebellum, or in cerebellum and medulla. The acceptor content (B_{max}) in rat brain cryostat sections increased caudally; this was also apparent from the autoradiography studies (Chapter 4). Hill plots of all

Figure 2.3. Concentration dependence of ^{125}I-DTX binding to cryostat sections of rat forebrain



(a) Cryostat sections (10 μm) from rat forebrain at the level of the caudate putamen were incubated for 45 min at 22°C in various concentrations of ^{125}I-DTX in Krebs phosphate medium. Concentrations of free and bound ^{125}I-DTX were determined as described (see Sections 2.3.5 and 2.3.6). Specific binding (●) was calculated by subtracting non-specific binding, determined in the presence of 0.5 μM unlabelled DTX (□), from the total binding (▲). Error bars indicate standard errors for triplicate samples.

(b) A Scatchard plot of the specific binding in (a). The best straight line was fitted by linear regression. From this line, K_d =1.1 nM and B_{max} =0.51 pmol/mg protein.

Table 2.2. Saturable binding of ^{125}I-DTX to cryostat sections from rat and chick brain

Cryostat sections	K_d (nM)	B_{max} (pmol bound per mg total section protein)
Rat forebrain (coronal) at level of caudate putamen	1.1	0.31
Rat forebrain at level of hippocampus and thalamus	1.2 (±0.2)[a]	0.58 (±0.06)[a]
Unfixed sections	1.2	0.52
Rat cerebellum (sagittal)	2.3 (±0.4)[b]	0.42 (±0.02)[b]
Rat cerebellum and medulla (coronal)	1.7	0.71
1-day old chick cerebellum (sagital)	1.4	0.19

Cryostat sections (10 µm) from various regions of rat or chick brain, fixed by perfusion with 0.1% formaldehyde except where stated, were labelled with ^{125}I-DTX and assayed as in Figure 2.3. Binding parameters were derived from Scatchard plots.
a: Mean (±S.E.M) of three experiments.
b: Mean (±S.E.M) of two experiments.
Other values were from a single experiment

saturation binding experiments gave estimates of n_H close to 1.

Saturable binding of ^{125}I-DTX was also observed on cryostat sections of 1-day-old chick cerebellum, with K_d =1.4 nM and B_{max} ≃0.19 pmol/mg total section protein.

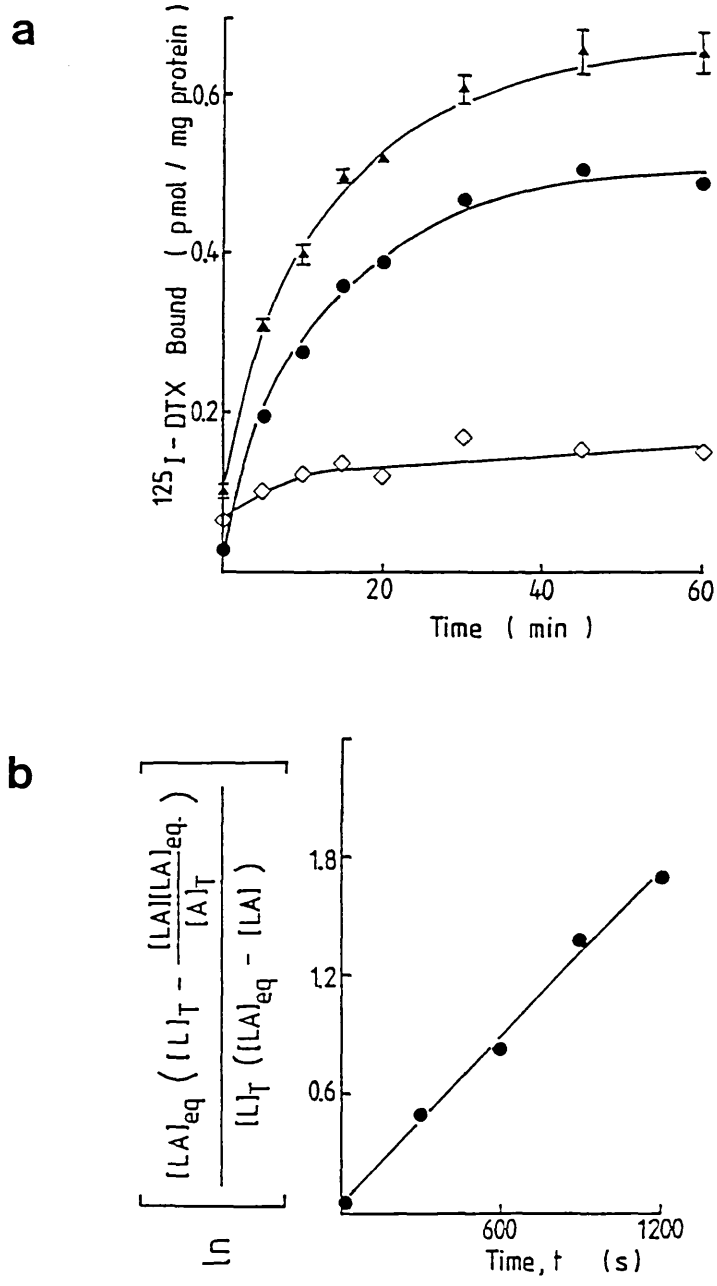
2.4.1.3. *Kinetics of the binding of ^{125}I-DTX to rat brain cryostat sections*

The time course of ^{125}I-DTX binding to rat brain cryostat sections is shown in Figure 2.4a. Using 2.5 nM ^{125}I-DTX, the specific binding reached saturation after ≃30 min. A second order analysis of the binding (see Appendix A.2.3, equation (7), Figure 2.4b) gave an association rate constant k_1 =2.97 × 10^5 $M^{-1}s^{-1}$ (mean of two experiments). A similar value for k_1, 2.92 × 10^5 $M^{-1}s^{-1}$, was derived from the first order approximation (Appendix A.2.3, equation (8)).

The dissociation of ^{125}I-DTX binding during washing in Krebs phosphate medium at 4°C, the condition used in all equilibrium binding and autoradiography experiments, was studied as shown in Figure 2.5. "Non-specific binding", measured as the binding of ^{125}I-DTX in the presence of 0.5 µM unlabelled DTX, decreased very rapidly as the unbound ^{125}I-DTX in the depths of the sections diffused out into the wash buffer; half of this "trapped" ^{125}I-DTX was removed within 3.5 min. The wash-out of unbound ^{125}I-DTX subsequently slowed down, until a constant level, the true non-specific binding, was reached after 15-30 min (see also the first order plot, Figure 2.5b). The initial rapid wash-out of unbound ^{125}I-DTX was also reflected in the levels of total ^{125}I-DTX bound. Specific binding, calculated as the difference of the total and "non-specific binding", remained essentially constant within the error of the experiment. The first order plot (Figure 2.5b) showed a linear rate of dissociation for the specifically bound ^{125}I-DTX after ≃15 min; the dissociation rate constants, k_{-1} from two experiments were 1.1 × 10^{-5} s^{-1} and 2.4 × 10^{-5} s^{-1}, corresponding to dissociation half-lives ($t_{½}$) at 4°C of 8-17 hrs. In one experiment, >80% of the specific binding remained after washing the labelled sections for 5 hr.

The equilibrium dissociation constant, K_d, derived from $K_d = \frac{k_{-1}}{k_1}$ (equation (3), Appendix A.2) was 0.04-0.08 nM, compared with the K_d =1.2 nM from saturation binding experiments on similar sections (Section 2.4.1.2). Furthermore, the k_{-1} values

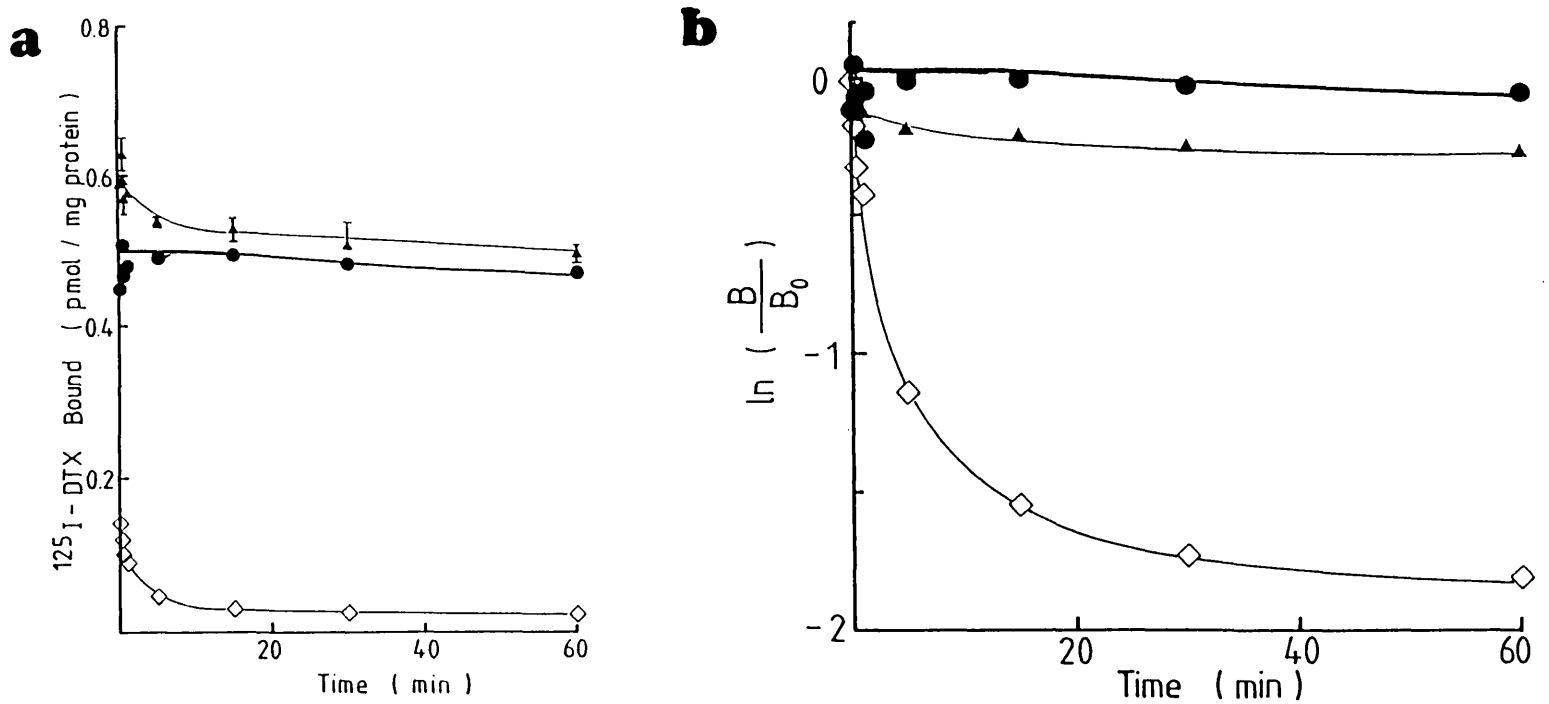
Figure 2.4. Time course of the association of ^{125}I-DTX with its acceptors on rat brain cryostat sections



(a) The rate of binding of 2.5 nM ^{125}I-DTX to rat forebrain cryostat sections (10 µm) from the level of the hippocampus at 22°C was measured as described (see Sections 2.3.5 and 2.3.6). Specific binding (●) was calculated by subtracting non-specific binding, determined in the presence of 0.5 µM unlabelled DTX (◇), from the total binding (▲). Error bars indicate standard errors for duplicate samples.

(b) The data in (a) plotted according to the integrated form of the second order rate equation (see Appendix A.2.3, equation (7)). $[L]_T$, the total concentration of ligand, was 2.5 nM; $[A]_T = B_{max}$ was 0.86 pmol/mg protein (after washing) for the sections used; $[LA]_{eq}$, the concentration of ligand-acceptor complex at equilibrium was 0.5 pmol/mg protein.

Figure 2.5. Dissociation of ^{125}I-DTX from its acceptors on rat brain cryostat sections



(a) Cryostat sections (10 μm) from rat forebrain at the level of the hippocampus were labelled with 2.5 nM ^{125}I-DTX at 22°C for 30 min. The sections were drained, rinsed for 2 s and then washed for 15 s to 60 min at 4°C (see Sections 2.3.5 and 2.3.6). Non-specific binding was measured in the presence of 0.5 μM DTX. The specific binding (●) was calculated by subtracting the non-specific binding (◇) from the total binding (▲). Error bars indicate the standard deviation for duplicate samples.

(b) A first-order plot of the data in (a). B is the amount of ^{125}I-DTX bound (pmol/mg protein) at various times. B_0, the maximum ^{125}I-DTX bound in this experiment was (pmol/mg protein after incubation) 0.63 for the total (▲), 0.145 for the non-specific (◇) and 0.5 for the specific binding (●).

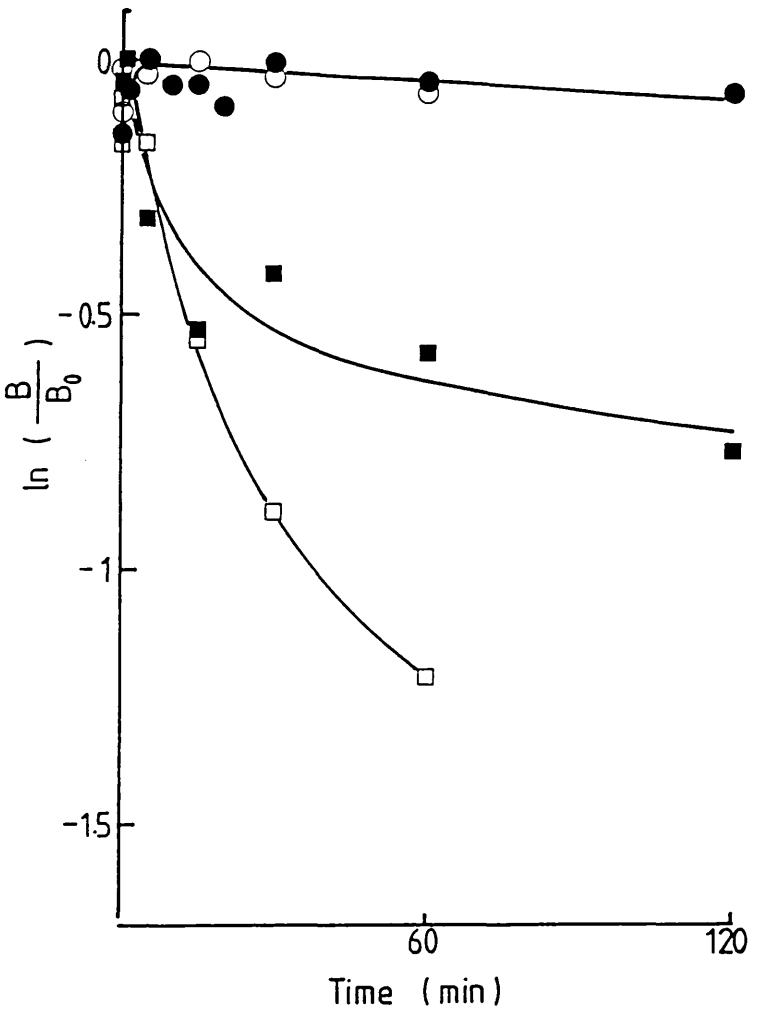
differed from that reported by Black *et al.* (1986) for rat brain synaptosome suspensions (k_{-1} =1.03 × 10^{-3} s^{-1}, corresponding to $t_{½}$ ≈11 min) when dissociation was measured at 22°C by incubating ^{125}I-DTX-labelled synaptosomes in 0.2 µM DTX. The dissociation of ^{125}I-DTX from cryostat sections was therefore studied further, both by washing in buffer at 22°C rather than at 4°C, and by displacing bound ^{125}I-DTX with unlabelled DTX (see Figure 2.6) The wash-out of "non-specific binding" was identical under all conditions (see above). Dissociation of specifically bound ^{125}I-DTX measured by dilution was similar at 22°C and at 4°C. In contrast, dissociation under "chase" conditions was significantly faster, and the first order plots (Figure 2.6) showed definite curvature. Linear approximation of the initial dissociation rate (up to 60 min) after 5 min, when the bulk of the trapped "non-specific" ^{125}I-DTX had been removed, gave a k_{-1} =4.8 × 10^{-4} s^{-1} (corresponding $t_{½}$ =24 min) at 22°C or 5.8 ×10^{-5} s^{-1} ($t_{½}$ =200 min) at 4°C. The K_d calculated using k_{-1} =4.8 × 10^{-4} s^{-1} was 1.6 nM.

The binding of ^{125}I-DTX on cryostat sections of different thicknesses was studied as shown in Figure 2.7a. The specific binding appeared proportional to section thickness up to 10 µm, but relatively less ^{125}I-DTX was bound to thicker sections. As expected, non-specific binding increased linearly with section thickness, indicating that there was no steric hindrance to the diffusion of the toxin into the sections. The loss of proportionality of the specific binding above 10 µm was therefore probably due to a significant reduction in the ^{125}I-DTX concentration remaining "free" within the sections (300 µl of 2.5 nM ^{125}I-DTX was used per slide; 6, 12, and 20% of this was found to be bound to 5, 10 and 30 µm sections, respectively), especially as diffusion of the toxin into the sections could not be enhanced by agitation during the incubation. The protein content of the sections was found to be linear with section thickness (Figure 2.7b). From this experiment it is clear that 10 µm sections (the thickness routinely used) were fully labelled under the standard incubation conditions.

2.4.1.4. *Inhibition of the binding of ^{125}I-DTX to cryostat sections by unlabelled DTX and ß-BuTX*

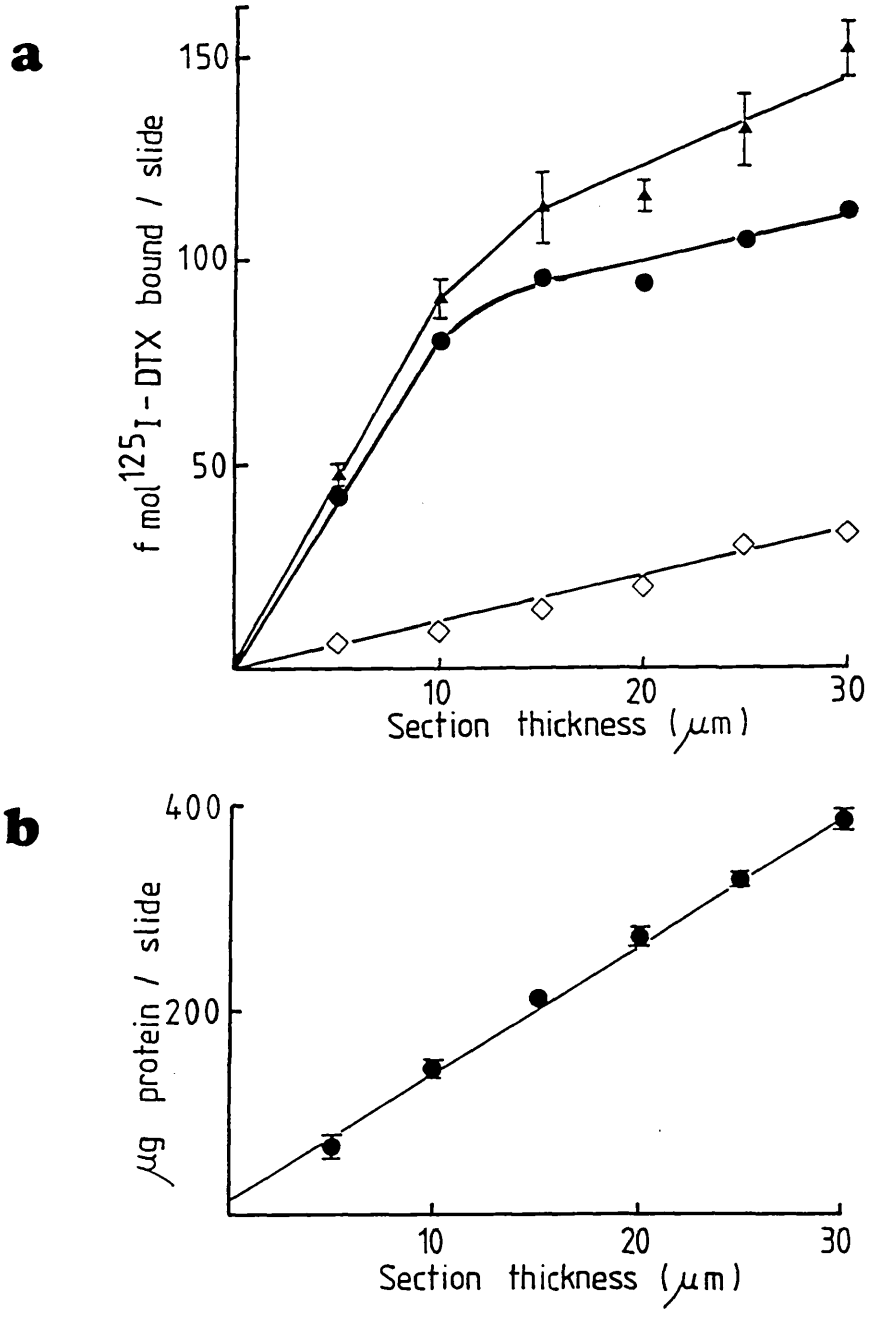
Competition experiments in which various concentrations of unlabelled DTX or ß-BuTX were used to inhibit ^{125}I-DTX binding were performed as described in Figure 2.8. The results from all such

Figure 2.6. First order plots of the dissociation of ^{125}I-DTX from its acceptors on rat brain cryostat sections under various conditions



Rat forebrain cryostat sections at the level of the caudate nucleus or hippocampus were labelled with 2.5 nM ^{125}I-DTX at 22°C for 30 min. The slides were drained, rinsed 2 s in Krebs phosphate medium, and then either washed in Krebs phosphate medium containing 1 mg/ml of BSA at 22°C (○) or at 4°C (●), or incubated in 0.5 µM unlabelled DTX in Krebs/BSA medium at 22°C (□) or at 4°C (■). First order plots of the dissociation of the specific binding are shown. B is the amount of ^{125}I-DTX bound (pmol/mg protein) at various times. B_o (pmol/mg of section protein after incubation) was 0.5 (○), 0.45 (●), 0.5 (□) or 0.78 (■).

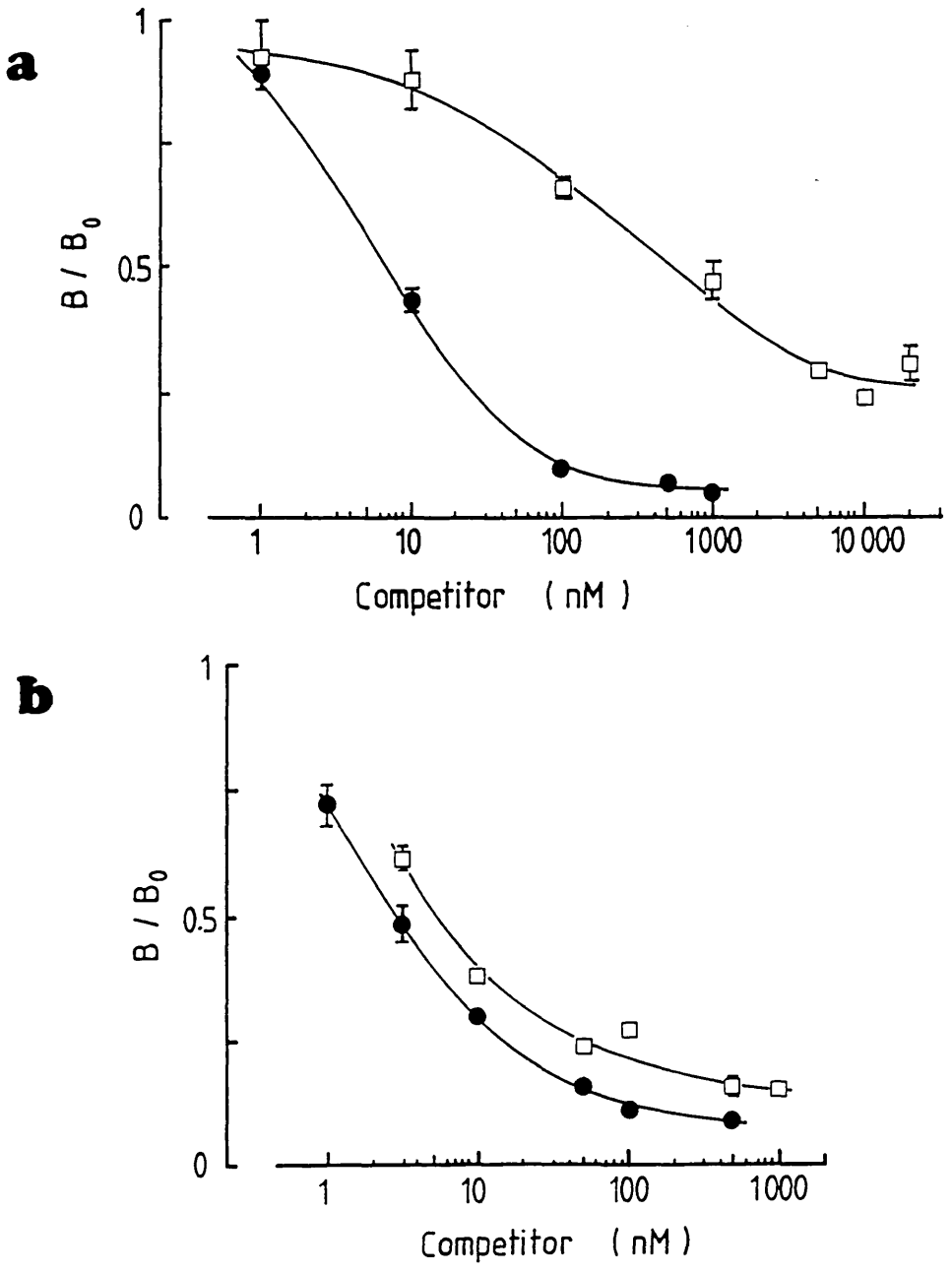
Figure 2.7. Binding of ^{125}I-DTX to cryostat sections of different thickness



(a) Rat forebrain cryostat sections, 5-30 μm, cut at the level of the caudate and septal nuclei were labelled in 2.5 nM ^{125}I-DTX for 45 min at 22°, and washed and processed as usual (see Sections 2.3.5 and 2.3.6). Specific binding (●) was calculated by subtracting the non-specific binding in the presence of 0.5 μM DTX (◇) from the total binding (▲). Error bars indicate standared errors for triplicate samples.

(b) The sections from (a) were dissolved in 0.45 M NaOH and assayed for protein by the method of Lowry *et al.* (1959; see also Section 2.3.6). The linear relationship of protein content with section thickness demonstrates the accuracy of sectioning of the cryostat.

Figure 2.8. Inhibition by unlabelled DTX and ß-BuTX of the binding of ^{125}I-DTX to cryostat sections of rat and chick brain



Cryostat sections (10 µm) were incubated for 45 min at 22°C in Krebs phosphate medium containing 3 nM (a) or 2.8 nM (b) ^{125}I-DTX and various concentrations of unlabelled DTX (●) or ß-BuTX (□). Total binding of ^{125}I-DTX was determined in the absence of competing toxins. Sections were washed and processed as described (see Sections 2.3.5 and 2.3.6). Error bars indicate standard errors for duplicate samples. B is the amount of ^{125}I-DTX bound (pmol/mg protein) at various times.

(a) A competition experiment on rat hippocampus-level sections. The total binding, B_o, was 0.7 pmol/mg protein (after incubation).

(b) A similar experiment on chick cerebellum cryostat sections (cut sagitally). The total binding was 0.27 pmol/mg protein.

experiments are summarized in Table 2.3. DTX displaced 90-95% of the total ^{125}I-DTX binding. The ratio of the DTX concentrations required to inhibit 90% and 10% of the displaceable binding of ^{125}I-DTX was usually 68-91. Thus, DTX interacted with ^{125}I-DTX at an apparently homogeneous set of sites (the theoretical ratio of IC_{90}/IC_{10} for such a situation is 81), with an average equilibrium binding constant (K_I) in rat brain of 1.7 ± 0.4 nM (see Table 2.3); this concurs with the K_d determined by direct binding studies.

β-BuTX, however, was much less effective in inhibiting ^{125}I-DTX binding to rat brain cryostat sections, and the results from several experiments with β-BuTX were very variable, in contrast to the reproducible inhibition constants which were always obtained with unlabelled DTX. The competition binding curves with β-BuTX were always extended as in Figure 2.8a, giving IC_{90}/IC_{10} ratios between 170 and 2,000, and the apparent K_I ranged from 12 to 170 nM (Table 2.3).

The divalent cation dependence of the binding of ^{125}I-DTX, and of the competition by DTX and β-BuTX, was studied in the experiment shown in Figure 2.9. Similar levels of ^{125}I-DTX binding were found in all three buffers, and unlabelled DTX always blocked ≈95% of this binding; thus DTX binding was not affected by the divalent cation concentration. However, the effectiveness of β-BuTX in blocking ^{125}I-DTX was reduced significantly in the absence of divalent cations, although some inhibition did persist. Sr^{2+} restored the ability of β-BuTX to block ^{125}I-DTX binding.

In contrast to these results on rat brain sections, β-BuTX appeared almost as potent as DTX in blocking ^{125}I-DTX binding on chick cerebellum cryostat sections (Figure 2.8b), displacing nearly all of the specific ^{125}I-DTX binding with an apparent K_I =1.2 nM, and IC_{90}/IC_{10} =71. This agrees with the observation of Black and Dolly (1986a) that β-BuTX can efficiently inhibit ^{125}I-DTX binding at the high affinity DTX acceptor population in chick brain, but is ineffective in competing with ^{125}I-DTX binding at the low affinity site (see also Sections 1.4.4 and 1.5). The inhibition by β-BuTX was dependent on Ca^{2+} (or Sr^{2+}) as in the case of rat brain cryostat sections, with only a slight competition (14% with 1 μM β-BuTX) persisting in the absence of divalent cations (data not shown).

2.4.2. ^{125}I-β-BuTX Binding to Specific Acceptors

Cryostat sections contain acceptors for β-BuTX, as has

Table 2.3. Inhibition of the binding of ^{125}I-DTX to cryostat sections by unlabelled DTX and β-BuTX

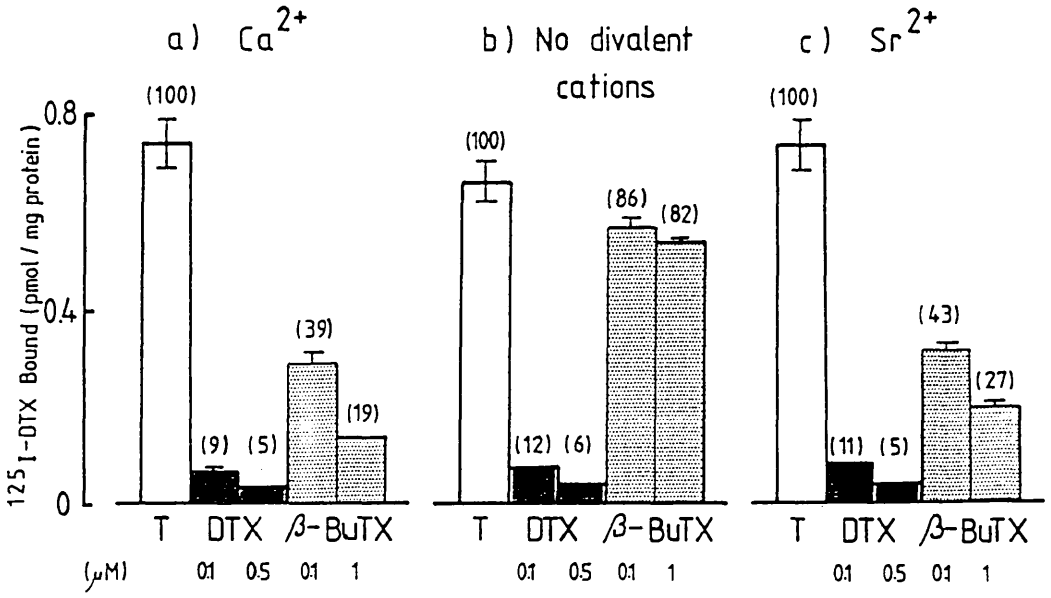
Cryostat sections used		Concentration of ^{125}I-DTX (nM)	Competition with unlabelled DTX				Competition with unlabelled β-BuTX			
			N.S.B.[a] (%)	IC_{50} (nM)	App. K_I (nM)	$\frac{IC_{90}}{IC_{10}}$	N.S.B.[a] (%)	IC_{50} (nM)	App. K_I (nM)	$\frac{IC_{90}}{IC_{10}}$
Rat; Forebrain sections (coronal at the level of the hippocampus	1)[b]	3	5	6	1,9	68	30	138	44	1900
	2)	3	7	5	1,6	78	32	100	32	630
	3)	3	5	5,3	1,7	91	31	50	15,8	1000
	4)	2,8	5	3,6	1,1	41	19	40	12,3	540
	5)	1	7	4,2	2,3	28	20	302	169	170
Rat; Cerebellum sections (sagittal)		2,8	5	3,5	1,5	79	15	68	29	1000
Chick; Cerebellum sections (sagittal)[b]		2,8	10	2	0,7	79	15	3,6	1,2	71

Cryostat sections (10 μm) from various regions of rat or chick brain were incubated in ^{125}I-DTX in the presence of unlabelled DTX or β-BuTX as detailed in Figure 2.8. The results of all competition experiments are summarized here.

a: The level of total ^{125}I-DTX binding not displaced by the unlabelled toxin (i.e. the non-specific binding determined with DTX, or the β-BuTX-resistant binding determined with β-BuTX).

b: Unfixed tissue was used to prepare the cryostat sections used in these experiments. IC_{90}/IC_{10} is the ratio of the amount of unlabelled ligand required to block 90% and 10%, respectively, of the specific binding.

Figure 2.9. Dependence of ^{125}I-DTX binding, and its inhibition by β-BuTX, on divalent cations



Rat forebrain cryostat sections (10 μm) were labelled with 2.8 nM ^{125}I-DTX alone, or in the presence of unlabelled DTX (0.1 or 0.5 μM) or β-BuTX (0.1 or 1 μM), as described in Figure 2.8. The numbers in brackets above the histogram bars indicate binding as a percentage of the total binding ($\overset{(T)}{\wedge}$) in that buffer. The buffers used were:

(a) Ca^{2+}: Krebs phosphate medium, as in Section 2.3.2.

(b) **No divalent cations**: Krebs phosphate medium prepared without $CaCl_2$; EDTA (5 mM) was added to sequester any divalent cations (Mg^{2+}, and residual Ca^{2+} present in the sections).

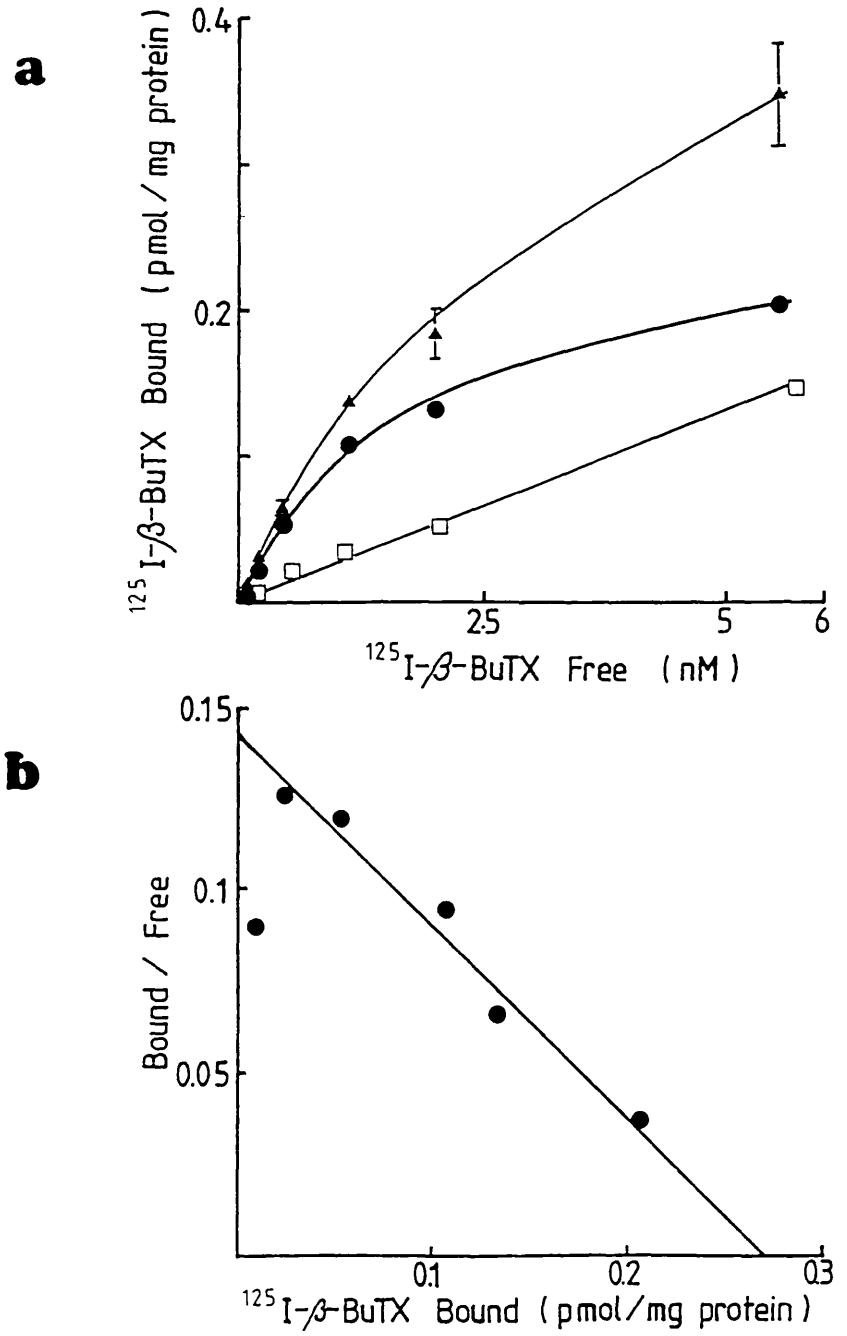
(c) Sr^{2+}: Krebs phosphate medium prepared with 2.5 mM $SrCl_2$ instead of $CaCl_2$; EGTA (1 mM) was added to sequester any Ca^{2+} present in the sections.

been shown by Othman *et al.* (1983) using ^{3}H-propionylated β-BuTX. A biologically active preparation of ^{125}I-β-BuTX also bound saturably and with high affinity to rat brain cryostat sections. The results of one concentration dependent binding experiment are shown in Figure 2.10. A Scatchard plot of the data (Figure 2.10b) revealed high affinity binding (K_d =1.9 nM) to a low number of sites: B_{max} =0.27 pmol/mg protein. Again ≈40% of the protein was lost from the sections during the incubation. The true content of ^{125}I-β-BuTX acceptor sites in rat forebrain was, therefore, ≈0.16 pmol/mg total section protein. ^{125}I-β-BuTX binding did not differ in quantity or distribution when tested on 0.1% formaldehyde-fixed or unfixed sections. Neither was the binding affected by pre-incubation of the sections in Krebs/BSA buffer containing Triton X-100 at 22°C for up to 30 min.

The results from all concentration dependent saturation binding studies with ^{125}I-β-BuTX are summarized in Table 2.4. Only five of the seven batches of ^{125}I-β-BuTX were suitable for these experiments, as some preparations exhibited very high non-specific binding, which rapidly increased towards 100% of the total binding within a few days of the radioiodination; this was particularly obvious with batches of ^{125}I-β-BuTX prepared by the lactoperoxidase method (Rehm and Betz, 1982). Relatively high levels of non-specific binding (30-50% of the total at 2-2.5 nM ^{125}I-β-BuTX) were, however, found with all the toxin preparations. The results obtained with ^{125}I-β-BuTX prepared using chloramine-T were in reasonable agreement, with a K_d of ≈1.8 nM being observed on rat brain cryostat sections. ^{125}I-β-BuTX also bound to 1-day-old chick cerebellum sections with K_d =0.8 nM and B_{max} =40 fmoles/mg total section protein.

The binding of ^{125}I-β-BuTX was dependent on the presence of divalent cations, particularly on Ca^{2+} or Sr^{2+}, as shown in Figure 2.11. Very low levels of specific binding were observed in Ca^{2+}-free Krebs medium (3, 0 and 3% in three experiments relative to the specific binding in normal Krebs phosphate medium). However, in buffer containing Sr^{2+} the specific binding was as high as or higher than in standard Krebs phosphate buffer. This was due mainly to a significant reduction in the non-specific binding observed in this buffer (in Figure 2.11; non-specific binding was 49 and 32% of the total binding in standard Krebs and Sr^{2+}-Krebs phosphate medium, respectively), indicating that a proportion of

Figure 2.10. Concentration dependence of ^{125}I-β-BuTX binding to cryostat sections of rat forebrain



(a) Cryostat sections (10 μm) from rat forebrain at the level of the hippocampus were incubated for 45 min at 22°C in various concentrations of ^{125}I-β-BuTX in Krebs phosphate medium. Concentrations of free and bound ^{125}I-β-BuTX were determined as described (see Sections 2.3.5 and 2.3.6). Specific binding (●) was calculated by subtracting the non-specific binding, determined in the presence of 1 μM unlabelled β-BuTX (□), from the total binding (▲). Error bars indicate standard errors for duplicate samples.

(b) A Scatchard plot of the specific binding in (a). The best straight line through the points gave a K_d =1.9 nM and B_{max} =0.27 pmol/mg protein.

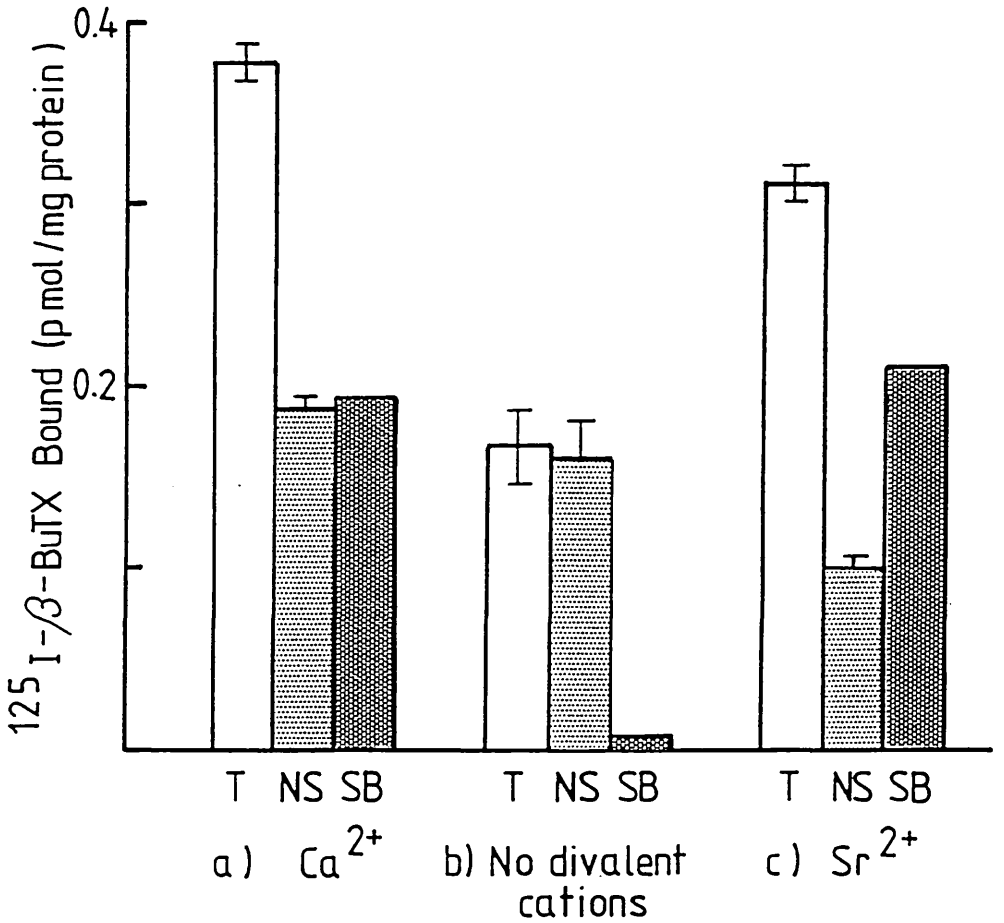
Table 2.4. Saturable binding of ^{125}I-ß-BuTX to cryostat sections from rat and chick brain

^{125}I-ß-BuTX prepared by	Cryostat sections	K_d (nM)	B_{max} (pmol/mg protein)
A. Lactoperoxidase[a] (3 preparations)	Forebrain, hippocampus level	4.7	0.48
B. Chloramine-T (2 preparations)	Forebrain, hippocampus level	1.9	0.16
C. Chloramine-T (2 preparations)	Forebrain, hippocampus level	1.6	0.17
	Cerebellum, sagittal sections	2.1	0.17
	Chick cerebellum	0.8	0.04

a: These values are not very reliable because these preparations of ^{125}I-ß-BuTX showed very high levels of non-specific binding, and were very unstable.

The binding of all ^{125}I-ß-BuTX preparations was Ca^{2+}-dependent.

Figure 2.11. Divalent cation dependence of ^{125}I-ß-BuTX binding to cryostat sections



Rat forebrain cryostat sections cut at the level of the hippocampus were labelled with 2.7 nM ^{125}I-ß-BuTX alone (total, T) or in the presence of 1 µM unlabelled ß-BuTX (non-specific, NS), and processed as described (Sections 2.3.5 and 2.3.6). The difference between T and NS is the specific binding (SB). The buffers used were:

(a) Ca^{2+}: Krebs phosphate medium, as in Section 2.3.2.

(b) **No divalent cations**: Krebs phosphate medium prepared without $CaCl_2$; EDTA (5 mM) was added to sequester any divalent cations (Mg^{2+}, and residual Ca^{2+} present in the sections).

(c) Sr^{2+}: Krebs phosphate medium prepared with 2.5 mM $SrCl_2$ instead of $CaCl_2$; EGTA (1 mM) was added to sequester any Ca^{2+} present in the sections.

the (rather high) non-specific binding may be due to interactions of the Ca^{2+}-dependent phospholipase A_2 active site with membranes.

Both β-BuTX and DTX inhibited ^{125}I-β-BuTX binding with similar potency. In one experiment, using 2.3 nM ^{125}I-β-BuTX, an IC_{50} ≃1 nM was observed with either of the unlabelled toxins, giving a K_i ≃0.5 nM. The non-specific binding in this experiment was rather high, representing ≃40% of the total binding; nonetheless 95% of the specific binding of ^{125}I-β-BuTX was blocked by either of the unlabelled toxins at 50 nM.

2.5. Discussion

Saturable high affinity binding of both ^{125}I-DTX and ^{125}I-β-BuTX to rat brain cryostat sections has been demonstrated. The gentle fixation of the tissue in 0.1% formaldehyde did not affect the binding of ^{125}I-DTX to synaptosomes, or its inhibition by β-BuTX, indicating that the acceptors for both toxins are resistant to this fixative. Kinetic studies of ^{125}I-DTX binding showed that the association of the toxin was rapid at 22°C and complete within the 30-45 min incubation routinely used, while the dissociation studies confirmed that the washing protocol employed (3 × 5 min at 4°C) produced the highest levels of specific binding. In competition studies ^{125}I-DTX binding was blocked by DTX with high affinity (the K_i of DTX was approximately equal to the K_d of ^{125}I-DTX binding), while β-BuTX inhibited ^{125}I-DTX binding with lower efficacy; this interaction of the toxins is similar to that observed on synaptosomes (Black *et al.*, 1986; Dolly *et al.*, 1987; see also Section 1.5). While ^{125}I-DTX binding was independent of divalent cation concentration, the binding of ^{125}I-β-BuTX showed a requirement for Ca^{2+} or Sr^{2+} as reported for synaptosomes from both chick (Rehm and Betz, 1982) and rat brain (Dolly *et al.*, 1987). Such a divalent cation requirement for toxin binding was also observed in electrophysiological studies in both the peripheral and central nervous systems (Caratsch *et al.*, 1985; Dolly *et al.*, 1980; cf. Section 1.3), indicating that the acceptors labelled are physiologically relevant.

It appears, therefore, that functional toxin acceptors similar to those identified on synaptosomes (Othman *et al.*, 1982, Black *et al.*, 1986; Dolly *et al.*, 1987) can be labelled on cryostat sections. The labelling conditions derived here (incubation with

2-2.5 nM radiolabelled toxin for 30-45 min, followed by three 5 min washes) have therefore been used in the autoradiography studies (Chapters 3 and 4).

2.5.1. Binding of Ligands to Cryostat Sections

The apparent K_d determined for the binding to cryostat sections of both ^{125}I-DTX and ^{125}I-β-BuTX was higher than that found on synaptosomes or synaptosomal plasma membranes, while the kinetic studies demonstrated that ^{125}I-DTX bound to and dissociated more slowly from its acceptors on the sections (Table 2.5). Similar discrepancies have been observed for opiate ligands (Simatov *et al.*, 1978; Young and Kuhar, 1979), kainic acid (Foster *et al.*, 1981; Monaghan and Cotman, 1982) or muscarinic cholinergic ligands (Yamamura *et al.*, 1979; Wamsley *et al.*, 1981). Dohanich *et al.* (1986) and Nonaka and Moroji (1984) have shown that the apparent K_d of [^{3}H]N-methyl scopolamine and [^{3}H]quinuclidinyl benzilate, respectively, increased with increasing section thickness, while the B_{max} values, when corrected for the higher protein content on thicker sections, were constant. Both groups also observed slower association rates for ligand binding on cryostat sections. This is probably due to delayed diffusion of the radioligand into the sections.

The essential difference between ligand binding studies on particulate preparations (e.g. brain homogenates, synaptosomes, or synaptic plasma membranes) and cryostat sections is that the former can be suspended in the incubation solution, and are thus in direct contact with a constant ligand concentration. Sections, on the other hand, are covered with a drop of the solution, from where the ligand diffuses into them. On entering the tissue, it is likely to be immediately removed by binding to its acceptors, which are highly concentrated there. Hence a gradient of ligand concentration is established, with unbound ligand being more dilute in deeper layers of the solution (within the sections) than in the drop of overlying incubation solution, from where an aliquot is removed to determine the "free" toxin concentration, F. Thus an error is introduced into estimates of F, and especially into the B/F ratio at low values of F on the Scatchard plot. Nonaka and Moroji (1985) observed a decrease in the apparent K_d when the incubation times were increased to allow equilibrium to be reached, but this was not confirmed by Dohanich *et al.* (1986), or in this study,

Table 2.5. Binding of ^{125}I-β-BuTX and ^{125}I-DTX to acceptors in the rat central nervous system: Equilibrium and kinetic constants for cryostat section and subcellular fractions

	Forebrain cryostat sections	Cerebrocortical synaptosomes	Cerebrocortical synaptic plasma membranes
β-BuTX			
Equilibrium Binding:			
K_d (nM)	1.8	0.6 [a] 0.2 [b]	-
B_{max} (pmol/mg protein)	0.16 - 0.17	0.3 [b]	-
DTX			
Equilibrium Binding:			
K_d (nM)	1.2	0.43 [c] 0.3 [b]	0.3 [d]
B_{max} (pmol/mg protein)	0.58	1 - 1.2 [c] 1.1 [b]	1.7 [d]
Kinetic Studies:			d
Association: $t_{1/2}$	7 min.	-	≃1.5 min.
at 22°C k_1	3×10^5 $M^{-1}s^{-1}$	-	~8×10^6 $M^{-1}s^{-1}$
Dissociation: $t_{1/2}$	24 min.	-	11 min.
at 22°C k_{-1}	4.8×10^{-4} s^{-1}	-	1.03×10^{-3} s^{-1}
K_d ($=k_{-1}/k_1$, nM)	1.6	-	0.13

a: Data from Othman *et al.* (1982).
b: From Dolly *et al.* (1987).
c: From Mehraban *et al.* (1984).
d: From Black *et al.* (1986).

where the apparent K_d for ^{125}I-DTX binding to forebrain sections was unaffected by incubation for 30 or 45 min.

The existence of diffusion restrictions to toxin binding was also apparent when ^{125}I-DTX was used to label cryostat sections of different thicknesses (Section 2.4.1.3, Figure 2.7a): Even at F =2.5 nM, insufficient ^{125}I-DTX penetrated deep enough to fully label sections thicker than 10 μm. A further indication that the K_d discrepancies observed (Table 2.5) may be due to limited diffusion of the toxins is the fact that the effect was somewhat greater for the larger toxin β-BuTX (M_r ≃21,000d; ratio of the K_d on sections to K_d on synaptosomes ≃4.5) than for DTX (M_r ≃7,000d; K_d on sections ÷ K_d on synaptosomes =3-4), while the 18-amino acid bee venom polypeptide apamin showed a K_d only ≃1.5× higher on sections (15 μm; K_d =25 pM, Mourre *et al.*, 1986) than on synaptosomes (K_d =15-20 pM, Romey *et al.*, 1984).

Diffusion restrictions in the sections are also suggested by the observation that the rate of dissociation of ^{125}I-DTX from cryostat sections varied with the method by which it was measured, being more rapid when bound ^{125}I-DTX was displaced by excess unlabelled DTX. Furthermore the first order dissociation plots for the "chase" experiments showed definite curvature. These effects usually suggest the existence of negative cooperativity of binding. However, restricted diffusion of the dissociating ^{125}I-DTX from stationary layers of solution deep in the section may allow significant re-binding of the toxin; under "chase" conditions unlabelled DTX immediately binds to the vacated acceptors, preventing re-binding of the labelled toxin. As the dissociation of ^{125}I-DTX from synaptosomes has only been measured by chasing with an excess of unlabelled toxin, it is not clear whether a similar discrepancy exists there; however, linear first order dissociation plots were obtained in all such experiments on synaptosomes (Black *et al.*, 1986). Nonetheless it appears that the discrepancies in the dissociation rates cannot be solely due to the cryostat section assay system, as similar differences have been observed for the binding of the iodinated peptides insulin, thyrotropin and nerve growth factor (Olefsky *et al.*, 1978; Powell-Jones *et al.*, 1980; Tait *et al.*, 1981; respectively) to cell preparations, and for ^{125}I-β-BuTX binding to chick brain synaptic membranes (Rehm and Betz, 1982). None of these authors considered negative cooperativity of binding an adequate explanation for the

differing dissociation rates.

The above discussion has highlighted some of the difficulties in the interpretation of the results of binding experiments on cryostat sections. Nonetheless, when these difficulties are borne in mind, such binding studies can give useful information on the properties of the acceptor sites compared to those on broken cell preparations. Furthermore they can help to identify relevant binding sites and thus validate further autoradiographic localization studies of the acceptors.

2.5.2. Acceptors for DTX and β-BuTX in Chick Brain

Toxin binding studies on chick brain synaptic membranes (see Sections 1.4.4 and 1.5) have identified a common high affinity acceptor for both ^{125}I-β-BuTX and ^{125}I-DTX, while, in addition, DTX and the facilitatory neurotoxins bind to a lower affinity acceptor variant. Thus β-BuTX can distinguish two classes of DTX acceptors in this tissue.

The binding of β-BuTX and DTX to chick brain cryostat sections has also been studied here. Since preliminary autoradiography studies with both toxins (see Chapters 3 and 4) suggested that high densities of toxin acceptors are found in the cerebellum molecular layer, sections from the cerebellum have been used for these experiments. As on the synaptosomal membrane preparations, both toxins bound with high affinity to the sections. ^{125}I-DTX labelled an apparently homogeneous population of acceptors with K_d =1.4 nM and B_{max} =190 fmol/mg protein; this binding was inhibited almost totally and with high affinity by β-BuTX (K_I =1.2 nM, Figure 2.8). Similarly, ^{125}I-β-BuTX bound to chick cerebellum sections with K_d ≃0.8 nM and B_{max} ≃40 fmol/mg total section protein, although, due to the high levels of non-specific binding observed, this B_{max} value is only tentative. The low affinity acceptors on synaptosomes, which bind only DTX (Black and Dolly, 1986a), have not been detected directly under the conditions used here, probably because the highest ^{125}I-DTX concentrations used were insufficient to saturate these binding sites. The presence of these sites is indicated by the small proportion of the specific ^{125}I-DTX binding which could not be inhibited by excess unlabelled β-BuTX (cf. Figure 2.8).

2.5.3. Characterization of the Acceptors for DTX and β-BuTX in Rat Brain Cryostat Sections

The present experiments on rat brain cryostat sections have revealed a single Ca^{2+} dependent ^{125}I-β-BuTX binding site, the affinity of which was only slightly lower than that of the toxin binding on synaptosomes under the same conditions (Dolly *et al.*, 1987; Table 2.5). Likewise a population of high affinity acceptors for ^{125}I-DTX has been observed on rat forebrain sections. One possible cause for the slightly reduced affinity of toxin binding on cryostat sections has already been discussed (Section 2.5.1). Alternatively this could be due to the presence of additional toxin binding sites with a lower affinity in the sections. All Scatchard plots of ^{125}I-DTX or ^{125}I-β-BuTX binding optimally fitted straight lines, and thus suggested that each of the toxins bound to a homogeneous and non-interacting population of acceptors. However, the likelihood of resolving two or more binding sites on a Scatchard plot depends on the ratio of their K_d values and on the proportion of high and low affinity acceptors (Bürgisser, 1984); additionally, high levels of non-specific binding (as observed with the ^{125}I-β-BuTX preparations) may mask the presence of low affinity sites. Moreover, in contrast to purified nerve terminals, cryostat sections of whole brain allow the simultaneous study of acceptors on a variety of tissue components such as synapses, neuronal cell bodies, axons and dendrites, as well as glial elements; the affinity of acceptors in these locations, if present, may vary somewhat. It is unlikely that the lower affinity on the sections is due to competition for the toxin acceptors by some endogenous ligand, since pre-incubation for up to 30 min in Krebs Ringer or Krebs Ringer containing 0.01% Triton X-100 did not affect the binding properties of either ^{125}I-DTX or ^{125}I-β-BuTX.

In accordance with the variety of tissue elements present in cryostat sections, it is interesting to compare the acceptor contents on sections and synaptosomes (Table 2.5). The B_{max} of both DTX and β-BuTX binding, when expressed relative to the total protein content in the samples, is ~1.8× and 1.9× greater, respectively, in the synaptosomes. This represents a substantial enrichment of the acceptors in the synaptic preparation, being only slightly lower than that observed for the synaptic marker protein synapsin I in synaptosomes compared to crude brain homogenates (Ueda *et al.*, 1979). The data in Table 2.5 also shows that DTX the

acceptors are further enriched on synaptic plasma membranes.

2.5.4. Interactions of β-BuTX and DTX

As indicated in Section 1.5, the interaction of the two toxins in rat brain preparations is complicated. In particular, the properties of β-BuTX binding show some dependence on the buffer system used in the experiments. The binding studies on rat brain cryostat sections described here exclusively used Krebs phosphate buffers. All of the specific ^{125}I-β-BuTX binding to acceptors on the sections could be blocked by unlabelled DTX with high affinity. The inhibition of ^{125}I-DTX binding by β-BuTX was Ca^{2+} dependent and had a greater efficacy (K_i =12-170 nM) than observed on synaptosomes in Krebs Ringer (cf. Section 1.5). This suggests that the low affinity β-BuTX binding site detectable in synaptosome binding assays using imidazole buffer or on the solubilized DTX acceptors is also present and accessible to β-BuTX on the sections. On synaptosomes, it appears that the change in buffer unmasks a second Ca^{2+} dependent lower affinity binding site for β-BuTX, possibly by inducing a conformational change in the acceptors for β-BuTX (and DTX, though not detected with this toxin). Such variability in the conformation of the acceptors may also explain the range of inhibition constants obtained in several competition experiments with β-BuTX (cf. Table 2.3). In view of the improved competition of β-BuTX on cryostat sections, it is surprising that the low affinity β-BuTX acceptor site found on synaptosomes in imidazole buffer was not detected directly in the binding experiments with ^{125}I-β-BuTX described here. It is possible that this site was masked by the rather high levels of non-specific binding observed with most of the ^{125}I-β-BuTX preparations tested.

The interaction of β-BuTX with ^{125}I-DTX binding suggests that there is some heterogeneity among the DTX acceptors on cryostat sections. Firstly, even high concentrations (5-10 μM) of β-BuTX could not displace ≈25% of the specific ^{125}I-DTX binding. This apparently β-BuTX-resistant ^{125}I-DTX binding is reminiscent of the β-BuTX-resistant low affinity acceptor population in chick brain (see above), although it does not appear to have a reduced affinity in the rat tissue. The β-BuTX-resistant ^{125}I-DTX binding appeared to be localized specifically in white matter regions on autoradiography (see Chapter 4). Secondly, the high affinity (K_d =1.9 nM) binding of ^{125}I-β-BuTX, compared to the lower affinity

competition of β-BuTX with ^{125}I-DTX binding suggests further heterogeneity (acceptor variants, sub-types or conformations) in the affinity of β-BuTX on the (common) DTX acceptors. Additional indications of DTX acceptor heterogeneity come from the observation that the overall affinity of ^{125}I-DTX binding was reduced on sections from cerebellum and brainstem (Table 2.2; see Section 2.4.1.2). Thus there may exist higher and lower affinity acceptors whose relative distribution may vary in different brain regions.

The possible heterogeneity of DTX acceptors is particularly interesting in view of the existence of several types of rapidly-activating voltage-dependent K^+-currents which can be blocked by DTX with different potency (see Section 1.4.3).

CHAPTER 3

Distribution of Acceptors for ß-Bungarotoxin in the Central Nervous System

3.1. Introduction

The presence of specific high affinity acceptors for ß-BuTX has been demonstrated in synaptic membranes from both rat and chick brain (see Chapter 1, Section 1.3.5). Similar high affinity acceptors were identified when rat brain cryostat sections were incubated with a radioiodinated derivative of this toxin, as described in Chapter 2. It should, therefore, be possible to study the distribution of these ß-BuTX acceptors by *in vitro* labelling autoradiography.

This method has become very popular in neurobiology. It has been used to map the distribution of the receptors/receptor sub-types of many neurotransmitters and neuropeptides, and of neurotransmitter uptake sites and central nervous system enzymes (reviewed by Kuhar *et al.*, 1986). Recently the binding sites of the neurotoxins tetrodotoxin (Mourre *et al.*, 1984), batrachotoxin (Worley and Baraban, 1987) and apamin (Mourre *et al.*, 1986) have also been localized. The method involves the labelling of cryostat sections with the ligand of interest, followed by exposure to photographic emulsions. This *in vitro* labelling of cryostat sections allows precise control of the incubation conditions to optimize ligand binding, after which the sections can easily be rinsed to reduce the non-specific binding. Compared to *in vivo* intravenous or intra-cerebroventricular administration of the

ligand, an even access to its binding sites in all brain areas can be ensured (e.g. restrictions due to the blood brain barrier are removed), and metabolic degradation of the ligand can be minimized. The reversibly bound water-soluble ligands are then localized by "dry" autoradiography, using either emulsion-coated coverslips (Roth *et al.*, 1974; Young and Kuhar, 1979) or ^{3}H-sensitive sheet film (Palacios *et al.*, 1981; Penney *et al.*, 1981a).

^{3}H-sensitive Ultrofilm (LKB) has a very high sensitivity for ^{3}H and other low-energy radiation emitters because the gelatine/silver bromide ratio of the emulsion layer has been reduced and the anti-scratch supercoating present in traditional films, which would normally absorb low energy electrons, has been omitted. When the film is applied there is thus direct contact between the emulsion and the radiolabelled sample, making high resolution autoradiography possible (Ehn and Larsson, 1979). The absence of the anti-scratch coating also minimizes artifacts from bremsstrahlung. Most importantly, Ultrofilm autoradiography images can be analysed by densitometry (Palacios *et al.*, 1981): A number of computerized analysis systems have been described (see e.g. Goochee *et al.*, 1980; Altar *et al.*, 1984; or Baskin *et al.*, 1986). When the densities of the image are compared to images from radioactive standards (Unnerstall *et al.*, 1982) quantitative data is obtained on the radioligand distribution.

In this Chapter, *in vitro* sheet film autoradiography of ^{125}I-β-BuTX-labelled cryostat sections was employed to study the distribution of β-BuTX acceptors. In order to obtain quantitative data, ^{125}I-labelled standards were prepared and used to characterize the response of Ultrofilm to the radioactive emissions of iodine-125. It was then possible to determine the distribution of ^{125}I-β-BuTX acceptors in various parts of the rat central nervous system or in 1-day-old chick brain.

3.2. Materials

β-BuTX was purified, and ^{125}I-β-BuTX (specific activity 400-800 Ci/mmol) and ^{3}H-β-BuTX (140 Ci/mmol) were prepared as described in Appendix A.1. ^{3}H-sensitive Ultrofilm was purchased from LKB, Croydon, Surrey, D19 developer from Kodak, Hertfordshire, and Hypam photographic fixer from Ilford Ltd, Cheshire. All other materials were as in Section 2.2.

3.3. Methods

3.3.1. Preparation of Cryostat Sections and Incubation with Radiolabelled ß-BuTX

Cryostat sections (10 µm) from rat brain or spinal cord were cut from tissue blocks lightly fixed by intra-cardiac perfusion with 0.1% formaldehyde (see Section 2.3.4 for details). Cryostat sections were also prepared from perfusion-fixed or fresh brains of 1-day-old leghorn chicks. The sections from this immature tissue were very fragile; fragments of material were often lost during the incubation and washes. Chick brain sections were therefore routinely stabilized by dipping the slides for 2 s in a solution of 0.5% gelatine and air drying.

Cryostat sections were labelled with 2-2.5 nM ^{125}I-ß-BuTX or ^{3}H-ß-BuTX as described in Section 2.3.5.

3.3.2. Ultrofilm Autoradiography

Autoradiograms were produced with ^{3}H-sensitive Ultrofilm. Slides containing the dried, toxin-labelled sections were mounted on cardboard using double-sided Sellotape and placed in an X-ray cassette. Under photographic safe-light a sheet of Ultrofilm was positioned over the sections. The film was exposed at 4°C for 24 hr to 10 days for ^{125}I-ß-BuTX, or 25 days for ^{3}H-ß-BuTX-labelled sections. After exposure, the film was developed for 5 min at 18°C in undiluted D19 developer, washed thoroughly, and fixed in Hypam (diluted 1+4). Enlarged photographic darkfield images were produced by printing directly from these autoradiograms. Brain areas were identified using the brain atlas of Paxinos and Watson (1982) and "Craigie's neuroanatomy of the rat" (Zeman and Innes, 1963) for rat, and the atlas by van Tienhoven and Juhasz (1962) for chick brain sections. To facilitate identification of these brain areas, some sections were stained in 1% pyronin Y in 50 mM sodium acetate buffer, pH 4.8, or 0.7% Sudan black B in ethanol, or 2% aqueous safranin.

3.3.3. ^{125}I-Labelled Brain Paste Standards

These were prepared using a method similar to that described by Unnerstall *et al.* (1982). Rat brain tissue was ground to a paste and placed in wells formed around 12 mm cork blocks using pressure-sensitive silver tape. Known amounts of ^{125}I-labelled DTX (~10^{4}-10^{7} d.p.m./well) were thoroughly mixed into the

paste. The standards were repeatedly degassed in a vacuum dessicator and remixed, before being frozen over solid CO_2. Cryostat sections (10 μm) were cut from these standards and thaw-mounted onto subbed microscope slides. Six sets of sections from 8 standards containing different amounts of iodine-125 were prepared.

All standard sections were exposed to ^{3}H-sensitive Ultrofilm for 4 days (see Section 3.2.3), standards cut from the same blocks producing identical images. Sections from two sets of standards were then wiped from the slides onto damped Whatman GF/C glass microfibre filter discs, dried and counted in a γ-counter. After digesting the sections from each disc in 0.45 M sodium hydroxide, the protein contents were measured by the method of Lowry *et al.* (1951; see Section 2.3.6 for details). The areas of the standard sections were determined by weighing excised enlarged printed images of autoradiograms thereof. All standards contained ≈2 μg of protein per mm^2 or 350-160 000 d.p.m./mg protein on the day when the standards were prepared (the reference date).

The remaining 4 sets of standards were then exposed to Ultrofilm for 4 hr-50 days to produce a series of images; sometimes standards were also exposed alongside experimental cryostat sections labelled with ^{125}I-β-BuTX or ^{125}I-DTX. The radiation dose which produced each image, D, could then be determined in units of d.p.m. × days × mm^{-2}. Due to the decay of iodine-125 over the exposure period, the radiation dose had to be calculated by integrating the radioactive decay equation

$$A = A_0 \times e^{-\lambda t}$$

where A is the activity at time = t, A_0 is the activity on the reference date, and λ is the decay constant, $\lambda = \frac{\ln 2}{t_{½}}$

(for ^{125}I, $t_{½}$ = 60 days and thus λ = 0.01155 days^{-1})

with respect to t over the exposure period. Thus:

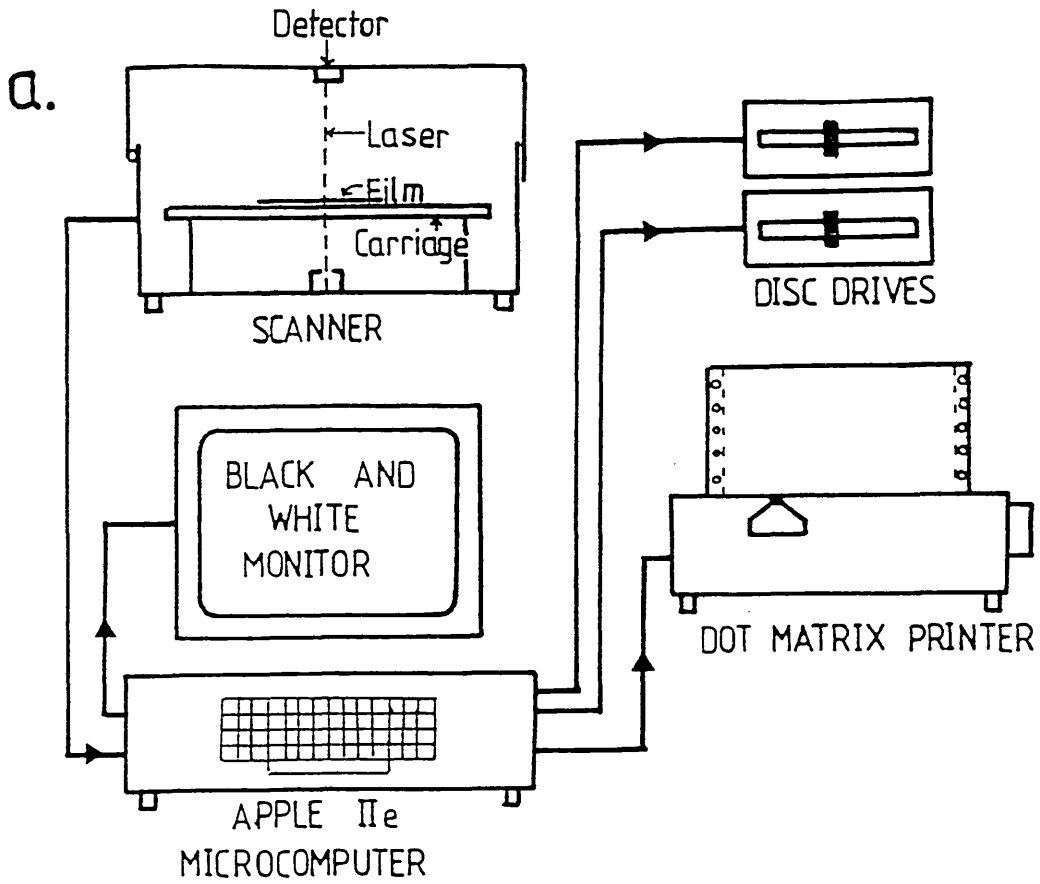
$$D = \frac{A_0}{-\lambda}(e^{-\lambda b} - e^{-\lambda a})$$

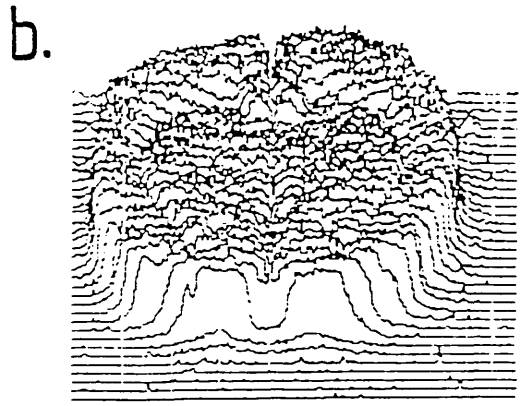
where a and b are the start and end of the exposure, respectively, in days after the reference date.

3.3.4. Densitometric Analysis of Autoradiograms

Ultrofilm autoradiograms were analysed using a BIOMED Instruments 1D,2D soft laser scanning densitometer controlled by an Apple IIe microcomputer with two disc drives and connected to a black and white monitor and a dot matrix printer (Figure 3.1a). An

Figure 3.1. Densitometric Analysis of Autoradiograms







(a) Diagram of the Apple IIe-controlled scanning densitometry system.

(b) An example of a relief picture of a scan of an autoradiogram.

(c) An example of a contour map of a scan of an autoradiogram.

autoradiogram was scanned while passing between a 3 μm diameter ruby laser source and a photodiode which measured the density (blackening) of the image on an arbitrary scale of 255 grey levels. The scanner was calibrated to give grey level readings of 18-20 for unexposed clear film, and 245-250 for totally blackened (light-exposed) Ultrofilm. A rectangular image area was digitized as 256 × 192 pixels, and the data obtained stored on 5-inch floppy discs at a capacity of one scanned image per disc. The smallest image area which could be scanned was 0.2 × 0.13 cm (step size between readings of 10 μm), while the largest brain section autoradiogram fitted into an area of 1.8 × 1.23 cm (step size of 70 μm). Depending on the chosen image size, scanning required 15 min-1 hr per image.

The digitized data was analysed using the "2D/1D PCI V" program (© BIOMED Instruments). This allowed pictorial representations of the data, either as relief images (Figure 3.1b, front or back views) with a base set at any grey level, or as "contour maps", where bands of chosen grey levels were differentiated in up to six black-and-white shadings (Figure 3.1c). Most importantly, the grey level value of any individual pixel, as identified with a cursor, could be read out directly. For routine analysis of images, relief pictures were used to ensure the image was optimally exposed (all optical densities above grey level 30, but below 200; see Results, Section 3.4.2 below). Then a series of contours was designed which allowed identification of the brain areas of interest. 2-3 patches of 9 density readings (a 3 × 3 pixel square) were taken for each brain area and averaged. The densities were converted to d.p.m./mm² by comparison with the standards (Section 3.3.4 above), and then, using the specific activity of the toxin, to fmol/mm².

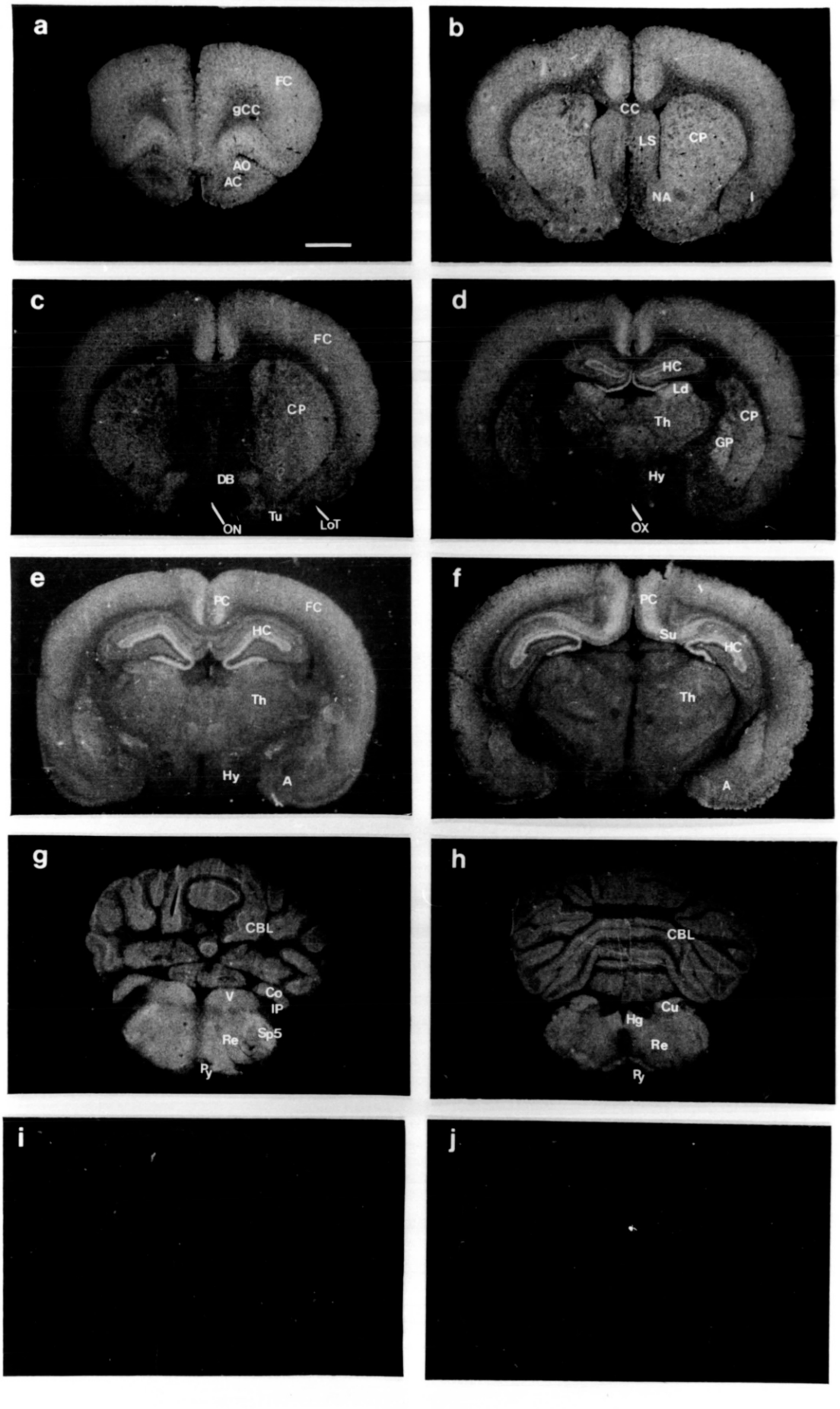
3.4. Results

3.4.1. β-BuTX Acceptors Can Be Localized by *In Vitro* Autoradiography

Ultrofilm autoradiograms of sections incubated with 2-2.5 nM ^{125}I-β-BuTX (a concentration shown to saturate the specific binding sites, see Chapter 2, Figure 2.10) revealed a widespread and heterogeneous distribution of the β-BuTX acceptors in rat brain (Figure 3.2). The bulk of the ^{125}I-β-BuTX binding was saturable,

Figure 3.2. Distribution of ß-BuTX acceptors in rat brain

Representative darkfield images (silver grains appear white) of autoradiograms from cryostat sections of rat forebrain at the level of the anterior olfactory nucleus (a), anterior (b) and posterior (c) caudate putamen, anterior (d), mid (e, i and j) and posterior (f) hippocampus, and of cerebellum with brainstem (g and h). All sections were labelled in 2-2.5 nM ^{125}I-ß-BuTX alone (a-h) or in the presence of 1 µM ß-BuTX (i) or 1 µM DTX (j). As the images represent the results of different experiments and were printed separately, grain densities cannot be compared between photographs. A, amygdala; AC, anterior commissure; AO, anterior olfactory nucleus; CBL, cerebellum; CC, corpus callosum; Co, cochlear nucleus; CP, caudate putamen; Cu, cuneate nucleus; DB, diagonal band; FC, frontoparietal cortex; gCC, genu of corpus callosum; GP, globus pallidus; HC, hippocampal formation; Hg, Hypoglossal nucleus; Hy, hypothalamus; I, insular cortex; Ip, inferior cerebellar peduncle; Ld, laterodorsal thalamic nucleus; LS, lateral septal nucleus; LoT, lateral olfactory tract; NA, nucleus accumbens; ON, optic nerve; OX, optic chiasma; PC, posterior cingulate cortex; Py, pyramidal tracts; Re, reticular formation; Sp5, nucleus of the spinal trigeminal nerve; Su, subiculum; Th, thalamus; Tu, olfactory tubercle; V, vestibular nucleus. Scale bar (in a) =2 mm.


a
FC
gCC
AO
AC
b
CC
LS
CP
NA
I
c
FC
CP
DB
ON
Tu
LoT
d
HC
Ld
Th
CP
GP
Hy
OX
e
PC
FC
HC
Th
Hy
A
f
PC
Su
HC
Th
A
g
CBL
V
Co
IP
Re
Sp5
Ry
h
CBL
Cu
Hg
Re
Ry
i
j

as it could be displaced by co-incubation with an excess of β-BuTX (Figure 3.2i), when only faint labelling was observed. DTX which, like toxin I, completely inhibits the binding of radiolabelled β-BuTX to synaptosomes (Othman *et al.*, 1982; Dolly *et al.*, 1987) and cryostat sections (see Section 2.4.2) similarly blocked the ^{125}I-β-BuTX binding (Figure 3.2j). As will be described in detail below, ^{125}I-β-BuTX bound to areas containing grey matter more strongly than to white matter regions; the highest levels of labelling were observed in the cerebral cortex, particularly the posterior cingulate cortex, caudate putamen, and the molecular layer of the dentate gyrus.

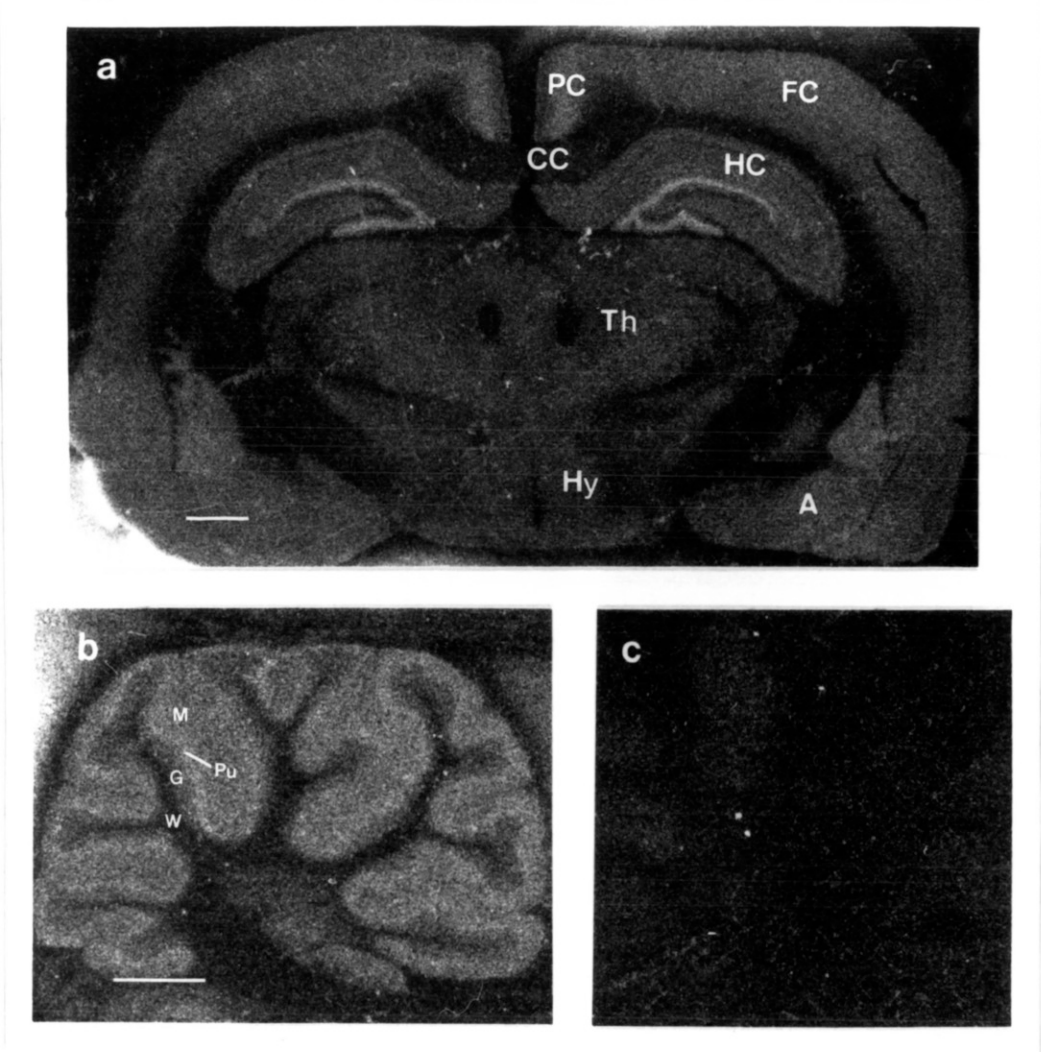
A similar distribution of β-BuTX acceptors was observed when tissue sections were incubated with 2.5 nM ^{3}H-β-BuTX (Figure 3.3). A section through rat forebrain at the level of the hippocampus (Figure 3.3a) showed the highest ^{3}H-β-BuTX binding in the posterior cingulate cortex and the molecular layer of the dentate gyrus. In the cerebellum specific acceptors were also labelled by both ^{125}I-β-BuTX (Figure 3.2g,h) and ^{3}H-β-BuTX (Figure 3.3b): The moderately labelled molecular layer was separated from the weakly labelled granule cell layer by the strongly labelled Purkinje cell layer, while labelling in the central white matter bundles was very weak. It should be noted that autoradiography with ^{3}H-β-BuTX required much longer exposure times before an image was visible on the Ultrofilm (see Methods, Section 3.3.3). ^{125}I-β-BuTX was, therefore, used in all remaining studies.

3.4.2. Response of ^{3}H-Sensitive Ultrofilm to Iodine-125

Autoradiography with ^{3}H-sensitive Ultrofilm can yield quantitative information on radioligand binding, provided the response of the film to the radioisotope used is known. To characterize the film response, ^{125}I-labelled brain paste standards were prepared and cryostat sections were cut at the same thickness (10 μm) as in the toxin localization studies. When these standards were exposed to Ultrofilm, uniformly labelled autoradiograms were obtained (Figure 3.4a). On laser densitometry, 20 random density readings from each image usually varied by less than 5%.

A plot of relative optical density (equivalent to the grey level measured by laser densitometry) against radiation dose for a series of images is shown in Figure 3.4b. The optical density of the film was clearly not linearly related to the radiation dose:

Figure 3.3. Localization of acceptors for ^{3}H-β-BuTX



Darkfield images of autoradiograms of rat brain sections labelled in 2.5 nM ^{3}H-β-BuTX.

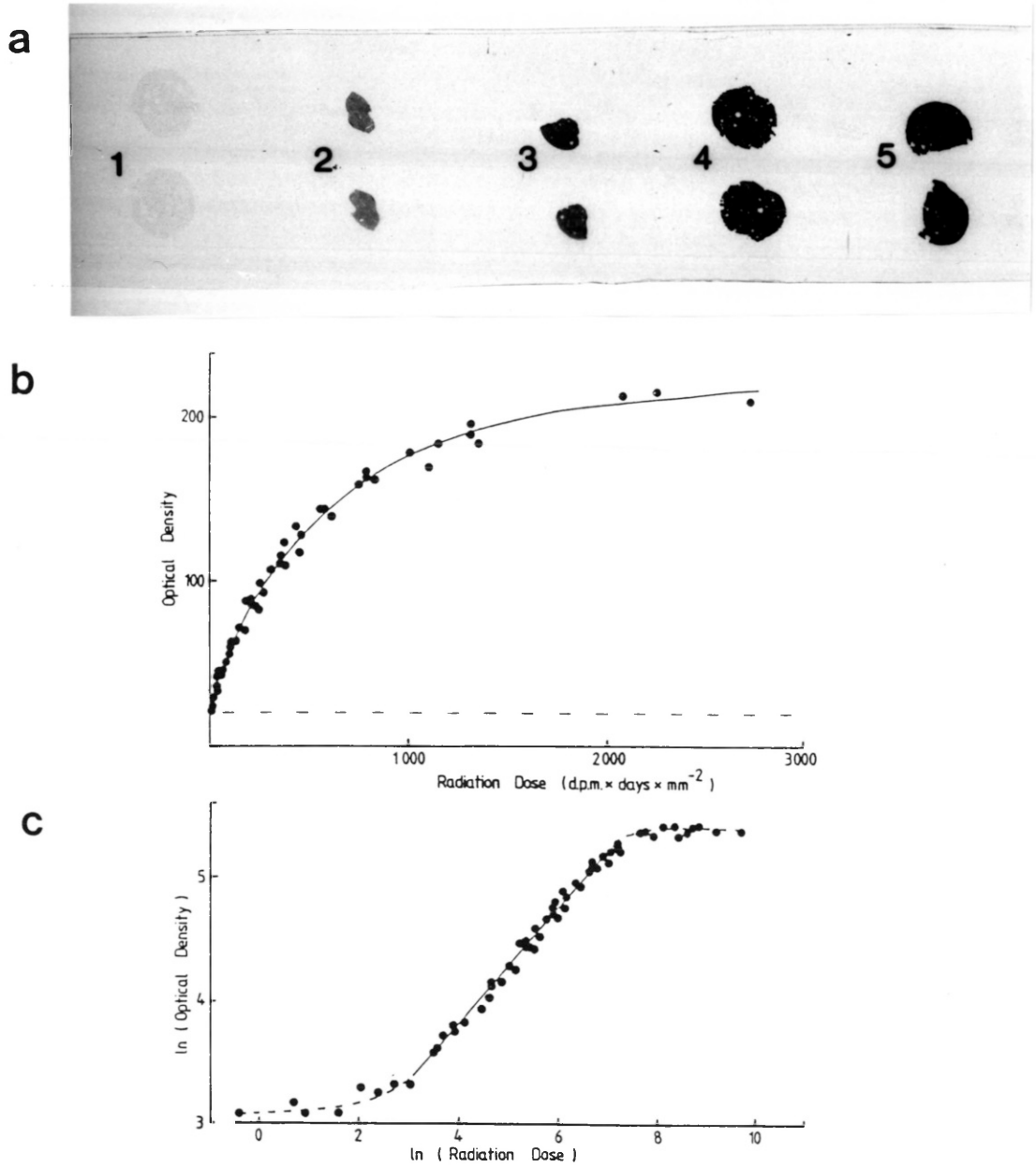
(a) Forebrain at the level of the hippocampus. A, amygdala; CC, corpus callosum; FC, frontoparietal cortex; HC, hippocampal formation; Hy, hypothalamus; PC, posterior cingulate cortex; Th, thalamus.

(b) A sagital section of cerebellum. G, granule cell layer; M, molecular layer; Pu; Purkinje cell layer; W, white matter laminae.

(c) A control section from cerebellum, incubated in 2.5 nM ^{3}H-β-BuTX in the presence of 1 μM unlabelled β-BuTX.

All scale bars =1 mm.

Figure 3.4. Response of ^{3}H-sensitive Ultrofilm to ^{125}I-labelled brain paste standards



(a) Photographs of a set of ^{125}I-labelled brain paste standards after 96 hr exposure to ^{3}H-sensitive Ultrofilm. Each section contains a different amount of radioactivity per mm^2: 1: 5 d.p.m.; 2: 52 d.p.m.; 3: 87 d.p.m.; 4: 106 d.p.m.: 5: 191 d.p.m. Magnification 1×.

(b) The variation of film optical density (=grey level determined by laser densitometry) with radiation dose. Each point represents the mean of the density readings at 20 pixels on scans of autoradiograms generated from sections containing 8 different concentrations of iodine-125 (see Methods Section 3.3.3.) exposed for different lengths of time.

(c) The data from b above, re-plotted as ln (optical density) vs ln (radiation dose). The central linear portion (that is optical density 30-200 or radiation dose 22-1,311 d.p.m. × days × mm^{-2}) fitted a straight line defined by $y = 1.968 + 0.464x$ with $r = 0.994$. This straight line portion was used to convert optical density in brain section autoradiograms to d.p.m. × days × mm^{-2} of ^{125}I-tracer bound.

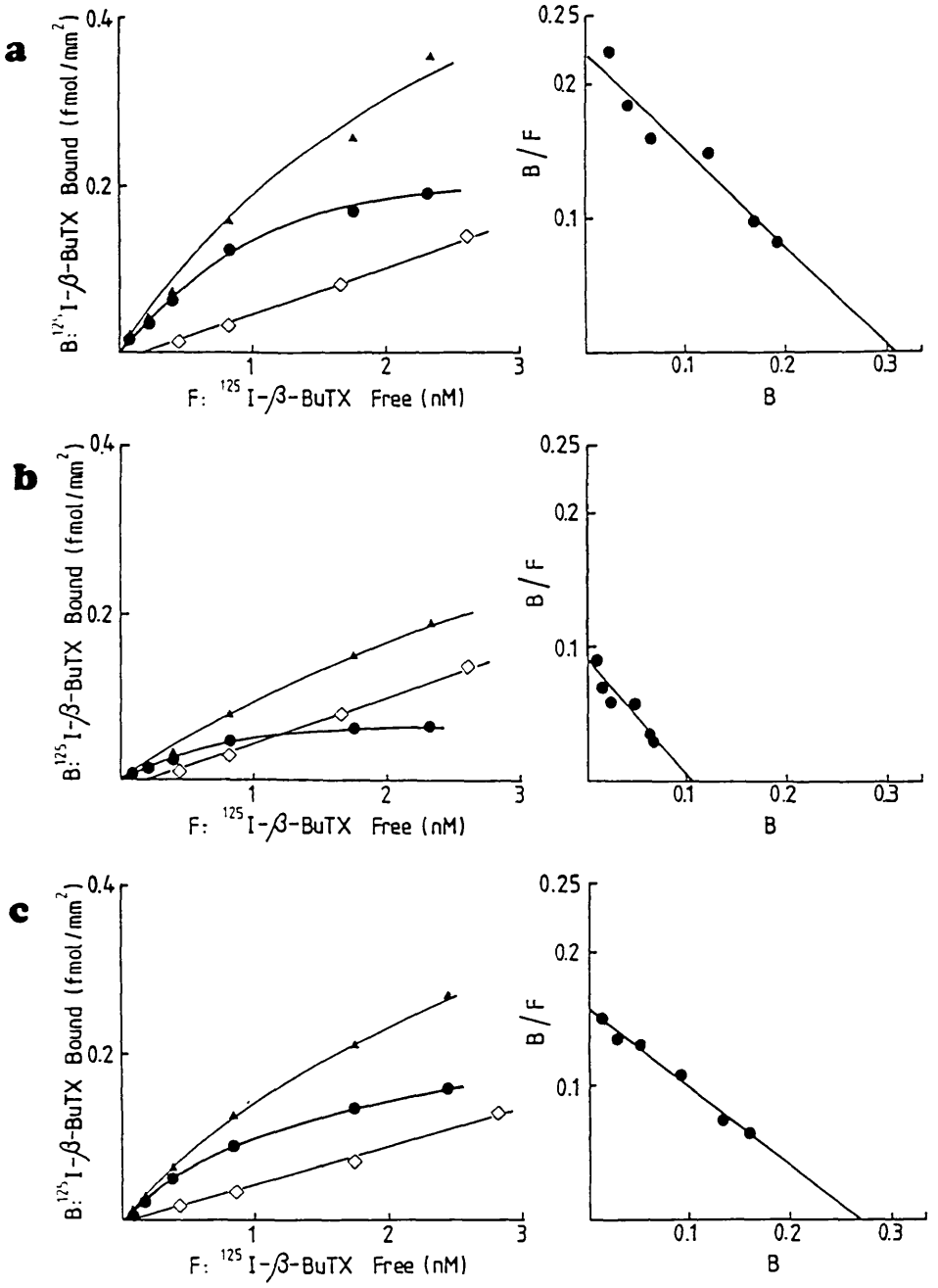
The film appeared to saturate at radiation doses above ~1 300 d.p.m. × days × mm^{-2}. The data from Figure 3.4b was re-plotted as ln (optical density) vs ln (radiation dose) to produce the curve shown in Figure 3.4.c (see also Unnerstall *et al.*, 1982; Israel *et al.*, 1984). The slope of this curve provides an estimate of the photographic contrast of Ultrofilm. At low radiation doses the film had a very slow response, whereas at high doses saturation was observed (see above). The film was most sensitive at radiation doses between ~20 and 1 300 d.p.m. × days × mm^{-2}, corresponding to optical density grey levels of 30-200. Thus for quantitative analysis, exposures of autoradiograms were adjusted to yield optical density grey levels in this range. The central portion of this graph could be fitted to a straight line, which was used to convert optical density on autoradiograms to radiation dose in d.p.m. × days × mm^{-2}, and hence, from the specific activity of the toxin on the first day of the exposure, to fmol of ^{125}I-β-BuTX bound/mm^2. Autoradiograms could thus be analysed quantitatively.

Several calibration curves such as the one in Figure 3.4c were constructed when ^{125}I-standards were exposed alongside experimental sections. The results were always very reproducible; however, the temperature of the D19 developer had to be precisely controlled. For quantitative autoradiography ^{3}H-sensitive Ultrofilm was always developed at 18°C.

3.4.3. Concentration-dependent Binding of ^{125}I-β-BuTX to Rat Brain Cryostat Sections

When autoradiograms were prepared from sections incubated with a range of different concentrations of ^{125}I-β-BuTX and analysed, typical saturation binding curves could be constructed for discrete brain regions (Figure 3.5). These binding curves and the corresponding Scatchard plots are similar to those obtained in concentration dependent binding studies for whole brain sections in Chapter 2 (Figure 2.10). Binding parameters were calculated for forebrain sections at the level of the hippocampus and the cerebellum (Table 3.1). The K_d values were similar for all regions examined, with the average being 1.3 nM; the range obtained (0.6-2.1 nM) was within the error in the analytical method, particularly when studying comparatively small anatomical areas (e.g. the contrastingly labelled layers of the hippocampus). There were significant variations in B_{max} values (fmol/mm^2) throughout the

Figure 3.5 Autoradiographic determination of ^{125}I-β-BuTX binding to rat brain cryostat sections



Rat brain cryostat sections (10 μm) were incubated in a range of concentrations of ^{125}I-β-BuTX, washed, dried and exposed to ^{3}H-sensitive Ultrofilm. The resulting autoradiograms were analysed by laser densitometry. Bound toxin could thus be determined in fmol/mm^2. Binding curves (left) and Scatchard plots (right) are shown for frontal cerebral cortex (a), corpus callosum (b), and the molecular layer of the cerebellum (c). The specific binding (●) was determined by subtracting the non-specific labelling, measured in the presence of 1 μM β-BuTX (◇) from the total binding (▲). The Scatchard plots were calculated for the specific binding in each brain area.

Table 3.1. Binding constants obtained from measuring the saturable binding of ^{125}I-β-BuTX to regions of rat brain

Brain region studied	K_d (nM)	B_{max} (fmol/mm^2)
GREY MATTER		
Frontoparietal cerebral cortex	1.6	0.33
Posterior cingulate cortex	1.5	0.40
Caudate putamen	1.7	0.32
Globus pallidus	1.2	0.17
Hippocampal formation		
CA_1-CA_2:		
Stratum oriens	1.7	0.25
Pyramidal cell layer	2.1	0.19
Stratum radiatum	2.1	0.28
Dentate Gyrus:		
Stratum moleculare	1.8	0.53
Granule cell layer	1.5	0.19
Hilus	1.4	0.23
Lateral habenular nucleus	0.67	0.081
Thalamus		
Laterodorsal nucleus	1.6	0.41
Ventroposterior nucleus	1.0	0.10
Hypothalamus		
Lateral hypothalamic area	0.68	0.079
Basal/cortical amygdala	1.0	0.18
Cerebellum		
Molecular layer	1.8	0.28
Granule cell layer	1.2	0.15
WHITE MATTER		
Corpus callosum	1.4	0.11
External capsule	1.1	0.076
Internal capsule	1.2	0.086
Fimbria hippocampi	0.62	0.054
Cerebellar white matter	0.60	0.058

Cryostat sections (10 μm) from rat forebrain or cerebellum were incubated in a range of concentrations of ^{125}I-β-BuTX, as described in Figure 3.5. Sections were exposed to ^{3}H-sensitive Ultrofilm, and the resulting autoradiograms were analysed by laser densitometry. Bound ^{125}I-β-BuTX could thus be determined in fmol/mm^2. Non-specific binding was subtracted from the total, and a Scatchard plot of the specific binding was used to determine the binding constants listed.

brain, ranging from 0.05-0.11 in white matter to 0.53 in the molecular layer of the dentate gyrus.

As noted in Chapter 2 (Section 2.4.2), ^{125}I-β-BuTX binding was dependent on the presence of divalent cations; very little specific ^{125}I-β-BuTX binding was observed in Ca^{2+}-free buffer, although toxin binding was restored in the presence of Sr^{2+}. These results were confirmed by autoradiography of sections incubated with ^{125}I-β-BuTX in buffers containing different cations. In the absence of divalent cations, only background labelling was observed. The level of non-specific binding was reduced in Sr^{2+}-buffer, but quantitative analysis of autoradiograms revealed similar levels of specifically bound ^{125}I-β-BuTX in Sr^{2+}- or Ca^{2+}-containing buffer. Furthermore, the distribution of this specific ^{125}I-β-BuTX binding, when expressed relative to the binding in frontoparietal cerebral cortex, did not differ significantly in these buffers (Table 3.2), indicating that the toxin acceptors in all regions were similar in their requirement for Ca^{2+} or Sr^{2+}.

3.4.4. Detailed Analysis of the Location of β-BuTX Acceptors in Various Brain Regions

As the affinity (K_d) of ^{125}I-β-BuTX binding was shown above not to vary significantly between different brain regions, levels of autoradiographic labelling at saturating ^{125}I-β-BuTX concentrations can be interpreted as differences in the number of β-BuTX acceptors present; this allows a very large number of brain regions to be studied. Results obtained from quantitative densitometric analysis of autoradiograms from sections incubated in 2-2.5 nM ^{125}I-β-BuTX are summarized in Table 3.3. At this concentration the non-specific binding (usually 0.08-0.13 fmol/mm^2) was at an acceptably low level, representing <25% of the total ^{125}I-β-BuTX bound in most brain areas. Occasionally, the distribution of the non-specific binding was somewhat uneven, white matter tracts tending to show less labelling (~0.06-0.08 fmol/mm^2), while the cell layers in the hippocampal formation or in the cerebellum contained higher levels of non-specifically bound ^{125}I-β-BuTX (≈0.15 fmol/mm^2). The distribution of the specific binding agrees with that shown in Table 3.1, the levels of binding listed representing 70-80% of the B_{max} values reported.

In the description below, levels of specific ^{125}I-β-BuTX binding were classified into six groups, from "very low" to "very

Table 3.2. Divalent cation dependence of ^{125}I-β-BuTX binding in rat brain

	Normal Krebs Ringer		Ca^{2+}-free Sr^{2+} Krebs Ringer	
Brain region studied	Total binding (fmol/mm^2)	Specific binding (% of cortex)	Total binding (fmol/mm^2)	Specific binding (% of cortex)
GREY MATTER				
Front. cerebral cortex	0.312	100	0.309	100
Post. cingulate cortex	0.352	122	0.340	113
Caudate putamen	0.298	92	0.264	82
Hippocampal formation				
CA_1-CA_2:				
Stratum oriens	0.262	73	0.290	92
Pyramidal cell layer	0.216	47	0.266	66
Stratum radiatum	0.285	85	0.284	90
Dentate Gyrus:				
Stratum moleculare	0.411	154	0.369	124
Granule cell layer	0.217	48	0.197	55
Thalamus				
Laterodorsal nucleus	0.358	125	0.294	94
Ventroposterior nucleus	0.304	96	0.272	85
Basal/cortical amygdala	0.226	53	0.225	66
WHITE MATTER				
Corpus callosum	0.188	32	0.180	48
External capsule	0.174	24	0.146	34
Internal capsule	0.177	26	0.156	38

Cryostat sections were labelled in 2.5 nM ^{125}I-β-BuTX in Krebs Ringer (0.75 mM Ca^{2+}) or a Ringer in which Ca^{2+} had been replaced by Sr^{2+} (2.5 mM) in the presence of 1 mM EGTA to chelate any residual Ca^{2+} in the sections. Autoradiograms were prepared using ^{3}H-sensitive Ultrofilm and analysed by laser densitometry. Non-specific binding in this experiment was 0.130 and 0.062 fmol/mm^2 in the Ca^{2+} and Sr^{2+} buffers, respectively.

Table 3.3. Distribution of ^{125}I-β-BuTX acceptors in the central nervous system of the rat

Region	n[a]	^{125}I-β-BuTX bound specifically (fmol/mm²)	Relative content of β-BuTX acceptors [b]
GREY MATTER			
Olfactory system			
Anterior olfactory nucleus	2	0.166 ± 0.051	* * *
Olfactory tubercle	3	0.094 ± 0.014	* *
Cerebral Cortex			
Frontoparietal (anterior to Bregma)	3	0.318 ± 0.033	* * * * * *
Frontoparietal (posterior to Bregma)	4	0.243 ± 0.044	* * * * *
Insular cortex	3	0.136 ± 0.012	* * *
Posterior cingulate cortex	4	0.321 ± 0.057	* * * * * *
Forebrain			
Caudate putamen	3	0.256 ± 0.024	* * * * *
Globus Pallidus	3	0.153 ± 0.025	* * *
Nucleus accumbens	3	0.197 ± 0.033	* * * *
Lateral septal nucleus	3	0.232 ± 0.044	* * * *
Amygdala			
Basal nuclei	5	0.130 ± 0.022	* * *
Cortical nuclei	5	0.124 ± 0.018	* * *
Lateral nucleus	2	0.201 ± 0.105	* * * *
Hippocampal formation			
CA_1-CA_2:			
Stratum oriens	4	0.203 ± 0.027	* * * *
Pyramidal cell layer	4	0.136 ± 0.031	* * *
Stratum radiatum	4	0.212 ± 0.022	* * * *
Subiculum	1	0.246	* * * * *
CA_3:			
Stratum oriens	4	0.164 ± 0.014	* * *
Pyramidal cell layer	4	0.106 ± 0.027	* *
Stratum radiatum	4	0.189 ± 0.024	* * * *
Dentate Gyrus:			
Stratum moleculare	4	0.314 ± 0.041	* * * * * *
Granule cell layer	4	0.131 ± 0.026	* * *
Hilus	4	0.192 ± 0.014	* * * *
Lateral habenular nucleus	3	0.104 ± 0.013	* *
Medial habenular nucleus	4	0.080 ± 0.009	* *
Thalamus			
Laterodorsal nucleus	4	0.227 ± 0.021	* * * *
Ventroposterior nucleus	5	0.184 ± 0.020	* * * *
Reuniens nucleus	3	0.091 ± 0.011	* *
Posterior nuclear group	5	0.151 ± 0.018	* * *
Hypothalamus			
Ventromedial nucleus	3	0.082 ± 0.007	* *
Arcuate nucleus	5	0.012 ± 0.005	*
Lateral hypothalamic area	4	0.077 ± 0.010	* *
Lateral geniculate nucleus	3	0.117 ± 0.017	* *
Cerebellum			
Molecular layer	3	0.161 ± 0.041	* * *
Purkinje cell layer	2	0.185 ± 0.092	* * * *
Granule cell layer	3	0.107 ± 0.024	* *

contd.

Table 3.3. contd.

Region	n[a]	^{125}I-β-BuTX bound specifically (fmol/mm^2)	Relative content of β-BuTX acceptors [b]
Brainstem			
Cochlear nucleus	1	0.198	* * * *
Reticular formation	1	0.186	* * * *
Vestibular nucleus	1	0.207	* * * *
Cuneate nucleus	1	0.218	* * * *
Nucleus of spinal trigeminal nerve	1	0.221	* * * *
Nucleus of hypoglossal nerve	1	0.220	* * * *
WHITE MATTER			
Lateral olfactory tract	3	0.017 ± 0.009	*
Anterior commissure	3	0.103 ± 0.019	* *
Corpus callosum	5	0.111 ± 0.011	* *
External capsule	3	0.112 ± 0.017	* *
Internal capsule	3	0.104 ± 0.025	* *
Diagonal band	2	0.089 ± 0.028	* *
Fornix	4	0.074 ± 0.010	* *
Optic nerve	1	0	
Optic chiasma	1	0.040	*
Optic tract	3	0.049 ± 0.010	*
Fimbria hippocampi	4	0.060 ± 0.013	* *
Stria medullaris thalami	4	0.096 ± 0.031	* *
Mammillothalamic tract	4	0.111 ± 0.015	* *
Cerebellar white matter	3	0.055 ± 0.014	*
Inferior cerebellar peduncle	1	0.028	*
Spinal trigeminal nerve	1	0.066	* *
Pyramids	1	0.068	* *
SPINAL CORD			
Grey matter	1	0.275	* * * * *
White matter	1	0.086	* *

Cryostat sections were labelled with 2-2.5 nM ^{125}I-β-BuTX, and autoradiograms were prepared using ^{3}H-sensitive Ultrofilm. These autoradiograms were analysed by laser densitometry as described.

a: n is the number of experiments using different ^{125}I-β-BuTX preparations. Specific binding of ^{125}I-β-BuTX was determined by subtraction of the non-specific binding and is given as mean ± S.E.M.

b: Relative levels of ^{125}I-β-BuTX binding in fmol/mm^2 are given as:

Very low	= *	= 0 - 0.059;
low	= * *	= 0.060 - 0.119;
moderate	= * * *	= 0.120 - 0.179;
moderately high	= * * * *	= 0.180 - 0.239;
high	= * * * * *	= 0.240 - 0.299;
very high	= * * * * * *	= 0.300 - 0.359.

The average protein content of cryostat sections was 1.2 μg/mm^2.

high", as defined in the legend to Table 3.3. In addition the distribution of the acceptors is shown in the darkfield autoradiograms in Figures 3.6 to 3.10. Since these photographs were all printed with different exposures, and the apparent grain densities cannot therefore be compared directly between the figures, calibrated scanned representations of the images are also shown in Figures 3.6, 3.7, 3.8 and 3.9. Note that the four bands of shading on the scans differ from the six density levels defined above.

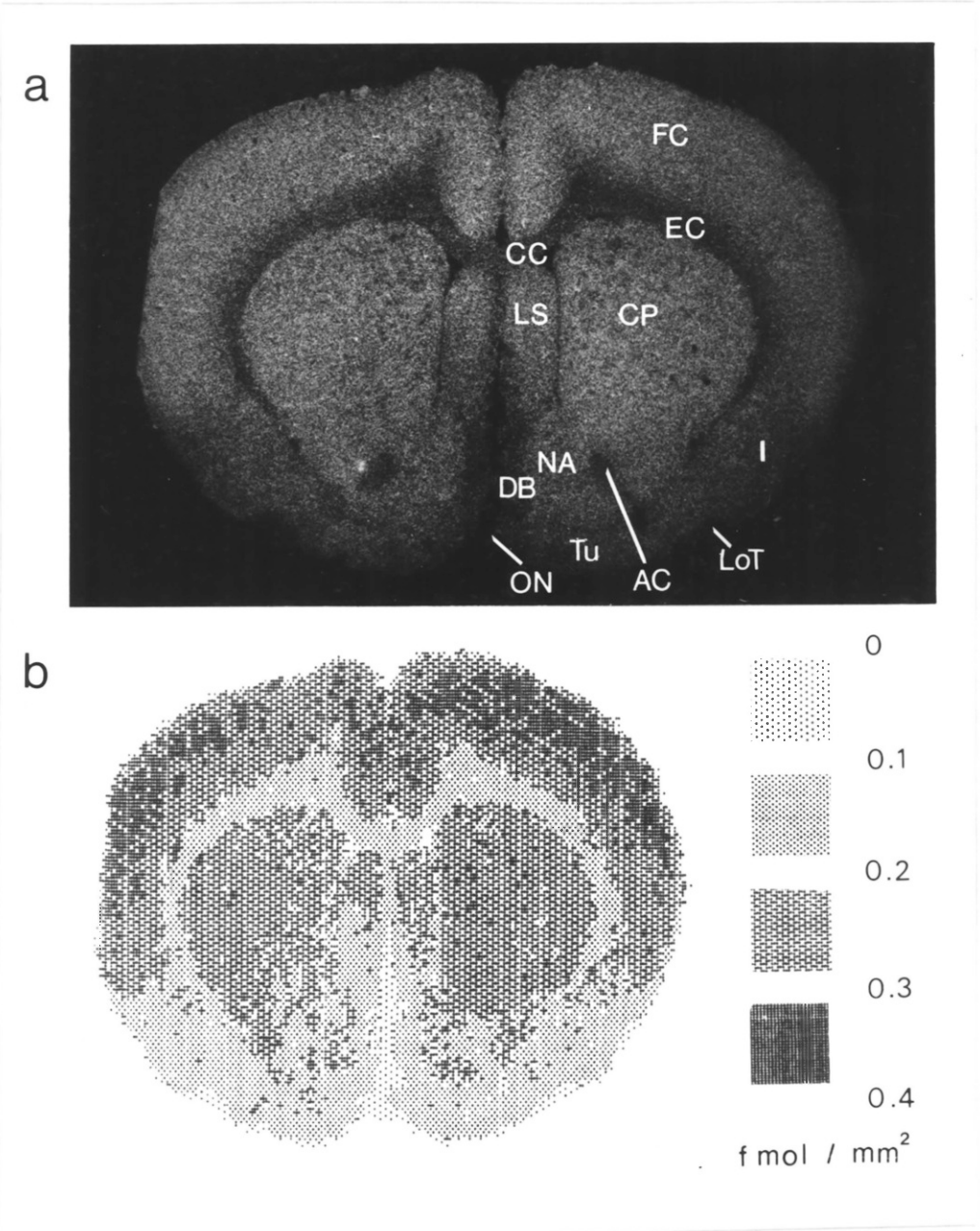
3.4.4.1. *The telencephalon*

In the rhinal system, the olfactory nucleus (Figure 3.2a) contained moderate and the olfactory tubercle (Figure 3.6) low levels of β-BuTX acceptors. High autoradiographic grain densities were observed throughout the cerebral cortex (Figures 3.2a,b,c, 3.6 and 3.7). The anterior frontoparietal cerebral cortex was labelled very strongly by ^{125}I-β-BuTX. The acceptor concentration decreased ventrally, where the insular (rhinal) cortex showed only moderate labelling, and posteriorly. However, very high levels of toxin binding were observed in the posterior cingulate cortex (Figures 3.2e and 3.7), which is continuous with the subiculum of the hippocampus (Figure 3.2f). The cerebral cortex was always labelled uniformly throughout its thickness; its six layers could not be distinguished on autoradiograms.

A high concentration of β-BuTX acceptors was also found in the neostriatum (Figures 3.2b,c,d,e, 3.6 and 3.7). The caudate putamen contained high and the globus pallidus moderate levels of toxin binding. The myelinated fibre bundles traversing the striatum could easily be distinguished on autoradiograms due to the reduced grain densities overlying them. The resolution of the scanner densitometer was not sufficient, however, to distinguish between the neuropil and white matter bundles in the striatum; hence, the acceptor densities listed in Table 3.3 for caudate putamen and globus pallidus are probably underestimates. The nucleus accumbens contained moderately high levels of β-BuTX binding (Figure 3.6).

In the amygdala (Figures 3.2d,e,f and 3.7) the basal and cortical nuclei contained moderate numbers of acceptors, while the lateral nuclei showed moderately high grain densities. A characteristic distribution of β-BuTX acceptors was always found in the hippocampal formation (Figure 3.8). The neuropil layers,

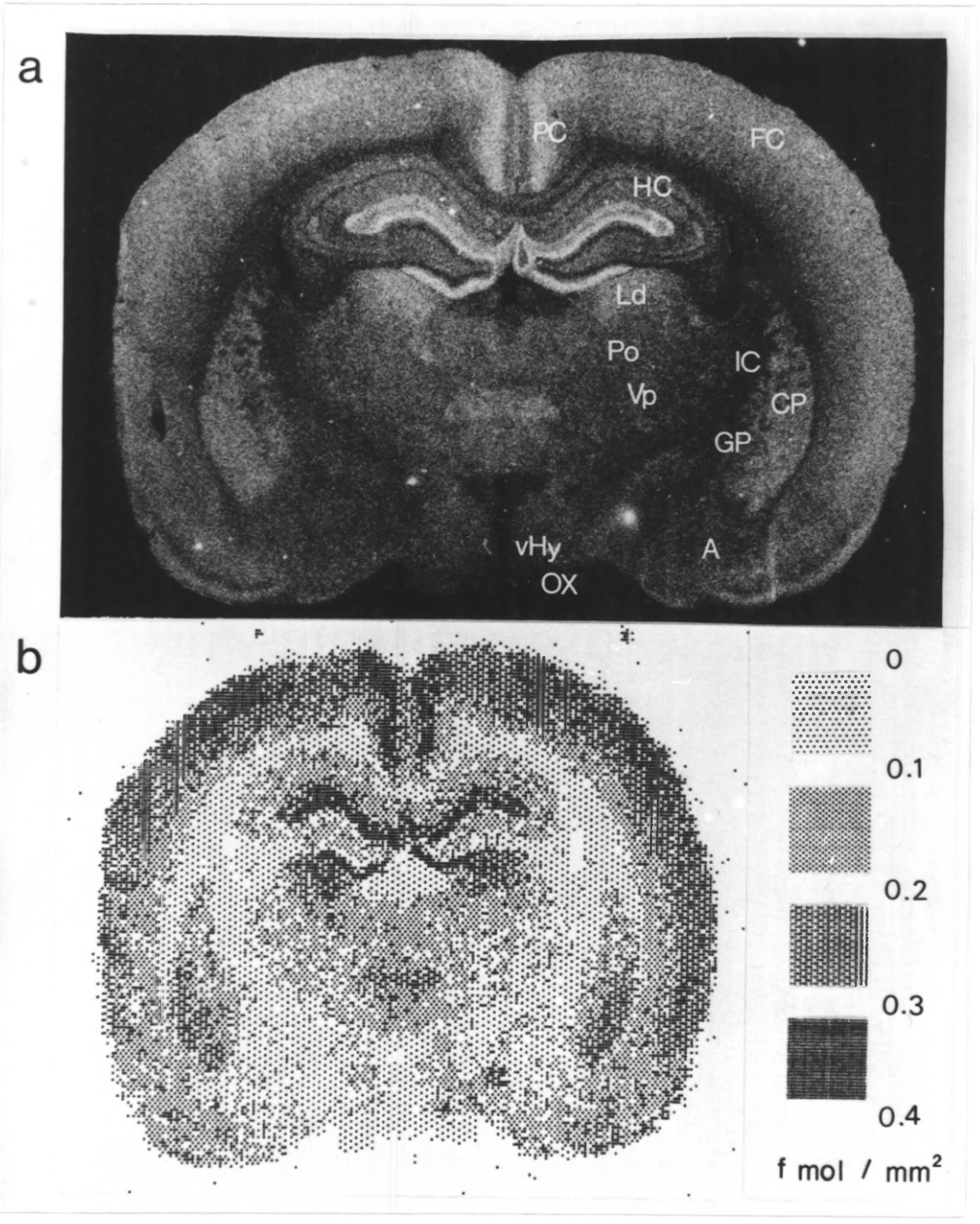
Figure 3.6. Distribution of ^{125}I-ß-BuTX acceptors in rat forebrain at the level of the striatum



(a) Darkfield image of an autoradiogram from a section of rat forebrain labelled with 2.5 nM ^{125}I-ß-BuTX. AC, anterior commissure; CC, corpus callosum; CP, caudate putamen; DB, diagonal band; EC, external capsule; FC, frontoparietal cortex; I, insular cortex; LS, lateral septal nucleus; LoT, lateral olfactory tract; NA, nucleus accumbens; ON, optic nerve; Tu, olfactory tubercle. An adjacent control section incubated in 2.5 nM ^{125}I-ß-BuTX in the presence of an excess of unlabelled ß-BuTX showed a negligible level of labelling.

(b) Scanned representation of the image in (a).

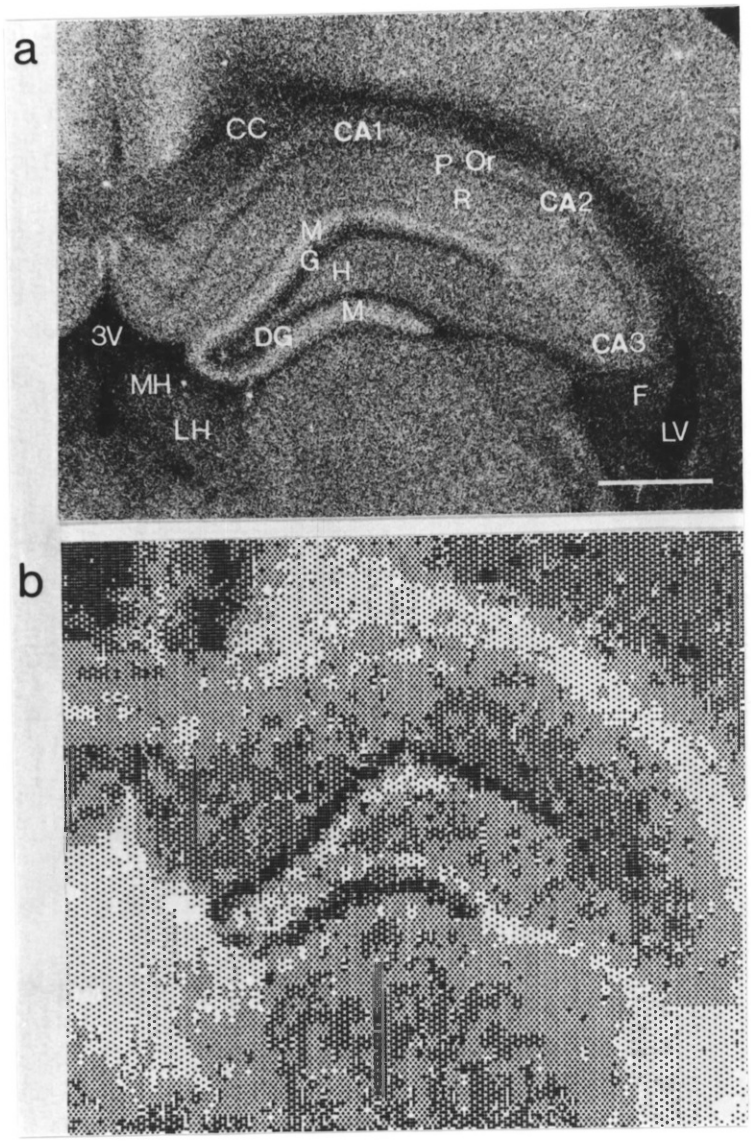
Figure 3.7. Distribution of ^{125}I-ß-BuTX acceptors in rat forebrain at the level of the hippocampus



(a) Darkfield image of an autoradiogram from a rat forebrain section through the hippocampus, labelled with 2.2 nM ^{125}I-ß-BuTX. A, amygdala; CP, caudate putamen; FC, fronto-parietal cortex; GP, globus pallidus; HC, hippocampal formation; IC, internal capsule; Ld, laterodorsal thalamic nucleus; OX, optic chiasma; PC, posterior cingulate cortex; Po, Posterior thalamic nuclear group; vHy, ventral hypothalamic area; Vp, ventroposterior thalamic nucleus;

(b) Scanned representation of the image in (a).

Figure 3.8. Location of ^{125}I-β-BuTX acceptors in the hippocampus



Cryostat sections were incubated in 2 nM ^{125}I-β-BuTX and exposed to ^{3}H-sensitive film. A detail of the hippocampal formation is shown in (a), while (b) is a high resolution scan of the same area, using the shadings as identified in Figure 3.7. Hippocampal formation: F, fimbria; G, granule cell layer; H, hilus; M, stratum moleculare; Or, stratum oriens; P, pyramidal cell layer; R, stratum radiatum. CA1, CA2, and CA3 define the subfields of the hippocampus, while DG identifies the dentate gyrus. Other abbreviations: 3V, third ventricle; CC, corpus callosum; LH, lateral habenular nucleus; LV, lateral ventricle; MH medial habenular nucleus.
Scale bars =1 mm.

stratum oriens and stratum radiatum contained moderately high levels of binding sites. Labelling increased medially in the stratum oriens, reaching high levels in the subiculum, and tended to decrease laterally, CA_1 and CA_2 usually showing higher grain densities than CA_3. On anterior sections, localized high ^{125}I-β-BuTX binding was observed in the stratum lacunosum moleculare and in the stratum lucidum (cf. Figure 3.7). Moderate grain densities were localized over the pyramidal cell layer. The molecular layer of the dentate gyrus exhibited very high numbers of binding sites, thus standing out prominently against the moderately labelled granule cell layer on autoradiograms. The hilus of the dentate gyrus contained moderately high numbers of toxin acceptors.

3.4.4.2. *The diencephalon*

This region presented very variable levels of β-BuTX acceptors. The septum showed moderately high ^{125}I-β-BuTX binding (see lateral septal nucleus, Figure 3.6), which decreased posteriorly as white myelinated tracts from the fornix increasingly penetrated the septum (Figure 3.2c). Only low levels of toxin binding sites were found over the habenular nuclei. The lateral habenular nucleus was labelled more prominently than the medial habenular nucleus (Figure 3.8).

Autoradiographic grain densities in the thalamus (Figures 3.2d,e,f and 3.7) ranged from moderately high in the laterodorsal and ventroposterior nuclei, to low in the reuniens nucleus. The posterior thalamic nuclear group exhibited intermediate levels of toxin binding.

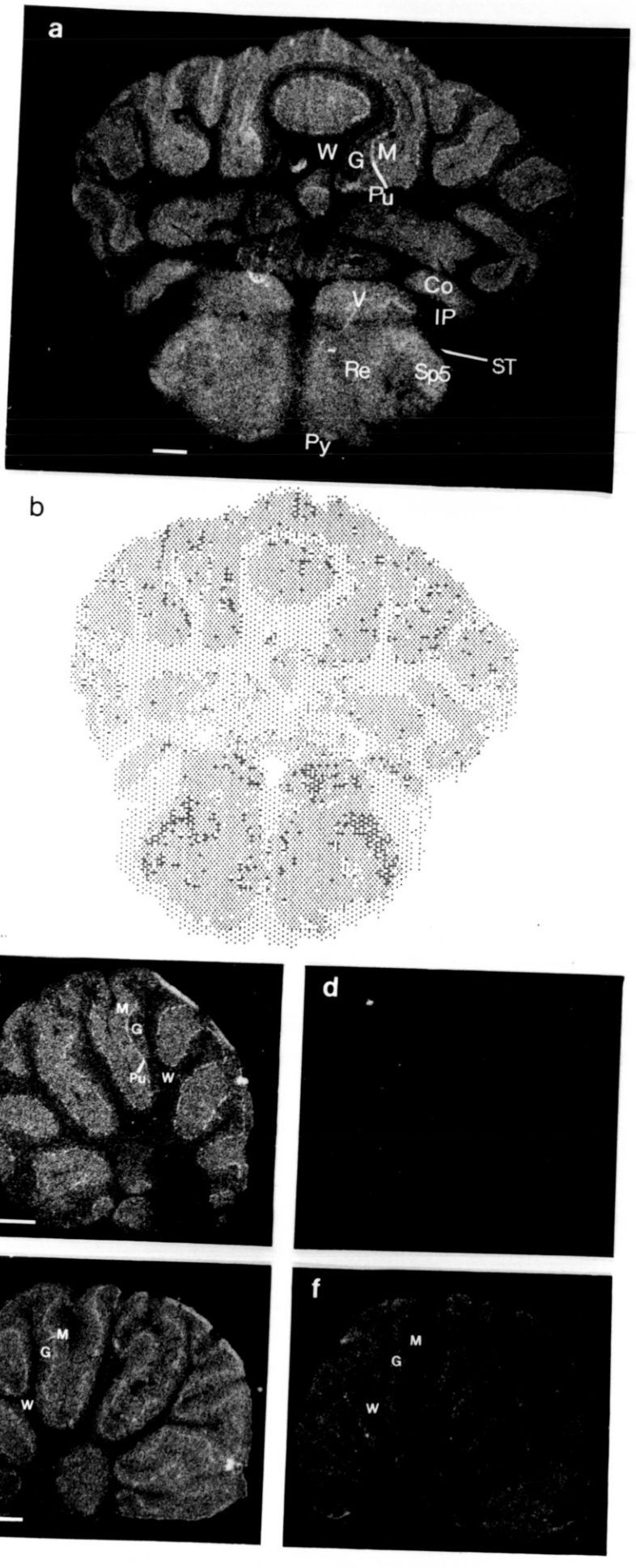
The hypothalamus (Figures 3.2e,f and 3.7) showed only low levels of β-BuTX acceptors: The ventromedial nucleus and the lateral hypothalamic area contained low grain densities, while the periventricular and arcuate nuclei appeared almost unlabelled.

3.4.4.3. *Cerebellum and brainstem*

Autoradiograms of ^{125}I-β-BuTX labelled cryostat sections from the cerebellum exhibited a distinctive distribution of silver grains (Figures 3.2g,h and 3.9). The highest levels of β-BuTX binding were found over the Purkinje cell layer. The molecular layer was labelled moderately and the granule cell layer weakly. Occasionally some ^{125}I-β-BuTX preparations exhibited high levels of non-specific binding over the granule cell layer (Figure 3.9f).

Figure 3.9. Distribution of ^{125}I-ß-BuTX acceptors in the cerebellum and brainstem

Representative darkfield images (silver grains appear white) of autoradiograms from a cryostat section of rat cerebellum and brainstem (a), or sagital cerebellum sections (c, d, e and f). The sections were labelled in 2.4 nM ^{125}I-ß-BuTX alone (a, c and e) or in the presence of 1 µM ß-BuTX (d and f). (b) is a scanned representation of the image shown in (a), using the same shadings as identified in Figure 3.7. Cerebellum: G, granule cell layer; M, molecular layer; Pu; Purkinje cell layer; W, white matter. Other abbreviations: Co, cochlear nucleus; Ip, inferior cerebellar peduncle; Py, pyramidal tracts; Re, reticular formation; Sp5, nucleus of the spinal trigeminal nerve; ST, Spinal Trigeminal nerve; V, vestibular nucleus. Scale bars 2 mm (a) or 1 mm (c and e).


a
W
G
M
Pu
V
Co
IP
ST
Re
Sp5
Py
b
c
M
G
Pu
W
d
e
M
G
W
f
M
G
W

Test section autoradiograms of such ^{125}I-β-BuTX preparations showed virtually equal labelling of the molecular and granule cell layers, separated by a strongly labelled band of Purkinje cells (Figure 3.9e). However, when the autoradiograms were analysed and non-specific binding was subtracted, the molecular layer was always found to contain more β-BuTX acceptors.

Moderately high grain densities were found over all grey nuclei of the brainstem (Figures 3.2g,h and 3.9a). Anteriorly the cochlear and vestibular nuclei were prominently labelled, while posteriorly the cuneate nucleus and the nucleus of the hypoglossal nerve presented high toxin acceptor numbers. The reticular formation, which occupies the bulk of the medulla, also contained high levels of β-BuTX acceptors.

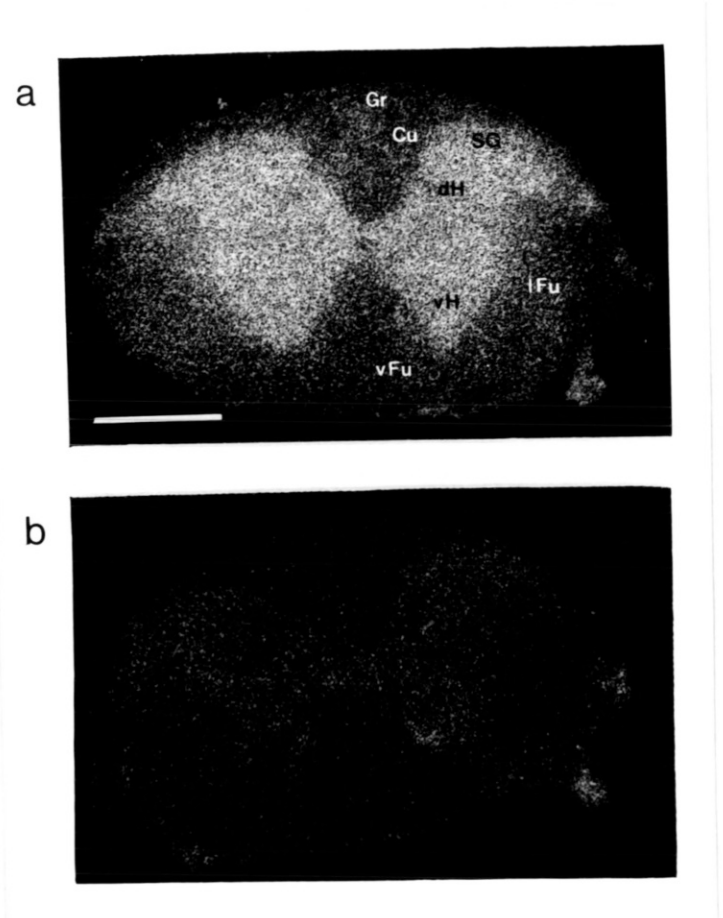
3.4.4.4. *White matter tracts*

Brain areas rich in myelinated tracts, and therefore known as white matter regions, generally contained only low levels of β-BuTX acceptors. Whereas most of the grey matter areas of rat brain (discussed above) bound more than 0.15 fmol/mm^2 of ^{125}I-β-BuTX, the white matter regions were labelled on average with only ≈0.07 fmol/mm^2. Among the myelinated tracts, the anterior commissure (Figure 3.6), the corpus callosum, external capsule, internal capsule (Figure 3.6 and 3.7) and the mammillothalamic tract contained the highest levels of β-BuTX acceptors. Very low grain densities were found over the lateral olfactory tract. The optic nerve was unlabelled, while the optic chiasma and the optic tract presented very low levels of toxin binding. Other myelin-rich brain areas showed intermediate levels of labelling. In the hindbrain, few β-BuTX acceptors were observed in the cerebellar white matter laminae or in the cerebellar peduncle (Figure 3.9).

3.4.4.5. *Spinal cord*

The distribution of ^{125}I-β-BuTX acceptors in the spinal cord is shown in Figure 3.10. In agreement with the results in rat brain, the central grey matter contained the highest levels of toxin binding sites, with the substantia gelatinosa binding slightly more ^{125}I-β-BuTX (0.30 fmol/mm^2) than the dorsal and ventral grey horns (≈0.28 fmol/mm^2) although this difference was not significant. The surrounding white matter was uniformly but weakly labelled (≈0.086 fmol/mm^2). These densities of β-BuTX

Figure 3.10. Distribution of ^{125}I-β-BuTX acceptors in the spinal cord



Darkfield autoradiograms of cervical spinal cord cryostat sections labelled in 2.5 nM β-BuTX alone (a) or in the presence of 1 μM unlabelled β-BuTX (b). Cu, fasciculus cuneatus; dH, dorsal horn; Gr, fasciculus gracilis; lFu, lateral funiculus; SG substantia gelatinosa; vFu, ventral funiculus; vH, ventral horn.
Scale bar =1 mm.

acceptors in grey and white matter are similar to those found in the brainstem (medulla oblongata).

3.4.5. Distribution of ß-BuTX Acceptors in Chick Brain

Cryostat sections from 1-day-old chick brain were labelled in 1 or 2.5 nM ^{125}I-ß-BuTX and processed for autoradiography (Figure 3.11). The level of ^{125}I-ß-BuTX binding in chick brain was generally very low, many structures remaining virtually unlabelled. Apparently the binding also saturated at lower concentrations of ^{125}I-ß-BuTX than in rat brain. Only certain grey matter areas were prominently labelled. The quantitative distribution of ^{125}I-ß-BuTX binding in chick brain is summarized in Table 3.4.

In the forebrain (telencephalon), the highest concentration of silver grains was found over the ectostriatum. The paleostriatum was moderately labelled, while low levels of ß-BuTX acceptors were found in the neostriatum (Figure 3.11a).

A characteristic distribution of silver grains was found over the optic lobes (Figure 3.11b). The superficial stratum opticum, comprising the incoming fibres from the optic tract, contained very few ß-BuTX acceptors. Moderate amounts of acceptors were found in the stratum griseum et fibrosum superficiale, the stratum griseum centrale and the stratum griseum periventriculare. The stratum album centrale contained a low level of binding sites. High grain densities were found over the nucleus intercollicularis. The formatio reticulatris lateralis of the brainstem contained moderate acceptor levels.

In the cerebellum the molecular layer was strongly labelled (Figure 3.11b and d), but no significant specific binding was found in any other layer. The high levels of non-specific binding over the granule cell layer, already mentioned for rat brain, was always much more pronounced in chick cerebellum (Figure 3.11c and e): While the average non-specific binding in most brain areas was ≈0.12 fmol/mm^2 (at 2.5 nM ^{125}I-ß-BuTX), ≈0.2 fmol/mm^2 were found over the granule cell layer, with a somewhat lower amount over the external granule cell layer.

3.5. Discussion

3.5.1. Quantitative Autoradiography Using Iodine-125

A biologically active ^{125}I-labelled derivative of ß-BuTX

Figure 3.11. Distribution of ß-BuTX acceptors in chick brain

Representative darkfield images (silver grains appear white) of autoradiograms from coronal cryostat sections of chick forebrain (a), cerebellum with midbrain and optic lobes (b and c), or sagital sections of cerebellum (d and e). All sections were labelled in 0.5 nM (d and e) or 1 nM (a,b and c) ^{125}I-ß-BuTX alone (a,b and d) or in the presence of 1 µM ß-BuTX (c and e). Forebrain: aH, accessory hyperstriatum; Es, ectostriatum; iH, intercalated hyperstriatum; LP, lobus parolfactorius; N, neostriatum; P, paleostriatum; vH, ventral hyperstriatum.
Optic lobe: O, stratum opticum; GF, stratum griseum et fibrosum superficiale; GC, stratum griseum centrale; AC, stratum album centrale; GP, stratum griseum periventriculare; In, nucleus intercollicularis; Re, formatio reticularis lateralis.
Cerebellum: EG, external granule cell layer; G, granule cell layer; M, molecular layer; W, white matter. All scale bars =1 mm.

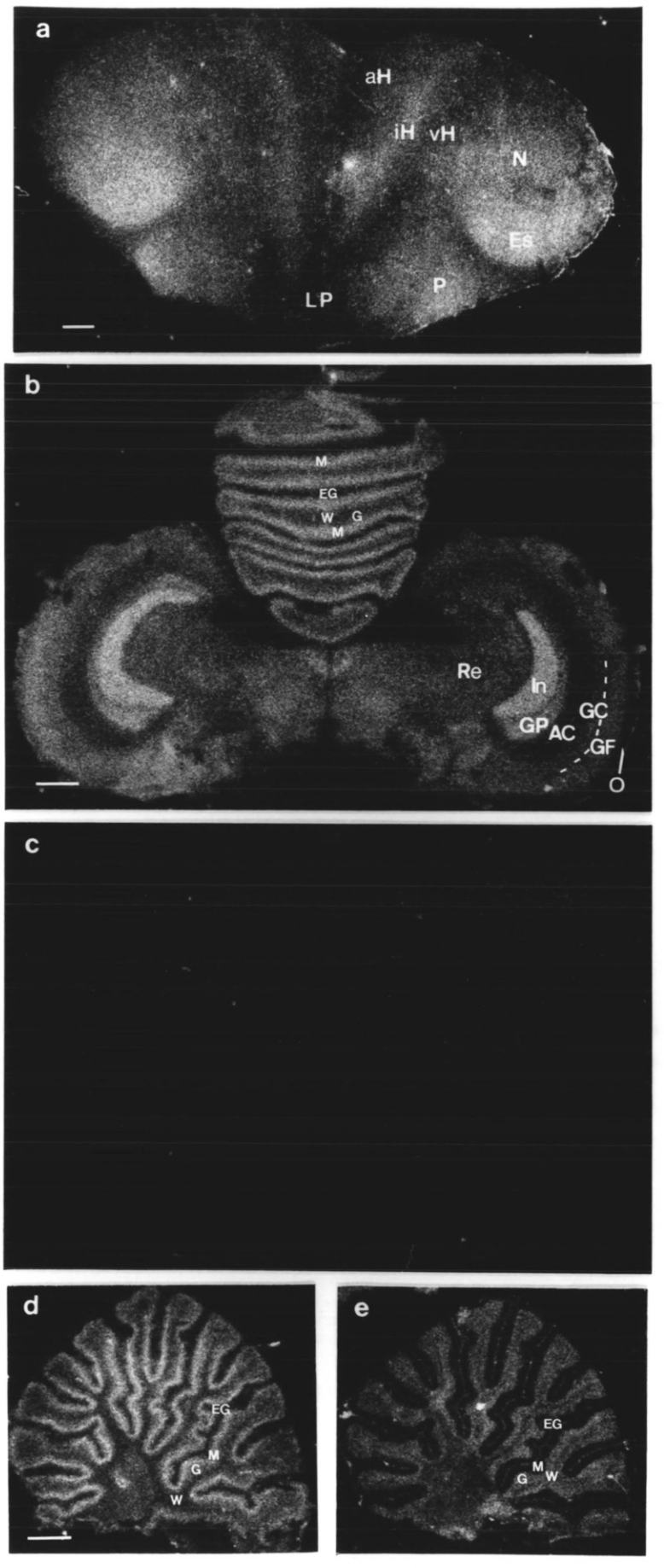

a
aH
iH
vH
N
Es
P
LP
b
M
EG
W
G
M
Re
In
GP
AC
GC
GF
O
c
d
EG
M
G
W
e
EG
M
G
W

Table 3.4. Distribution of ^{125}I-β-BuTX binding in chick brain

Brain area studied	Specific binding of 125I-β-BuTX (fmol/mm²) at 1 nM	2.5 nM	Relative level of β-BuTX acceptors
Forebrain			
Accessory hyperstriatum	0.005 †	0.017 †	
Intercalated hyperstriatum	0.039	0.047	*
Ventral hyperstriatum	0.009 †	0.016 †	
Neostriatum	0.056	0.058	*
Ectostriatum	0.175	0.201	* * * *
Paleostriatum	0.107	0.128	* * *
Lobus parolfactorius	0	0	
Optic Lobe			
Stratum opticum	0.038	0.028	*
Stratum griseum et fibrosum superficiale	0.112	0.126	* * *
Stratum griseum centrale	0.093	0.107	* *
Stratum album centrale	0.048	0.043	*
Stratum griseum periventriculare	0.169	0.136	* * *
Nucleus intercollicularis	0.206	0.269	* * * * *
Formatio reticularis lateralis	0.082	0.130	* * *
Cerebellum			
External granule cell layer	0.006 †	0.035 †	
Molecular layer	0.149	0.207	* * * *
Granule cell layer	0.012 †	0.011 †	
White matter laminae	0.018 †	0.012 †	

Cryostat sections were labelled with 1 or 2.5 nM ^{125}I-β-BuTX, and autoradiograms were prepared using ^{3}H-sensitive Ultrofilm. These autoradiograms were analysed by laser densitometry. Specific binding of ^{125}I-β-BuTX was calculated by subtraction of the non-specific binding. † indicates that the difference between the total binding and the non-specific binding was not significant. Relative levels of ^{125}I-β-BuTX binding at 2.5 nM are given as * for comparison with the data in Table 3.3.

has been used to map the distribution of β-BuTX acceptors in the rat and chick central nervous systems. The pattern of ^{125}I-β-BuTX binding was very similar to that observed by autoradiography using ^{3}H-β-BuTX (see Figure 3.4 and Othman *et al.*, 1983). Thus, the localization patterns observed reflect the distribution of functional acceptors for the toxin rather than artifactual patterns resulting from the radiolabelling method or the radionuclide employed.

The use of ^{125}I-labelled ligands offers considerable advantages in quantitative autoradiography. Firstly, due to the short half-life of iodine-125, radioiodinated ligands can be prepared with high specific activities. Secondly, the decay scheme for ^{125}I is complex, leading to the emission of several internal conversion and Auger electrons per nuclear decay (Atkins, 1969), and thus increasing the probability of detection. These effects allow much shorter exposure times to be used in autoradiography with ^{125}I compared with ^{3}H. In the experiments presented here, sections labelled with ^{125}I-β-BuTX were usually exposed for 1-4 days, while autoradiography with ^{3}H-β-BuTX yielded only faint images even after 25 days. Thirdly, and most importantly, the energy of the electrons emitted by ^{125}I is higher than that of ^{3}H electrons (Atkins, 1969). While this (minimally) reduces the autoradiographic resolution attainable, it has the effect of abolishing the variable tissue quenching problem observed with ^{3}H (Taylor *et al.*, 1984): In brain tissue white matter regions, being denser than grey matter, absorb more ^{3}H-electrons (Alexander *et al.*, 1981); this leads to significant underestimates of the amount of ^{3}H-ligand bound in white matter rich brain areas. A number of methods of correcting for this problem have been described (reviewed by Kuhar and Unnerstall, 1985), but as none of these is very reliable Clark and Hall (1986) have suggested that ^{125}I-labelled probes should be used in preference to tritiated ligands in autoradiography.

^{125}I-labelled standards can easily be prepared to calibrate the response of ^{3}H-sensitive Ultrofilm for quantitative autoradiography. Brain paste standards (Unnerstall *et al.*, 1982) into which an ^{125}I-labelled ligand has been incorporated (Israel *et al.*, 1984; Rostène and Mourre, 1985), have cutting properties and densities similar to cryostat sections, and were therefore used in this study. Because variations in section thickness affect the

optical density of the image in ^{125}I autoradiography, the thicknesses of standard and experimental cryostat sections must be identical. The response of Ultrofilm to ^{125}I was found to be very reproducible, even when different batches of film were compared. A natural logarithm plot of optical density versus radiation dose always yielded a straight-line relationship (see also Unnerstall *et al.*, 1982; Israel *et al.*, 1984) which was therefore used in all conversions.

Following quantitative analysis, densities of radioligand bound are frequently presented per mg of protein by comparison with the protein content of the brain paste standards. This conversion is not, however, valid because **a)** the protein content of the brain paste standards may differ from that of tissue cryostat sections and **b)** the tissue protein content is not uniform. Densities of ^{125}I-β-BuTX binding are therefore cited here per unit section area as recommended by Clark and Hall (1986). When a number of sections from different brain areas were compared, they were found to have an average protein content of 1.2 $\mu g/mm^2$ (section thickness 10 μm).

3.5.2. Analysis of Autoradiograms by Laser Densitometry

A computer-linked laser densitometer designed to scan polyacrylamide gels and autoradiograms thereof in one or two dimensions has been used to measure optical densities of Ultrofilm images of toxin-labelled cryostat sections. The scanner was used in the high resolution mode in two dimensions. Measurements of optical densities were very reproducible: When images of standard sections were scanned repeatedly over several months, identical readings were always obtained. Although the resolution achievable varied with the size of the image scanned (Section 3.3.5), the highest possible resolution (10μm) was comparable to that of the Ultrofilm autoradiographic method when silver grain size and scatter of the signal electrons are taken into consideration. Laser densitometry also avoids the problems of glare and uneven back-illumination associated with manual densitometry methods, where the autoradiographic image is projected onto a photodiode using an enlarger (see e.g. Pan *et al.*, 1981; Penney *et al.*, 1984a,b; Greenamyre *et al.*, 1984), or some computerized systems which use projection of the image onto a video camera linked to a digitizer (e.g. Altar *et al.*, 1984; Baskin *et al.*, 1986 and references therein). Although some of the video camera-linked

computerized analysis systems have much more sophisticated image processing capabilities, the laser scanner system was satisfactory for the studies described here.

3.5.3. Distribution of β-BuTX Acceptors in Rat Brain

Autoradiography has revealed a widespread distribution of β-BuTX acceptors in both the rat and chick central nervous systems. This agrees with the potent toxicity of β-BuTX in the brain (Hanley and Emson, 1979; Othman *et al.*, 1982). Focal intra-cerebral injections of β-BuTX caused local lesions with neuronal cell death and glial proliferation. The cerebral cortex, striatum and hippocampus appeared to be particularly sensitive to the toxin in these studies (Hanley and Emson, 1979; Gulya *et al.*, 1984). β-BuTX also had potent electrophysiological effects on slices from olfactory cortex and hippocampus (Halliwell *et al.*, 1982; Halliwell and Dolly, 1982; see also Chapter 1, Section 1.3.4). In accordance with these observations, specific high affinity β-BuTX acceptors have now been directly localized in all of these toxin-sensitive brain areas. β-BuTX binding sites have also been found in the cerebellum and spinal cord.

Quantitative autoradiography has permitted studies of the binding parameters (K_d and B_{max}) of the β-BuTX acceptors in localized brain regions. The absence of significant variation in the binding affinity of the toxin (Section 3.4.3, Table 3.1) indicates that the β-BuTX acceptors have similar properies in all of the brain areas examined. Likewise β-BuTX binding in all regions was dependent on divalent cations, and the distribution of the acceptors was the same when sections were labelled in the presence of Sr^{2+} instead of Ca^{2+}. It appears, therefore, that there is a single, uniform population of high affinity β-BuTX acceptors in all parts of the rat brain. There was no evidence for ^{125}I-β-BuTX binding to a low affinity site similar to that observed on synaptosomes when imidazole buffer is used in the incubation (Dolly *et al.*, 1987). The physiologically irrelevant low affinity binding site detected in some very early binding experiments in chick membrane preparations (Rehm and Betz, 1982) may, however, be responsible for some of the comparatively high non-specific binding observed over cell layers in some experiments (cf. Sections 3.4.4, 3.4.4.3 and 3.4.5). It is interesting in this context that this low affinity ^{125}I-β-BuTX binding to chick brain membranes

disappeared when the membranes were treated with deoxyribonuclease (Rehm and Betz, 1982)

In keeping with the lack of neurotransmitter specificity of β-BuTX in the central nervous system (see Chapter 1, Section 1.4.5), the distribution of the acceptors described here does not resemble that of any neurotransmitter receptor, or of any neurotransmitter uptake sites mapped so far (for further references on these distributions, see Kuhar *et al.*, 1986). In particular, there was no correspondence to cholinergic systems (reviewed by Wainer *et al.*, 1984; see also Clarke *et al.*, 1985). Only glutamate receptors (Greenamyre *et al.*, 1984; Halpain *et al.*, 1984) and aspartic/glutamic acid uptake sites (Parsons and Rainbow, 1983) have a widespread distribution that is superficially similar to that of β-BuTX binding (e.g. [^{3}H]glutamate shows extensive binding in the forebrain, with a distinct rostral to caudal gradient, patchy labelling in the striatum and prominent binding to hippocampal and cerebellar synaptic layers, while white matter areas contain only low levels of binding sites), but the distributions of glutamate receptors and β-BuTX binding sites differ in certain brain regions (e.g. β-BuTX binds strongly in the midbrain, brainstem and spinal cord, while glutamate labels prominently only the substantia gelatinosa; Greenamyre *et al.*, 1984). In this regard it is noteworthy that glutamate is almost universally excitatory, suggesting that glutamate receptors exist on most central neurones (Watkins and Evans, 1981). Furthermore glutamate synapses have been suggested to be one of the targets for the presynaptic action of β-BuTX in olfactory cortex or hippocampus slices (Halliwell *et al.*, 1982; Halliwell and Dolly, 1982).

3.5.4. Predominantly Synaptic Location of β-BuTX Acceptors

The distribution of β-BuTX acceptors broadly corresponds to the density of synapses in rat brain as deduced from the immunohistochemical localization of the synaptic marker synapsin I (De Camilli *et al.*, 1983). Synapse-rich areas such as the cerebral cortex, the stratum oriens and radiatum of the hippocampus and, particularly, the stratum moleculare of the dentate gyrus, as well as the molecular layer of the cerebellum, are prominently labelled by β-BuTX. This agrees with the apparent enrichment of β-BuTX acceptors in synaptosomes as compared to cryostat sections noted in Section 2.5.3, and also concurs with the electrophysiological

studies (Halliwell *et al.*, 1982; Halliwell and Dolly, 1982) which revealed a primary effect of β-BuTX in reducing neurotransmitter release presynaptically, with the postsynaptic response being unaffected at the time when the presynaptic blockade was complete (Section 1.3.4). However, due to the limited resolution of the autoradiography method used here, an exclusively synaptic location of the acceptors cannot be deduced. Furthermore, while the acceptors were noticably enriched in synaptic areas, low but significant levels were observed in white matter regions, although the optic nerve was unlabelled.

The ^{125}I-β-BuTX binding demonstrated here was blocked with high efficacy by DTX (see also Section 2.4.2), the facilitatory neurotoxin which has been shown to block certain rapidly activating voltage-sensitive K^+ currents (Section 1.4.3). Furthermore, following the demonstration of the interaction of β-BuTX and DTX in a number of systems (Section 1.5), β-BuTX has also recently been shown to block some K^+ currents (Petersen *et al.*, 1986; Anderson *et al.*, 1987). In view of the predominance of β-BuTX acceptors in synapse-rich areas, it appears that the toxin may act on a synaptic K^+ channel which may be critically involved in the control of neurotransmitter release. It will, therefore, be of interest to compare the distribution of the high affinity β-BuTX binding sites with that of DTX acceptors, particularly since the higher site content of DTX acceptors, both on synaptosomes (Section 1.5) and cryostat sections (Chapter 2) suggests that β-BuTX labels one subgroup of the DTX sensitive K^+ channels. DTX acceptors have been localized directly, as will be described in Chapter 4. A number of other ion channels have also been mapped in the rat central nervous system using autoradiography methods similar to the one employed here (e.g. Na^+ channels have been studied using [^{3}H]tetrodotoxin or [^{3}H]batrachotoxin, Ca^{2+}-dependent K^+ channels using ^{125}I-apamin, while Ca^{2+} channels have been identified with a number of ligands), and their distribution will be compared to those of the β-BuTX and DTX acceptors in the Discussion to Chapter 4 (Section 4.4.5).

3.5.5. β-BuTX Acceptors in Chick Brain

Quantitative autoradiography revealed much lower β-BuTX acceptor densities in chick brain cryostat sections than in similar sections from rat brain. This may be due to the immaturity of the 1-day-old chick tissue studied, which may not yet have expressed

the acceptors to their final levels. Brain areas which are more mature in the young chick brain, like the optic lobes and the cerebellum, contained higher densities of acceptors. The low acceptor densities agree with the lower B_{max} value reported by Rehm and Betz (1982) for ^{125}I-β-BuTX binding to synaptic membranes from young chicks, compared to the levels of acceptors in adult rat brain synaptosomes observed by Dolly *et al.* (1987). The distribution of β-BuTX acceptors in young chick cerebellum resembled that found in adult rat cerebellum.

CHAPTER 4

Distribution of Dendrotoxin Acceptors in the Central Nervous System

4.1. Introduction

Specific acceptors binding ^{125}I-DTX with high affinity have been identified on cryostat sections from both rat and chick brain (Chapter 2). Like the DTX acceptors on synaptosomes (Sections 1.4.4 and 1.5), the acceptors on cryostat sections show a complex interaction with β-BuTX (see Section 2.5.4). This suggests some heterogeneity among the DTX acceptor population with respect to their affinity for β-BuTX. In the present Chapter, DTX acceptors on cryostat sections have been studied by quantitative sheet film autoradiography methods, in order to compare their distribution with that of the β-BuTX acceptors, which have already been successfully localized in Chapter 3. To examine whether different DTX acceptor variants are distinctly localized, the interaction of β-BuTX with ^{125}I-DTX binding has also been studied by autoradiography.

4.2. Materials and Methods

All materials used, and the procedures for the preparation, labelling and autoradiography of cryostat sections, and for the quantitative analysis of the resulting Ultrofilm images were as detailed in Chapters 2 and 3.

4.3. Results

4.3.1. Distribution of DTX Acceptors in the Rat Central Nervous System

Like ^{125}I-β-BuTX binding, the binding of ^{125}I-DTX to cryostat sections of rat brain saturated at low toxin concentrations (see Section 2.4.1.2 and Figure 2.3a). To allow comparison with the distribution of ^{125}I-β-BuTX acceptors described in Chapter 3, cryostat sections from various brain areas were labelled in 2-2.5 nM ^{125}I-DTX and exposed to ^{3}H-sensitive Ultrofilm. A set of representative darkfield autoradiographic images is shown in Figure 4.1. Autoradiograms were also analysed quantitatively by laser densitometry. The ^{125}I-DTX labelling thus observed was saturable, as it could be blocked efficiently by unlabelled DTX. The level of non-specific binding, determined in the presence of 1 μM DTX, was 0.015-0.03 fmol/mm², representing ≤10% of the total ^{125}I-DTX binding in most brain areas. Levels of specific binding, calculated by subtracting the non-specific from the total binding, are summarized in Table 4.1.

In keeping with the overall higher B_{max} of DTX compared to β-BuTX on cryostat sections (Chapter 2, Table 2.5), ^{125}I-DTX bound to more acceptors than ^{125}I-β-BuTX in all brain areas examined (Table 4.1). Furthermore inspection of Figure 4.1, in comparison to Figure 3.2, reveals a more widespread distribution of the DTX acceptors: In addition to synapse-rich grey matter areas, ^{125}I-DTX also labelled white matter regions and myelin-rich fibre tracts. A detailed description of the distribution of ^{125}I-DTX binding is given below. Levels of specific ^{125}I-DTX binding were again classified into groups as defined in the legend to Table 4.1. It should be noted that, since the absolute levels of specific ^{125}I-DTX binding were higher, these density bands are wider than those used to describe ^{125}I-β-BuTX binding in Chapter 3.

4.3.1.1. *The telencephalon*

In the rhinal system, the anterior olfactory nucleus (Figure 4.1a) contained moderate and the olfactory tubercle (Figure 4.2a) low levels of DTX acceptors. The frontoparietal cerebral cortex exhibited a high level of specific ^{125}I-DTX binding, with the acceptor content increasing posteriorly. On some sections the number of DTX acceptors in lamina IV of the cortex appeared to be slightly reduced (see e.g. Figures 4.1b,e,f and 4.2). Very high

(continued on p. 120)

Figure 4.1. Distribution of DTX acceptors in rat brain

Representative darkfield images of autoradiograms from cryostat sections of rat forebrain at the level of the anterior olfactory nucleus (a), anterior (b) and posterior (c) caudate putamen, anterior (d), mid (e and i) and posterior (f) hippocampus, and of cerebellum with brainstem (g and h). All sections were labelled in 2-2.5 nM ^{125}I-DTX alone (a-h) or in the presence of 1 μM DTX (i). As the images represent the results of different experiments and were printed separately, grain densities cannot be compared between photographs.

A, amygdala; AC, anterior commissure; AO, anterior olfactory nucleus; CBL, cerebellum; CC, corpus callosum; CP, caudate putamen; Cu, cuneate nucleus; DB, diagonal band; f, fornix; FC, fronto-parietal cortex; gCC, genu of corpus callosum; GP, globus pallidus; HC, hippocampal formation; Hy, hypothalamus; I, insular cortex; Ip, inferior cerebellar peduncle; Ld, laterodorsal thalamic nucleus; LG lateral geniculate body; LS, lateral septal nucleus; LoT, lateral olfactory tract; NA, nucleus accumbens; ON, optic nerve; OT, optic tract; OX, optic chiasma; PC, posterior cingulate cortex; Po, posterior thalamic nuclear group; Py, pyramidal tracts; Re, reticular formation; Sm, stria medullaris thalami; Sp5, nucleus of the spinal trigeminal nerve; ST, spinal trigeminal nerve; Su, subiculum; Th, thalamus; Tu, olfactory tubercle; V, vestibular nucleus; W, cerebellar white matter bundles; ZI, zona incerta.

Scale bar (in a) =2 mm.

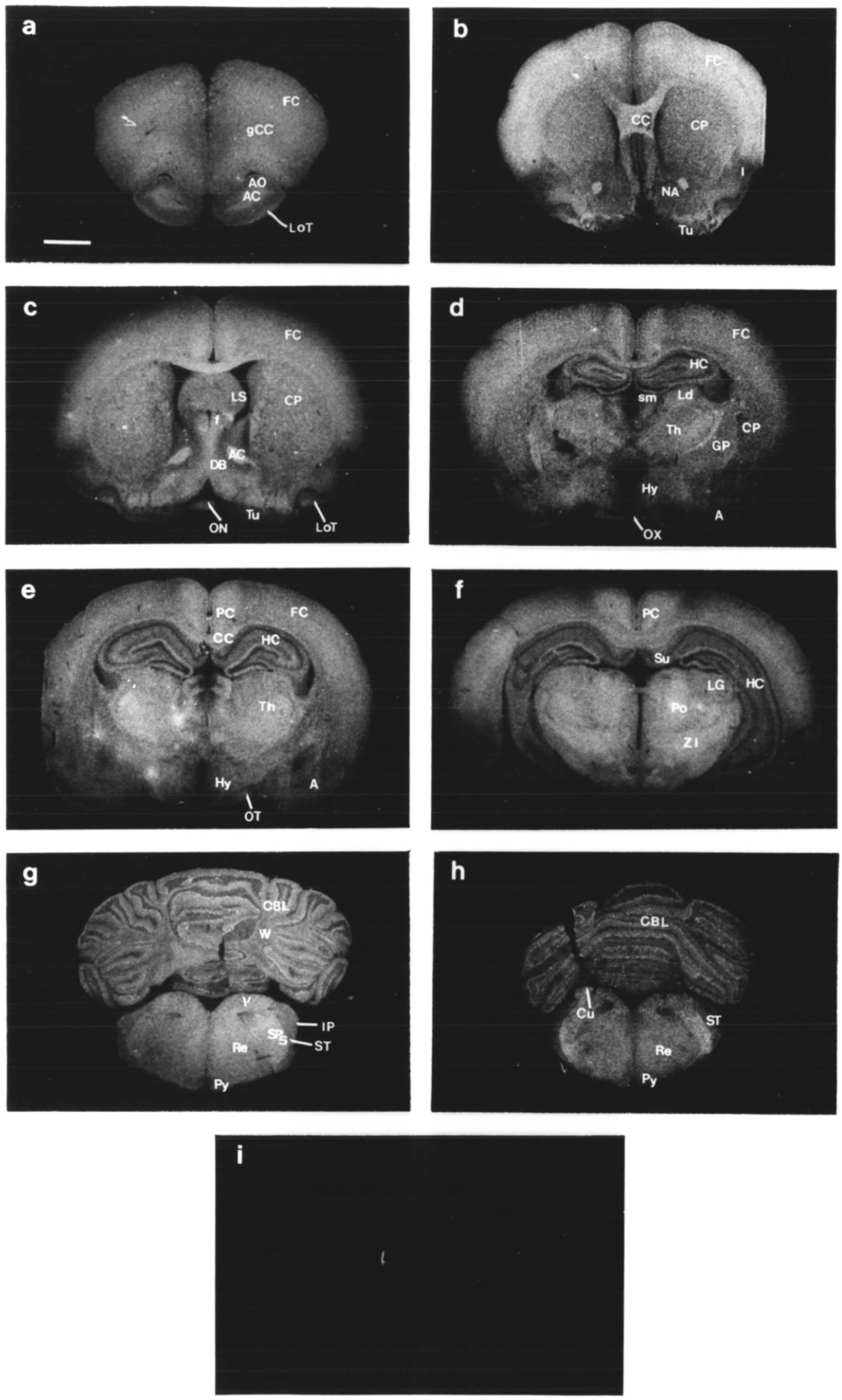

a
FC
gCC
AO
AC
LoT
b
FC
CC
CP
I
NA
Tu
c
FC
LS
CP
I
AC
DB
Tu
ON
LoT
d
FC
HC
sm
Ld
Th
CP
GP
Hy
A
OX
e
PC
FC
CC
HC
Th
Hy
A
OT
f
PC
Su
LG
HC
Po
ZI
g
CBL
W
V
IP
SP5
ST
Re
Py
h
CBL
Cu
ST
Re
Py
i

Table 4.1. Distribution of ^{125}I-DTX acceptors in the rat central nervous system

Region	n[a]	^{125}I-DTX bound specifically (fmol/mm^2)	Relative content of DTX acceptors [b]	DTX/β-BuTX binding ratio [c]
GREY MATTER				
Olfactory system				
Anterior olfactory nucleus	2	0.317 ± 0.062	* * *	1.9
Olfactory tubercle	4	0.226 ± 0.031	* *	2.4
Cerebral cortex				
Frontoparietal (anterior to Bregma)	3	0.647 ± 0.072	* * * * *	2.0
Frontoparietal (posterior to Bregma)	3	0.765 ± 0.065	* * * * * *	3.1
Insular cortex	3	0.247 ± 0.044	* *	1.8
Posterior cingulate cortex	3	0.913 ± 0.148	* * * * * * *	2.8
Forebrain				
Caudate putamen	4	0.461 ± 0.031	* * * *	1.8
Globus pallidus	3	0.573 ± 0.040	* * * *	3.7
Nucleus accumbens	4	0.288 ± 0.028	* *	1.5
Lateral septal nucleus	3	0.365 ± 0.032	* * *	1.6
Amygdala				
Basal nuclei	3	0.342 ± 0.026	* * *	2.6
Cortical nucleus	3	0.386 ± 0.036	* * *	3.1
Lateral nucleus	1	0.432	* * *	2.1
Hippocampal formation				
CA_1-CA_2: Stratum oriens	3	0.630 ± 0.055	* * * * *	3.1
Pyramidal cell layer	3	0.432 ± 0.043	* * *	3.2
Stratum radiatum	3	0.624 ± 0.041	* * * * *	2.9
Subiculum	2	0.437 ± 0.117	* * *	1.8
CA_3: Stratum oriens	3	0.665 ± 0.036	* * * * *	4.1
Pyramidal cell layer	3	0.473 ± 0.042	* * * *	4.5
Stratum radiatum	3	0.692 ± 0.049	* * * * *	3.7

contd.

Table 4.1. (contd.)

Region	n[a]	^{125}I-DTX bound specifically (fmol/mm^2)	Relative content of DTX acceptors [b]	DTX/β-BuTX binding ratio [c]
Dentate gyrus: Stratum moleculare	3	0.683 ± 0.045	* * * * *	2.2
Granule cell layer	3	0.354 ± 0.034	* * *	2.7
Hilus	3	0.515 ± 0.017	* * * *	2.7
Lateral habenular nucleus	4	0.656 ± 0.073	* * * * *	6.3
Medial habenular nucleus	4	0.389 ± 0.077	* * *	4.9
Thalamus				
Laterodorsal nucleus	3	0.669 ± 0.047	* * * * *	2.9
Ventroposterior nucleus	3	0.938 ± 0.088	* * * * * * *	5.1
Reuniens nucleus	2	0.463 ± 0.013	* * * *	5.1
Posterior nuclear group	4	0.710 ± 0.084	* * * * *	4.7
Hypothalamus				
Ventromedial nucleus	2	0.336 ± 0.044	* * *	4.1
Arcuate nucleus	3	0.208 ± 0.039	* *	17.3
Lateral hypothalamic area	3	0.629 ± 0.103	* * * * *	8.2
Premammillary nucleus	3	0.314 ± 0.026	* * *	
Zona incerta	4	0.777 ± 0.099	* * * * * *	
Entopeduncular nucleus	1	0.954	* * * * * * *	
Pituitary				
Adenohypophysis	1	0.004		
Neurohypophysis	1	0.046	*	
Midbrain				
Substantia nigra	1	0.587	* * * *	
Superior collic. superficial grey layer	1	0.322	* * *	
Superior colliculus optic nerve layer	1	0.670	* * * * *	
Inferior colliculus	1	0.661	* * * * *	
Lateral geniculate nucleus	2	0.654 ± 0.042	* * * * *	5.6
Medial geniculate nucleus	1	0.872	* * * * * *	
Central grey	1	0.610	* * * * *	
Interpeduncular nucleus	1	0.462	* * * *	
Pineal body	1	0.054	*	

contd.

Table 4.1. (contd.)

Region	n[a]	^{125}I-DTX bound specifically (fmol/mm^2)	Relative content of DTX acceptors [b]	DTX/β-BuTX binding ratio [c]
Cerebellum				
Molecular layer	4	0.628 ± 0.045	* * * * *	3.9
Purkinje cell layer	3	0.824 ± 0.077	* * * * * *	4.5
Granule cell layer	4	0.409 ± 0.040	* * *	3.8
Brainstem				
Cochlear nucleus	2	0.533 ± 0.098	* * * *	2.7
Reticular formation	2	0.779 ± 0.160	* * * * * *	4.2
Vestibular nucleus	2	0.615 ± 0.106	* * * * *	3.0
Nucleus cuneatus	2	0.801 ± 0.222	* * * * * *	3.7
Nucleus gracilis	1	0.773	* * * * * *	
Nucleus of spinal trigeminal nerve	2	0.957 ± 0.164	* * * * * * *	4.3
Nucleus of hypoglossal nerve	1	0.886	* * * * * *	4.0
WHITE MATTER				
Lateral olfactory tract	3	0.422 ± 0.089	* * *	24.8
Anterior commissure	4	0.541 ± 0.029	* * * *	5.3
Corpus callosum	5	0.682 ± 0.073	* * * * *	6.1
External capsule	3	0.550 ± 0.064	* * * *	4.9
Internal capsule	3	0.523 ± 0.085	* * * *	5.0
Diagonal band	3	0.469 ± 0.049	* * * *	5.3
Fornix	3	0.455 ± 0.056	* * * *	6.1
Optic nerve	1	0.305	* * *	No β-BuTX [d]
Optic chiasma	2	0.391 ± 0.068	* * *	9.8
Optic tract	3	0.388 ± 0.069	* * *	7.9
Fimbria hippocampi	3	0.444 ± 0.017	* * *	7.4
Stria medullaris thalami	3	0.512 ± 0.050	* * * *	5.3
Mammillothalamic tract	4	0.686 ± 0.138	* * * * *	6.2
Posterior commissure	2	0.297 ± 0.147	* *	
Lateral lemniscus	1	0.513	* * * *	
Cerebral peduncle	1	0.409	* * *	
Cerebellar white matter	4	0.624 ± 0.038	* * * * *	11.3

contd.

Table 4.1. (contd.)

Region	n[a]	^{125}I-DTX bound specifically (fmol/mm^2)	Relative content of DTX acceptors [b]	DTX/β-BuTX binding ratio [c]
Inferior cerebellar peduncle	2	0.480 ± 0.195	* * * *	17.1
Spinal trigeminal nerve	2	0.491 ± 0.157	* * * *	7.4
Pyramids	2	0.539 ± 0.121	* * * *	7.9
SPINAL CORD				
Grey matter				
Substantia gelatinosa	2	0.827 ± 0.079	* * * * * *	
Dorsal horn	2	0.747 ± 0.053	* * * * *	2.9
Ventral horn	2	0.796 ± 0.075	* * * * * *	
White matter				
Fasciculus gracilis	2	0.469 ± 0.082	* * * *	
Fasciculus cuneatus	2	0.302 ± 0.015	* * *	4.6
Dorsal and lateral funiculi	2	0.409 ± 0.024	* * *	

Cryostat sections were labelled with 2-2.5 nM ^{125}I-DTX, and autoradiograms were prepared using ^{3}H-sensitive Ultrofilm. These autoradiograms were analysed by laser densitometry as described in Chapter 3.

a: n is the number of experiments using different ^{125}I-DTX preparations. Specific binding of ^{125}I-DTX was determined by subtraction of the non-specific binding and is given as mean ± S.E.M.

b: Relative levels of ^{125}I-DTX binding in fmol/mm^2 are given as:

Very low	= *	= 0 - 0.149;
low	= * *	= 0.150 - 0.299;
moderate	= * * *	= 0.300 - 0.449;
moderately high	= * * * *	= 0.450 - 0.599;
high	= * * * * *	= 0.600 - 0.749;
very high	= * * * * * *	= 0.750 - 0.899.
very, very high	= * * * * * * *	> 0.900.

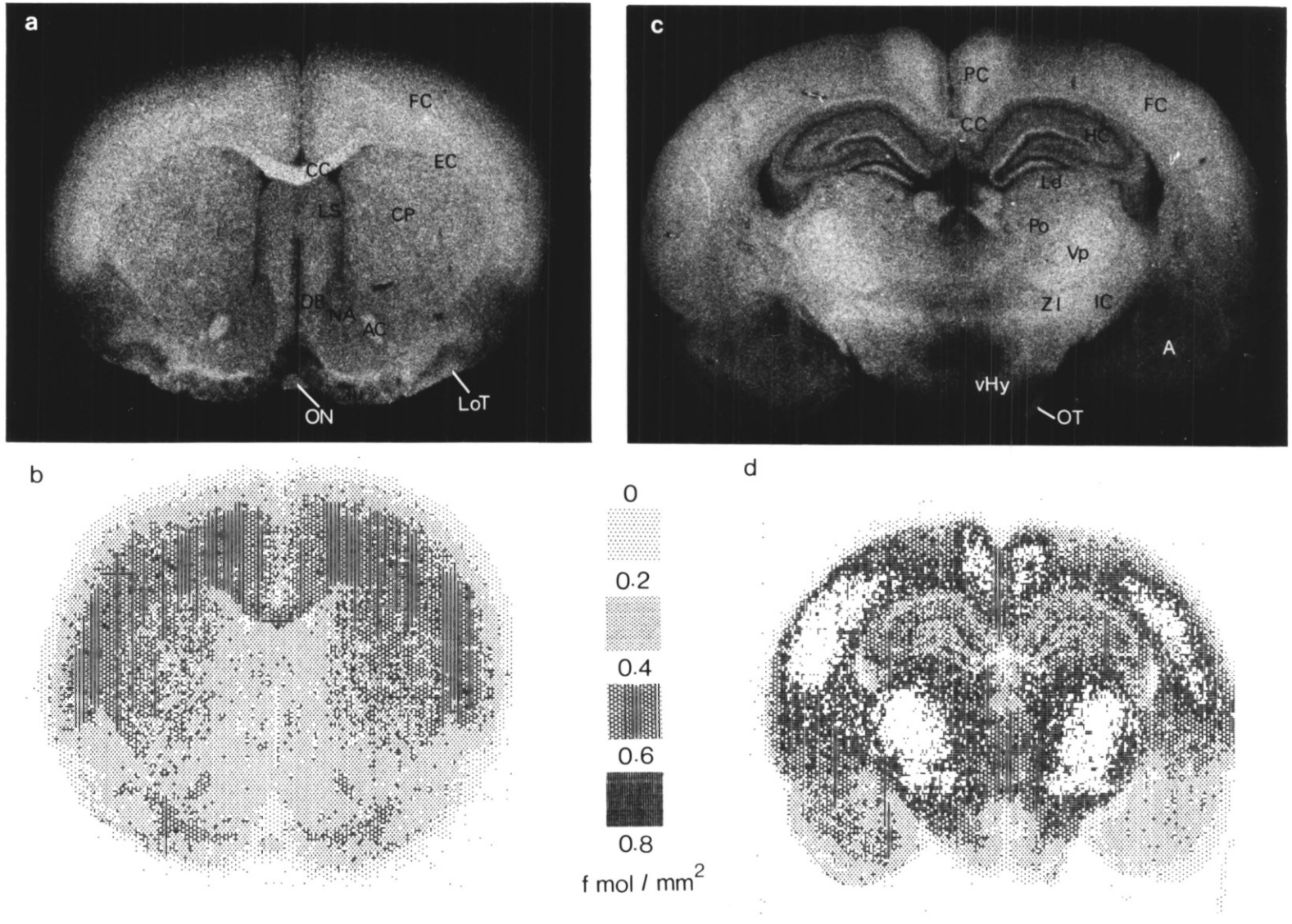
The average protein content of cryostat sections was 1.2 μg/mm^2.

c: The ratio of specific binding of ^{125}I-DTX : specific binding of ^{125}I-β-BuTX was calculated from the data here and in Table 3.2.

d: There was no specific ^{125}I-β-BuTX binding in optic nerve.

Figure 4.2. Distribution of ^{125}I-DTX acceptors in rat forebrain

Darkfield images of autoradiograms from sections of rat forebrain at the level of the caudate putamen (a) or hippocampus (c) are shown together with scanned representations thereof (b and d, respectively). The sections were labelled with 2.5 nM ^{125}I-DTX. Adjacent control sections incubated in 2.5 nM ^{125}I-DTX in the presence of an excess of unlabelled DTX remained virtually unlabelled. Note that, in order to include more detail, a fifth density band (showing areas binding 0.8-1.0 fmol/mm^2 of ^{125}I-DTX), which is unshaded, has been included in the scan shown in (d).
A, amygdala; AC, anterior commissure; CC, corpus callosum; CP, caudate putamen; DB, diagonal band; EC, external capsule; FC, frontoparietal cerebral cortex; HC, hippocampal formation; I, insular cortex; IC, internal capsule; Ld, laterodorsal thalamic nucleus; LS, lateral septal nucleus; LoT, lateral olfactory tract; NA, nucleus accumbens; ON, optic nerve; OT, optic tract; PC, posterior cingulate cortex; Po, Posterior thalamic nuclear group; Tu, olfactory tubercle; vHy, ventral hypothalamic area; Vp, ventroposterior thalamic nucleus; Zi, zona incerta.


a
FC
EC
CC
LS
CP
DB
NA
AC
ON
LoT
c
PC
FC
CC
HC
Ld
Po
Vp
ZI
IC
A
vHy
OT
b
0
0·2
0·4
0·6
0·8
f mol / mm2
d

levels of toxin binding were observed in the posterior cingulate cortex. In contrast the insular (rhinal) cortex showed only moderate labelling.

A moderately high concentration of DTX binding sites was also found throughout the neostriatum (caudate putamen and globus pallidus, see Figures 4.1b,c,d and 4.2). A mottled pattern of labelling was observed over the caudate putamen, with the density of grains increasing in the dorsal and lateral aspects. The globus pallidus appeared more uniformly labelled (Figure 4.1d). The nucleus accumbens presented a low level of specific DTX binding.

In the amygdala (Figures 4.1d,e,f and 4.2c), the basal, cortical and lateral nuclei all contained a moderate number of toxin acceptors. A characteristic laminated pattern of autoradiographic labelling was observed in the hippocampal formation (Figure 4.3). The synapse-rich strata oriens and radiatum exhibited high levels of DTX binding sites, while the pyramidal cell layer was moderately labelled. The level of acceptors increased laterally, with the strata oriens and radiatum and the pyramidal cell layer in CA_3 binding more ^{125}I-DTX than the same layers in CA_1 and CA_2. A moderate grain density was found over the subiculum. The molecular layer of the dentate gyrus presented a high level of DTX binding sites, comparable in intensity to the labelling in the stratum radiatum in CA_3, while the granule cell layer contained only a moderate number of acceptors. The hilus of the dentate gyrus showed a moderately high number of toxin acceptors.

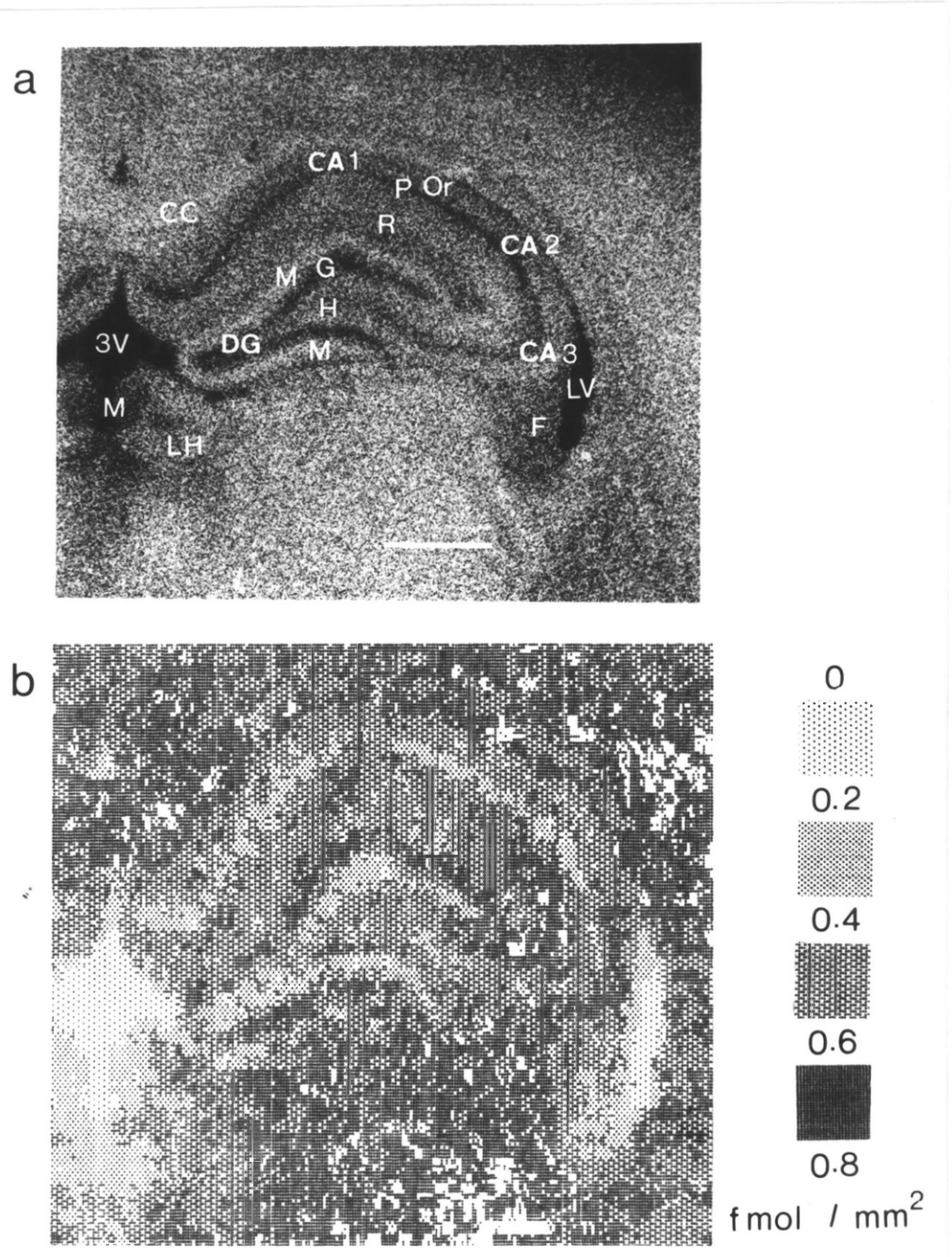
4.3.1.2. *The diencephalon*

The lateral septal nucleus presented a moderate density of silver grains (Figures 4.1c and 4.2a). A high number of acceptors occurred in the lateral habenular nucleus, while the medial habenular nucleus was moderately labelled.

In the thalamus (Figures 4.1d,e,f and 4.2c), the laterodorsal nucleus contained a high number of acceptors, while the ventroposterior nuclear group was among the most strongly labelled areas in the rat central nervous system. The zona incerta similarly exhibited very high levels of DTX acceptors. A high level of labelling was also found over the posterior nuclear group.

The hypothalamus was among the less acceptor-rich areas of the rat brain. The ventromedial nucleus showed a moderate, and the

Figure 4.3. Distribution of ^{125}I-DTX acceptors in the hippocampus



Cryostat sections were incubated in 2.5 nM ^{125}I-DTX and exposed to ^{3}H-sensitive film. (a) is a detail of an autoradiogram showing the hippocampal formation, while (b) is a high resolution scan of the area shown in (a). Note that, in order to include more detail, a fifth density band showing areas binding 0.8-1.0 fmol/mm^2 of ^{125}I-DTX, which is unshaded, has been included in the scan (b). Hippocampal formation: F, fimbria; G, granule cell layer; H, hilus; M, stratum moleculare; Or, stratum oriens; P, pyramidal cell layer; R, stratum radiatum. CA1, CA2, and CA3 define the subfields of the hippocampus, while DG identifies the dentate gyrus. Other abbreviations: 3V, third ventricle; CC, corpus callosum; LH, lateral habenular nucleus; LV, lateral ventricle; MH medial habenular nucleus. Scale bar =1 mm.

lateral hypothalamic area a high level of acceptors, while only low levels of silver grains were observed over the paraventricular and arcuate nuclei.

4.3.1.3. *The pituitary*

Autoradiograms of coronal sections through the pituitary are shown in Figure 4.4. The adenohypophysis (anterior lobe) was unlabelled, while a very low level of binding could be observed over the neurohypophysis (posterior lobe). The level of labelling was so low, however, that the sections had to be exposed to Ultrofilm for 4 days (specific activity of ^{125}I-DTX ≈300 Ci/mmol) before the grain densities were high enough to be measured accurately. Forebrain sections incubated in parallel in the same experiment (e.g. the section shown in Figure 4.1b) required only 1-day exposure to prominently blacken the film.

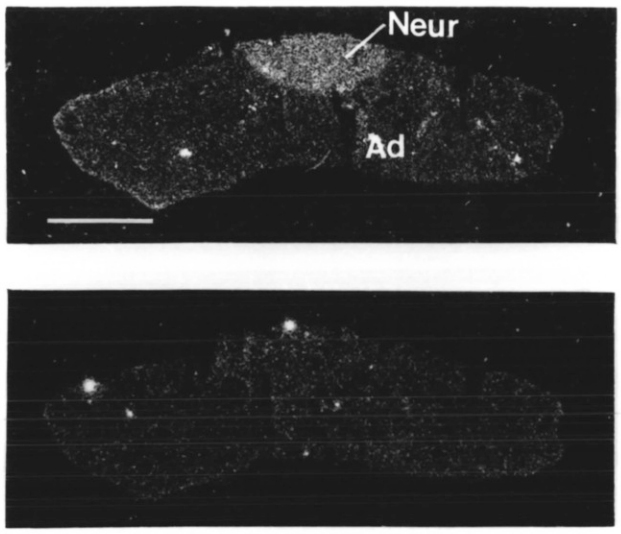
4.3.1.4. *The mesencephalon*

Most midbrain nuclei contained moderately high to high levels of DTX binding sites (Figure 4.5). The superficial grey layer of the superior colliculus was covered by a moderate number of silver grains, while high levels of labelling were observed over the optic nerve layer (Figure 4.5a). The inferior colliculus also exhibited a high level of DTX binding sites. The lateral geniculate nucleus (Figure 4.1f) presented a high, and the medial geniculate nucleus (Figure 4.5a) a very high density of acceptors. High levels of DTX binding were also found in the central grey. The substantia nigra contained a moderately high number of acceptors. More posteriorly, the pontine reticular formation showed moderately high and the nucleus pontis moderate labelling (Figure 4.5b). The pineal body was very weakly labelled (Figure 4.5b), possessing a similar level of acceptors to that observed in the neurohypophysis of the pituitary.

4.3.1.5. *Cerebellum and brainstem*

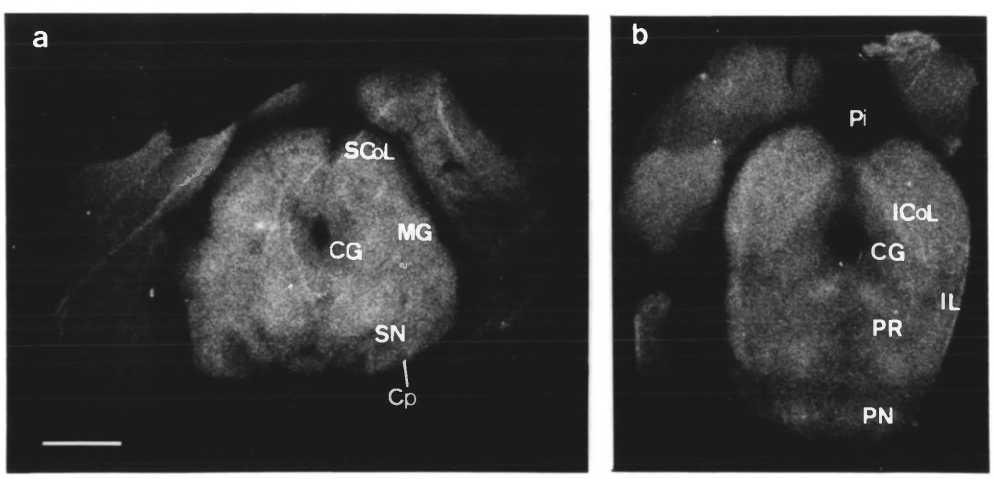
Autoradiograms of ^{125}I-DTX labelled cryostat sections from the cerebellum displayed a distinctive layered distribution of silver grains (Figures 4.1g,h and 4.6). Very high levels of toxin binding were found over the Purkinje cell layer. The molecular layer contained a high, and the granule cell layer a moderate density of silver grains.

Figure 4.4. Distribution of ^{125}I-DTX acceptors in the pituitary



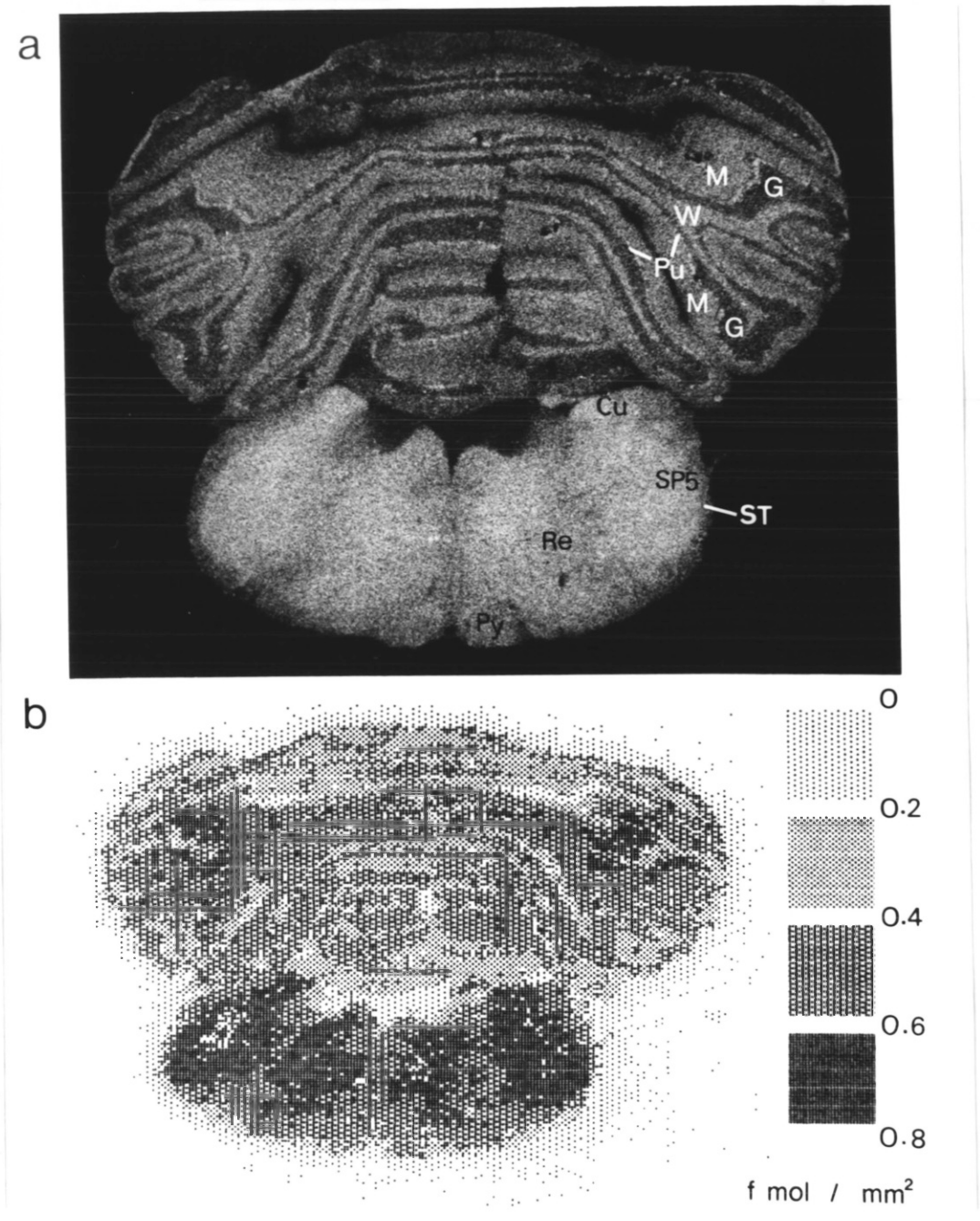
Darkfield images of autoradiograms from coronal sections of rat pituitary labelled with 2.5 nM ^{125}I-DTX alone (a) or in the presence of 1 µM unlabelled DTX (b). **Neur** identifies the neurohypophysis (posterior lobe), while **Ad** is the adenohypophysis (anterior lobe). Scale bar (in a) =1 mm.

Figure 4.5. Distribution of ^{125}I-DTX acceptors in the mesencephalon



Darkfield images of autoradiograms from coronal sections of rat brain cut at the level of the substantia nigra (a) or the inferior colliculus (b). The sections were labelled with 2.5 nM ^{125}I-DTX. Adjacent control sections incubated in 2.5 nM ^{125}I-DTX in the presence of an excess of unlabelled DTX remained virtually unlabelled. CG, central grey; Cp, cerebral peduncle; ICoL, inferior colliculus; lL, lateral lemniscus; MG, medial geniculate body; Pi, pineal body; PN, nucleus pontis; PR, pontine reticular formation; SCoL; superior colliculus; SN, substantia nigra. Scale bar (in a) =2 mm.

Figure 4.6. Distribution of ^{125}I-DTX acceptors in the cerebellum and brainstem



(a) A darkfield image of an autoradiogram from a cryostat section of rat cerebellum and brainstem, labelled in 2.5 nM ^{125}I-DTX. An adjacent control section incubated in 2.5 nM ^{125}I-DTX in the presence of an excess of unlabelled DTX remained virtually unlabelled.
Cerebellum: G, granule cell layer; M, molecular layer; Pu; Purkinje cell layer; W, white matter. Other abbreviations: Cu, cuneate nucleus; Py, pyramidal tracts; Re, reticular formation; Sp5, nucleus of the spinal trigeminal nerve; ST, Spinal Trigeminal nerve; V, vestibular nucleus.
(b) is a scanned representation of the image shown in (a). Again some very prominently labelled areas (e.g. in the nucleus of the spinal trigeminal nerve) are included in a fifth density band showing areas binding 0.8-1.0 fmol/mm² of ^{125}I-DTX, which remains unshaded.

The brainstem nuclei bound moderately high to very high levels of ^{125}I-DTX (Figures 4.1g,h and 4.6). The cochlear nucleus exhibited a moderately high, and the vestibular nucleus a high density of DTX acceptors. The cuneate and gracile nuclei, as well as the nucleus of the hypoglossal nerve and the formatio reticularis presented high numbers of toxin acceptors. Very high levels of labelling were found over the nucleus of the spinal trigeminal nerve.

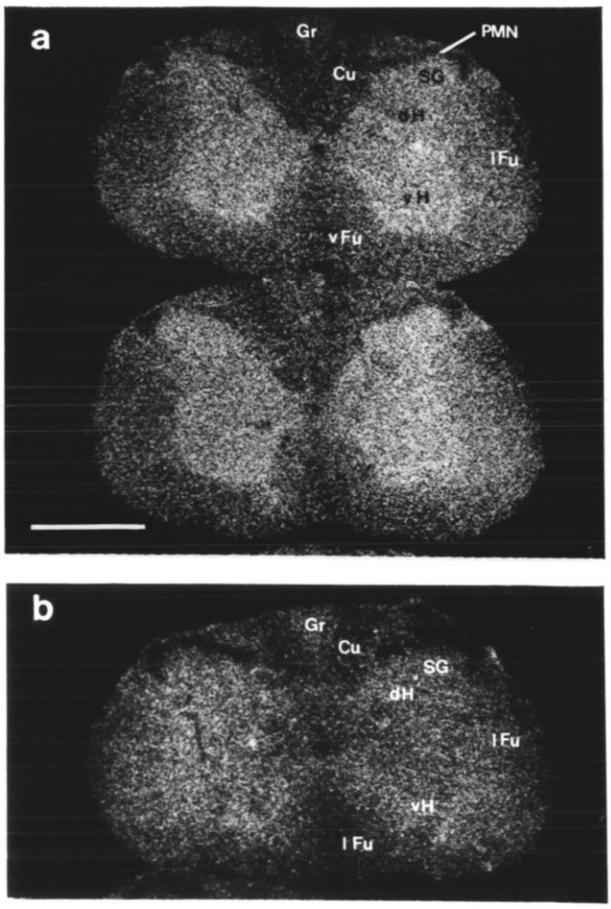
4.3.1.6. *White matter tracts*

In contrast to the labelling obtained with ^{125}I-β-BuTX (Section 3.4.4.4), brain areas rich in myelinated tracts generally contained moderate to high densities of ^{125}I-DTX binding sites. Anteriorly, the lateral olfactory tract exhibited moderate and the anterior commissure moderately high numbers of acceptors (Figures 4.1a,b,c and 4.2a). The corpus callosum, and the external and internal capsule (Figures 4.1a-f and 4.2) bound moderately high or high levels of ^{125}I-DTX. The optic nerve, the optic chiasma and the optic tract were labelled moderately by the toxin (Figures 4.1c,d,e and 4.2). The fimbria of the hippocampus (Figure 4.3) presented a moderate number of acceptors, while the stria medullaris thalami, which envelopes and penetrates the lateral habenular nuclei (see e.g. Figure 4.1c), showed moderately high labelling. A high grain density was found over the mammillothalamic tract. In the midbrain, the posterior commissure (Figure 4.1f) contained a low level of DTX acceptors, while the cerebral peduncle (Figure 4.5a) exhibited moderate and the lateral lemniscus (Figure 4.5b) moderately high densities of silver grains. The cerebellar white matter laminae (Figures 4.1g,h and 4.6) presented high numbers of DTX binding sites. Moderately high grain densities were observed over the inferior cerebellar peduncle, the spinal trigeminal nerve and the pyramidal tracts (Figures 4.1g,h and 4.6).

4.3.1.7. *The spinal cord*

The distribution of DTX acceptors in the spinal cord is shown in Figure 4.7a. The central grey matter contained high or very high levels of toxin binding sites. In particular, the substantia gelatinosa and ventral horn were prominently labelled. By contrast, very few silver grains were found over the posterior marginal nucleus adjacent to the substantia gelatinosa (Figure

Figure 4.7. Distribution of ^{125}I-DTX acceptors in the spinal cord



Darkfield autoradiograms of cervical spinal cord cryostat sections labelled in 2.5 nM ^{125}I-DTX alone (a) or in the presence of 1 µM unlabelled ß-BuTX (b). Adjacent control sections incubated in 2.5 nM ^{125}I-DTX in the presence of an excess of unlabelled DTX remained virtually unlabelled. Cu, fasciculus cuneatus; dH, dorsal horn; Gr, fasciculus gracilis; lFu, lateral funiculus; PMN, posterior marginal nucleus; SG substantia gelatinosa; vFu, ventral funiculus; vH, ventral horn. Scale bar =1 mm.

4.7a). The white matter areas generally showed moderate toxin binding, while the fasciculus gracilis presented a moderately high number of acceptors. Thus, as for β-BuTX (see Section 3.4.4.5), the densities of DTX acceptors in the spinal cord grey and white matter areas were similar to those found in the brainstem.

4.3.2. Evidence for Heterogeneity of DTX Binding Sites in Rat Brain

The binding studies with ^{125}I-DTX on cryostat sections described in Chapter 2 have already given some indications of possible heterogeneity or variability among the DTX binding sites in rat brain (cf. Section 2.5.4). More direct evidence that DTX labels several acceptor sub-types or variants was obtained using quantitative autoradiography, as detailed below.

4.3.2.1. *β-BuTX distinguishes two types of ^{125}I-DTX binding sites*

It has already been noted above (Section 4.3.1) that all brain areas which have been examined specifically bound higher levels of ^{125}I-DTX than of ^{125}I-β-BuTX. Furthermore, Table 4.1 shows that the ratio of DTX : β-BuTX binding varied in different parts of the rat brain. In the frontoparietal cerebral cortex and most forebrain areas (e.g. in the anterior olfactory nucleus, olfactory tubercle, caudate putamen or amygdala) the ratio of DTX : β-BuTX binding ranged from 2 to 3. Areas which contained relatively higher concentrations of β-BuTX acceptors, such as the nucleus accumbens or the lateral septal nucleus (cf. Table 3.3), had a lower ratio of sites (≃1.5). In the hippocampus, where the density of ^{125}I-β-BuTX binding sites decreased laterally (in CA_3 relative to CA_1 and CA_2), while that of ^{125}I-DTX binding increased in CA_3, the DTX : β-BuTX ratio also increased laterally, from ~3 in CA_1 and CA_2 to ~4 in CA_3. The thalamus showed a DTX : β-BuTX binding ratio of ~5, except in the laterodorsal nucleus, which was prominently labelled by ^{125}I-β-BuTX (e.g. compare Figure 3.7 and Figure 4.2b). In the cerebellum and brainstem, the DTX : β-BuTX ratio varied between 3 and 4. However, all white matter regions exhibited DTX : β-BuTX ratios of at least 5, and often significantly higher. It should be noted that in these white matter regions, where the levels of ^{125}I-DTX and ^{125}I-β-BuTX binding were very different, a small error in the measurement of either can cause a major change in the ratio. This may explain the wide range of binding site

ratios (5-25, cf. Table 4.1) observed here. In the spinal cord, the DTX : β-BuTX ratio varied between ~3 in the grey matter areas to again close to 5 in the surrounding white matter.

When cryostat sections were labelled with ^{125}I-DTX in the presence of a 400- to 500-fold excess of unlabelled β-BuTX (i.e. in 2-2.5 nM ^{125}I-DTX + 1 μM β-BuTX) the levels of specific ^{125}I-DTX binding observed were significantly reduced. A set of autoradiograms of sections labelled under these conditions is shown in Figure 4.8; note that these images were from sections adjacent to those shown in Figure 4.1. It is striking that the major proportion of the residual ^{125}I-DTX binding is found in white matter tracts (e.g. the anterior commissure, lateral olfactory tract, corpus callosum, external and internal capsule, optic tracts, the cerebellar white matter bundles, spinal trigeminal nerve and pyramids) or in areas frequently traversed by myelinated fibres, such as the thalamus or the brainstem reticular formation. The white matter bundles passing through the caudate putamen, and the fibres penetrating from the corpus callosum and external capsule into the frontoparietal cortex (the corona radiata) are clearly differentiated.

Selected autoradiograms from these experiments have also been analysed by scanner densitometry. Some representative scans are shown in Figures 4.9 and 4.10; these images are from sections adjacent to those in Figures 4.2 and 4.6, respectively. Note, however, that in order to include more detailed information the shading bands used in Figures 4.9 and 4.10 in the scanned images are narrower (0.1 fmol/mm^2 intervals) than those in Figures 4.2 and 4.6 (0.2 fmol/mm^2 intervals). In addition, levels of β-BuTX-resistant ^{125}I-DTX binding are reported in Table 4.2.

Approximately 20% of the specific ^{125}I-DTX binding in the frontoparietal cerebral cortex appeared resistant to blockade by 1 μM β-BuTX. This residual labelling corresponded largely to the corona radiata fibres. In contrast, β-BuTX blocked ~90% of the specific ^{125}I-DTX binding in the posterior cingulate cortex, which is one of the areas more prominently labelled by ^{125}I-β-BuTX (cf. Chapter 3, Section 3.4.4.1). In most anterior forebrain areas (e.g. the olfactory tubercle, nucleus accumbens and lateral septal nucleus, Figure 4.9a), as well as in the amygdala and in the hippocampal formation (Figure 4.9b), <10% of the specific ^{125}I-DTX binding was resistant to blockade by excess β-BuTX. The caudate

(continued on p. 133)

Figure 4.8. Distribution of ^{125}I-DTX binding in the presence of excess unlabelled ß-BuTX

Representative darkfield images of autoradiograms from cryostat sections of rat forebrain at the level of the anterior olfactory nucleus (a), anterior (b) and posterior (c) caudate putamen, anterior (d), mid (e) and posterior (f) hippocampus, and of cerebellum with brainstem (g and h). The images shown are from sections adjacent to those in Figure 4.1. All sections were labelled in 2-2.5 nM ^{125}I-DTX in the presence of 1 μM unlabelled ß-BuTX. As the images represent the results of different experiments and were printed separately, grain densities cannot be compared between photographs.

A, amygdala; AC, anterior commissure; AO, anterior olfactory nucleus; CBL, cerebellum; CC, corpus callosum; CP, caudate putamen; Cu, cuneate nucleus; DB, diagonal band; f, fornix; FC, fronto-parietal cortex; gCC, genu of corpus callosum; GP, globus pallidus; HC, hippocampal formation; Hy, hypothalamus; I, insular cortex; Ip, inferior cerebellar peduncle; Ld, laterodorsal thalamic nucleus; LG lateral geniculate body; LS, lateral septal nucleus; LoT, lateral olfactory tract; NA, nucleus accumbens; ON, optic nerve; OT, optic tract; OX, optic chiasma; PC, posterior cingulate cortex; Po, posterior thalamic nuclear group; Py, pyramidal tracts; Re, reticular formation; Sm, stria medullaris thalami; Sp5, nucleus of the spinal trigeminal nerve; ST, spinal trigeminal nerve; Su, subiculum; Th, thalamus; Tu, olfactory tubercle; V, vestibular nucleus; W, cerebellar white matter bundles; ZI, zona incerta. Scale bar (in a) =2 mm.

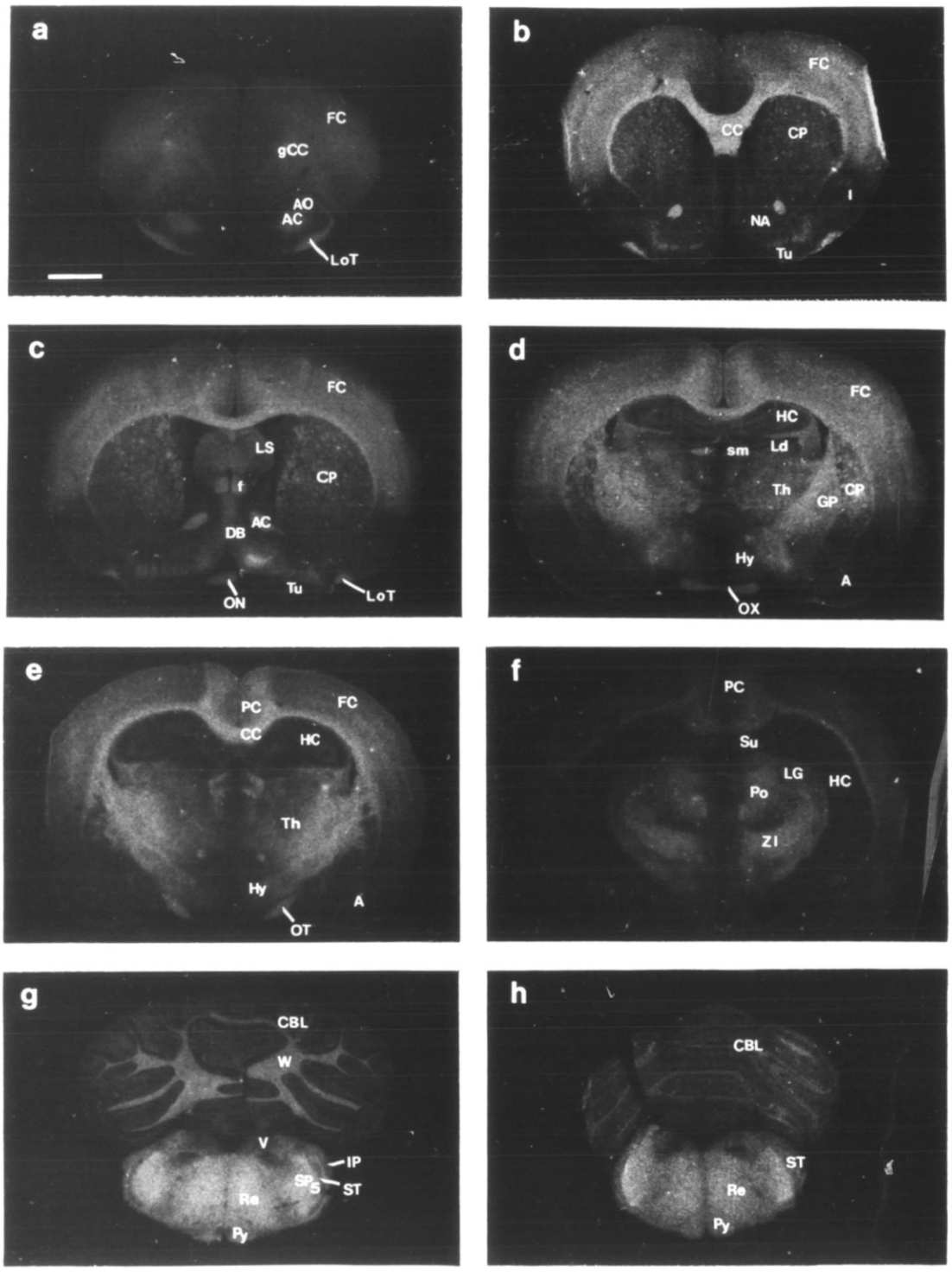

a
FC
gCC
AO
AC
LoT
b
FC
CC
CP
I
NA
Tu
c
FC
LS
CP
f
DB
AC
ON
Tu
LoT
d
FC
HC
sm
Ld
Th
GP
CP
Hy
A
OX
e
PC
FC
CC
HC
Th
Hy
A
OT
f
PC
Su
LG
HC
Po
ZI
g
CBL
W
V
IP
SP
S
ST
Re
Py
h
CBL
ST
Re
Py

Figure 4.9. Distribution of ^{125}I-DTX binding in rat forebrain in the presence of excess unlabelled β-BuTX

Darkfield images of autoradiograms from sections of rat forebrain at the level of the caudate putamen (a) or hippocampus (c) are shown together with scanned representations thereof (b and d, respectively). The sections were labelled with 2.5 nM ^{125}I-DTX in the presence of 1 μM unlabelled β-BuTX. These images are from sections adjacent to those shown in Figure 4.2.

A, amygdala; AC, anterior commissure; CC, corpus callosum; CP, caudate putamen; DB, diagonal band; EC, external capsule; FC, frontoparietal cerebral cortex; HC, hippocampal formation; I, insular cortex; IC, internal capsule; Ld, laterodorsal thalamic nucleus; LS, lateral septal nucleus; LoT, lateral olfactory tract; NA, nucleus accumbens; ON, optic nerve; OT, optic tract; PC, posterior cingulate cortex; Po, Posterior thalamic nuclear group; Tu, olfactory tubercle; vHy, ventral hypothalamic area; Vp, ventroposterior thalamic nucleus; Zi, zona incerta.

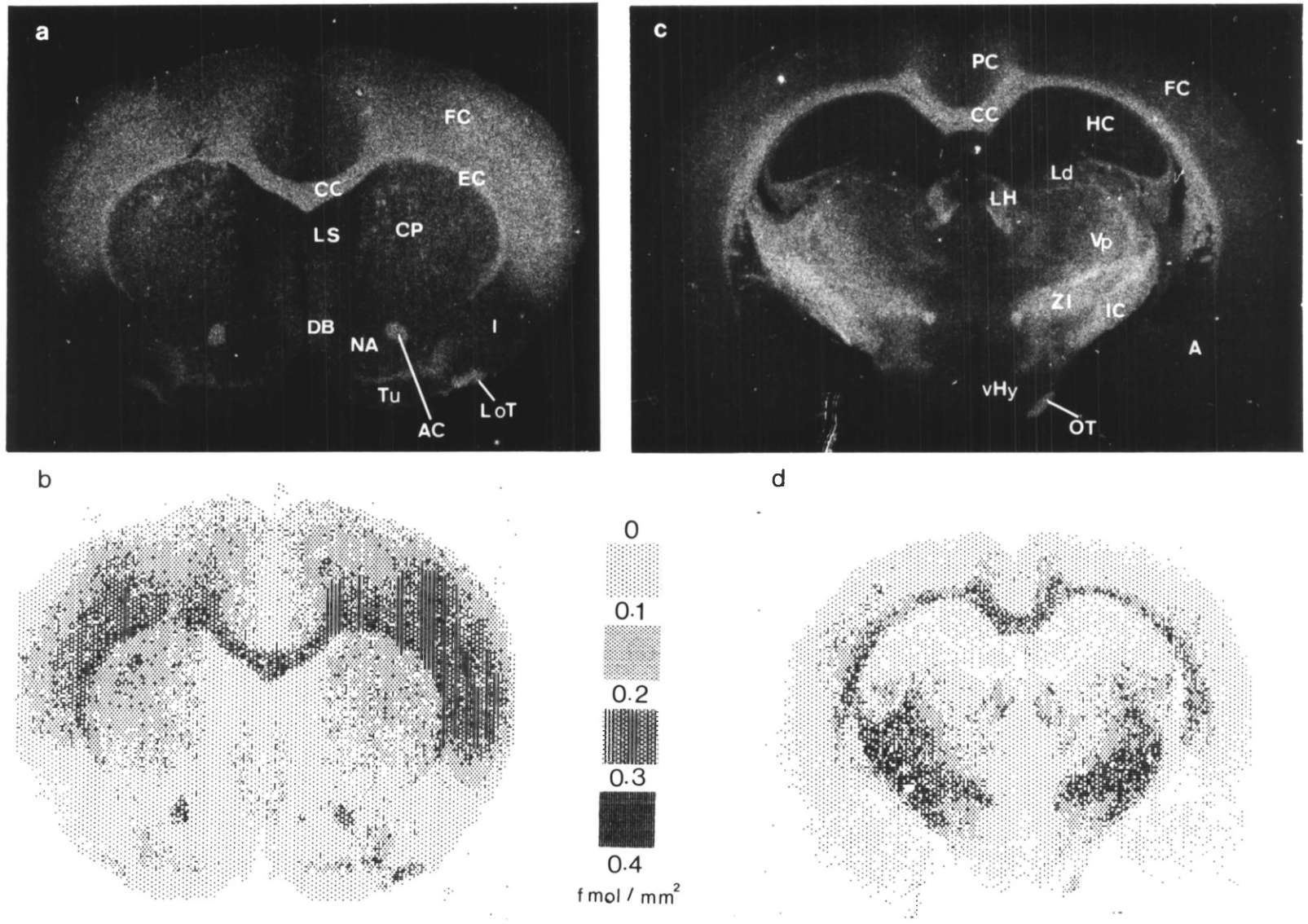
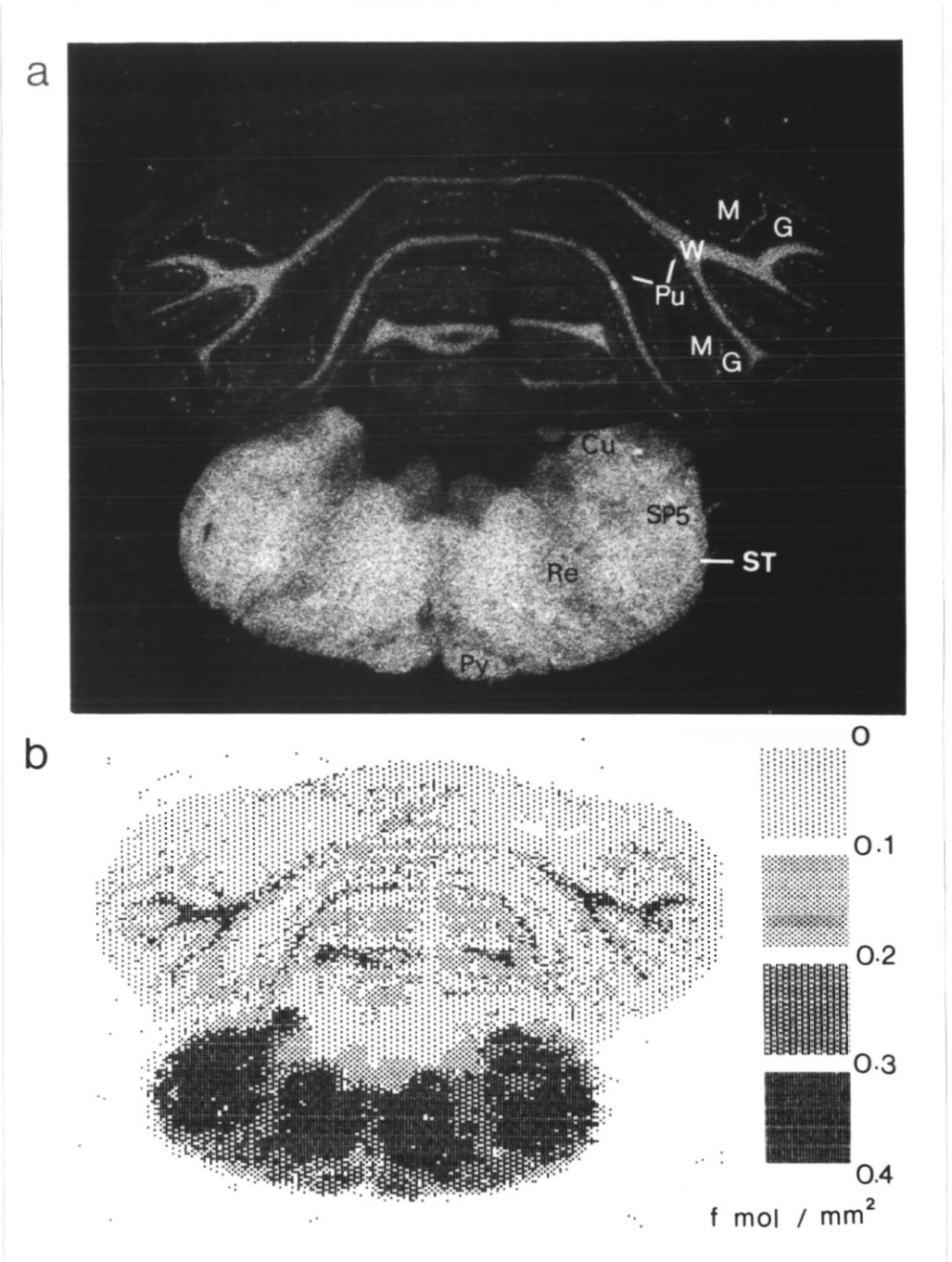

a
FC
CC
EC
LS
CP
DB
NA
I
Tu
AC
LoT
c
PC
FC
CC
HC
Ld
LH
Vp
ZI
IC
A
vHy
OT
b
0
0.1
0.2
0.3
0.4
f mol / mm²
d

Figure 4.10. Distribution of ^{125}I-DTX binding in the cerebellum and brainstem in the presence of excess ß-BuTX



(a) A darkfield image of an autoradiogram from a cryostat section of rat cerebellum and brainstem, labelled in 2.5 nM ^{125}I-DTX in the presence of 1 µM unlabelled ß-BuTX. The image shown is from a section adjacent to that in Figure 4.6.
Cerebellum: G, granule cell layer; M, molecular layer; Pu; Purkinje cell layer; W, white matter. Other abbreviations: Cu, cuneate nucleus; Py, pyramidal tracts; Re, reticular formation; Sp5, nucleus of the spinal trigeminal nerve; ST, spinal trigeminal nerve; V, vestibular nucleus.
(b) is a scanned representation of the image shown in (a).

Table 4.2. Distribution of ^{125}I-DTX binding in the presence of excess unlabelled β-BuTX

Region	n[a]	^{125}I-DTX bound specifically (fmol/mm^2)	% of ^{125}I-DTX binding not blocked [b]
GREY MATTER			
Olfactory tubercle	3	0.019 ± 0.009	8.4
Frontoparietal cerebral cortex	7	0.131 ± 0.028	18.6
Posterior cingulate cortex	5	0.091 ± 0.020	10.0
Caudate putamen	5	0.075 ± 0.017	16.3
Globus pallidus	3	0.181 ± 0.072	31.6
Nucleus accumbens	3	0.030 ± 0.012	10.4
Lateral septal nucleus	3	0.040 ± 0.021	11.0
Basal/cortical amygdala	4	0.036 ± 0.009	9.9
Hippocampal formation			
CA_3: Stratum oriens	4	0.054 ± 0.011	8.1
Pyramidal cell layer	4	0.042 ± 0.011	8.9
Stratum radiatum	4	0.057 ± 0.015	8.2
Dentate gyrus: Stratum moleculare	4	0.063 ± 0.020	9.2
Granule cell layer	4	0.038 ± 0.011	10.7
Lateral habenular nucleus	3	0.216 ± 0.040	32.9
Medial habenular nucleus	2	0.061 ± 0.038	15.7
Thalamus: Laterodorsal nucleus	4	0.114 ± 0.035	17.0
Ventroposterior nucleus	4	0.264 ± 0.084	28.1
Lateral hypothalamic area	3	0.071 ± 0.021	11.3
Cerebellum: Molecular layer	3	0.143 ± 0.050	22.8
Granule cell layer	3	0.072 ± 0.025	17.6
Brainstem: Reticular formation	2	0.341 ± 0.058	43.8
Nucleus of spinal trigeminal nerve	2	0.351 ± 0.053	36.7
WHITE MATTER			
Lateral olfactory tract	3	0.164 ± 0.038	38.9
Anterior commissure	3	0.165 ± 0.041	30.5
Corpus callosum	6	0.239 ± 0.050	35.0
External capsule	3	0.207 ± 0.058	37.6
Internal capsule	5	0.202 ± 0.043	38.6
Fornix	3	0.142 ± 0.045	31.2
Optic tract	3	0.145 ± 0.055	37.4
Fimbria hippocampi	2	0.157 ± 0.029	35.4
Cerebellar white matter	3	0.315 ± 0.038	50.5
Spinal trigeminal nerve	2	0.201 ± 0.009	40.9
Pyramids	2	0.208 ± 0.012	38.6
SPINAL CORD			
Grey matter: Substantia gelatinosa	2	0.382 ± 0.013	46.2
Dorsal horn	2	0.380 ± 0.034	50.9
Ventral horn	2	0.417 ± 0.005	52.4
White matter: Fasciculus gracilis	2	0.270 ± 0.013	57.6
Fasciculus cuneatus	2	0.149 ± 0.008	49.3
Dorsal and lateral funiculi	2	0.202 ± 0.004	49.4

Cryostat sections were labelled with 2-2.5 nM ^{125}I-DTX in the presence of 1 μM β-BuTX, and autoradiograms were prepared using ^{3}H-sensitive Ultrofilm and analysed by laser densitometry.
a: n is the number of experiments using different ^{125}I-DTX preparations. Specific binding of ^{125}I-DTX in the presence of excess β-BuTX was determined by subtraction of the non-specific binding and is given as mean ± S.E.M.
b: Determined by comparison with Table 4.1.

putamen (Figure 4.9a) and the globus pallidus, which are traversed by many white matter bundles, showed higher overall levels of β-BuTX-resistant ^{125}I-DTX acceptors. In the habenular formation (Figure 4.9b), 30% of the specific ^{125}I-DTX binding in the lateral nucleus and 15% of that in the medial nucleus was resistant to blockade by excess β-BuTX. The high level of resistant sites in the lateral habenular nucleus is probably due to its extensive penetration by myelinated fibres from the stria medullaris thalami. About 30% of the specific ^{125}I-DTX binding in the ventroposterior thalamic nucleus, but only ≈18% of that in the laterodorsal thalamic nucleus was resistant to excess β-BuTX (Figure 4.9b). Furthermore, most of the ^{125}I-DTX binding in the hypothalamus was blocked by excess β-BuTX.

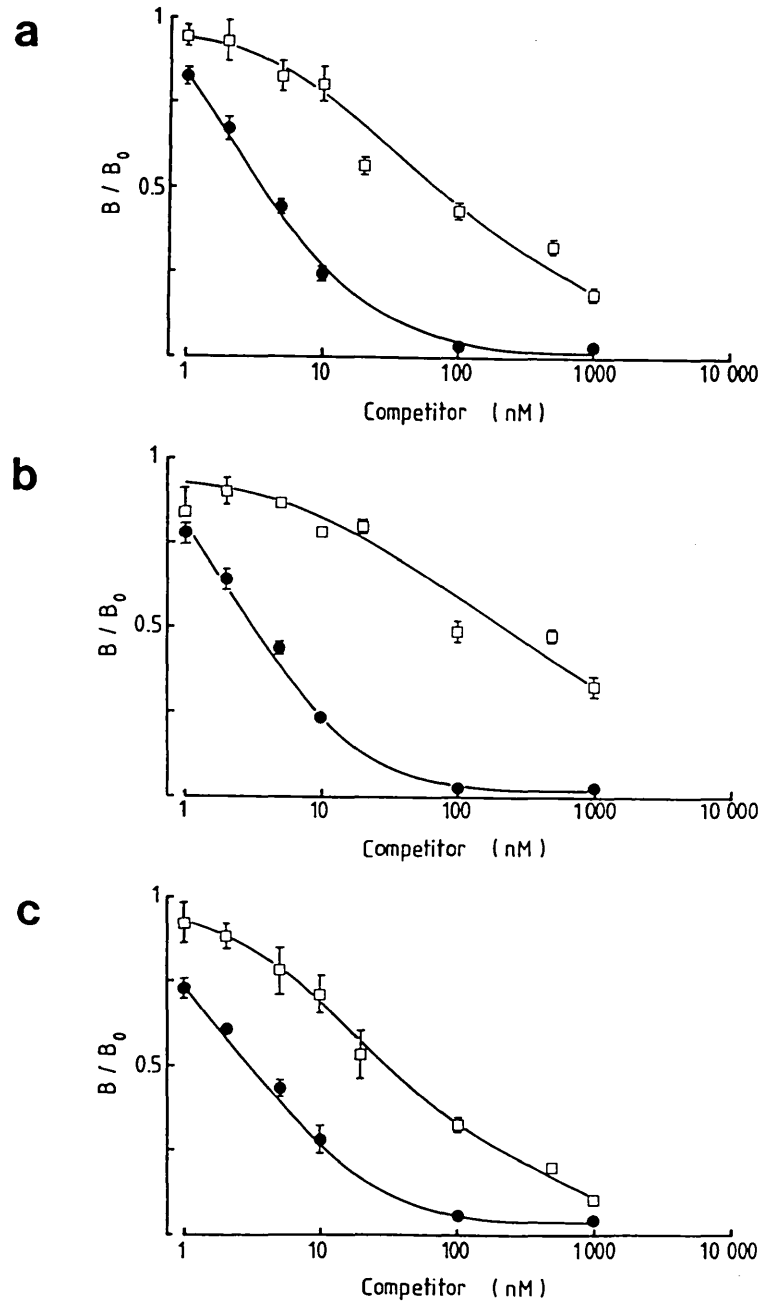
The efficiency of β-BuTX in inhibiting ^{125}I-DTX binding decreased posteriorly in rat brain: β-BuTX blocked ≈90% of the specific ^{125}I-DTX binding in many forebrain areas, but only ≈80% in the the cerebellar molecular and granule cell layers (Figure 4.10). The brainstem nuclei contained 35-45% β-BuTX-resistant ^{125}I-DTX acceptors. Additionally, 30-50% of the specific ^{125}I-DTX binding in all white matter areas was retained in the presence of excess β-BuTX. The highest levels of β-BuTX-resistant ^{125}I-DTX binding were found in the cerebellar white matter laminae (Figure 4.10), but other white matter areas such as the corpus callosum, external and internal capsules, as well as the white matter tracts in the brainstem (e.g. the spinal trigeminal nerve or the pyramids, Figure 4.10), also contained high levels of β-BuTX-resitant ^{125}I-DTX binding sites. Throughout the spinal cord ≈50% of the specific binding observed with ^{125}I-DTX alone remained in the presence of 1 μM β-BuTX (Figure 4.7b).

4.3.2.2. *Inhibition of ^{125}I-DTX binding by various concentrations of unlabelled β-BuTX*

Further evidence that β-BuTX distinguishes different populations of ^{125}I-DTX binding sites was obtained by analysing autoradiograms from competition experiments in which a range of concentrations of unlabelled DTX or β-BuTX were used to inhibit ^{125}I-DTX binding. Some representative inhibition curves are shown in Figures 4.11 and 4.12.

Unlabelled DTX always blocked ^{125}I-DTX binding with high affinity, the IC_{50} values varying between about 3 and 5 nM in all

Figure 4.11. Autoradiographic determination of the competition by unlabelled DTX and β-BuTX of ^{125}I-DTX binding: Rat forebrain areas

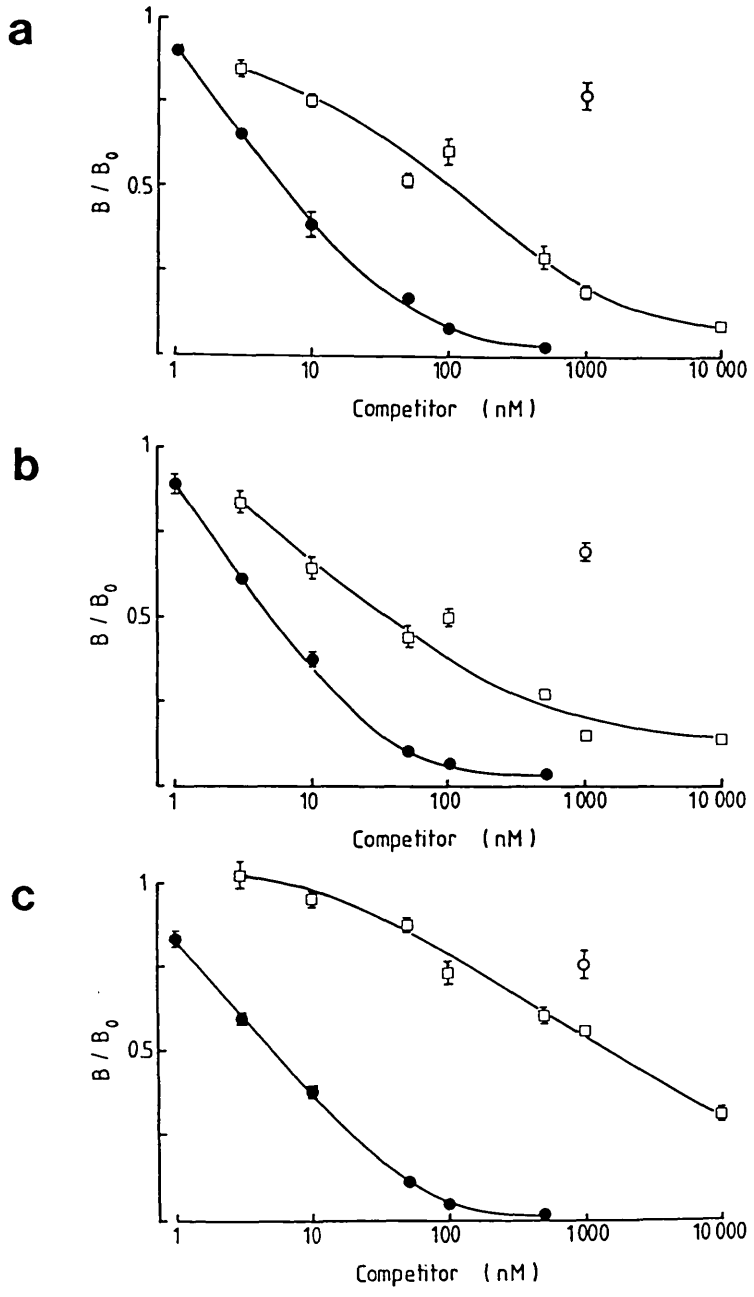


Rat forebrain cryostat sections at the level of the hippocampus were incubated in 2.9 nM ^{125}I-DTX in the presence of a range of concentrations of unlabelled DTX (●) or β-BuTX (□), washed, dried and exposed to ^{3}H-sensitive Ultrofilm. The resulting autoradiograms were analysed by laser densitometry. Total binding of ^{125}I-DTX was determined in the absence of competing toxins.

(a) Frontal cerebral cortex.
(b) Corpus callosum.
(c) Amygdala.

Error bars indicate standard errors for six patches of density readings in the frontal cerebral cortex (a), three patches in the corpus callosum (b), or four patches in the amygdala (c).

Figure 4.12. Autoradiographic determination of the competition by unlabelled DTX and β-BuTX of ^{125}I-DTX binding: Rat cerebellum sections



Cryostat sections from rat cerebellum were incubated in 2.8 nM ^{125}I-DTX in the presence of a range of concentrations of unlabelled DTX (●) or β-BuTX (□). Some sections were also incubated in in Ca^{2+}-free Krebs ringer (containing 5 mM EDTA, ○). Sections were washed, dried and exposed to ^{3}H-sensitive Ultrofilm. The resulting autoradiograms were analysed by laser densitometry. Error bars indicate standard errors for six patches of density readings in each of the cerebellar layers.

(a) Molecular layer
(b) Granule cell layer
(c) White matter laminae

brain areas studied. The inhibition constants, K_I, averaged 1.0 nM on forebrain cryostat sections (Figure 4.11, overall K_d of ^{125}I-DTX binding =1.2 nM, see Chapter 2, Table 2.2) and 2.1 nM on cerebellum sections (Figure 4.12, overall K_d of ^{125}I-DTX binding ≈2 nM). Thus, DTX and ^{125}I-DTX apparently bound to all brain areas with similar affinities.

In contrast, the potency of β-BuTX in blocking ^{125}I-DTX binding varied in different brain areas. In one experiment, the K_I of β-BuTX was ≈13 nM in the frontoparietal cerebral cortex (Figure 4.11a), the brain region from which synaptosomes were usually prepared (cf. Dolly *et al.*, 1984; Black *et al.*, 1986). ^{125}I-DTX binding in the corpus callosum was more resistant to competition with β-BuTX; the curve in Figure 4.11b shows that the blockade was incomplete even when 1 μM β-BuTX was used. Such incomplete inhibition by 1 μM β-BuTX in some brain areas probably accounts for the large errors (± S.E.M) reported in Table 4.2. From the curve in Figure 4.11b, it can be deduced that the K_I of β-BuTX in the corpus callosum must be greater than 50 nM. The inhibition curves for ^{125}I-DTX binding in the caudate putamen, internal capsule, and laterodorsal and ventroposterior thalamic nuclei resembled that of the corpus callosum (data not shown). In contrast, β-BuTX blocked ^{125}I-DTX binding more efficiently in the amygdala (Figure 4.11c) or in the synaptic layers of the hippocampal formation (data not shown), where K_I values ranged from 5-8 nM. Although these K_I's are only tentative, and somewhat different values were obtained in a second competition experiment, all the inhibition curves with β-BuTX showed a constant displacement to the right in white matter-rich brain areas relative to grey matter regions.

Similar results were also obtained with cerebellum sections; in one experiment, β-BuTX blocked ^{125}I-DTX binding with K_I ≈30 nM in the molecular layer (Figure 4.12a) and K_I ≈10 nM in the granule cell layer (Figure 4.12b), while inhibition in the white matter laminae was incomplete even with 10 μM unlabelled β-BuTX (the curve in Figure 4.12c suggests a K_I of at least 100 nM). In all areas of the cerebellum the efficiency of β-BuTX in blocking ^{125}I-DTX binding was significantly reduced in the absence of divalent cations (Figure 4.12)

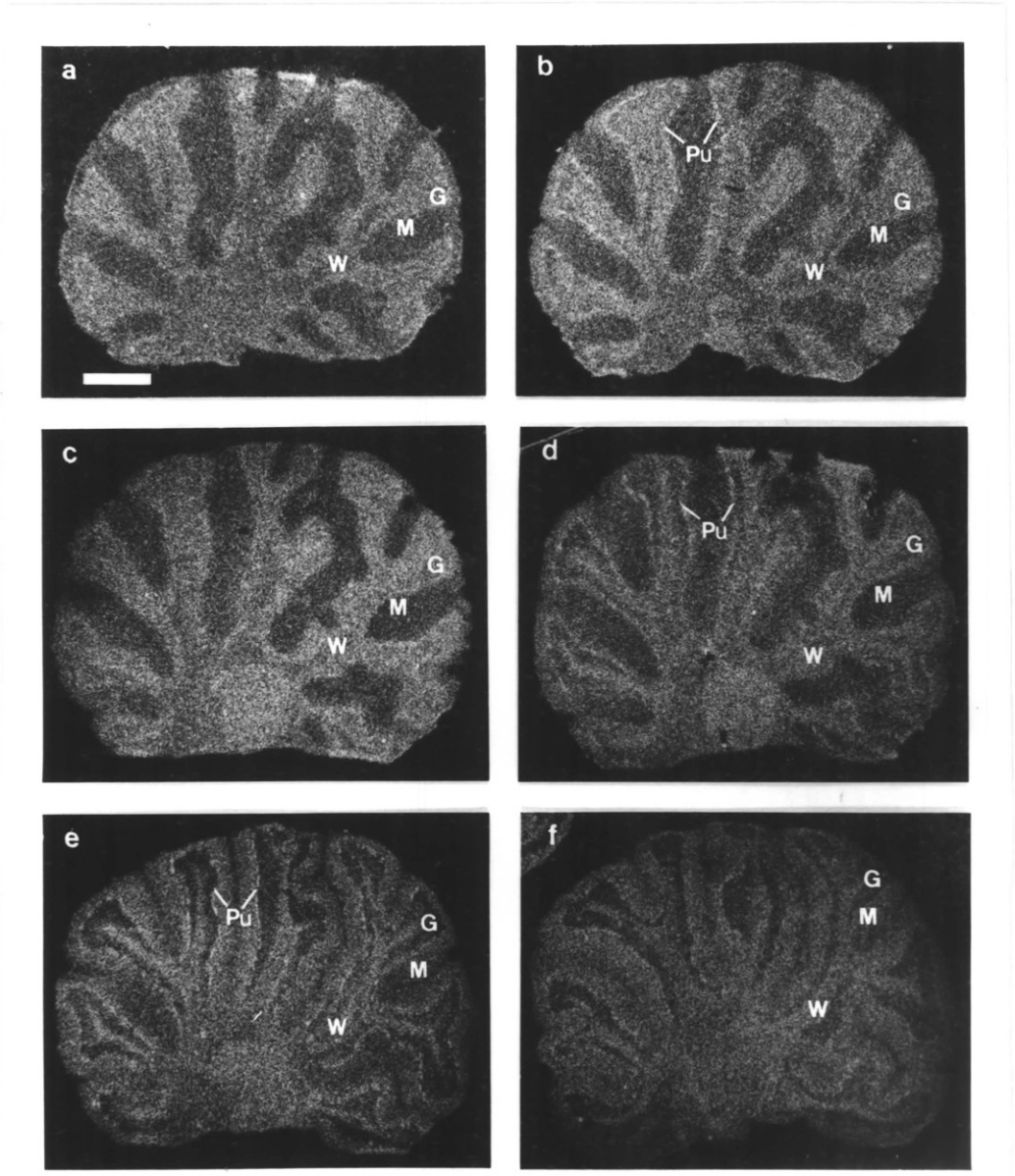
These inhibition curves suggest the existence of at least two variants of ^{125}I-DTX binding sites, differing in their sensitivity to competition by β-BuTX. The proportions of these sites

appear to vary in different brain areas, white matter regions being apparently more enriched in the resistant sites (see also Section 4.4.2).

4.3.2.3. *Concentration-dependence of ^{125}I-DTX binding in the cerebellum*

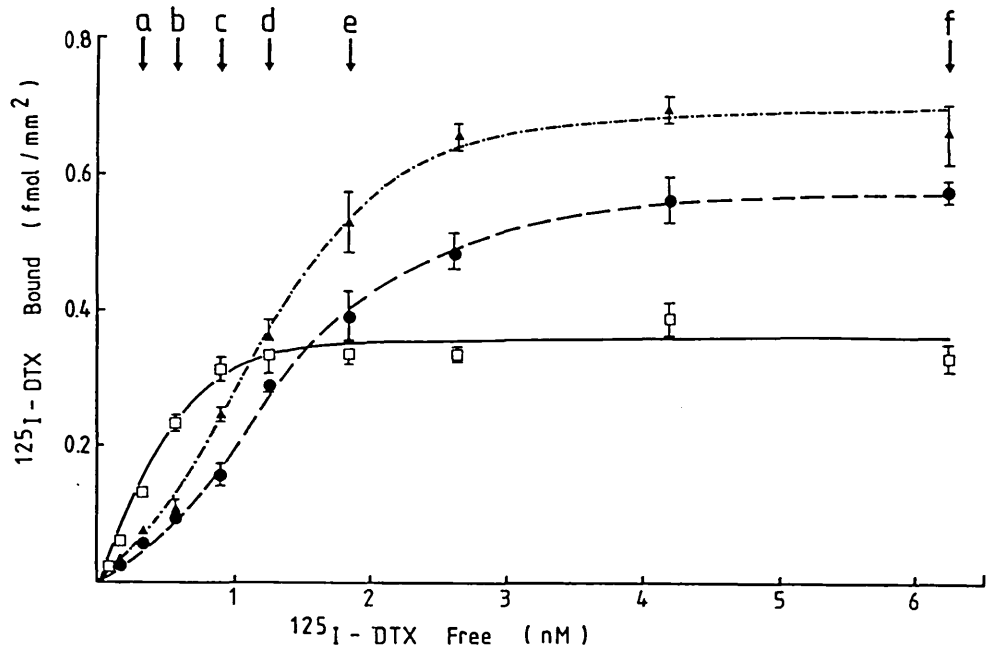
To investigate the apparently reduced affinity of ^{125}I-DTX binding in the cerebellum (Section 2.4.1.2 and Table 2.2), serial sagittal sections were incubated in a range of ^{125}I-DTX concentrations and exposed to ^{3}H-sensitive Ultrofilm. Some representative darkfield images of autoradiograms are shown in Figure 4.13. Low concentrations of ^{125}I-DTX (up to 0.3 nM, Figure 4.13a) prominently labelled the granule cell layer, while only little specific ^{125}I-DTX binding was observed in the molecular layer and white matter laminae. A similar pattern of silver grains was found with 0.6 nM ^{125}I-DTX (Figure 4.13b), except that the Purkinje cell layer could now be distinguished in some areas. With 0.9 nM ^{125}I-DTX (Figure 4.13c), the granule cell layer bound only slightly more toxin than the white matter regions, while the molecular layer still contained the lowest levels of toxin binding. Autoradiograms of sections labelled with 1.3 nM ^{125}I-DTX (Figure 4.13d) showed high densities of labelling in the white matter laminae and the Purkinje cell layer, which separated the approximately equally labelled granule cell and molecular layers. Higher concentrations of ^{125}I-DTX (1.9 nM, Figure 4.13e or 6.2 nM, Figure 4.13f) produced the autoradiographic pattern described earlier (Section 4.3.1.5, see also Figures 4.1g,h and 4.6), with prominent labelling of the Purkinje cell layer, high levels of toxin binding in the molecular layer and white matter laminae, and moderate labelling in the granule cell layer. A similar concentration dependence of ^{125}I-DTX binding in the cerebellum was found in three other experiments. It appears, therefore, that autoradiography can distinguish a population of high affinity acceptors for ^{125}I-DTX in the granule cell layer from lower affinity acceptors in the molecular and white matter layers. Densitometric analysis of these autoradiograms has allowed the construction of saturation binding curves for the layers of the cerebellum (Figure 4.14). A hyperbolic curve was observed for toxin binding in the granule cell layer, the specific binding saturating with ≈1 nM ^{125}I-DTX. The binding curves for the molecular layer and white matter laminae, in contrast, had sigmoid

Figure 4.13. Concentration-dependence of ^{125}I-DTX binding to rat cerebellum cryostat sections



Adjacent sagittal cryostat sections (10 µm) from rat cerebellum were incubated in various concentrations of ^{125}I-DTX (nM): 0.3 (a); 0.6 (b); 0.9 (c); 1.3 (d); 1.9 (e) and 6.2 (f). The sections were washed, dried and exposed to ^{3}H-sensitive Ultrofilm. Because of the wide range of silver grain densities on these images, the photographs shown here were printed at different exposures so that the cell layers can be differentiated easily. Therefore, grain densities cannot be compared between photographs. Note, however, that the autoradiographic patterns depend on the concentration of ^{125}I-DTX used to label the sections.
M, Molecular layer; Pu, Purkinje cell layer; G, granule cell layer; W, white matter laminae. Scale bar (in a) =1 mm.

Figure 4.14. Quantitative analysis of the concentration-dependence of ^{125}I-DTX binding to discrete areas of rat cerebellum



The autoradiograms shown in Figure 4.13 were analysed by laser densitometry, together with other images of sections labelled with intermediate concentrations of ^{125}I-DTX. Bound toxin could thus be determined in fmol/mm^2. The binding curves shown are for the molecular layer (●—●), granule cell layer (□—□) or the white matter laminae (▲···▲). The specific binding was determined by subtracting the non-specific labelling in the presence of 1 μM DTX from the total binding. Markers a-f refer to the sections shown in Figure 4.13. Error bars indicate standard errors for six patches of density readings in each of the cerebellar layers.

shapes, crossing over the granule cell layer curve between 1 and 1.5 nM, and saturating with ≈2.5 nM ^{125}I-DTX. Because of limitations in the sensitivity of the quantiative autoradiography method (the wide range of ligand concentrations tested required sections to be exposed to Ultrofilm for different lengths of time and films to be developed separately; errors associated with the densitometric measurements) it was impossible to analyse the data further, for example by constructing Scatchard plots.

Similar binding experiments on sections from rat forebrain or brainstem did not reveal any obvious concentration dependence of the autoradiographic labelling patterns with ^{125}I-DTX in any other brain area. This was further confirmed by densitometry of the images. In some brain areas, such as the frontoparietal cortex, the thalamus, caudate putamen, and certain white matter areas, slightly sigmoid binding curves were obtained after densitometric analysis of autoradiograms. Such results probably arise from failure of the ligand binding to reach equilibrium at very low ^{125}I-DTX concentrations (Weiland and Molinoff, 1981), and from uneven rates of equilibration of ligand binding in different brain areas (see also Chapter 2, Section 2.5.1).

4.3.3. Distribution of DTX Acceptors in Chick Brain

Cryostat sections from 1-day-old chick brain were labelled with a constant concentration of ^{125}I-DTX (≈2.2 nM), comparable to that used in the study of ^{125}I-DTX binding in the rat central nervous system (Section 4.3.1). Some typical autoradiograms, together with scanned representations thereof, are shown in Figure 4.15. As noted for ^{125}I-β-BuTX binding (Chapter 3, Section 3.5.2), only low levels of ^{125}I-DTX acceptors were observed in chick brain. Therefore the shading bands used to represent the scans in Figure 4.15 are narrower (0.1 fmol/mm^2 intervals) than those used in the rat brain scans. The quantitative distribution of ^{125}I-DTX binding in chick brain is summarized in Table 4.3.

Very low densities of ^{125}I-DTX acceptors were found in the forebrain, where many areas bound less than 0.1 fmol/mm^2, while the ectostriatum and paleostriatum contained ≈0.2 fmol/mm^2 of ^{125}I-DTX binding. The latter areas also contained higher levels of ^{125}I-β-BuTX acceptors (cf. Table 3.4). In most forebrain regions the ratio of DTX : β-BuTX acceptors was between 1 and 3, as in rat forebrain (Section 4.3.2.1).

Figure 4.15. Distribution of ^{125}I-DTX acceptors in one-day-old chick brain

Darkfield images of autoradiograms from sections of chick forebrain (a) or optic lobe and cerebellum (c) are shown together with scanned representations thereof (b and d, respectively). The sections were labelled with 2.2 nM ^{125}I-DTX. Adjacent control sections incubated in 2.2 nM ^{125}I-DTX in the presence of an excess of unlabelled DTX remained virtually unlabelled. Note that, in order to include more detail, a fifth density band (showing areas binding 0.4-0.5 fmol/mm^2 of ^{125}I-DTX), which is unshaded, has been included in the scan shown in (d).
Forebrain: aH, accessory hyperstriatum; Es, ectostriatum; iH, intercalated hyperstriatum; LP, lobus parolfactorius; N, neostriatum; P, paleostriatum; vH, ventral hyperstriatum.
Optic lobe: O, stratum opticum; GF, stratum griseum et fibrosum superficiale; GC, stratum griseum centrale; AC, stratum album centrale; GP, stratum griseum periventriculare; In, nucleus intercollicularis; Re, formatio reticularis lateralis.
Cerebellum: EG, external granule cell layer; G, granule cell layer; M, molecular layer; W, white matter. Scale bar (in a) =1 mm.

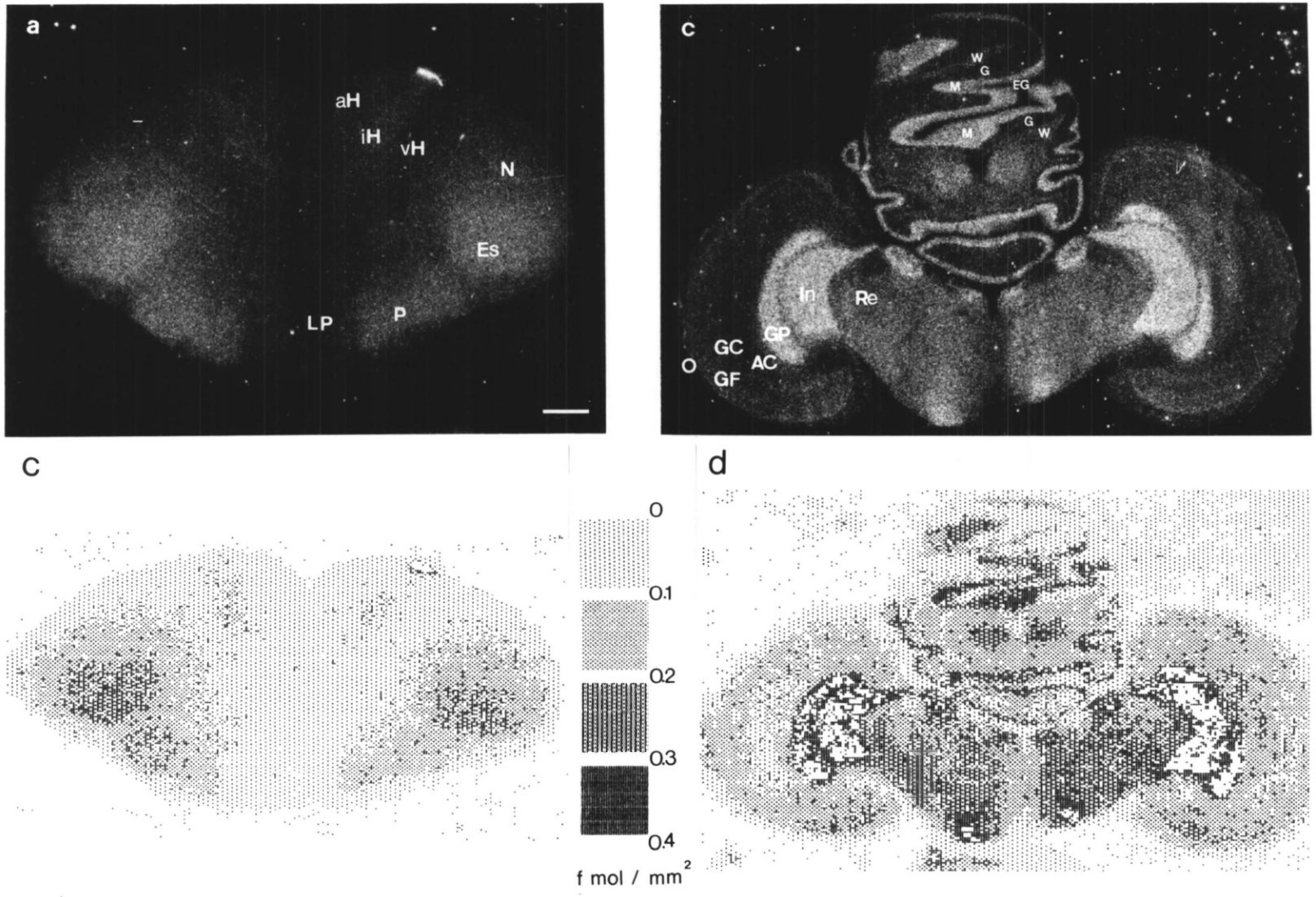

a
aH
iH
vH
N
Es
LP
P
c
W
G
M
EG
G
M
W
In
Re
GP
GC
AC
O
GF
c
d
0
0.1
0.2
0.3
0.4
f mol / mm²

Table 4.3. Distribution of ^{125}I-DTX binding in chick brain

Brain area studied	Specific binding of ^{125}I-DTX (fmol/mm^2)	Relative level of DTX acceptors	DTX/β-BuTX binding ratio [a]
Forebrain			
Accessory hyperstriatum	0.047 ± 0.006	*	2.8
Intercalated hyperstriatum	0.082 ± 0.008	*	1.7
Dorsal hyperstriatum	0.062 ± 0.010	*	
Ventral hyperstriatum	0.065 ± 0.002	*	4.1
Neostriatum	0.097 ± 0.003	*	1.7
Ectostriatum	0.203 ± 0.010	* *	1.0
Paleostriatum	0.189 ± 0.009	* *	1.5
Lobus parolfactorius	0.054 ± 0.002	*	No β-BuTX [b]
Optic Lobe			
Stratum opticum	0.073 ± 0.019	*	2.6
Stratum griseum et fibrosum superficiale	0.124 ± 0.013	*	1.0
Stratum griseum centrale	0.118 ± 0.022	*	1.1
Stratum album centrale	0.181 ± 0.029	* *	4.2
Stratum griseum periventriculare	0.429 ± 0.031	* * *	3.2
Nucleus intercollicularis	0.466 ± 0.014	* * * *	1.7
Formatio reticularis lateralis	0.239 ± 0.020	* *	1.8
Cerebellum			
External granule cell layer	0.062 ± 0.012	*	1.8
Molecular layer	0.240 ± 0.008	* *	1.2
Granule cell layer	0.073 ± 0.011	*	6.6
White matter laminae	0.134 ± 0.011	*	11.2

Cryostat sections were labelled with ≈2.2 nM ^{125}I-DTX. Autoradiograms were prepared using ^{3}H-sensitive Ultrofilm and analysed by laser densitometry. Specific binding of ^{125}I-DTX was calculated by subtraction of the non-specific binding in the presence of 1 μM DTX. The results are given as mean ± S.E.M. from 3 experiments using two different preparations of ^{125}I-DTX. Relative levels of ^{125}I-DTX binding are given as * for comparison with the data in Table 4.1.

a: The ratio of specific binding of ^{125}I-DTX : specific binding of ^{125}I-β-BuTX was calculated from the data here and in Table 3.4 (using the specific ^{125}I-β-BuTX binding at 2.5 nM).

b: There was no specific ^{125}I-β-BuTX binding in this area.

In the optic lobe, the outer layers (stratum opticum, stratum griseum et fibrosum superficiale, stratum griseum centrale and stratum album centrale) contained low levels of DTX acceptors. In contrast, the stratum griseum periventriculare and the nucleus intercollicularis were prominently labelled; as in the forebrain, these areas have also been shown to be rich in ^{125}I-β-BuTX binding sites. The ratios of DTX : β-BuTX binding were usually close to 1.5. However, higher ratios were observed in the stratum opticum, which contains the incoming fibres from the optic tract, and the stratum album centrale (a white matter layer), both of which contained levels of ^{125}I-DTX binding comparable to the nearby grey matter layers, while they were much less strongly labelled by ^{125}I-β-BuTX (cf. Figure 3.11).

In the cerebellum, the molecular layer contained the highest number of ^{125}I-DTX acceptors. The external granule cell layer and the granule cell layer presented a very low level of ^{125}I-DTX acceptors. Significant toxin binding was found in the white matter laminae. The ratio of DTX : β-BuTX binding in the cerebellar white matter regions was ≈11.

4.3.3.1. *Inhibition of ^{125}I-DTX binding by β-BuTX*

Autoradiograms from sections incubated in 2.2 nM ^{125}I-DTX in the presence of 1 μM β-BuTX always presented very low densities of silver grains, comparable to the control autoradiograms from sections treated with an excess of unlabelled DTX. The levels of β-BuTX-resistant ^{125}I-DTX binding hence proved difficult to measure accurately. Excess unlabelled β-BuTX completely blocked all ^{125}I-DTX binding on chick forebrain sections such as the one shown in Figure 4.15a. More posteriorly, a low level of β-BuTX-resistant sites (<6% of the specific ^{125}I-DTX binding) was found over the neostriatum, ectostriatum and paleostriatum. As in rat brain, the efficiency of β-BuTX in blocking ^{125}I-DTX binding decreased posteriorly. In the optic lobe, low concentrations of β-BuTX-resistant ^{125}I-DTX binding sites were observed in the stratum album centrale, stratum griseum periventriculare, nucleus intercollicularis and formatio reticularis lateralis, comprising ≈10% of the specific ^{125}I-DTX binding each of these areas. In the cerebellum, 6% of the ^{125}I-DTX binding in the molecular layer, and 20% of that in the white matter laminae appeared to be resistant to inhibition by excess β-BuTX.

4.3.3.2. *Concentration dependent binding of ^{125}I-DTX to chick cerebellum sections*

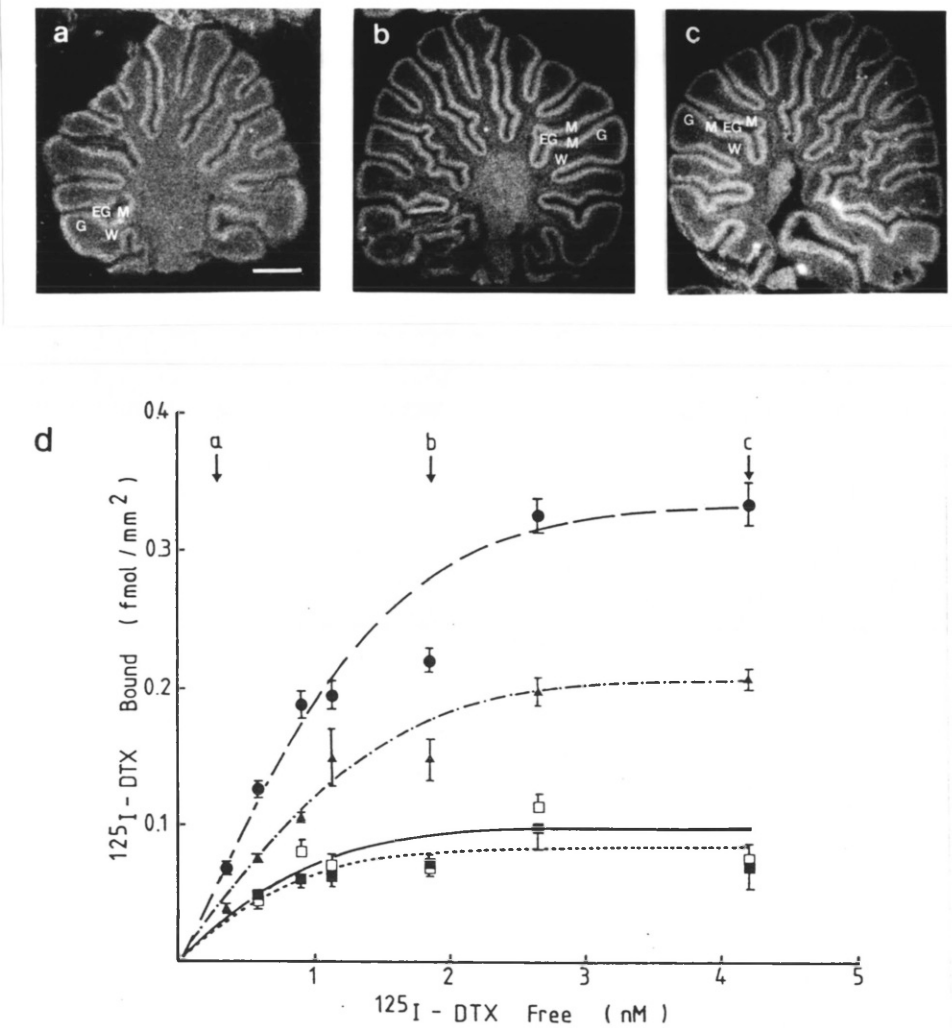
In view of the occurrence of ^{125}I-DTX acceptors of different affinities in rat cerebellum (Section 4.3.2.3), and the presence of high and low affinity ^{125}I-DTX binding sites on membranes of whole chick brain (Black and Dolly, 1986a), cryostat sections from chick cerebellum were incubated in a range of ^{125}I-DTX concentrations, exposed to Ultrofilm, and analysed by densitometry. The results from this experiment are shown in Figure 4.16. Autoradiograms at all concentrations showed similar labelling patterns. Hyperbolic binding curves, which saturated with ≃ 2 nM ^{125}I-DTX, but plateaued with different amounts of ^{125}I-DTX bound, were observed in all cerebellar layers. Hence there was no evidence for the presence of ^{125}I-DTX binding sites of different affinities as in rat cerebellum.

4.4. Discussion

4.4.1. Distribution of DTX Acceptors in the Rat Central Nervous System

Autoradiography has revealed a unique and widespread distribution of DTX acceptors in the rat central nervous system. Densities of ^{125}I-DTX binding >0.6 fmol/mm^2 (i.e. >0.5 pmol/mg protein) were found in the frontoparietal cerebral cortex, the synaptic layers of the hippocampal formation, the thalamus, lateral and medial geniculate nuclei, the superior and inferior colliculi of the midbrain, the molecular layer of the cerebellum, certain nuclei of the brainstem and the grey horns of the spinal cord. High concentrations of specific toxin binding sites were also observed in many white matter regions. This widespread occurrence of DTX acceptors suggests that they serve important roles in neuronal function. Only the non-neuronal anterior pituitary did not contain any specific ^{125}I-DTX binding. Very low levels of DTX acceptors were observed in the posterior lobe of the pituitary and in the pineal body; both of these consist mainly of glial secretory tissue. In addition, the neurohypophysis contains the oxytocin and vasopressin-releasing terminals of the magnocellular neurones from the supraoptic and paraventricular nuclei of the hypothalamus, while the pineal body receives a sparse preganglionic noradrenergic sympathetic innervation. The low levels of DTX binding in these

Figure 4.16. Concentration-dependence of ^{125}I-DTX binding to chick cerebellum cryostat sections



Adjacent sagittal cryostat sections (10 µm) from chick cerebellum were incubated in various concentrations of ^{125}I-DTX (nM): 0.3 (a); 1.9 (b) and 4.2 (c). The section were washed, dried and exposed to ^{3}H-sensitive Ultrofilm. Because of the wide range of silver grain densities on these images, the photographs shown here were printed at different exposures so that the cell layers can be differentiated easily. Therefore grain densities cannot be compared between photographs.
EG, External granule cell layer; M, molecular layer; G, granule cell layer; W, white matter laminae. Scale bar (in a) =1 mm.

These autoradiograms were also analysed by laser densitometry, together with other images labelled with intermediate concentrations of ^{125}I-DTX (d). The binding curves shown are for the molecular layer (●—●), granule cell layer (□—□), external granule cell layer (■----■) or the white matter laminae (▲···▲). Specific binding was determined by subtracting the non-specific labelling in the presence of 1 µM DTX from the total binding. Markers a, b, c refer to the sections shown above. Error bars indicate standard errors for six patches of density readings in each of the cerebellar layers.

areas may, therefore, suggest that the acceptors occur predominantly on neurones. A neuronal distribution of the DTX acceptors was also suggested by electron microscope autoradiography studies (Chapter 5).

Like β-BuTX acceptors, ^{125}I-DTX binding was enriched ≈2-fold in synaptosomes relative to cryostat sections (Section 2.5.2). A similar 2-fold enrichment was observed when binding site densities on cerebrocortical synaptosomes (1-1.2 pmol/mg protein; Mehraban *et al.*, 1984) were compared with those in the cerebral cortex (≈0.6-0.8 fmol/mm^2, ≡0.5-0.7 pmol/mg protein). As this enrichment is comparable to that of the synaptic marker synapsin I (Ueda *et al.*, 1979), a large proportion of the ^{125}I-DTX acceptors is likely to occur on synapses. In addition, a high density of toxin binding sites was associated with white matter fibre tracts.

4.4.2. Interaction of β-BuTX with DTX Binding Sites Suggests Heterogeneity Among DTX Acceptors

In agreement with previous direct binding studies on cryostat sections (Chapter 2, Section 2.5.4), β-BuTX has here been used to distinguish variants of ^{125}I-DTX acceptors in different brain regions. Superficially, two types of DTX binding sites may be differentiated. The first site, common to DTX and β-BuTX, is most easily identified by ^{125}I-β-BuTX, and its predominantly synaptic distribution has been described in Chapter 3; as noted, all of the direct binding of ^{125}I-β-BuTX can be inhibited with high efficacy by DTX (Section 2.4.2 and Figure 3.2j). The second site appears to be unique for DTX. Autoradiography of ^{125}I-DTX binding in the presence of an excess of unlabelled β-BuTX has revealed a heterogeneous distribution of this second site. In the forebrain, the β-BuTX-resistant DTX acceptors occur mainly in white matter tracts such as the corpus callosum, external and internal capsules, lateral olfactory tract or anterior commissure. More posteriorly, regions traversed by myelinated fibres in the thalamus, midbrain or brainstem also contain high levels of β-BuTX-resistant DTX acceptors. In the spinal cord approximately half of the ^{125}I-DTX binding in both the grey and white matter areas is resistant to inhibition by unlabelled β-BuTX. Thus, the β-BuTX-resistant ^{125}I-DTX binding site is found mainly in areas containing low levels of high affinity ^{125}I-β-BuTX binding. This is strikingly apparent when the overall distribution of ^{125}I-DTX binding sites in

rat brain (Figure 4.1) is compared with that of ^{125}I-β-BuTX binding on equivalent sections (Figure 3.2): The "difference" between these distributions is the β-BuTX-resistant ^{125}I-DTX binding site shown in Figure 4.8. Figure 4.2a and c may similarly be compared with Figures 3.6a and 3.7a, respectively, the β-BuTX-resistant ^{125}I-DTX binding being apparent in Figure 4.9a and c.

The comparison breaks down, however, in the brainstem (Figures 4.6a, 3.9a and 4.10a) and spinal cord (Figures 4.7a, 3.10a and 4.7b), where relatively high levels of both ^{125}I-DTX and ^{125}I-β-BuTX binding, as well as β-BuTX-resistant ^{125}I-DTX binding, were observed, for example, in the nucleus of the spinal trigeminal nerve, the reticular formation, or the grey horns and substantia gelatinosa of the spinal cord. Further clear discrepancies in this complementary distribution of β-BuTX-sensitive and β-BuTX-resistant ^{125}I-DTX acceptors become apparent when the acceptor distributions are compared quantitatively. When the densities of ^{125}I-β-BuTX binding at saturation, as summarized in Table 3.3, are subtracted from the levels of ^{125}I-DTX binding determined under similar conditions (listed in Table 4.1), the differences are usually at least twice the values listed in Table 4.2, which shows the residual ^{125}I-DTX binding in the presence of 1 μM unlabelled β-BuTX. As the inhibition of ^{125}I-DTX binding by 1 μM β-BuTX may have been incomplete in some brain areas (Section 4.3.2.2), the disparity may be underestimated. Interestingly, the ratio of the difference between the values in Table 4.1 and Table 3.3 and the values in Table 4.2 (i.e. $\frac{\text{Table 4.1 - Table 3.3}}{\text{Table 4.2}}$) was highest (between 6 and 10) in grey matter areas such as the insular cortex, olfactory tubercle, amygdala or hippocampal formation, while lower ratios (2 to 2.5) were found in white matter regions.

More detailed analysis of the toxin interactions also revealed considerable variability in the affinity of β-BuTX. Thus, direct binding studies demonstrated a high affinity interaction of ^{125}I-β-BuTX with its acceptors in all brain regions (cf. Figure 3.5 and Table 3.1). In contrast, the inhibition constants (K_I) observed in the competition experiments with ^{125}I-DTX indicated a significantly lower affinity for β-BuTX, and the K_I's appeared to vary in different brain areas (Figures 4.11 and 4.12). A third type of ^{125}I-DTX acceptor, which interacts with β-BuTX with lower affinity ($K_I \simeq$10-20 nM; this is similar to the second ^{125}I-β-BuTX binding site revealed in imidazole buffer, Dolly *et al.*, 1987) may

be proposed to resolve these discrepancies. Variable proportions of DTX acceptors in different brain regions, binding β-BuTX with high or low affinity or not at all, may then explain the data described. Alternatively there could be an even greater range of DTX acceptor variants, the extremes being represented by the common high affinity ^{125}I-DTX/^{125}I-β-BuTX binding site enriched in synaptic regions, and a β-BuTX-resistant ^{125}I-DTX acceptor occurring predominantly in white matter regions.

4.4.3. Concentration-Dependence of the Interaction of ^{125}I-DTX with its Acceptors

Experiments in which serial cryostat sections were labelled in a range of ^{125}I-DTX concentrations have revealed striking variations in the autoradiographic labelling patterns over the cerebellum. No other brain area examined showed a similar change in the silver grain distributions. These results indicate that there may be a unique population of binding sites with slightly lower affinity for ^{125}I-DTX in the molecular layer and white matter bundles of the cerebellum. The existence of such sites may explain the higher overall K_d values derived from ^{125}I-DTX binding studies on cerebellum cryostat sections (see Chapter 2, Section 2.4.1.2). Similar "lower affinity" DTX acceptor sites may be still more widespread in the rat central nervous system, possibly occurring also in other white matter regions, but only detected in the cerebellum, where, fortuitously, they are highly concentrated in the molecular layer and white matter laminae, and absent from the adjacent granule cell layer. It should also be noted, however, that significant levels of β-BuTX-resistant ^{125}I-DTX binding were found in the cerebellum molecular layer, although this layer does not contain any myelinated axons (it is the only grey matter brain region where this was observed), but is instead rich in the unmyelinated processes of the granule cells, the parallel fibres. Perhaps the toxin binding observed in white matter tracts and the molecular layer of the cerebellum is to axonal DTX acceptors.

4.4.4. DTX Acceptors in Chick Brain

In agreement with the saturation binding studies described in Chapter 2 (Section 2.4.1.2), the density of ^{125}I-DTX binding sites detected by autoradiography in 1-day-old chick brain cryostat sections was much lower than that in rat brain sections of similar

thickness. However, all ^{125}I-DTX acceptors present in the chick sections may not have been labelled to saturation in the present experiments. Black and Dolly (1986a) have identified two DTX acceptor sub-types with different affinities on chick synaptic membranes (cf. Sections 1.4.4 and 1.5). As indicated in Section 2.5.2, the ^{125}I-DTX concentrations used in the present localization studies were insufficient to label significantly the low affinity (K_d ≈15 nM) DTX acceptor population described by these authors. Thus the ^{125}I-DTX binding observed (which was mainly to the high affinity acceptor sub-type) was inhibited potently and almost completely by β-BuTX. In one experiment, however, very low levels of β-BuTX-resistant ^{125}I-DTX binding were detected in the myelin-containing areas of the optic lobes and cerebellum (Section 4.3.3.1). As noted above, these sites were definitely not saturated; their densities have therefore not been measured accurately. Nonetheless it appears that the distribution of these β-BuTX-resistant sites in white matter regions may be similar to that of the β-BuTX-resistant sites studied in rat brain.

4.4.5. DTX Acceptors and K^+ Channels

As described in Section 1.4.3, DTX and its homologue toxin I have been shown to block selectively certain rapidly activating voltage dependent K^+ currents. It is not yet clear whether this blockade is due to a direct effect of the toxins on a K^+ channel protein, or whether it is elicited indirectly, for example via neuronal receptors involving a second messenger. However, the observations that the toxins are active at very low (nM) concentrations (Weller *et al.*, 1985; Benoit and Dubois, 1986; Stansfeld *et al.*, 1986; Penner *et al.*, 1986) and their ability to inhibit certain K^+ conductances within 30 s or a few minutes (Benoit and Dubois, 1986; Weller *et al.*, 1985; Penner *et al.*, 1986) in preparations offering unrestricted access of the toxin, suggest a direct action. In some systems, the effects of the toxins are reversible, although prolonged washing (for >1hr) may be required (Stansfeld *et al.*, 1987). Furthermore, DTX has been shown to affect a range of K^+ currents with different potencies, its efficacy in blocking K^+ fluxes being apparently related to the inactivation time of the particular K^+ current (see Section 1.4). Several DTX acceptor variants have been identified here in binding and autoradiography studies on cryostat sections, possibly corresponding to different

channels mediating various DTX-sensitive K^+ currents. If DTX acted through a second messenger system, a single acceptor population should conceivably suffice to mediate effects on several types of K^+ currents. Conclusive proof that DTX interacts directly with K^+ channels requires the purification of DTX acceptors, their reconstitution into artificial lipid vesicles, and electrophysiological studies on the reconstituted material, work which is now in progress in this laboratory.

The distribution of ^{125}I-DTX binding described here is compatible with a possible direct interaction of the toxin with K^+ channels or K^+ channel variants. Both β-BuTX and DTX share binding sites associated with synaptic regions (see also Section 3.5.4), which could represent K^+ channels involved in the regulation of synaptic potentials and neurotransmitter release. Furthermore, high levels of β-BuTX-resistant ^{125}I-DTX binding have been located in areas rich in myelinated fibres. This distribution is surprising in view of the reported absence of outward K^+ currents at the mammalian node of Ranvier (Chiu *et al.*, 1979; Brismar, 1980; Kocsis and Waxman, 1980). However, in developing neurones, or when the myelin around the node of Ranvier is disrupted (e.g. through stretching or enzyme treatment of the nerve fibres, or in demyelination diseases), delayed outward K^+ currents can be detected; it appears, therefore, that the K^+ channels in mammalian neurones are located at the internodes underneath the myelin sheath (Chiu and Ritchie, 1980, 1981; Bostock *et al.*, 1981). In adult neurones a tight seal between the myelin and axon membranes in the para-nodal region hinders electrophysiological studies, even preventing drugs such as 4-AP and TEA from reaching the channels (Chiu and Ritchie, 1981). The freeze/thaw cycle used here in the preparation of cryostat sections would, however, have disrupted this tight seal of the myelin insulation and made the hidden proteins accessible to probes such as ^{125}I-DTX. The distribution of DTX binding sites along white matter tracts is particularly interesting in view of recent evidence that, unlike squid giant axons, central and peripheral mammalian myelinated fibres primarily utilize a 4-AP sensitive K^+ channel and not the TEA-sensitive channel for repolarization of individual action potentials (Kocsis *et al.*, 1986, 1987). These 4-AP sensitive K^+ channels are particularly enriched at the internodes and are responsible for inhibiting bursts of action potentials at the nodes (Chiu and Ritchie, 1981; Baker *et al.*, 1987).

It appears that these channels, or acceptors closely linked to the functional channel proteins, have been localized here at loci inaccessible in fresh tissue preparations as used in electrophysiology experiments. The mammalian 4-AP-sensitive K^+ channels labelled by DTX thus appear similar to those mediating the DTX sensitive I_{Kf1} current at the frog node of Ranvier (Benoit and Dubois, 1986). The presence of the acceptors in a location normally inaccessible to neuromodulator ligands which might stimulate a second messenger system provides some further indirect support to the suggestion that DTX does not block K^+ currents via such a second messenger system, but interacts directly with a K^+ channel protein.

4.4.6. Distribution of Ion Channels in the Rat Central Nervous System

In view of the possible interaction of DTX and β-BuTX with K^+ channel variants, the distribution of their acceptors will now briefly be compared with the distribution of other channels which have so far been localized in the rat central nervous system.

Sodium channels have been mapped using tritated derivatives of tetrodotoxin (TTX; Mourre *et al.*, 1984) or batrachotoxin-A (Worley and Baraban, 1987). High densities of ^{3}H-TTX binding were located in the cerebral cortex, globus pallidus and substantia nigra, while lower levels of labelling were found in the caudate putamen and some thalamic nuclei. In the hippocampal formation, the stratum oriens, stratum radiatum and the hilus contained high, and the cell layers and the molecular layer of the dentate gyrus lower densities of Na^+ channels. In the cerebellum the Purkinje cells were intensely labelled, while the molecular layer presented high and the granule cell layer moderate levels of labelling. White matter tracts were unlabelled.

This distribution of Na^+ channels differs from, but overlaps with that of both β-BuTX and DTX acceptors, as might be expected from the opposing currents mediated by Na^+ and K^+ channels. In view of the prominent labelling of white matter tracts by DTX, and the involvement of Na^+ channels in action potential transmission, it is surprising that no ^{3}H-TTX or batrachotoxin binding was observed in these areas. Na^+ channels, being apparently concentrated only at the nodes of Ranvier, may be present at much lower overall levels than the DTX-sensitive K^+ channels, which seem to be enriched in the internodal regions (see

Section 4.4.4). Selective quenching of ^{3}H β-particles by white matter (Section 3.5.1) may further reduce the density of silver grains observed over white matter areas in experiments with these tritiated Na^{+} channel ligands

Calcium channels have been studied using a variety of ligands including [^{3}H]nitrendipine (Quirion, 1983; Gould *et al.*, 1985), dihydropyridine derivatives (Cortes *et al.*, 1984) and [^{3}H]desmethoxyverapamil (Ferry *et al.*, 1984). Binding sites for these Ca^{2+} channel antagonists were most abundant in the neocortex, amygdala and hippocampus, where the strata oriens and radiatum and, particularly, the molecular layer of the dentate gyrus were prominently labelled by all probes. It may be noted at this point that DTX reduced the current strength required to elicit Ca^{2+}-spikes in hippocampal slices (Halliwell *et al.*, 1986). A similar location of DTX binding/DTX-sensitive K^{+} channnels with Ca^{2+} channels in the hippocampus is in agreement with these electrophysiological observations. Low densities of Ca^{2+} antagonist binding were found in the cerebellum (Cortes *et al.*, 1984), with the granule cell layer being labelled more strongly than the molecular layer. White matter tracts were unlabelled or contained very low densities of Ca^{2+} antagonist binding sites.

Phencyclidine-sensitive potassium channels: The ketamine analogue phencyclidine (1-(1-phenyl-cyclohexyl)piperidine) and similar compounds may selectively block voltage-regulated slowly inactivating TEA-sensitive K^{+} channels distinct from the transient K^{+} channels mediating I_A and similar currents in rat brain synaptosomes (Bartschat and Blaustein, 1986). Binding sites for these drugs have been localized using [^{3}H]phencyclidine (Quirion *et al.*, 1981) or [^{3}H]thienylcyclopiperidine (TCP; Contreras *et al.*, 1986). Both compounds labelled the cerebral cortex, the synaptic layers of the hippocampus and dentate gyrus, and certain thalamic nuclei, while low levels of binding were observed in the cerebellum and brainstem. These distributions differ from those of both the DTX and β-BuTX acceptors studied here, as expected since different groups of K^{+} channels appear to be affected by these ligands.

Apamin receptors: The bee venom polypeptide apamin, which is believed to block one variety of Ca^{2+}-dependent K^{+} currents, binds saturably to rat brain cryostat sections with a B_{max} ≈15 fmol/mg protein (Mourre *et al.*, 1986); this density of binding sites is much lower than that of either ^{125}I-β-BuTX or ^{125}I-DTX (cf.

Chapter 2). Apamin labels certain brain nuclei very strongly, while areas rich in both β-BuTX and DTX acceptors are not always prominently labelled. In the cerebellum, for example, apamin labels approximately twice as many sites in the granule cell layer than in the molecular layer (Mourre *et al.*, 1986), whereas β-BuTX labels the molecular layer more strongly than the granule cell layer (Chapter 3). Furthermore, at low concentrations ^{125}I-DTX binds more strongly to the granule cell layer than the molecular layer, while higher concentrations produce greater labelling over the molecular layer than over the granule cells. This reciprocal distribution of the toxin acceptors is particularly interesting since the Ca^{2+}-dependent K^+ current blocked by apamin, and the transient K^+ currents inhibited by DTX, can serve similar roles in membrane repolarization and the control of excitability in neurones.

CHAPTER 5

A High Resolution Study of the Distribution of Acceptors for β-Bungarotoxin and Dendrotoxin

5.1. Introduction

The previous two Chapters have demonstrated a widespread occurrence of the acceptors for β-BuTX and DTX in the rat and chick central nervous systems. Both types of toxin acceptors were enriched in synaptic regions, while DTX acceptors were also found along myelinated fibre tracts. To investigate in greater detail the distribution of these acceptors on neurones or glial cells, and to study their ultrastructural location (e.g. whether they are found on synapses, axons, dendrites or on the cell soma) higher resolution localization methods are required. Thus, electron microscope autoradiography studies of ^{125}I-β-BuTX and ^{125}I-DTX binding have been attempted here.

5.1.1. Electron Microscope Autoradiography

High resolution autoradiography methods have been reviewed by Salpeter and Bachman (1972). Briefly, a tissue sample containing a radiolabelled tracer is embedded in plastic resin, and ultrathin sections are cut and mounted on microscope slides which have previously been coated with a thin plastic membrane. Reproducible emulsion layers can be placed over the sections by dipping the slides into liquid emulsion. On exposure, latent images are formed in those silver halide crystals of the emulsion which are hit directly by radiation (usually β-particles or

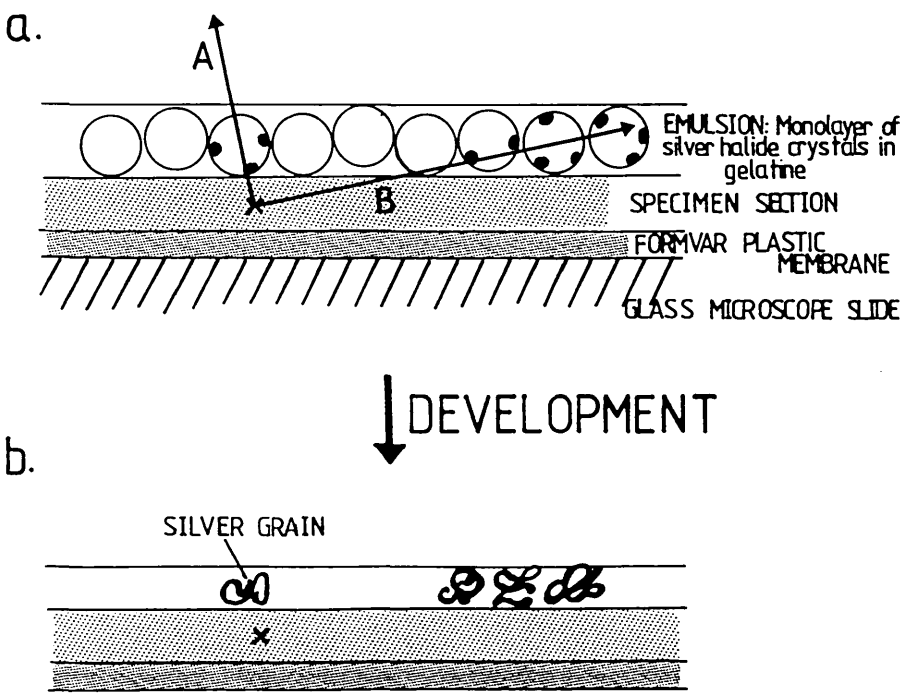
electrons) emitted from the specimen. After exposure these latent images are developed to form silver grains, the plastic membrane carrying the sections and emulsion is stripped from the slides and the sections are mounted on copper grids for observation in the electron microscope.

5.1.1.1. *Resolution of electron microscope autoradiography*

The method described above results in a section/emulsion geometry as shown in Figure 5.1. It is clear that the developed silver grains do not always lie directly over the source of radioactivity. The amount of scatter (i.e. the distance of a silver grain from the source of radiation) depends on the following: (i) the thicknesses of the section and emulsion (Salpeter *et al.*, 1969; Salpeter and Salpeter, 1971); (ii) the type of emulsion and development procedures employed (Salpeter *et al.*, 1979; Salpeter and McHenry, 1972); (iii) heavy metal staining of the sections

---

Figure 5.1. Specimen-emulsion geometry in electron microscope autoradiography



(a) Diagram of a cross-section of an ultrathin specimen section during exposure for autoradiography. A radioactive nuclide at x can emit a radioactive particle (β-particle or electron) in any direction. Particles such as A or B will produce latent images (●) in the silver halide crystals of the emulsion.
(b) On development, the latent images nucleate silver grains.

(Salpeter *et al.*, 1977), and, in particular, (iv) the radioisotope studied (Salpeter *et al.*, 1977; 1978; Blackett *et al.*, 1980), which determines the energy of the β-particles or electrons emitted. Low energy particles (e.g. ^{3}H-β-particles, E_{max} =18.6 keV) have a short range in the section and emulsion, and are efficient in producing latent images, while electrons of higher energy can travel further from the radiation source and are less likely to create latent images directly above the source.

Since so many factors affect the resolution, each experimental system for electron microscope autoradiography should be calibrated directly. This is done by studying the silver grain distribution over sections containing a radioactive line source (Salpeter *et al.*, 1969; 1977; Blackett and Parry, 1977). From the scatter of silver grains about the line, the half distance (HD, the perpendicular distance from the line within which 50% of all silver grains are found) can be estimated. When this value is inserted into the density probability equation, which describes the likelihood of a silver grain being formed at a defined distance from a point source (Blackett *et al.*, 1980), the half radius (HR, i.e. the radius of a circle about a point source of radioactivity, which has a 50% probability of containing the resulting silver grain) can be calculated.

5.1.1.2. *Iodine-125 as a tracer in electron microscope autoradiography*

Iodine-125 decays by electon capture, emitting (per 100 nuclear decays) 128 low energy electrons (2.77-3.6 keV) and 36 high energy electons (22-34 keV) in addition to photons (x- and γ-rays of 25-35 keV, Atkins, 1969). Due to the large number of low energy electons, autoradiography with ^{125}I has a high resolution (Fertuck and Salpeter, 1976), similar to that obtainable using ^{3}H as a tracer. The effect of the high energy electrons is unclear. Fertuck and Salpeter (1976) and Salpeter *et al.* (1977) suggest that the high energy electrons do not contribute significantly to grain numbers in electron microscope autoradiography and quote an HD of 80-90 nm for ^{125}I-autoradiography with Ilford L4 emulsion. In contrast Blackett *et al.* (1980) report that the high energy electrons do give rise to some silver grains, especially if they pass through the emulsion at shallow angles (as electron B in Figure 5.1), when they can produce multiple grains. This reduces the overall resolu-

tion obtainable with ^{125}I (HD =130 nm with Ilford L4 emulsion, Blackett and Parry, 1977; Blackett *et al.*, 1980).

5.1.1.3. *Analysis of autoradiograms*

Although radioactive decay and the production of autoradiographic silver grains are random processes, and the position of the radionucleus which produced a particular silver grain can never be identified, it is possible to relate silver grains to sources in the tissue by various statistical methods (see e.g. Williams, 1969; Salpeter and McHenry, 1972; Blackett and Parry, 1977; Salpeter *et al.*, 1978). In the simplest analysis, silver grains are scored into groups according to the tissue structure identified beneath the grain centre (the centre of the smallest circle which completely circumscribes the grain). Random points (e.g. intersection points on a square lattice overlay) are scored likewise and will give an indication of the area occupied by each structure. Grain densities (grains per unit area) can thus be calculated for various tissue elements of interest. In "relative density analysis", a related method, the percentage of grains and points over each structure is calculated and the ratio $\frac{\%\text{ of grains}}{\%\text{ of points}}$ is determined. A ratio greater than 1 for a particular structure indicates that the structure is selectively labelled, a ratio =1 suggests random labelling, while a ratio less than 1 implies it is unlabelled.

These simple grain density analysis methods do not take into account the scatter of grains described earlier (see Figure 5.1). Such "cross-fire" will cause an underestimate of the grain densities over small structures. Simple grain density analysis is, therefore, not suitable for high resolution work. For this reason "probability circle" analysis methods were introduced by Williams (1969). Here, silver grains are scored into classes depending on the tissue structures within a circle drawn about the grain centre. The size of the circle is calculated from the density probability equation (Section 5.1.1.1) so that it has a 50% probability of containing the source of the radiation which produced the grain (this is, in fact, =HR). Random points may be studied likewise. Probability circle grain density or relative density analysis is then possible.

More sophisticated analysis methods have also been described. In some situations where the radioactive labelling is suspec-

ted to be restricted to a single type of tissue element or organelle, the distribution of silver grains about that organelle may be compared to published theoretical grain distributions (Salpeter *et al.*, 1969; Downs and Williams, 1984). More complex situations may be analysed using the hypothetical grain analysis methods described by Blackett and Parry (1977) and Salpeter *et al.* (1978).

5.1.2. Study of the Distribution of Acceptors for β-BuTX and DTX

In the present Chapter, fresh slices from rat or chick brain were incubated with ^{125}I-β-BuTX or ^{125}I-DTX and processed for electron microscope autoradiography. Preliminary studies indicated the most suitable tissue slices and incubation protocols. The autoradiography system was characterized using a radioactive line source. The distribution of β-BuTX acceptors in chick cerebellum, and of DTX acceptors in chick and rat cerebellum and in rat hippocampus were then studied using a probability circle/relative density analysis method.

5.2. Materials

DTX and β-BuTX, and ^{125}I-DTX and ^{125}I-β-BuTX were as in Chapter 2 (Section 2.2). Most ^{125}I-DTX preparations used in the electron microscope localization studies had specific radioactivities of 250-300 Ci/mmol, while the ^{125}I-β-BuTX preparation had been labelled to ≃1,000 Ci/mmol using the chloramine-T method. Formaldehyde stock solutions were freshly prepared from solid paraformaldehyde as described in Section 2.3.2. Glutaraldehyde, osmium tetroxide, uranyl acetate, sodium cacodylate, monomeric Spurr's resin components, formvar and supplies for electron microscopy were purchased from Polaron, Watford, Hertfordshire, L4 liquid emulsion from Ilford Ltd, Cheshire, and D19 developer from Kodak, Hertfordshire. All other chemicals were from Sigma and BDH, Poole, Dorset.

5.3. Methods

5.3.1. Preparation of Brain Slices

Surface and second slices were cut manually from rat or chick cerebellum as described by Garthwaite *et al.* (1979). The cerebellum was dissected, rat cerebella were bisected mid-sagittally and mounted on the cut surfaces; thick slices (400μm) were then cut

using a bow cutter with a Gilette Techmatic cutting ribbon and a glass guide (for details see McIlwain, 1975). Rat hippocampal slices were prepared by chopping hippocampus perpendicularly to the septo-temporal axis at 400 µm intervals using a McIlwain tissue chopper (McIlwain, 1975).

5.3.2. Incubation of Brain Slices with Radiolabelled Toxins

Brain slices were transferred into 1 ml of Krebs-Henseleit bicarbonate Ringer (118 mM NaCl, 4.7 mM KCl, 1.18 mM KH_2PO_4, 1.19 mM $MgSO_4$, 2.5 mM $CaCl_2$, 25 mM $NaHCO_3$ and 11 mM D-glucose, sparged with 95% O_2/5% CO_2 gas and adjusted to pH 7.4) containing 1-2 mg/ml BSA and (for control conditions only) 5-10 µM of the appropriate unlabelled toxin. Slices were pre-incubated for 30 min at 37°C, with occasional agitation, under a constant stream of 95% O_2/5% CO_2 gas over the Ringer medium. After the pre-incubation, concentrated radioiodinated toxin solution was added to the required final concentration (5-30 nM) and mixed into the bathing solution with gentle swirling. Duplicate aliquots (10 µl) were immediately withdrawn to determine the actual concentration of radiolabelled toxin. Incubation was for 1 hr as above (37°C, gassing and occasional agitation). The incubation medium was then drained from the slices which were washed 5-6 times over 30 min in gassed Ringer at 37°C. The final washes contained negligible amounts of radioactivity.

5.3.3. Fixation and Embedding of Brain Slices

Toxin-labelled brain slices were fixed for 1 hr at ≈22°C in 2.5% glutaraldehyde, 4% para-formaldehyde in 0.1 M sodium phosphate buffer (pH 7.4) and washed twice in the phosphate buffer and twice in 0.1 M sodium cacodylate buffer (pH 7.4). The slices were post-fixed overnight in 0.5-1% osmium tetroxide in 0.1 M cacodylate buffer. Tissue slices were then dehydrated through 25%, 50% and 75% aqueous ethanol and two changes of absolute alcohol, and infiltrated with soft Spurr's resin (Spurr, 1969, medium C) using a series of resin/ethanol mixtures (25% resin in absolute alcohol: 1 hr; 50% resin: 1 hr; 75% resin: 1-2 hrs; two changes of 100% resin: 2 hrs). The resin was polymerized for 8 hrs at 70°C.

5.3.4. Sectioning

Resin-embedded tissue was sectioned on an LKB Ultrotome 3

using glass knives. The brain slices were usually sectioned perpendicular to their surface so that any uneven penetration of the labelled toxins into the tissue could be detected. Some hippocampus slices were sectioned parallel to the slice surface. Initial semithin sections (1 µm) were stained in 0.1% toluidine blue in 1% Borax. When a sufficiently large cross-section of tissue was found, sections were cut for autoradiography. For electron microscopy, ultrathin sections with pale gold interference colours (90-110 nm thick, Salpeter and Bachman, 1964) were placed onto slides which had been coated with a formvar film (silver interference colour, prepared by immersing slides into a solution of 1.5% formvar in chloroform using a custom-built dipping device). Test and control sections from several blocks were placed in adjacent positions on each slide. For light microscopy, semithin (1 µm) survey sections were dried onto acid-cleaned glass slides.

5.3.5. Autoradiography

5.3.5.1. *Exposure: Coating sections with Ilford L4 emulsion*

In the dark, 10 g of Ilford L4 emulsion were melted in 20 ml distilled water (15 min at 43°C). The emulsion was transferred to a custom-built semi-automatic coating machine and allowed to equilibrate to dipping temperature (33°C). Initially, emulsion layers were prepared on empty formvar-coated glass slides by adjusting the speed at which slides were withdrawn from the liquid emulsion. When even "dark purple" emulsion layers (150 nm thick, Salpeter and Bachman, 1964) were obtained, slides with the sections for electron microscopy were also dipped. The emulsion was gelled immediately by placing the slides on ice-cooled tiles. Slides containing 1 µm thick survey sections were dipped manually in the same Ilford L4 emulsion, gelled as above and dried; in this way emulsion layers with red-green interference colours were produced, which are estimated to be at least 0.2 µm thick (Salpeter and Bachman, 1964). All emulsion-coated slides were dried slowly at ≈22°C (ambient humidity ≈50%) for ≈2 hrs and then more thoroughly over silica gel, before being exposed at 4°C for the required period (up to 4 months).

5.3.5.2. *Development*

Slides containing sections for electron microscopy were brought to room temperature (≈22°C) and developed individually in

fresh full-strength Kodak D19 developer at 20°C for 2 min. Development was stopped by immersion in 1% acetic acid (30s) followed by a wash in distilled water (30s). Undeveloped silver halide was then removed by immersion in 25% sodium thiosulphate fixative for 4 min, before the slides were washed extensively in distilled water (6 x 5 min). The formvar film carrying the sections was stripped from the slides onto distilled water, copper grids (usually G200 high transmission) were dropped over the sections, and the film was recovered using a piece of parafilm.

For light microscope autoradiography, slides were warmed to room temperature and developed 4 min in Kodak D19 developer at 18°C. Development was stopped by immersion in 1% acetic acid (1 min), the emulsion was hardened in 3% potassium chrome alum and 6% sodium sulphate (3 min) and fixed 4 min in 25% sodium thiosulphate. After 3 x 5 min washes in distilled water, slides were dried thoroughly over silica gel, and mounted with DPX mounting medium.

5.3.6. Electon Microscope Observations

Grids containing autoradiography sections were rinsed in methanol before the sections were stained in 12% methanolic uranyl acetate for 30-45 min, washed thoroughly in methanol and distilled water and dried. All observations were made using a Hitachi H-600 electron microscope, usually with an accelerating voltage of 75 kV.

5.3.7. Preparation of ^{125}I-Labelled Radioactive Line Sources for Resolution Studies

Thick (1-2 mm) slices of rat forebrain were dissected manually, fixed in 2.5% glutaraldehyde, 4% formaldehyde in 0.1 M sodium phosphate buffer pH 7.4 for 1 hr and washed, post-fixed in osmium tetroxide, dehydrated and embedded in Spurr's resin as described above (Section 5.3.3). Using a glass knife on the ultramicrotome an even smooth surface was exposed on the tissue blocks, A drop of concentrated ^{125}I-DTX (25µl of 30 nM ^{125}I-DTX , ≈500 Ci/mmol, in phosphate buffer, pH 7.4) was placed on this smoothed surface for 5 min. As the basic ^{125}I-DTX molecules are very sticky in this buffer, a proportion of the toxin adhered non-specifically to the plastic. Excess ^{125}I-DTX was drained from the blocks, which were then air-dried. The ^{125}I-DTX was fixed by exposure to formaldehyde vapour at 70°C for 2 hrs. After fixation, the blocks were washed thoroughly in several changes of water and later in methanol

until no more radioactive material was removed, dried and embedded in fresh Spurr's resin.

Sections were cut from these blocks at a right angle to the ^{125}I-DTX-labelled tissue slice surface, so that the sections contained a thin line of ^{125}I-DTX bordered on one side by osmicated brain tissue and on the other by clear resin. This arrangement allows the effect of osmication on resolution to be studied. When such sections were stained in uranyl acetate (Section 5.3.6), the radiolabelled protein line was visible in the electron microscope and appeared to have a thickness of 50 nm. Ultrathin sections were processed for electron microscope autoradiography as described above (Section 5.3.5).

5.3.8. Analysis of Silver Grain Distributions

5.3.8.1. *Random sampling of tissue by photography*

For analysis of silver grain distributions, photographs were taken at a nominal magnification of 6,000× on the electron microscope (actual magnification of the negatives =6,110×, as calibrated using a cross-spaced grating replica with 2,160 lines/mm, Polaron). An initial photograph was taken of a well preserved area in a defined cell layer or synaptic region on the section. Two or three adjacent frames were then also photographed, regardless of the appearance or preservation of the tissue or the silver grain densities. This method allows unbiased photographic sampling of identified tissue areas. Photographs were printed from the negatives at a final magnification of 17,500×. At this magnification, a 50% probability circle (HR =175 nm, see Section 5.4.2) has a radius of 3 mm.

5.3.8.2. *Analysis of silver grain distributions*

Silver grain distributions were analysed using an adaptation of the probability circle method of Williams (1969). Grain centres were identified using an overlay mask of concentric circles, and marked with a needle. A mask showing a 50% probability circle (3 mm radius, Section 5.3.8.1) was placed over each grain centre and the underlying tissue structures were listed. A large number of silver grains was found over plasma membrane structures; therefore the 50% probability circles placed over these grains frequently contained more than one tissue element. For example, the 50% probability circle around a grain on the active

zone of a synapse may contain parts of both the presynaptic bouton and the postsynaptic dendrite. Grains were then divided into classes according to the contents of the 50% probability circle about the grain centre. To avoid the creation of excessive numbers of shared grain classes (since most grains were found over plasma membrane) shared grains were scored twice; for example, the hypothetical grain described above would be added to both the synaptic bouton and the dendrite class.

The photographs were also studied using overlay masks ruled with a regular 2 or 2.5 cm square grid, and grid intersection points were analysed with the 50% probability circle mask in the same way as the grain centres. The number of points collected was at least 3 times the number of grains, and all photographs used in the grain analysis were also used to collect points. From the grain and point distribution data, relative density values were calculated (see Section 5.1.1.3).

5.4. Results

5.4.1. Preliminary Studies to Define a Suitable Tissue Preparation for Localization Experiments

Fresh rat brain slices from hippocampus or the cerebellum were labelled *in vitro* with ^{125}I-β-BuTX or ^{125}I-DTX and processed for electron microscope autoradiography. Preliminary studies with such preparations indicated that the tissue was poorly preserved, especially at the chopped or cut surfaces of the slices. Furthermore cell bodies, particularly those of the granule cells of the cerebellum, were frequently pyknotic, while synaptic fields were usually reasonably well preserved (see also Garthwaite *et al.*, 1979; 1980). The tissue was probably damaged through suffering anoxia during the dissection and slice preparation procedures as well as in the small incubation volume (1 ml, cf. Garthwaite *et al.*, 1979) necessary to achieve high enough concentrations of the toxins. The preservation was also poorer in slices incubated with β-BuTX, probably due to the phospholipase activity of this toxin. As reported by Garthwaite *et al.* (1980), slices from young rat cerebellum (up to two weeks old) were more resistant to anoxia and showed better preservation. Similarly slices from 1-day-old chick cerebellum showed reasonably good preservation after the standard incubation procedure.

The preliminary studies also demonstrated that the toxins penetrated incompletely into the slices. In rat cerebellum slices incubated in 10 nM ^{125}I-β-BuTX, labelling was observed only within 30 μm of the cut surfaces; 10 nM ^{125}I-DTX appeared to penetrate further (to a depth of ≃150 μm). Hippocampal or cerebellar slices treated with 30 nM ^{125}I-DTX were labelled to a depth of 180-210 μm. The differences in the penetration of these two toxins suggest that molecular size is one factor restricting access. Furthermore, the penetration of the toxins into the slices may be greatly delayed through binding to the acceptors, which are highly enriched there (values of ≃0.5 pmol of ^{125}I-DTX binding/mg of protein on cryostat sections, see Chapter 2, represent close to μM concentrations in the membrane area bathed by the extracellular fluid, assuming a protein content of 5% of the wet tissue weight and 5-10% extracellular space). The role of toxin depletion was further supported by the observation that on control slices, incubated in an excess of unlabelled toxin, low but more uniform grain distributions were found. Studies on young chick cerebellum slices, in contrast, showed that both toxins were able to penetrate evenly through the slices. This may be due to the larger extracellular spaces in the developing tissue (Levi and Lattes, 1970; see also del Cerro *et al.*, 1968), as well as a lower acceptor site content (cf. Chapters 3 and 4).

1-Day-old chick cerebellar slices, which have been shown to contain acceptors for both β-BuTX and DTX (Chapters 3 and 4), thus appeared to be the most suitable preparation for high resolution autoradiography studies; both ^{125}I-β-BuTX and ^{125}I-DTX binding have therefore been examined in this tissue. The distribution of DTX acceptors was also studied on rat cerebellum and hippocampus, using tissue from both 14-day-old and adult animals.

5.4.2. Resolution of the Electron Microscope Autoradiographic Method

This was measured using radioactive line specimens (Section 5.3.7). As in all other electron microscope autoradiography experiments pale gold sections, 100-110 nm thick (measured directly from folds in the sections, Small, 1968), were exposed to a monolayer of Ilford L4 emulsion for 7 days and then developed in Kodak D19 developer (Section 5.3.5). The average background labelling observed on these sections was 0.09 grains/100 μm², but the grain

density increased significantly over the interface between tissue and resin (Figure 5.2a). A study of a montage prepared from photographs of an entire grid square on one section indicated that grains were scattered about the radioactive line for several μm. Hence a cut-off distance of 5 μm was chosen for the analysis.

Photographs from seven sections taken from two different resin blocks were printed at 20,000× magnification. The perpendicular distance from the centre of each of 1002 grains to the tissue/resin interface was measured, and a grain distribution histogram was constructed (Figure 5.2b). The grain distribution was approximately symmetrical about the ^{125}I-labelled line, indicating that osmication of the tissue did not significantly affect the scatter of the grains. Grains were therefore added from both sides of the ^{125}I-labelled line to give the normalized cumulative grain distibution shown in Figure 5.2c. From this curve the HD for ^{125}I was found to be 105 nm. Figure 5.2c also shows the theoretical grain distribution curves for a ^{125}I line source according to Salpeter *et al.* (1977) and Blackett *et al.* (1980), both adjusted for the HD of 105 nm (see also Section 5.1.1.2). The experimental curve derived here appeared to fit closely with the curve of Blackett *et al.* (1980), indicating that the high energy electrons do affect the resolution (cf. Section 5.1.1.2). The probability distributions for a ^{125}I-point source in this autoradiography system were therefore calculated according to the equations given in Blackett *et al.* (1980), using HD =105 nm, and are shown in Figure 5.2d. From these curves the radius of a 50% probability circle in my autoradiography system (HR) is 175 nm.

5.4.3. Localization of ß-BuTX Acceptors in Chick Cerebellum

Horizontally cut first and second slices from 1-day-old chick cerebellum were labelled with 5.5 nM ^{125}I-ß-BuTX, control slices being treated in addition with 5 μM ß-BuTX. To study the effect of the phospholipase activity of the toxin, some slices were incubated in Ca^{2+}-containing buffer, while others were labelled in a Ringer in which Ca^{2+} had been replaced with 2.5 mM Sr^{2+} in the presence of 1 mM EGTA. After fixation and embedding of the slices, semithin survey sections and ultrathin sections were processed for light and electron microscope autoradiography.

Figure 5.2. Distribution of silver grains about a ^{125}I-labelled radioactive line source

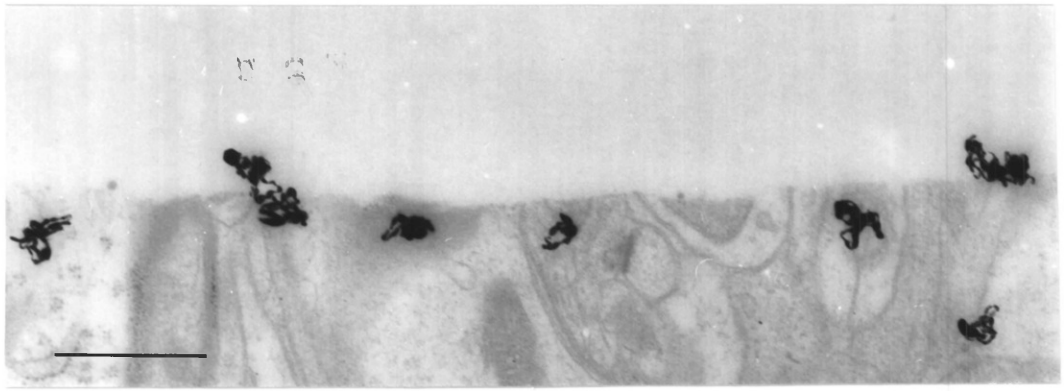
(a) A sample electron microscope autoradiogram of the ^{125}I-DTX labelled line source. Magnification: 20,000×. Scale bar =1 μm

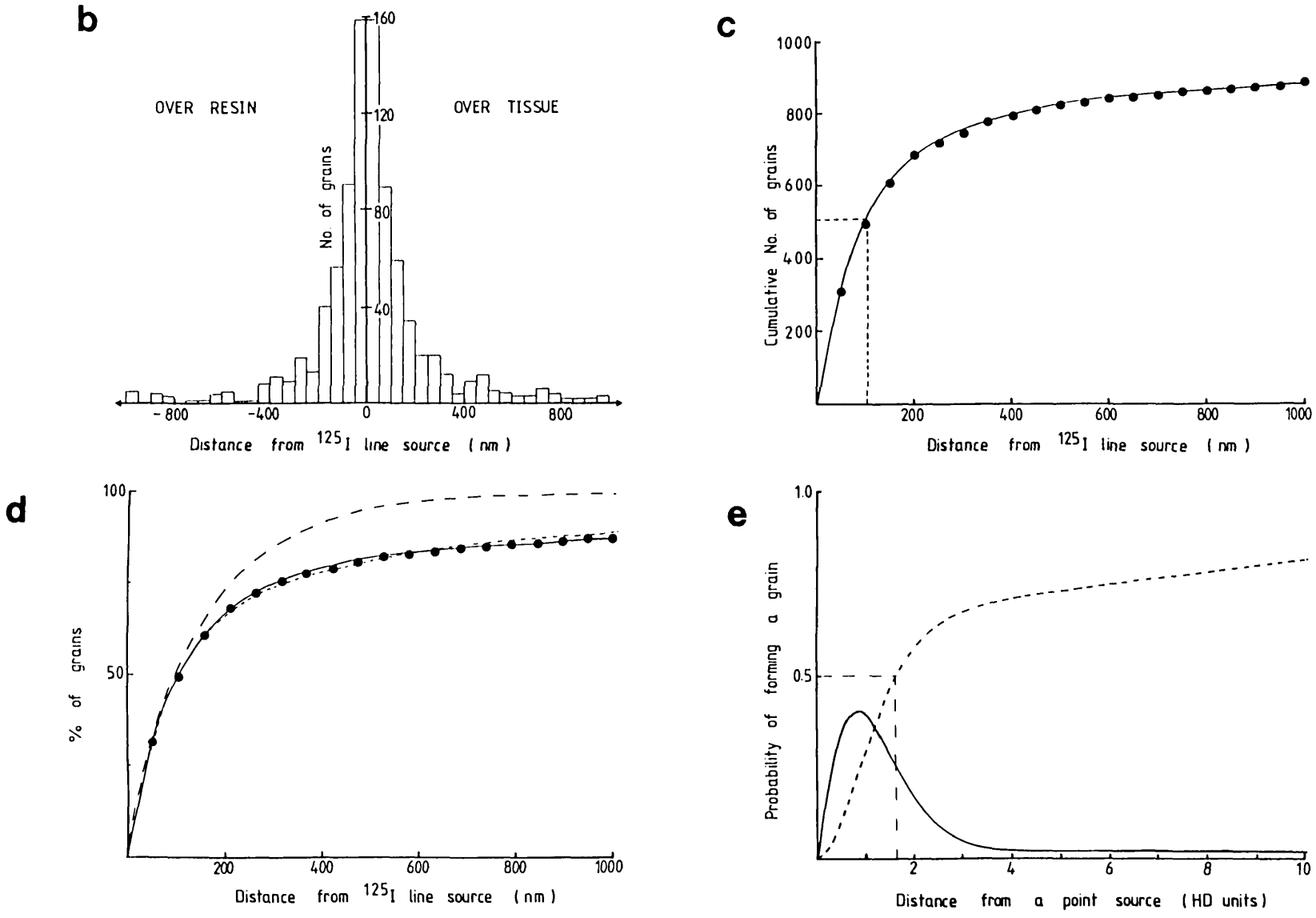
(b) Experimental grain density histogram for grains within 1 μm of the labelled line (88.2% of all grains counted). Negative distances are for grains over clear resin, positive distances for grains over osmicated tissue.

(c) The cumulative grain distribution about the line source. The grains (from b, both sides) were added consecutively with increasing distance from the line source. Only the first 1 μm (88.2% of grains) is shown. Half of the total number of grains (1002) are found within 105 nm of the line.

(d) The cumulative grain distribution, re-plotted from (c) as % of grains found with distance from the line (●—●—●). For comparison, the theoretical grain distribution for a ^{125}I line source according to Salpeter *et al.* (1977) (— —) and according to Blackett *et al.* (1980) (·····), both adjusted for a HD of 105 nm, are also shown.

(e) The probability function for the grain distribution about a point source, p, where $p = \frac{4.17x}{(x^2 + 2.25)^{1.5}} - \frac{28.82x}{(8.526 + x^2)^2}$ (from Blackett *et al.*, 1980; x is the distance from the point source in units of HD) was calculated and is shown as (———). The cumulative probability distribution, derived by integrating the equation above, is given as (– – – →). From this curve, the radius of a 50% probability circle (HR) is =1.67 HD, or 175 nm.




b
OVER RESIN
OVER TISSUE
No. of grains
160
120
80
40
-800
-400
0
400
800
Distance from 125I line source (nm)
c
Cumulative No. of grains
1000
800
600
400
200
200
400
600
800
1000
Distance from 125I line source (nm)
d
% of grains
100
50
200
400
600
800
1000
Distance from 125I line source (nm)
e
Probability of forming a grain
1.0
0.5
2
4
6
8
10
Distance from a point source (HD units)

5.4.3.1. *Light microscope autoradiography of semithin survey sections*

As in the Ultrofilm autoradiography experiments described in Chapter 3 (Section 3.4.5), the highest grain densities on semithin plastic survey sections were observed over the molecular layer of the cerebellum slices (Figure 5.3a,b). In addition, there was a distinct gradient of grain density over the molecular layer, the highest numbers of silver grains being found near the Purkinje cell layer and very few grains visible near the cerebellar surface. The external granule cell layer was unlabelled. Some Purkinje cells were also very strongly labelled; however, many well preseved Purkinje cells remained unlabelled (Figure 5.3a,b). Low levels of silver grains were found over the granule cell layer, while fairly high grain densities were observed over regions rich in myelinated axons. Control sections treated with excess unlabelled β-BuTX contained very low numbers of silver grains (Figure 5.3c,d), except that fairly high grain densities were observed over white matter bundles (not shown), suggesting that the labelling of white matter is due to non-specific binding of the ^{125}I-β-BuTX (see also Section 5.4.3.4).

A similar distribution of silver grains was observed over survey sections prepared from tissue slices incubated in Sr^{2+}-containing Krebs Ringer. However, control sections labelled in this buffer showed higher densities of silver grains (Figure 5.3e,f); in particular, there were more silver grains over the granule cell layer than over the molecular layer. This is similar to the high levels of non-specific binding on granule cells observed on chick cerebellum cryostat sections (cf. Figure 3.11e).

5.4.3.2. *Electron microscope autoradiography of ^{125}I-β-BuTX binding in chick cerebellum*

Most of the results described here are from cerebellar slices labelled with ^{125}I-β-BuTX in normal Ca^{2+}-containing Krebs Ringer. Sections from such slices showed an acceptably good preservation, although some tissue elements were shrunken, occasionally leaving large intercellular spaces. After autoradiography many silver grains were observed over the molecular layer. A large proportion of these grains appeared to be located over or close to vesicle-filled presynaptic boutons. For example, of the seven silver grains visible in Figure 5.4 five are close to synaptic

Figure 5.3. Survey of ^{125}I-ß-BuTX binding on chick cerebellum slices

Phase contrast (a, c, and e) and darkfield (b, d, and f) images of 1 µm thick survey section autoradiograms from 1-day-old chick cerebellum slices labelled in 5 nM ^{125}I-ß-BuTX alone (test condition, a and b) or in the presence of 5 µM unlabelled ß-BuTX (controls, c-f). In test slices (a and b) labelled with ^{125}I-ß-BuTX in Ca^{2+}-containing buffer, high grain densities are observed over the molecular layer (M), and lower grain densities over the granule cell layer (G). One poorly preserved Purkinje cell (identified by the arrowhead) is strongly labelled, while well preserved Purkinje cells (P) remain unlabelled. When the experiment was repeated in Ca^{2+}-free Sr^{2+} buffer, an identical labelling pattern was observed (not shown). A control slice incubated in Ca^{2+}-containing buffer (c and d) contains very low grain densities, while a control slice labelled in Sr^{2+}-containing buffer (e and f) exhibits higher labelling over the granule cell layer (G) than over the molecular layer (M), poorly preserved Purkinje cells (arrowheads) being weakly labelled. Magnification =400×. Scale bar (in e) =20 µm.

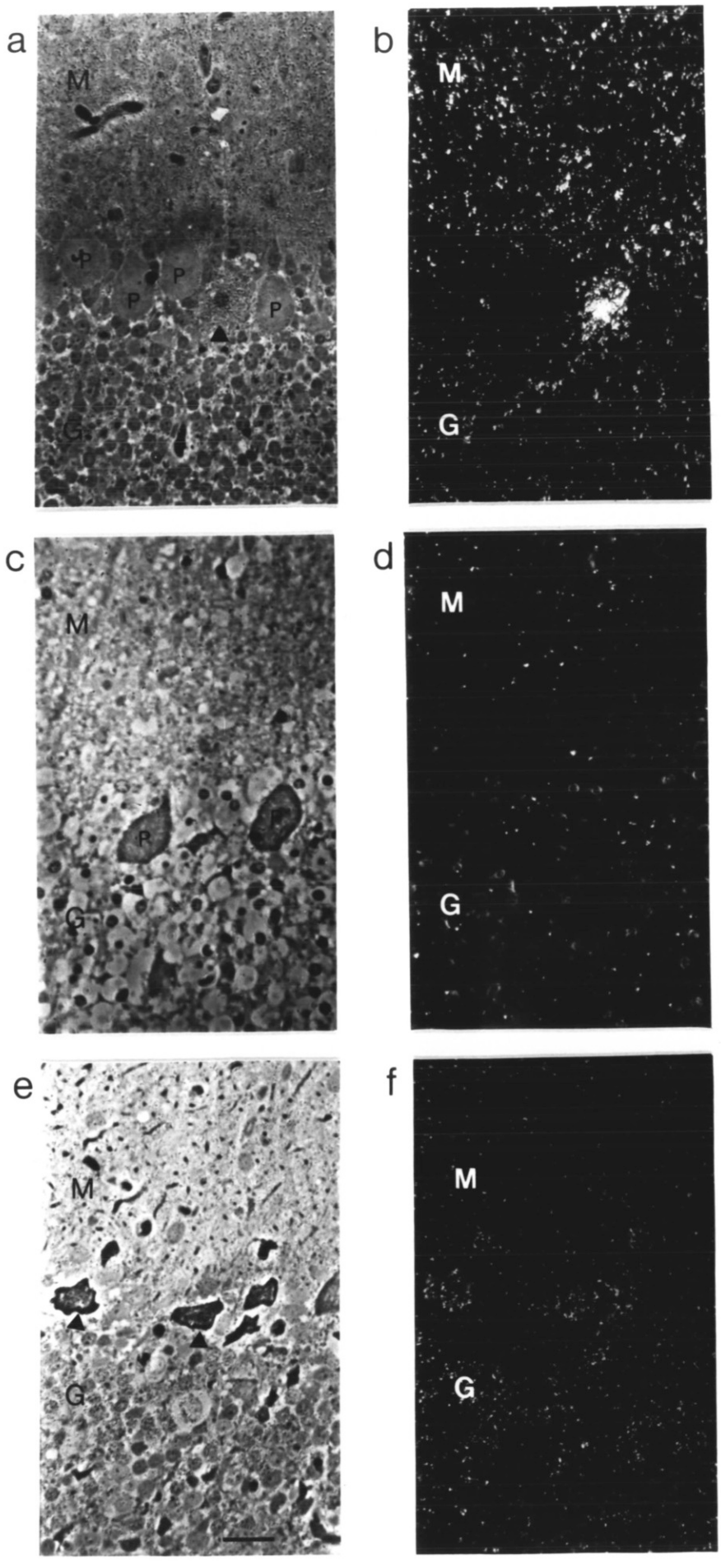
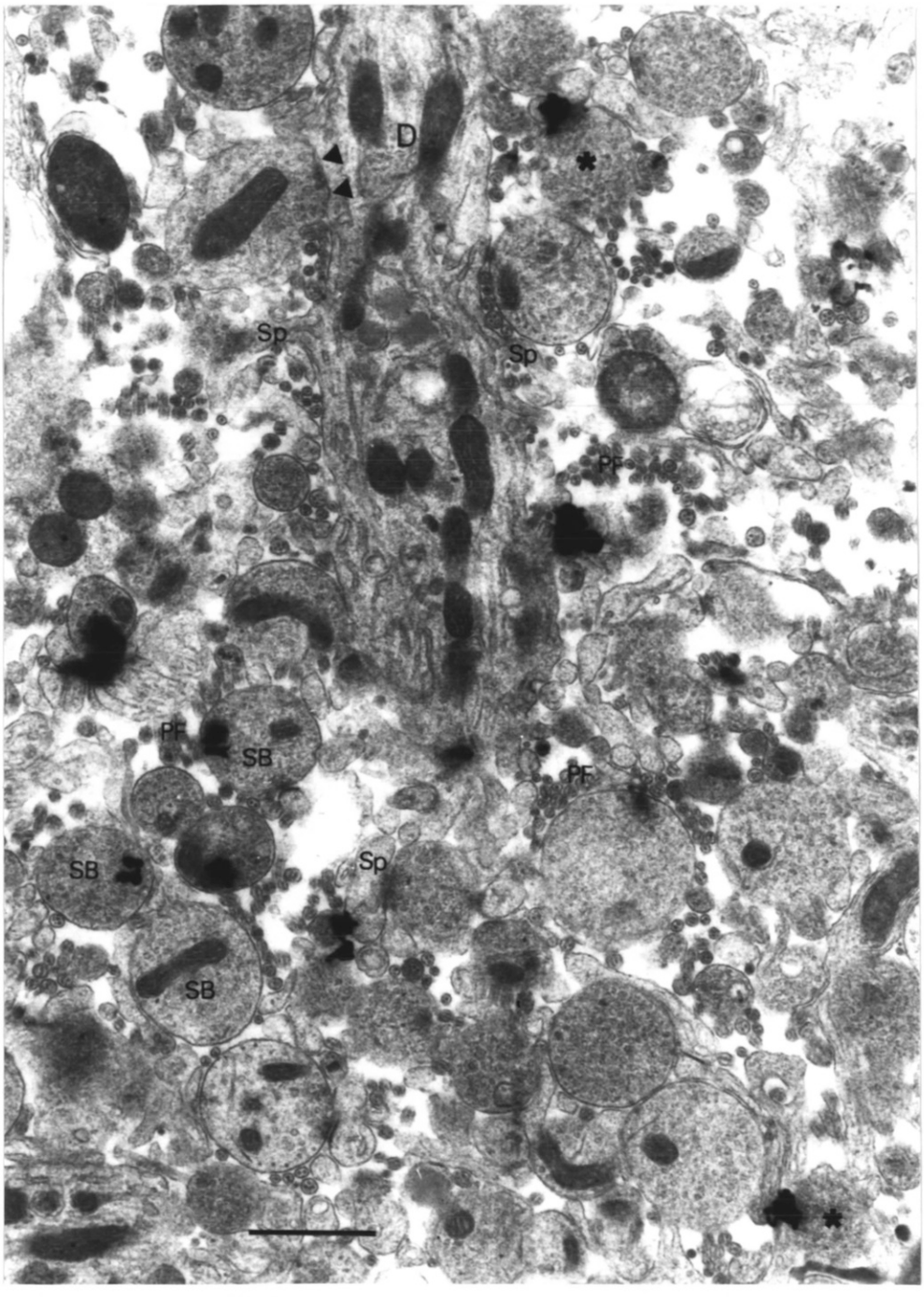

a
M
P
P
P
P
G
b
M
G
c
M
P
P
G
d
M
G
e
M
G
f
M
G

Figure 5.4. Localization of ^{125}I-β-BuTX binding in chick cerebellum molecular layer



Cerebellar slices from 1-day-old chick brain were incubated in 5 nM ^{125}I-β-BuTX (1000 Ci/mmol) in Ca^{2+}-containing Krebs Ringer, processed for electron microscope autoradiography and exposed for 120 days. The figure shows an area of the molecular layer. A Purkinje cell dendrite (D) rises through the upper half of the field of view. Groups of unmyelinated parallel fibre (PF) axons of granule cells, cut transversely in this section, swell to form synaptic boutons (SB), which synapse onto spines (Sp) protruding from the Purkinje cell dendrite. A basket cell nerve ending synapses directly with the Purkinje cell dendrite (arrowheads). Of the seven silver grains visible in this micrograph, five are close to synaptic bouton plasma membranes, although the membranes of the two boutons marked * are cut at very shallow angles and are therefore indistinct. Magnification =17,500×. Scale bar =1 μm.

boutons. Labelled synaptic boutons are also shown at higher magnification in Figure 5.5a and b. In addition high densities of silver grains were observed over membrane fragments and mitochondria of swollen and burst Purkinje cells in the the lower molecular layer (Figure 5.5c).

The tissue on control sections from slices treated with ^{125}I-β-BuTX and a large excess of unlabelled β-BuTX was completely disrupted by the phospholipase activity of the toxin, so that few structures other than cell nuclei could be identified (Figure 5.5d). As on the semithin survey section autoradiograms (Section 5.4.3.1), very few silver grains were found on these sections, presumably because unbound ^{125}I-β-BuTX can be efficiently washed out of the very disrupted tissue. These slices may not, therefore, be valid controls for the test section autoradiograms. Sections from slices labelled with ^{125}I-β-BuTX in Sr^{2+} Ringer, in which the phospholipase activity of the toxin is largely inhibited, showed a similar preservation to the Ca^{2+} test sections described above after incubation both in the presence or absence of an excess of unlabelled toxin (Figure 5.6). Silver grains on the test sections were again most abundant over the molecular layer, and were frequently found close to synaptic boutons (Figure 5.6a). Estimates of grain densities over the molecular layer suggested that the corresponding control sections contained only 30% of the number of silver grains observed on the test sections. The few grains on the control sections appeared to be randomly distributed (Figure 5.6b). By analogy with these results from studies in Sr^{2+} buffer, many of the silver grains on Ca^{2+} test section autoradiograms probably also represent specific ^{125}I-β-BuTX binding. Hence, the distribution of silver grains on Ca^{2+} test sections was studied in detail.

5.4.3.3. *Analysis of the distribution of ^{125}I-β-BuTX binding in the molecular layer of chick cerebellum*

Fifty photographs of the lower molecular layer taken from four sections cut from different brain slices, covering an area of ≈8,500 μm² and showing 701 silver grains (grain density ≈8.3 grains/100 μm², after 120 days exposure), were printed to a magnification of 17,500× and analysed as in Section 5.3.8. Briefly, the contents of a 50% probability circle placed around the grain centre were recorded, noting particularly the presence of neuronal plasma membrane (synaptic, axonal, dendritic or cell soma). The distance

Figure 5.5. Localization of ^{125}I-β-BuTX binding in chick cerebellum molecular and Purkinje cell layers

Cerebellar slices from chick brain were processed as detailed in Figure 5.4. (a and b) ^{125}I-β-BuTX binding to synaptic bouton membrane. Parallel fibres (PF) swell to form synaptic boutons (SB), synapsing with dendritic elements (D). (c) shows a poorly preserved Purkinje cell. The cytoplasm has disintegrated, endoplasmic reticulum (ER) and mitochondria (M) are severely swollen, and the plasma membrane is disrupted in some places (arrowheads). Silver grains are found throughout the cytoplasm and nucleus (N) of this cell. (d) Molecular layer of a control section from the same experiment. Magnifications: 22,900× in a, 26,100× in b, 10,100 in c and 13,400× in d. All scale bars =1 μm.

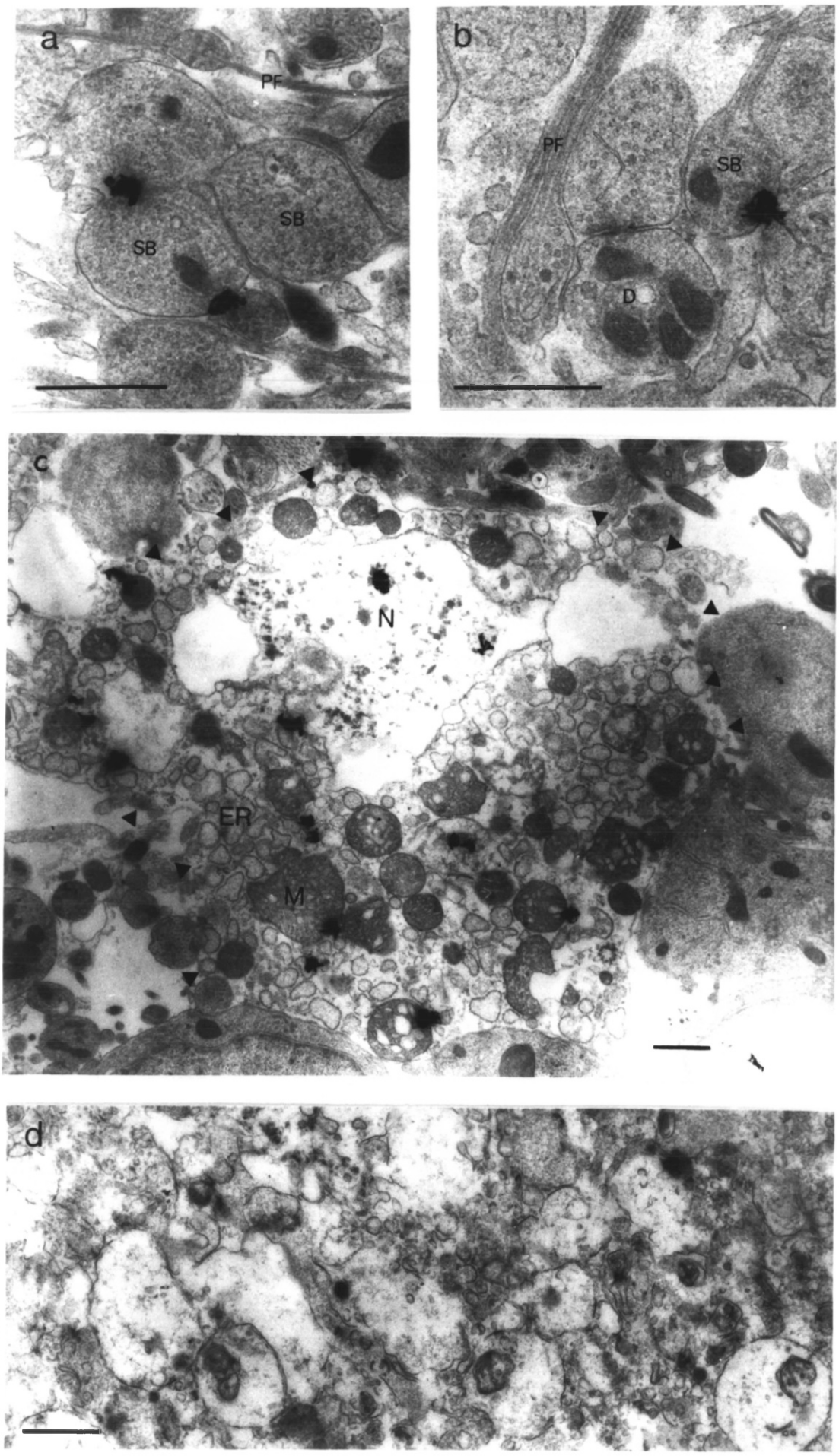
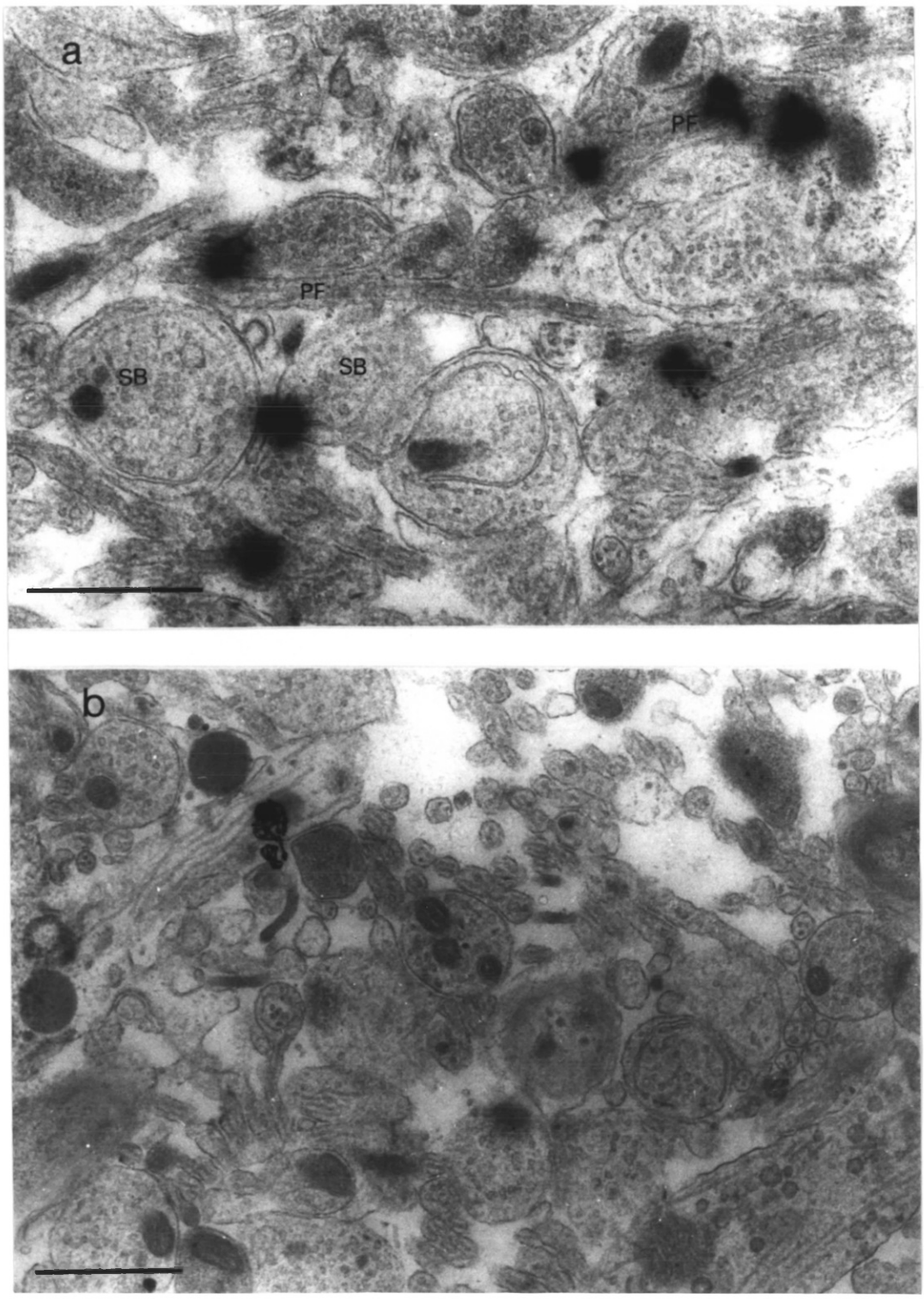

a
PF
SB
SB
b
PF
SB
D
c
N
ER
M
d

Figure 5.6. ^{125}I-ß-BuTX binding in chick cerebellum molecular layer in Sr^{2+} Ringer



Cerebellar slices from 1-day-old chick brain were incubated in 5 nM ^{125}I-ß-BuTX (1000 Ci/mmol) in Ca^{2+}-free Sr^{2+}-containing Krebs Ringer, processed for electron microscope autoradiography and exposed for 120 days. (a) ^{125}I-ß-BuTX binding in the molecular layer. Silver grains were found close to synaptic boutons (SB) and unmyelinated parallel fibres (PF). (b) Molecular layer of a control section labelled in 5 nM ^{125}I-ß-BuTX in the presence of 5 µM unlabelled ß-BuTX. Note the improved preservation compared to brain slices incubated in Ca^{2+}-containing Ringer (Figure 5.5d). Magnifications: 26,900× in a and 22,500× in b. All scale bars =1 µm.

from the grain centre to the nearest synaptic bouton membrane was also measured; 2970 random points were studied likewise.

In this analysis the 50% probability circles around 499 grains (i.e. 71% of all grains studied) contained neuronal plasma membrane, compared with only 58% of the random points, giving an enrichment (relative density ratio) of 1.2. This suggests that the β-BuTX acceptors occur on neuronal membranes. The grains and random points were then grouped into classes according to the contents of the corresponding 50% probability circles. The results from this analysis are summarized in Table 5.1. Significant relative density ratios were associated with the membrane of synaptic boutons and with the parallel fibres, the unmyelinated axons of the cerebellar granule cells. The parallel fibres frequently swell along their course to form synaptic boutons (see e.g. Figure 5.5b), and thus probably contain similar presynaptic membrane components to the synaptic boutons. Debris of burst cells and intercellular space appeared to be labelled only when they were found close to synaptic boutons.

Histograms of the distribution of silver grains and random points relative to the synaptic bouton membrane are shown in Figure 5.7. The distribution of random points represents an area correction for the silver grain histogram. Due to the large number of synaptic boutons in the cerebellum molecular layer neuropil, few random points were found far from synaptic bouton membrane. Comparison of the grain and point distribution histograms, however, reveals a relative enrichment of silver grains over the synaptic bouton membrane. This suggests that the toxin binds to acceptors in the synaptic bouton membrane.

5.4.3.4. *Analysis of the distribution of ^{125}I-β-BuTX binding in the granule cell layer and white matter regions of chick cerebellum*

Compared to the molecular layer, very few silver grains were observed over the granule cell layer on electron microscope autoradiograms; most of these grains were found in the neuropil and glomeruli between the granule cell bodies (Figure 5.8a). On control sections the granule cell layer was again very degraded by the phospholipase activity of the excess unlabelled β-BuTX, and almost totally devoid of grains (Figure 5.8b).

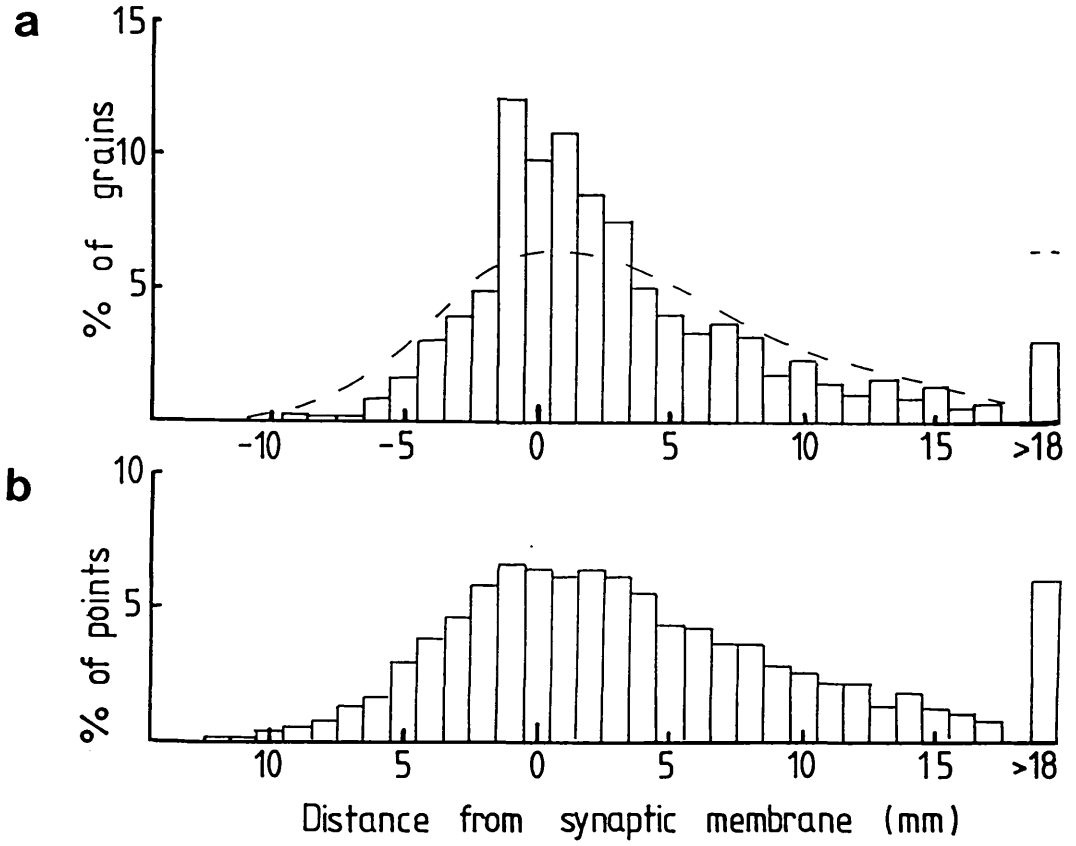
The distribution of silver grains in the granule cell

Table 5.1. ^{125}I-β-BuTX Binding in Chick Cerebellum Molecular Layer: Distribution of silver grains and relative grain densities over various tissue elements

	Number of Grains	% of Grains	% of Points	Relative Density
Synaptic bouton: Total	282	40.2	37.8	1.1
Internal	20	2.9	8.1	0.4
Membrane-associated	262	37.4	29.7	**1.3**
Parallel fibre: Total	179	25.5	15.8	**1.6**
Near synaptic bouton	51	7.3	3.8	**1.9**
Non-synaptic	128	18.3	12.0	**1.5**
Dendritic: Total	69	9.8	16.5	0.6
Internal	18	2.6	7.9	0.3
Membrane-associated	51	7.3	8.6	0.8
Near synaptic bouton	10	1.4	1.6	0.9
Non-synaptic	41	5.8	7.0	0.8
Cell soma: Total	2	0.3	0.8	0.4
Internal	1	0.1	0.6	0.2
Membrane-associated	1	0.1	0.2	0.5
Near synaptic bouton	0			
Non-synaptic	1	0.1	0.1	1.0
Glial: Total	251	35.8	34.2	1.0
Near synaptic bouton	82	11.7	10.7	1.1
Non-synaptic	169	24.1	23.5	1.0
Burst cell debris: Total	105	15.0	14.6	1.0
Near synaptic bouton	10	1.4	0.9	**1.6**
Non-synaptic	95	13.6	13.7	1.0
Intercellular space: Total	106	15.1	15.7	1.0
Near synaptic bouton	54	7.7	5.2	**1.5**
Non-synaptic	52	7.4	10.5	0.7
Unidentified:	7	1.0	1.9	0.5

Cerebellum slices from 1-day-old chick brain were incubated in 5 nM ^{125}I-β-BuTX (1,000 Ci/mmol) and processed for electron microscope autoradiography. After exposure for 120 days the autoradiograms were developed, and photographs of 8,500 μm² of the molecular layer were printed at 17,500× magnification. The contents of 50% density circles (HR =175 nm) about 701 silver grain centres or 2970 random points were studied. Shared grains or points were counted twice as detailed in Section 5.3.8. Probability circles of grains or points which contained portions of synaptic bouton membrane were grouped separately. Relative density is the ratio of % of grains ÷ % of points, as described in Section 5.3.8. Significant labelling was defined as a relative density ratio ≥1.3 from at least 5 silver grains, and is shown in bold type.

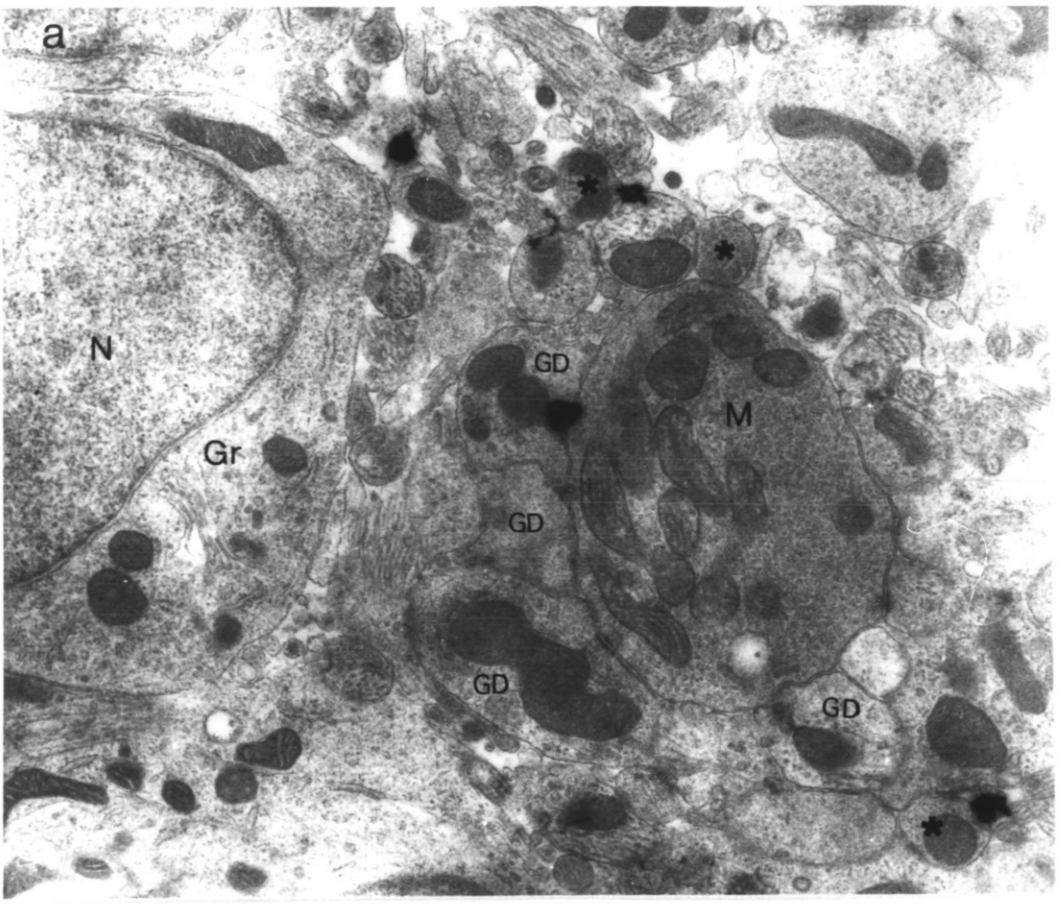
Figure 5.7. Distribution of silver grains about the presynaptic membrane

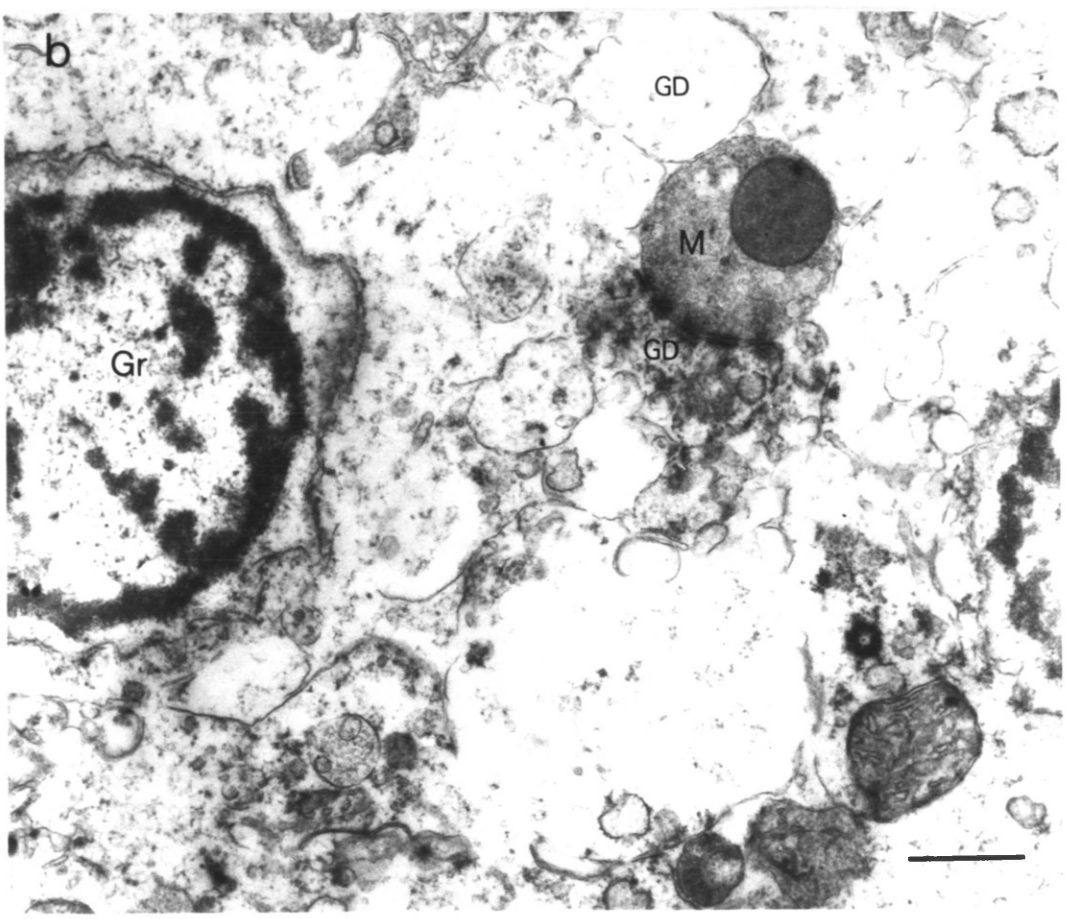


Autoradiographic prints of ^{125}I-β-BuTX labelled chick cerebellum molecular layer (magnification 17,500×; HR of 175 nm =3 mm) were studied. The distance on the prints from the centre of each silver grain to the nearest synaptic bouton membrane was measured in mm, and a histogram constructed as in (a). To obtain a tissue volume correction, random points were analysed likewise (b). The dashed line in a (— —) is a smooth curve drawn through this point distribution. It is apparent from this plot that only the synaptic bouton membrane, and structures in the immediate vicinity of synaptic bouton membrane, are specifically enriched in siver grains.

Figure 5.8. Localization of ^{125}I-β-BuTX binding in chick cerebellum granule cell layer

Cerebellar slices from chick brain were incubated in 5 nM ^{125}I-β-BuTX (1000 Ci/mmol) in Ca^{2+}-containing Krebs Ringer, processed for electron microscope autoradiography and exposed for 120 days. ^{125}I-β-BuTX binding in the granule cell layer. (a) A granule cell (Gr, N, nucleus) close to a glomerulus. This consists of a central vesicle-filled mossy fibre terminal (M), surrounded by granule cell dendritic processes (GD). Nerve terminals from Golgi cells (*) also synapse with the granule cell dendrites. Again three of the four silver grains are close to synaptic boutons. (b) Granule cell layer of a control section labelled in 5 nM ^{125}I-β-BuTX in the presence of 5 μM unlabelled β-BuTX. The remains of a granule cell and a glomerulus can be identified, but most of the tissue is degraded by the phospholipase activity of the toxin. Magnification =15,500×. Scale bar (in b) =1 μm.


a
N
Gr
GD
GD
GD
M
GD


b
GD
M'
GD
Gr

layer was studied on one section by taking a series of non-overlapping adjacent photographs over an entire grid square (≈9,000 μm^2). This area contained 107 silver grains, whose distribution was analysed and compared to that of random points by relative density analysis as detailed in Table 5.2. The point analysis revealed that a large proportion of the section area in the granule cell layer (53%) is taken up by granule cell bodies. This area is unlabelled (relative density ratio 0.4), probably because it is inaccessible to the toxin. Membrane rupture (e.g. due to swelling and subsequent bursting of anoxic cells, as in the Purkinje cells described in Sections 5.4.3.1 and 5.4.3.2) may be required before the toxin can reach the cytoplasm of the cells. It should be noted, however, that poorly preserved granule cells on other areas of the section were also unlabelled. The analysis data was adjusted to exclude the apparently inaccessible space by subtacting all grains and points further than 3 mm (=HR) inside the cell soma. The "corrected relative densities" thus obtained (Table 5.2) again indicated that synapses and unmyelinated axons are labelled. After the correction, dendrites, glial processes and cell somata appeared labelled only near synaptic boutons, indicating that silver grains over these structures are probably due to cross-fire rather than direct labelling by the toxin.

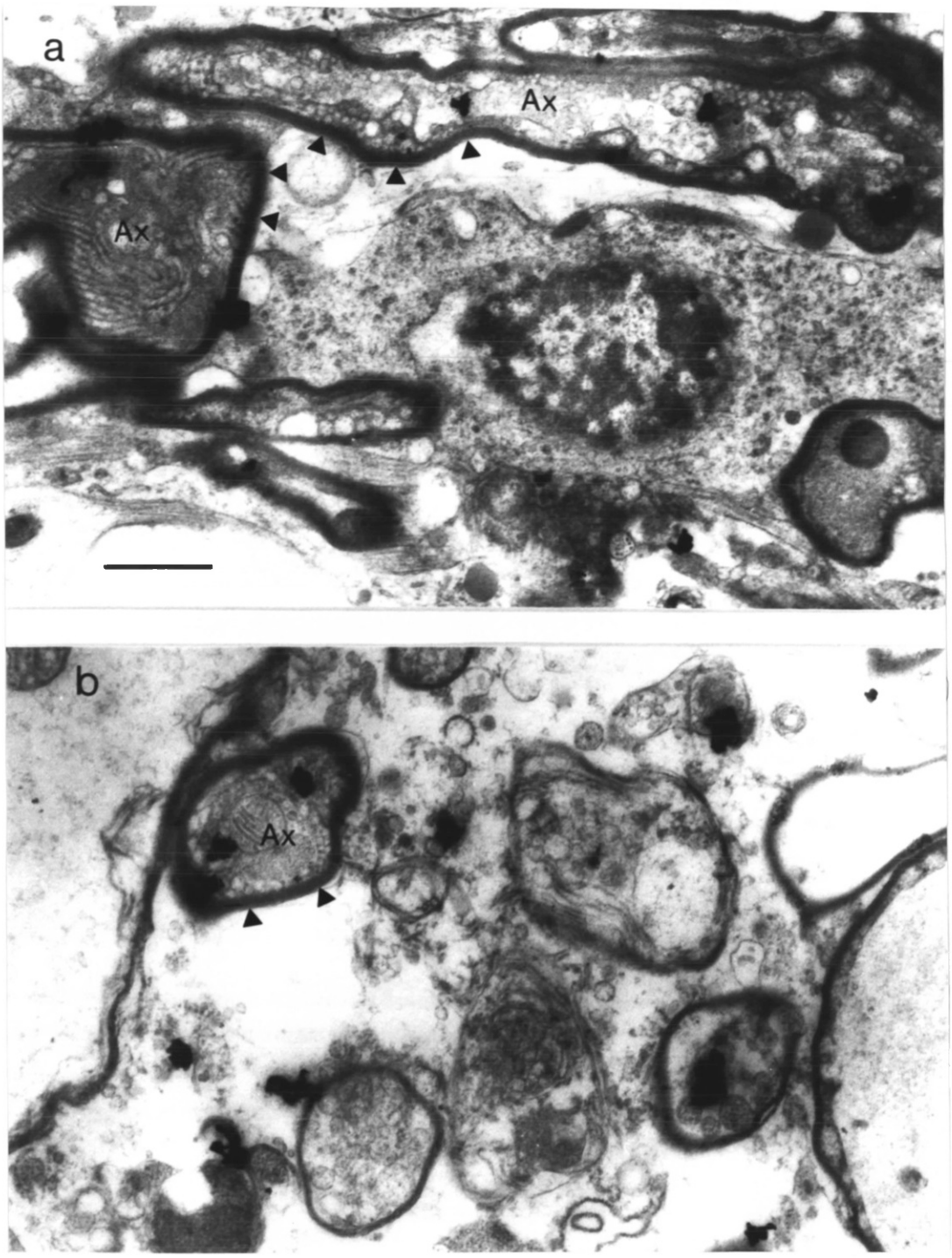
As noted earlier, the light microscopy survey sections showed high grain densities over white matter regions on both test and control tissue slices. Likewise, silver grains were observed in the electron microscope in areas containing myelinated axons on both test and control sections (Figure 5.9). Many of these grains were seen close to the myelin sheath. Relative density analysis was performed on prints covering 1,400 μm^2 of both test and control tissue (93 and 72 grains on test and control sections, respectively; analysis not shown). High relative density ratios were always observed over the myelin sheath or within the axons on <u>both</u> test and control sections. In addition, synaptic boutons, although rare in the deep granule cell layer/white matter areas, had significant relative grain densities on test sections; these structures were not identifiable in the control tissue. The distances from the grain centres to the nearest myelin surface were also measured on all photographs. Silver grains on both test and control samples were found to be enriched 3-6 mm from the myelin sheath, both inside and outside the axons. This suggests that β-BuTX is non-

Table 5.2. ^{125}I-β-BuTX Binding in Chick Cerebellum Granule Cell Layer: Distribution of silver grains and relative grain densities over various tissue elements

	Number of Grains	% of Grains	% of Points	Relative Density	Corrected Relative Density
Synaptic bouton: Total	39	36.4	15.3	**2.4**	**1.5**
Internal	7	6.5	5.2	**1.3**	0.8
Membrane-associated	32	29.9	10.2	**2.9**	**1.8**
Axonal: Total	27	25.2	9.5	**2.7**	**1.6**
Internal	3	2.8	0.9	**3.1**	**1.9**
Membrane-associated	24	22.4	8.6	**2.6**	**1.6**
Near synaptic bouton	7	6.5	1.4	**4.6**	**3.0**
Non-synaptic	17	15.9	7.3	**2.2**	**1.4**
Dendritic: Total	16	15.0	11.8	**1.3**	0.8
Internal	3	2.8	4.1	0.7	0.3
Membrane-associated	13	12.1	7.7	**1.6**	1.0
Near synaptic bouton	10	9.3	3.2	**2.9**	**1.8**
Non-synaptic	3	2.8	4.5	0.6	0.4
Cell soma: Total	41	38.3	63.8	0.6	
Internal	23	21.5	52.7	0.4	NA
Membrane-associated	18	16.8	11.1	**1.5**	0.9
Near synaptic bouton	9	8.4	1.5	**5.6**	**3.4**
Non-synaptic	9	8.4	9.5	0.9	0.5
Glial: Total	5	4.7	2.9	**1.6**	1.0
Internal	0		0.6		
Membrane-associated	5	4.7	2.3	**2.0**	**1.3**
Near synaptic bouton	3	2.8	0.9	3.1	1.9
Non-synaptic	2	1.9	1.4	1.4	0.9
Burst cell Debris: Total	2	1.9	0.8	2.4	1.6
Near synaptic bouton	1	0.9			
Non-synaptic	1	0.9	0.8	1.1	0.8
Unidentified	9	8.4	3.9	**2.2**	NA

Chick cerebellum slices were labelled with ^{125}I-β-BuTX and processed as detailed in Table 5.1. Photographs of 9,000 μm² of the granule cell layer were printed. The contents of 50% density circles about 107 silver grain centres or 660 random points were studied as before. The corrected relative density column shows recalculated relative density values after both grains and points located over the cell soma (internal) and unidentified grains and points were subtracted. After this correction, 75 grains and 286 points remained for analysis. Significant labelling was defined as a relative density ratio ≥1.3 from at least 5 silver grains, and is shown in bold type.

Figure 5.9. Localization of ^{125}I-ß-BuTX binding in chick cerebellum white matter regions



Cerebellar slices from chick brain were processed as detailed in Figure 5.6. On both test (a) and control (treated with 5 nM ^{125}I-ß-BuTX in the presence of 5 µM unlabelled ß-BuTX, b) sections silver grains were observed on or inside myelinated axons (Ax), suggesting that the toxin is non-specifically trapped in these areas. Arrowheads identify some of the darkly-stained myelin sheaths. Magnification =15,800×. Scale bar (in a) =1 µm.

specifically trapped in and around myelinated axons, leading to high grain densities in white matter areas. In the studies on cryostat sections (Chapter 3) more thorough washing was possible, and little toxin binding was observed in white matter areas.

5.4.4. Localization of DTX Acceptors in Chick Cerebellum

Chick cerebellum slices were also labelled with 5 or 35 nM ^{125}I-DTX, control slices being incubated in addition in the presence of 10 µM unlabelled DTX. Semithin survey section autoradiograms from slices labelled at both ^{125}I-DTX concentrations showed similar silver grain distributions, high grain densities being observed over the molecular layer, lower numbers of silver grains over the granule cell layer, while the external granule cell layer remained unlabelled (data not shown). Significant levels of saturable ^{125}I-DTX binding were also observed over white matter regions. Control sections contained uniform very low grain densities.

5.4.4.1. *Analysis of the distribution of ^{125}I-DTX binding in the molecular layer of chick cerebellum*

On sections prepared for electron microscope autoradiography, many silver grains were found in the molecular layer; these appeared to be located over synaptic boutons and parallel fibres (Figure 5.10a,b,c). Since higher silver grain densities (≈25.5 grains/100 µm²) were observed on sections from slices labelled at the higher toxin concentration (35 nM), these were used in the analysis of the silver grain distributions, as described below. The labelling was saturable, since control sections contained only 2.0 grains/100 µm² (see also Figure 5.10d). Photographs from sections cut from two different brain slices were studied in detail. As for ^{125}I-β-BuTX, a large proportion of the silver grains (78%), but not of the random points (only 57%) on these photographs were found over neuronal membrane. This significant enrichment (1.4×) suggests a membrane location for the DTX acceptors. In the relative density analysis (summarized in Table 5.3) only synaptic bouton membranes and the unmyelinated parallel fibre axons of the granule cells contained significant labelling (relative density ratios ≥1.3). The apparent labelling of dendritic structures and glial processes was restricted to tissue elements in close apposition to synaptic boutons (the 50% probability circles also contained synaptic bouton membrane), indicating that it was probably due

Figure 5.10. Localization of ^{125}I-DTX binding in chick cerebellum molecular layer

Cerebellar slices from 1-day-old chick brain were incubated in 35 nM ^{125}I-DTX (300 Ci/mmol), processed for electron microscope autoradiography and exposed for 135 days. (a) Overview of the molecular layer. Silver grains are found close to synaptic bouton (SB) membranes and near unmyelinated parallel fibre (PF) axons. D, dendritic process. (b) Detailed view of a synaptic area. (c) A group of parallel fibres, cut transversely. (d) Molecular layer of a control section labelled in 35 nM ^{125}I-DTX in the presence of 10 µM unlabelled DTX. Magnifications: 15,600× in a, 21,900× in b, 25,300 in c and 11,600× in d. All scale bars =1 µm.

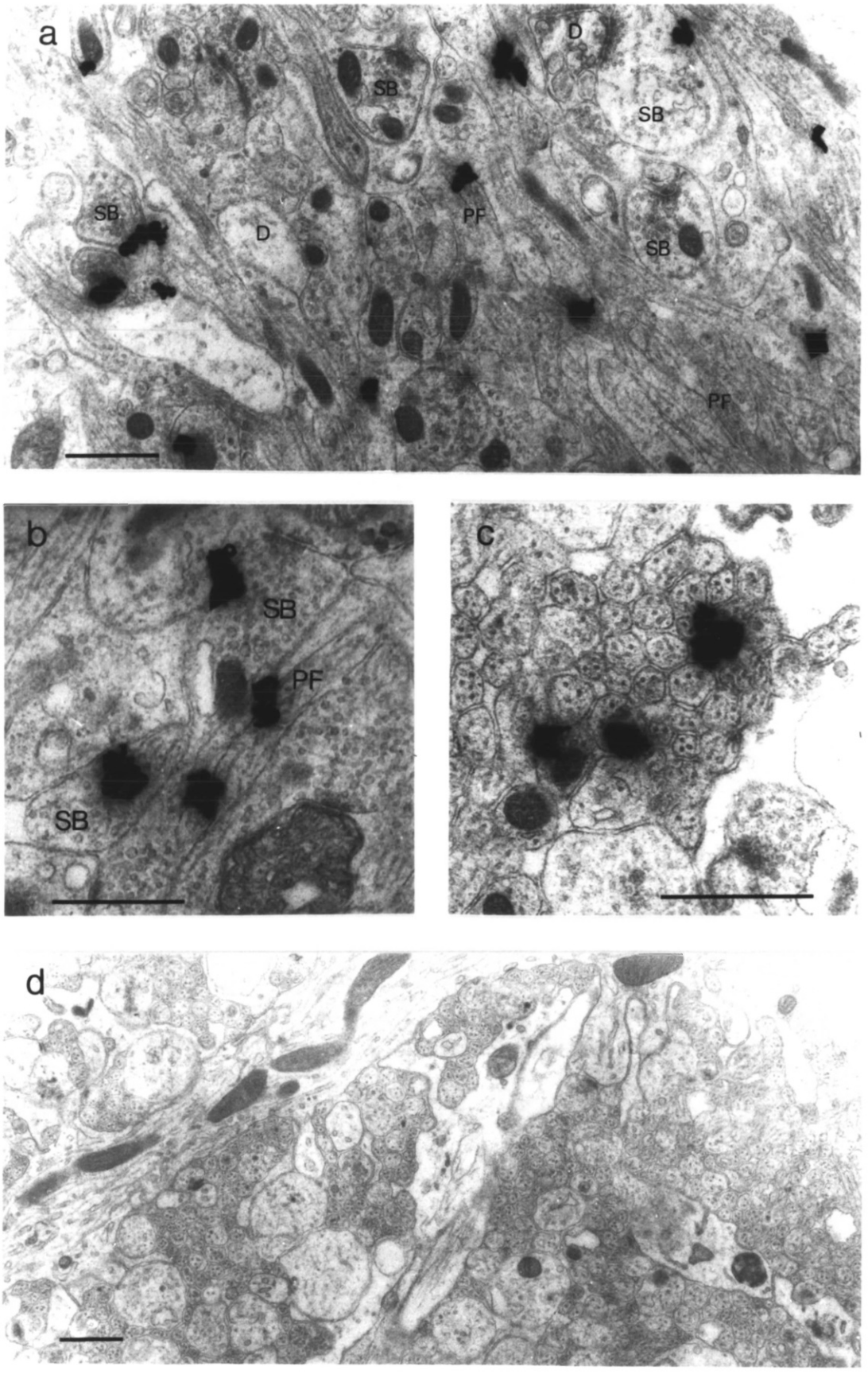

a
SB
D
SB
SB
D
PF
SB
PF
b
SB
PF
SB
c
d

Table 5.3. ^{125}I-DTX Binding in Chick Cerebellum Molecular Layer: Distribution of silver grains and relative grain densities over various tissue elements

	Number of Grains	% of Grains	% of Points	Relative Density
Synaptic bouton: Total	95	22.6	14.8	**1.5**
Internal	12	2.9	2.9	1.0
Membrane-associated	83	19.8	11.9	**1.7**
Parallel fibre: Total	244	58.1	39.7	**1.5**
Near synaptic bouton	36	8.6	3.7	**2.3**
Non-synaptic	208	49.5	36.0	**1.4**
Dendritic: Total	49	11.7	21.6	0.5
Internal	14	3.3	11.8	0.3
Membrane-associated	35	8.3	9.8	0.8
Near synaptic bouton	9	2.1	1.6	**1.3**
Non-synaptic	26	6.2	8.2	0.8
Cell soma: Total	12	2.9	7.3	0.4
Internal	10	2.4	6.7	0.4
Membrane-associated	2	0.5	0.7	0.7
Near synaptic bouton	1	0.2		
Non-synaptic	1	0.2	0.7	0.3
Glial: Total	54	12.9	19.1	0.7
Near synaptic bouton	16	3.8	2.6	**1.5**
Non-synaptic	38	9.0	16.6	0.5
Burst cell debris: Total	17	4.0	5.3	0.8
Near synaptic bouton			0.5	
Non-synaptic	17	4.0	4.9	0.8
Unidentified:	20	4.8	4.3	1.1

Cerebellum slices from 1-day-old chick brain were incubated in 35 nM ^{125}I-DTX (300 Ci/mmol) and processed for electron microscope autoradiography. After exposure for 135 days the autoradiograms were developed, and photographs of 1,810 μm^2 of the molecular layer were printed at 17,500× magnification. The contents of 50% density circles (HR =175 nm) about 420 silver grain centres or 1050 random points were studied. Shared grains or points were counted twice as detailed in Section 5.3.8. Probability circles of grains or points which contained portions of synaptic bouton membrane were grouped separately. Relative density is the ratio of % of grains ÷ % of points, as described in Section 5.3.8. Significant labelling was defined as a relative density ratio ≥1.3 from at least 5 silver grains, and is shown in bold type.

to cross-fire from nearby synaptic boutons. Thus the DTX acceptors appear to be neurone specific (as was suggested by the Ultrofilm localization studies, cf. Section 4.4.1), occurring mainly on synapses and axons.

5.4.4.2. *Analysis of the distribution of ^{125}I-DTX binding in the granule cell layer and white matter regions*

The granule cell layer contained lower grain densities than the molecular layer (only 9.3 silver grains/100 μm^2); most silver grains were found in the neuropil and glomerular regions between the granule cell somata (Figure 5.11). Occasional silver grains were also observed over the granule cell soma membrane (at least four of the grains shown in Figure 5.11a are located thus). The results from the detailed analysis of the silver grain distributions are summarized in Table 5.4. As for ^{125}I-β-BuTX, the granule cell bodies could thus be demonstrated to be unlabelled, although a relative density ratio of 1.5 was observed over the cell soma membrane. When the unlabelled tissue volume occupied by these somata was subtracted as before (cf. Section 5.4.3.4), the only significant grain densities were observed over synaptic boutons, unmyelinated axons, and denritic processes close to synapses. Notably, the granule cell soma membrane no longer appeared specifically labelled. In addition, significant relative grain density ratios were found over myelinated axons, although these were not very abundant (2.5% of the tissue area) on the photographs studied.

The distribution of silver grains in white matter regions of the cerebellum was therefore studied more closely. ^{125}I-DTX appeared to label myelinated axons very strongly (Figure 5.12a), with grain densities as high as 16.4 grains/100 μm^2 being observed in areas rich in myelinated fibre bundles. In contrast, few silver grains (5.7/100 μm^2, Figure 5.12b) were observed in equivalent areas on control sections. Thus, unlike the myelin labelling by ^{125}I-β-BuTX (cf. Sections 5.4.3.1 and 5.4.3.4), the binding of ^{125}I-DTX in these areas was saturable. Relative density analysis (not shown) revealed that the toxin bound specifically over the myelin sheath. This distribution of silver grains on myelinated axons agrees with the results of the Ultrofilm localization studies described in Chapter 4 (see also Section 4.4.5).

Figure 5.11. Localization of ^{125}I-DTX binding in chick cerebellum granule cell layer

Cerebellar slices from chick brain were processed as detailed in Figure 5.10. (a) Granule cell layer field. Many silver grains are found in the neuropil between granule cell somata (Gr). M, mossy fibre terminal; GD, granule cell dendrite; Ax, unmyelinated axon. (b) Granule cell layer of a control section from the same experiment. Magnification =11,600×. Scale bar (in b) =1 μm.

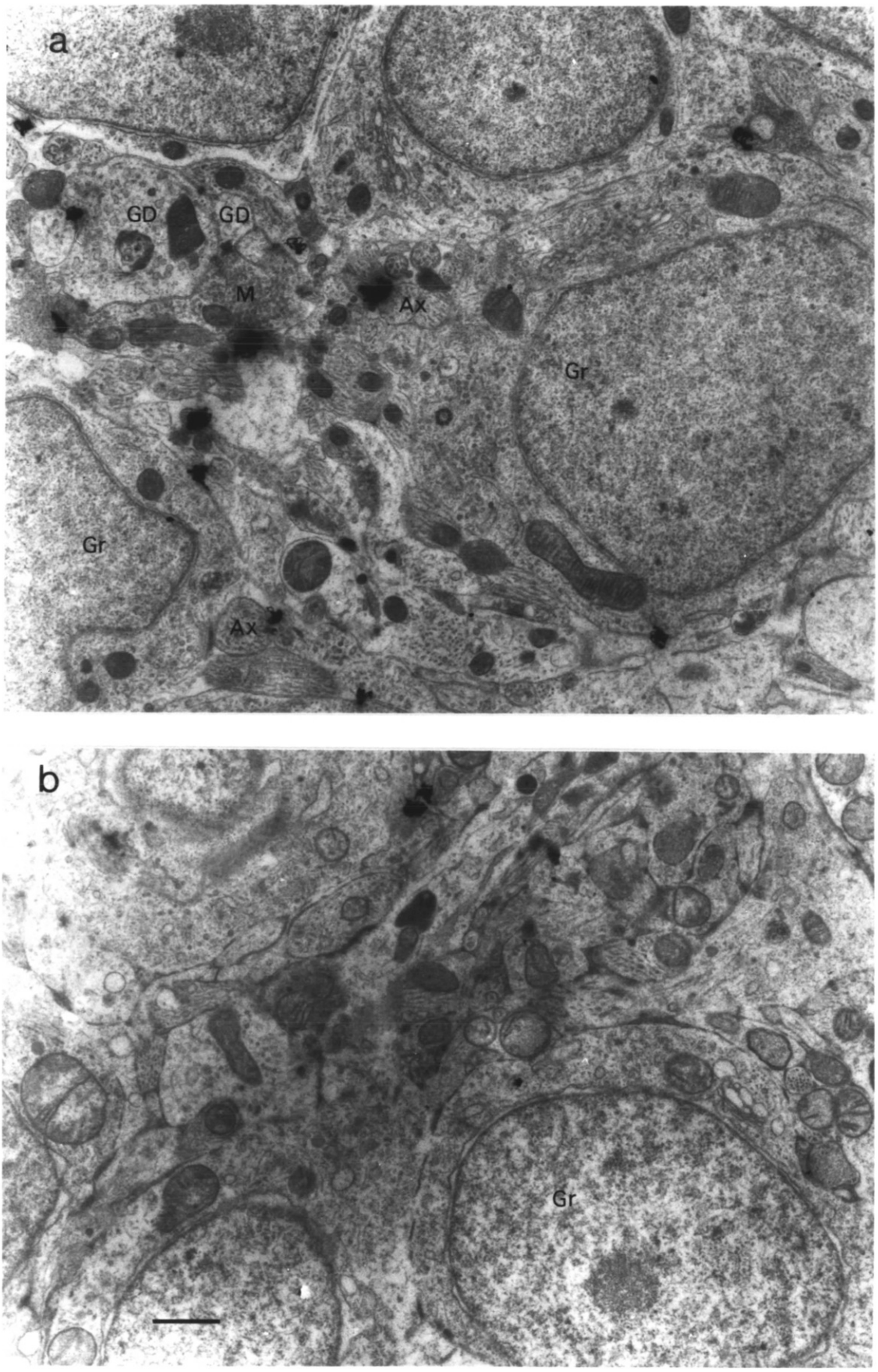
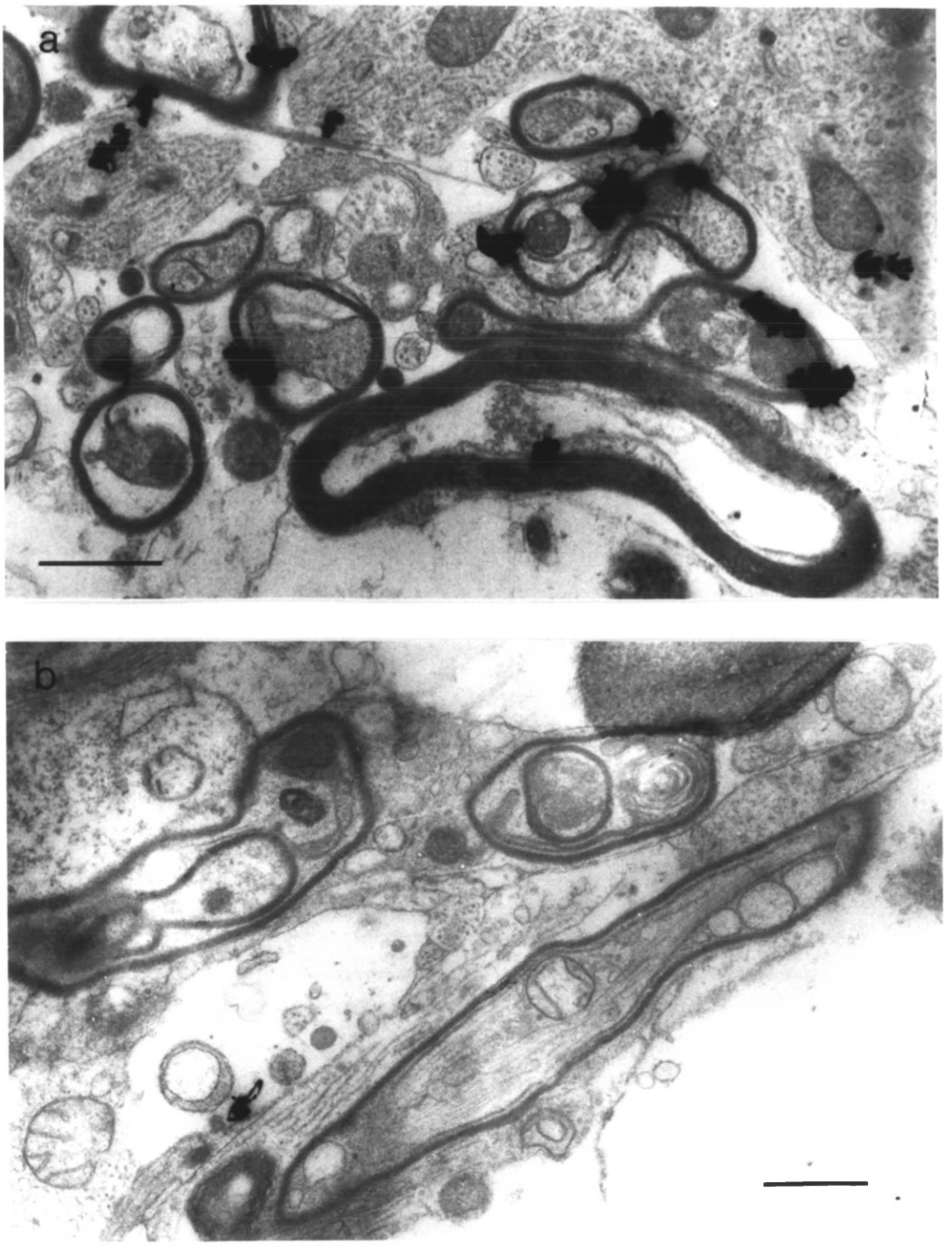

a
GD
GD
M
Ax
Gr
Gr
Ax
b
Gr

Table 5.4. ^{125}I-DTX Binding in Chick Cerebellum Granule Cell Layer: Distribution of silver grains and relative grain densities

	Number of Grains	% of Grains	% of Points	Relative Density	Corrected Relative Density
Synaptic bouton: Total	35	24.1	9.0	**2.7**	**1.6**
Internal	3	2.1	2.1	1.0	0.6
Membrane-associated	32	22.1	6.9	**3.2**	**2.0**
Unmyelinated axon: Total	42	29.0	11.3	**2.6**	**1.6**
Near synaptic bouton	3	2.1	1.2	1.8	1.0
Non-synaptic	39	26.9	10.1	**2.7**	**1.6**
Myelinated axon: Total	10	6.9	2.5	**2.8**	**1.7**
Myelin, near synaptic bouton	0		0.2		
Myelin, non-synaptic	7	4.8	1.6	**3.0**	**1.9**
Internal	3	2.1	0.7	3.0	1.8
Dendritic: Total	38	26.2	21.5	1.2	0.7
Internal	7	4.8	11.3	0.4	0.3
Membrane-associated	31	21.4	10.2	**2.1**	**1.3**
Near synaptic bouton	17	11.7	3.2	**3.7**	**2.3**
Non-synaptic	14	9.7	7.1	1.4	0.8
Cell soma: Total	44	30.3	59.8	0.5	
Internal	20	13.8	48.5	0.3	NA
Membrane-associated	24	16.6	11.3	**1.5**	0.9
Near synaptic bouton	1	0.7	0.5	1.4	0.8
Non-synaptic	23	15.9	10.8	**1.5**	0.9
Glial: Total	6	4.1	4.2	1.0	0.6
Internal	0		1.1		
Membrane-associated	6	4.1	3.2	1.3	0.8
Near synaptic bouton	3	2.1	0.4	5.3	3.4
Non-synaptic	3	2.1	2.8	0.8	0.5
Unidentified	14	9.7	4.8	2.0	NA

Chick cerebellum slices were labelled with ^{125}I-DTX and processed as detailed in Table 5.3. Photographs of 1,630 μm^2 of the granule cell layer were printed. The contents of 50% density circles about 145 silver grain centres or 567 random points were studied. The corrected relative density column shows re-calculated relative density values after both grains and points located over the cell soma (internal) and unidentified grains and points were subtracted. After this correction, 111 grains and 265 points remained for analysis. Significant labelling was defined as a relative density ratio ≥ 1.3 from at least 5 silver grains, and is shown in bold type.

Figure 5.12. Localization of ^{125}I-DTX binding in chick cerebellum white matter regions



Cerebellar slices from chick brain were processed as detailed in Figure 5.10. (a) A group of myelinated axons. Many silver grains are found over the darkly-staining myelin sheaths. (b) Myelinated axons on a control section labelled in the presence of 10 μM unlabelled DTX. Magnifications: 18,400× in a and 15,800× in b. All scale bars =1 μm.

5.4.5. Distribution of DTX Acceptors in Rat Cerebellum

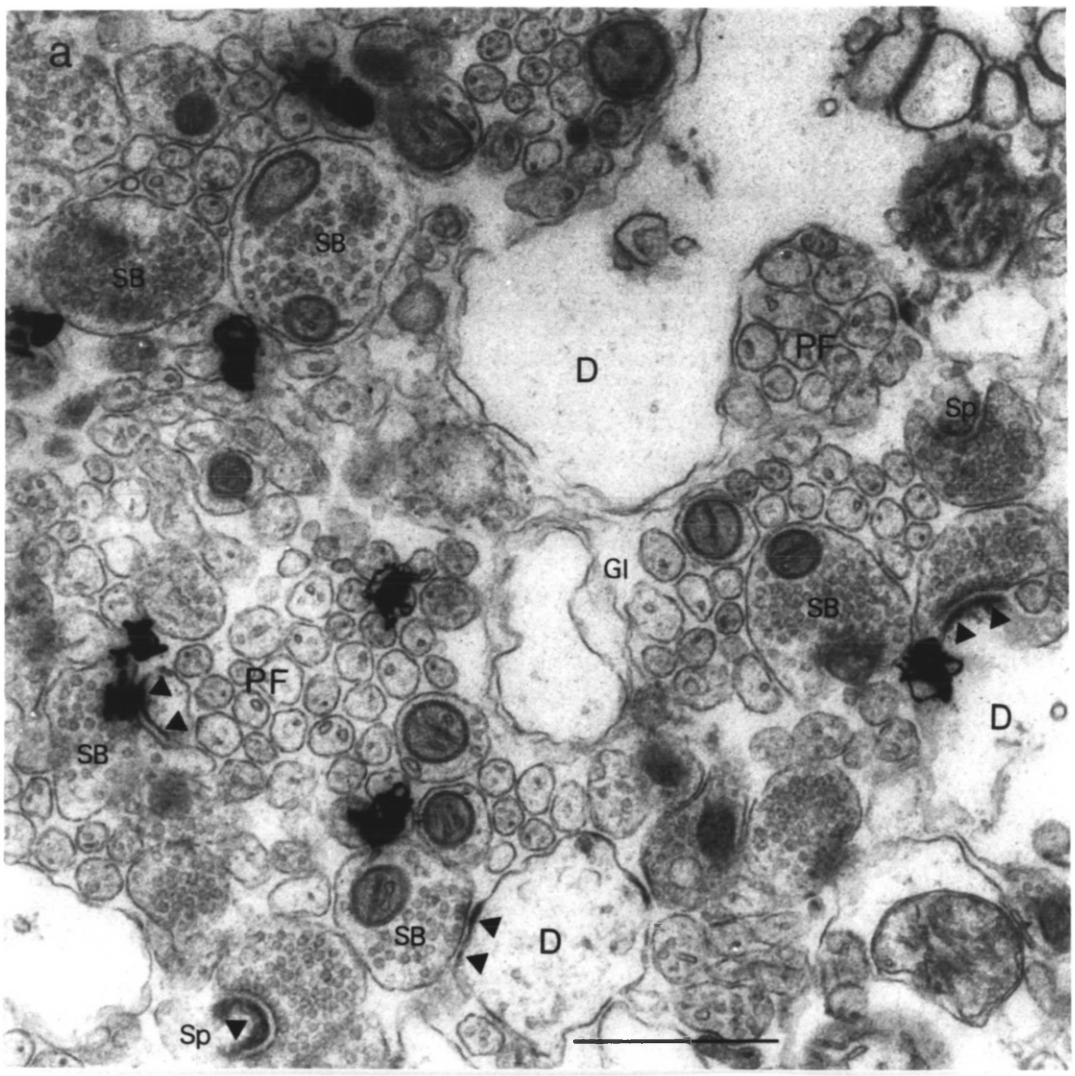
As described in Section 5.4.1, only ^{125}I-DTX was able to penetrate deeply enough into rat brain slices for a study of the distribution of its acceptors to be feasible. The preservation of rat cerebellar slices incubated in 30 nM ^{125}I-DTX by the usual method (Section 5.3.2) was very poor, all cell bodies being pyknotic, and all tissue layers appearing vacuolated. Survey autoradiograms of semithin sections were used to identify the tissue areas labelled by the toxin. These also showed that, under both test and control (10 μM unlabelled DTX) conditions, the cell bodies of all Purkinje cells to which the toxin had access were labelled.

In the electron microscope synaptic areas of the molecular layer appeared reasonably well preserved, although the dendrites of Purkinje cells and glial elements were often severely swollen. Silver grains were found in areas close to the surface of the molecular layer, where ^{125}I-DTX was able to penetrate into the tissue. Many of these were located over parallel fibres or close to synaptic boutons (Figure 5.13). The grain distribution in the molecular layer was studied on 12 photographs from two test sections cut from different tissue slices, and covering an area of ≃2,200 μm². The average grain density on these prints was 16.2/100 μm², compared to only 3.2 grains/100 μm² on corresonding control sections (118 day exposure) thus indicating that the toxin labelling was saturable. Furthermore 82% of the grains (277 of 336 grains analysed) were located on neuronal plasma membrane structures, while only 55% of the random points studied on the same prints were found in such a location. The result of the relative density analysis is summarized in Table 5.5. An enrichment of silver grains was observed only over the parallel fibre axons of the granule cells and over synaptic bouton membranes.

In the granule cell layer both the granule cell somata and the neuropil were severely disrupted (Figure 5.14a) and no analysis of the labelling was attempted. White matter areas to which the toxin had access were strongly labelled, the majority of silver grains being found over the axon's myelin sheaths (Figure 5.14b). As in chick cerebellum, this labelling by ^{125}I-DTX was specific, few silver grains being observed near myelinated axons on control sections from tissue incubated in excess unlabelled DTX (Figure 5.14c), even though only areas close to the tissue surface, where the toxin must have been able to penetrate, were studied. Since

Figure 5.13. Localization of ^{125}I-DTX binding in rat cerebellum molecular layer

Cerebellar slices from adult rat brain were incubated in 30 nM ^{125}I-DTX (250 Ci/mmol), processed for electron microscope autoradiography and exposed for 118 days. (a) In the molecular layer silver grains are observed close to synaptic bouton (SB) membranes and unmyelinated parallel fibre axons (PF), cut transversely in this section. While synaptic boutons and parallel fibres are reasonably well preserved, dendritic processes (D) and glial elements (Gl) are severely swollen. Arrowheads identify the postsynaptic thickening visible in some dendritic processes. (b) Molecular layer of a control section labelled in 30 nM ^{125}I-DTX in the presence of 10 μM unlabelled DTX. Magnifications: 26,800× in a and 18,500× in b. All scale bars =1 μm.


a
SB
SB
D
PF
Sp
Gl
SB
PF
SB
D
SB
D
Sp

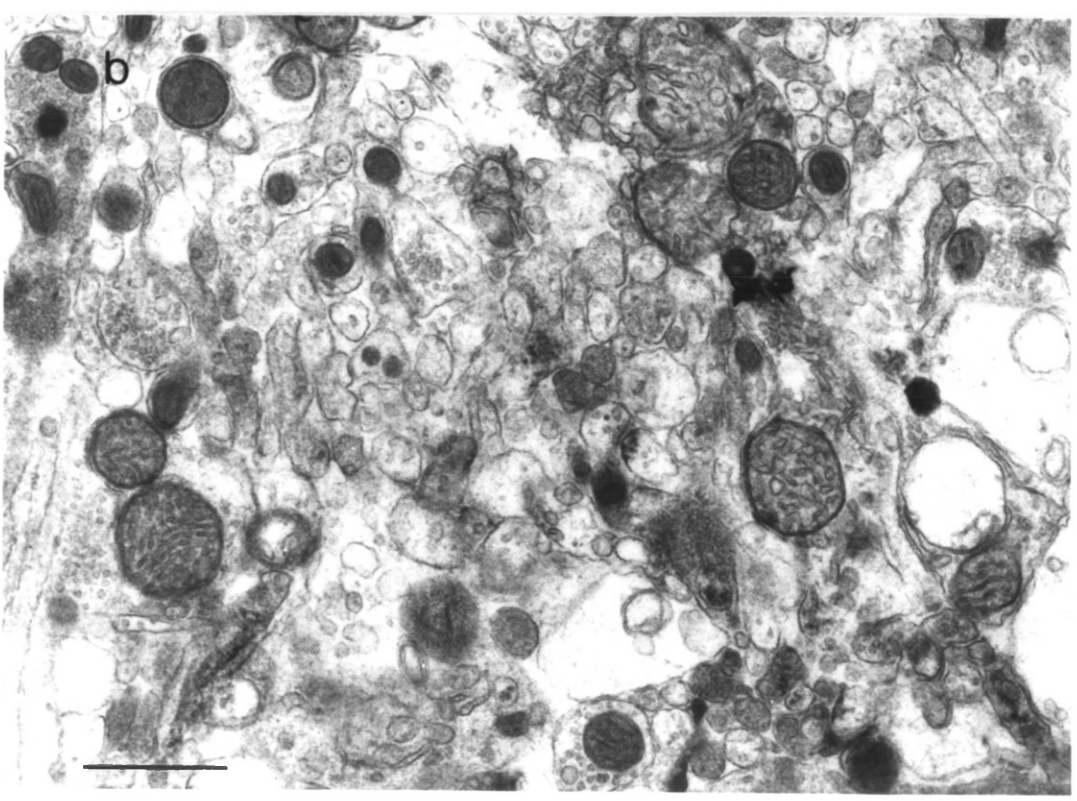

b

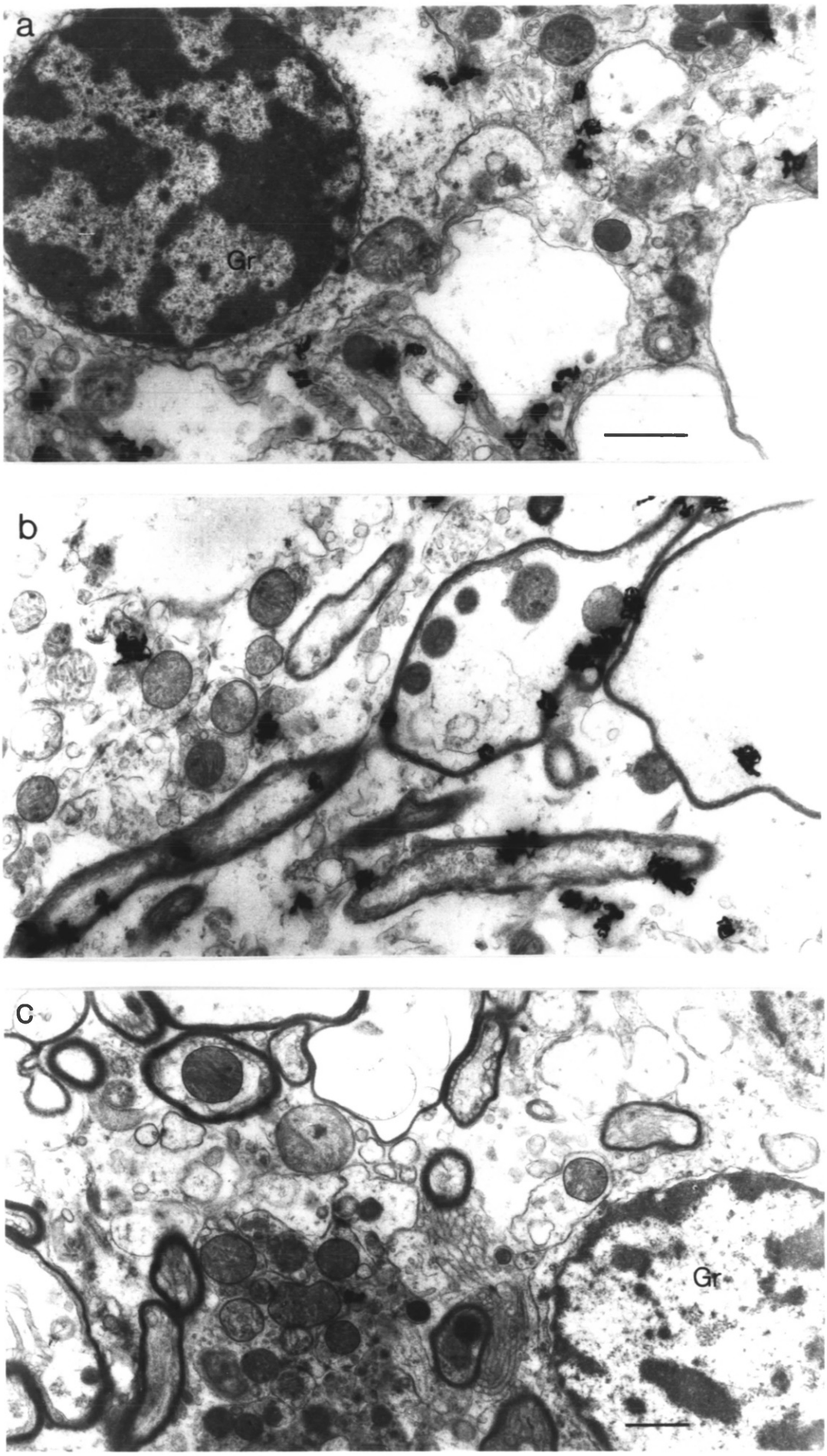
Table 5.5. ^{125}I-DTX Binding in Rat Cerebellum Molecular Layer: Distribution of silver grains and relative grain densities

	Number of Grains	% of Grains	% of Points	Relative Density
Synaptic bouton: Total	85	25.3	18.6	**1.4**
Internal	1	0.3	2.2	0.1
Membrane-associated	84	25.0	16.3	**1.5**
Parallel fibre: Total	190	56.5	30.9	**1.8**
Near synaptic bouton	55	16.4	4.5	**3.6**
Non-synaptic	135	40.2	26.3	**1.5**
Dendritic: Total	74	22.0	29.0	0.8
Internal	22	6.5	14.8	0.4
Membrane-associated	52	15.5	14.3	1.1
Near synaptic bouton	14	4.2	2.6	**1.6**
Non-synaptic	38	11.3	11.7	1.0
Glial: Total	83	24.7	34.0	0.7
Internal	17	5.1	16.3	0.3
Membrane-associated	66	19.6	17.7	1.1
Near synaptic bouton	18	5.4	4.4	1.2
Non-synaptic	48	14.3	13.3	1.1
Intercellular space: Total	9	2.7	2.5	1.1
Near synaptic bouton	3	0.9	0.8	1.1
Non-synaptic	6	1.8	1.7	1.1
Unidentified:	17	5.1	4.4	1.2

Adult rat cerebellum slices were incubated in 30 nM ^{125}I-DTX (250 Ci/mmol) and processed for electron microscope autoradiography. After exposure for 118 days the autoradiograms were developed, and photographs of 2,200 μm^2 of the molecular layer were printed at 17,500× magnification. The contents of 50% density circles about 336 silver grain centres or 1260 random points were studied as usual. Significant labelling was defined as a relative density ratio ≥ 1.3 from at least 5 silver grains, and is shown in bold type.

Figure 5.14. Localization of ^{125}I-DTX binding in rat cerebellum granule cell layer and white matter regions

Cerebellar slices from adult rat brain were processed as detailed in Figure 5.13. (a) Granule cell layer field. A granule cell can be recognized (Gr), but none of the labelled structures in the surrounding neuropil can be identified. (b) A group of myelinated axons. Many silver grains are found over the darkly-staining myelin sheaths. (c) A granule cell and myelinated axons on a control section from the same experiment are devoid of silver grains. Magnifications: 14,000× in a and b, and 10,500× in c. All scale bars =1 μm.


a
Gr
b
c
Gr

few of the electron microscope section autoradiograms contained areas with myelinated axons, insufficient tissue was available to study the distribution of ^{125}I-DTX binding in detail.

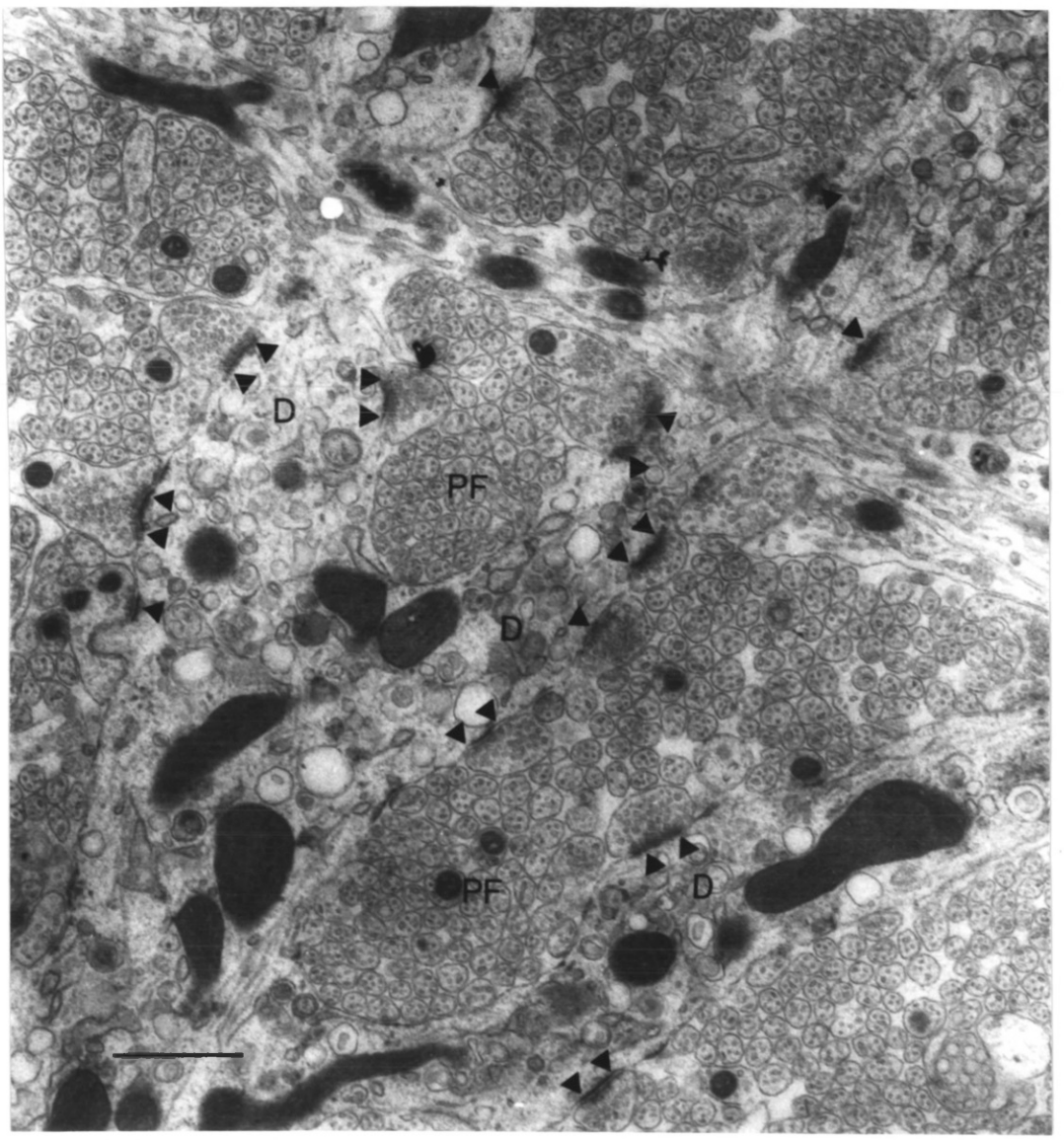
^{125}I-DTX binding was also examined on slices from the cerebellum of 14-day-old rats; this tissue, like chick cerebellum, is more resistant to anoxia than that of adult animals. Uniform very low grain densities were observed in all of the cerebellar layers on semithin survey sections from both test and control slices. Electron microscope autoradiography confirmed that the tissue was well preserved but contained very few silver grains (Figure 5.15); these were found close to parallel fibres or synaptic boutons. As the grain densities were below 0.5/100 μm^2, relative density analysis was not possible. The fact that the young rat cerebellum slices remained virtually unlabelled is probably due to the immaturity of the tissue. In contrast to 1-day-old chick cerebellum, no parallel fibre synapses with Purkinje cell dendrites have been formed in rat cerebellum 14 days postnatally, although climbing fibre synapses can frequently be seen on these dendrites (Figure 5.15; see also Altman, 1979). This labelling suggests, therefore, that DTX acceptors are not expressed in the parallel fibres until these become synaptically active.

5.4.6. Distribution of DTX Acceptors in Rat Hippocampus

High resolution autoradiographic methods have also been used to study the distribution of DTX acceptors in rat hippocampal slices, the tissue preparation in which inhibition by DTX of the fast transient K^+ current, I_A, was first demonstrated (Dolly *et al.*, 1984; Halliwell *et al.*, 1986). Transversely chopped slices (400 μm) were incubated in 30 nM ^{125}I-DTX, a concentration at which the toxin could label almost the entire thickness of the slices (see Section 5.4.1). Similar DTX concentrations were required in the electrophysiological studies to achieve effective blockade of the A-current, probably because of toxin binding and diffusion restrictions to penetration as discussed in Section 5.4.1.

Light microscope autoradiography of semithin survey sections revealed dense labelling of the synaptic layers of the hippocampus and dentate gyrus, while lower grain densities were observed over well preserved neuronal cell bodies. Control sections also contained low grain densities, except that some poorly preserved cell somata were more strongly labelled (not shown).

Figure 5.15. Localization of ^{125}I-DTX binding in 14-day-old rat cerebellum molecular layer



Cerebellar slices from 14-day-old rat brain were incubated in 30 nM ^{125}I-DTX (250 Ci/mmol), processed for electron microscope autoradiography and exposed for 118 days. Three branches of a Purkinje cell dendrite (D) are surrounded by tightly packed bundles of unmyelinated parallel fibres (PF). These parallel fibres are still immature and do not form any synaptic boutons. However, the Purkinje cell dendritic branches receive many synapses from basket and stellate cells (arrowheads identify the postsynaptic densities). Only few silver grains are found on this young tissue. The two silver grains shown here are close to synaptic bouton plasma membranes. Magnification =17,000×. Scale bar =1 µm.

The CA_1 region of the hippocampus was studied in detail by electron microscopy. As on the semithin survey sections, high densities of silver grains were found over the stratum oriens and stratum radiatum neuropil layers (Figure 5.16a). The distribution of silver grains in the stratum radiatum was examined in detail. In this layer, the Schaffer collaterals from the CA_3 pyramidal cells synapse onto the dendrites of CA_1 pyramidal cells. Silver grain densities in this area were estimated to be $\simeq$13.3/100 μm^2, compared to grain densities on control sections of $\simeq$3.0/100 μm^2 (118 day exposure). Relative density analysis of the grains on photographs covering $\simeq$1,400 μm^2 (Table 5.6) showed that, as in the cerebellum molecular layer, only synaptic boutons and unmyelinated axons were significantly labelled by ^{125}I-DTX.

The CA_1 pyramidal cells were also studied. Electrophysiological experiments using voltage clamp analysis of the currents in the pyramidal cell soma suggested that DTX acceptors are present in the cell soma membrane (Halliwell *et al.*, 1986). On the autoradiography sections the pyramidal cells were poorly preserved and frequently severely swollen. Occasionally some silver grains were observed on the plasma membrane of such cells (Figure 5.16c). Other cells had ruptured membranes and were intensely labelled internally. A group of seven reasonably preserved cells showing no dense internal labelling was photographed and a montage assembled at 17,500× magnification; this area contained 68 silver grains, which were studied by relative density analysis as detailed in Table 5.7. The analysis revealed an enrichment of grains over all tissue elements studied, except that the cell soma appeared inaccessible in the unruptured cells. When the analysis was corrected by subtracting the inaccessible (unlabelled) cell volumes (as in Section 5.4.3.4), significant labelling was only found on synaptic boutons. Thus the presence of DTX acceptors on the cell soma could not be demonstrated statistically.

As observed with the cerebellum slices, slices from 14-day-old rat hippocampus showed improved preservation. However, unlike the young cerebellum, many silver grains were observed over neuropil layers on semithin survey section autoradiograms and electron microscope autoradiograms. Grains in the CA_1 stratum radiatum again appeared to be located over synaptic boutons and unmyelinated axons (Figure 5.17a), although the grain distributions were not analysed in detail. The pyramidal cells were slightly shrunken,

 (continued on p. 198)

Figure 5.16. Localization of ^{125}I-DTX binding in rat hippocampus

Hippocampus slices from adult rat brain were incubated in 30 nM ^{125}I-DTX (250 Ci/mmol), processed for electron microscope autoradiography and exposed for 118 days. (a) In the stratum radiatum silver grains are observed close to synaptic bouton (SB) membranes and unmyelinated axons (Ax). (b) Stratum radiatum of a control section labelled in 30 nM ^{125}I-DTX in the presence of 10 μM unlabelled DTX. (c) A pyramidal cell (Py; N, nucleus) is severely swollen, but contains two silver grains on its cell soma membrane (identified by arrowheads). Magnifications: 23,000× in a, 13,000× in b and 13,400 in c. All scale bars =1 μm.

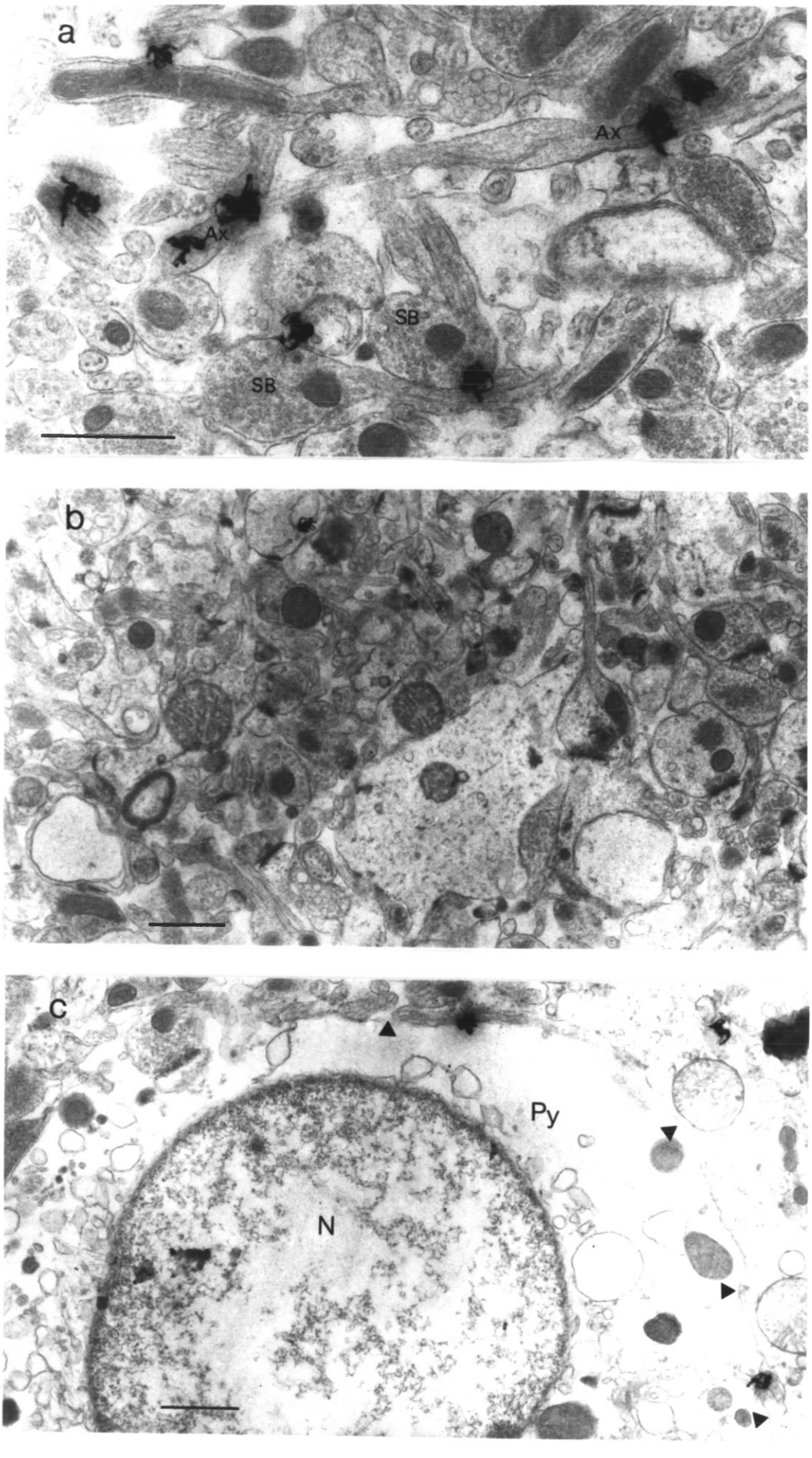

a
Ax
Ax
SB
SB
b
c
Py
N

Table 5.6. ^{125}I-DTX Binding in Rat Hippocampus Stratum Radiatum: Distribution of silver grains and relative grain densities

	Number of Grains	% of Grains	% of Points	Relative Density
Synaptic bouton: Total	52	28.6	22.9	1.2
Internal	6	3.3	2.6	**1.3**
Membrane-associated	46	25.3	20.2	**1.3**
Unmyelinated axon: Total	89	48.9	37.9	**1.3**
Near synaptic bouton	21	11.5	8.0	**1.4**
Non-synaptic	68	37.4	29.9	**1.3**
Myelinated axon: Total	6	3.3	3.6	0.9
Myelin, near synaptic bouton	4	2.2	0.4	5.5
Myelin, non-synaptic	2	1.1	3.0	0.4
Internal	0		0.2	
Dendritic: Total	27	14.8	19.8	0.7
Internal	12	6.6	8.3	0.8
Membrane-associated	15	8.2	11.4	0.7
Near synaptic bouton	5	2.7	3.0	0.9
Non-synaptic	10	5.5	8.5	0.6
Glial: Total	21	11.5	13.1	0.9
Near synaptic bouton	9	4.9	3.3	**1.5**
Non-synaptic	12	6.6	9.8	0.7
Burst cell debris: Total	21	11.5	15.0	0.8
Near synaptic bouton	3	1.6	0.7	2.3
Non-synaptic	18	9.9	14.3	0.7
Intercellular space: Total	25	13.7	15.7	0.9
Near synaptic bouton	5	2.7	2.6	1.0
Non-synaptic	20	11.0	13.1	0.8
Unidentified:	6	3.3	4.5	0.7

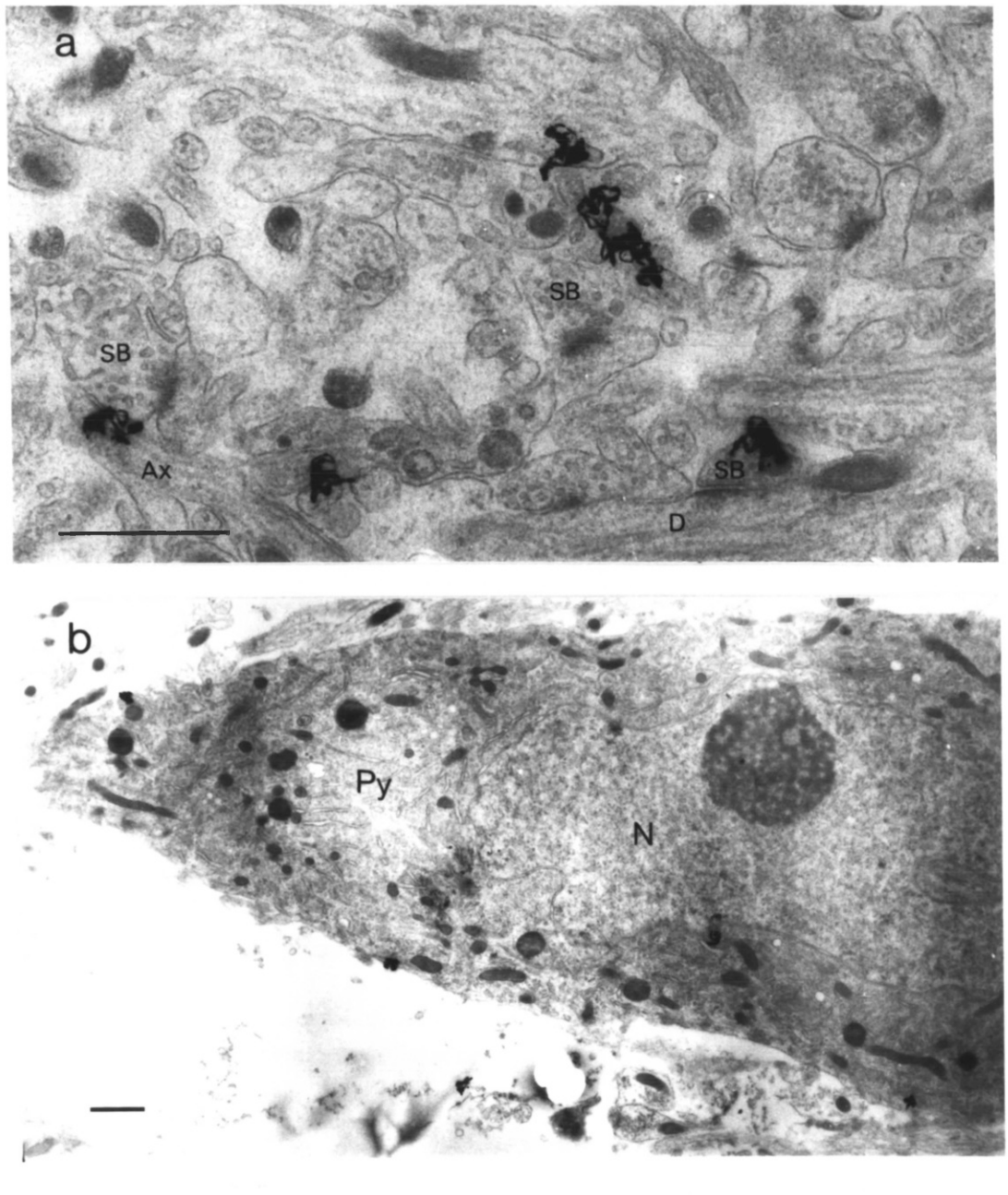
Hippocampal slices from adult rat brain were incubated in 30 nM ^{125}I-DTX (250 Ci/mmol) and processed for electron microscope autoradiography. After exposure for 118 days the autoradiograms were developed, and photographs of 1,400 μm^2 of the stratum radiatum (CA_1) were printed at 17,500× magnification. The contents of 50% density circles about 182 silver grain centres or 840 random points were studied as usual. Significant labelling was defined as a relative density ratio ≥ 1.3 from at least 5 silver grains, and is shown in bold type.

Table 5.7. ^{125}I-DTX Binding to Rat Hippocampus Pyramidal Cells: Distribution of silver grains and relative grain densities

	Number of Grains	% of Grains	% of Points	Relative Density	Corrected Relative Density
Synaptic bouton: Total	22	32.4	10.2	**3.2**	**1.6**
Internal	1	1.5	1.3	1.2	0.6
Membrane-associated	21	30.9	8.9	**3.5**	**1.7**
Unmyelinated axon: Total	23	33.8	17.0	**2.0**	1.0
Near synaptic bouton	2	2.9	2.7	1.1	0.6
Non-synaptic	21	30.9	14.3	2.2	1.1
Dendritic: Total	23	33.8	18.1	1.9	0.9
Internal	6	8.8	5.9	1.5	0.7
Membrane-associated	17	25.0	12.1	**2.1**	1.0
Near synaptic bouton	8	11.8	3.5	**3.4**	**1.7**
Non-synaptic	9	13.2	8.6	1.5	0.8
Cell soma: Total	15	22.1	63.3	0.3	
Internal	5	7.4	52.6	0.1	NA
Membrane-associated	10	14.7	10.8	1.4	0.9
Near synaptic bouton	1	1.5	0.8	1.9	0.7
Non-synaptic	9	13.2	10.0	1.3	0.7
Glial: Total	6	8.8	4.0	**2.2**	1.1
Near synaptic bouton	1	1.5			
Non-synaptic	5	7.4	4.0	1.9	0.9
Intercellular space: Total	6	8.8	3.5	**2.5**	**1.3**
Near synaptic bouton	3	4.4	1.1	**4.0**	**2.1**
Non-synaptic	3	4.4	2.4	1.8	0.9
Unidentified	0		0.8		

Hippocampal slices from adult rat brain were labelled with ^{125}I-DTX and processed as detailed in Table 5.6. A montage of 1,000 μm^2 of the pyramidal cell layer (CA_1) was prepared at 17,500× magnification. The contents of 50% density circles about 68 silver grain centres or 371 random points on photographs were studied. The corrected relative density column shows re-calculated relative density values after both grains and points located over cell soma (internal) and unidentified grains and points were subtracted. After this correction, 63 grains and 173 points remained for analysis. Significant labelling was defined as a relative density ratio ≥ 1.3 from at least 5 silver grains, and is shown in bold type.

Figure 5.17. Localization of ^{125}I-DTX binding in the hippocampus of 14-day-old rat brain



Hippocampus slices from 14-day-old rat brain were processed (together with adult tissue) as detailed in Figure 5.16. (a) In the stratum radiatum, silver grains are observed close to synaptic bouton (SB) membranes and unmyelinated axons (Ax). D, dendritic process. (b) A pyramidal cell (Py; N, nucleus) with three silver grains on its cell soma membrane. Note the improved preservation of this cell compared to that in Figure 5.16c. Magnifications: 23,800× in a and 7,200× in b. All scale bars =1 μm.

but otherwise appeared well preserved. Silver grains could be seen over the cell soma membrane on some cells.(e.g. Figure 5.17b). When montages of the pyramidal cell layer were analysed as for adult hippocampus, very similar results were obtained (data not shown), but corrected density analysis was again unable to demonstrate the presence of DTX acceptors on the cell body membranes.

5.5. Discussion

5.5.1. Ultrastructural Localization of Acceptors for ß-BuTX and DTX in the Central Nervous System: Comparison with the Peripheral Nervous System

Electron microscope autoradiography has here been used to study in detail the distribution of the acceptors for ß-BuTX and DTX in the central nervous system. In agreement with preliminary electron microscope autoradiography of the binding of both ^{3}H-ß-BuTX and ^{125}I-DTX to purified synaptosomes (Othman *et al.*, 1983; Othman, 1983), the present studies on brain slices have shown that the acceptors are enriched in synaptic bouton plasma membranes. In addition, unmyelinated axons (e.g. the parallel fibres of the cerebellum molecular layer) were shown to be labelled by both ^{125}I-ß-BuTX and ^{125}I-DTX. The autoradiography experiments furthermore indicated that some DTX acceptors exist on myelinated axons, and possibly also on neuronal soma membranes (see also Section 5.5.4). Glial elements and dendrites, however, appeared to be devoid of both ß-BuTX and DTX acceptors. Similar distributions of DTX acceptors were observed in slices of cerebellum from young chick and adult rat, and from rat hippocampus.

These results contrast with similar attempts to localize the toxin acceptors in the peripheral nervous system. Both ß-BuTX (Sections 1.3.2.1 and 1.3.3) and DTX (Section 1.4.2) have potent effects on neurotransmission in the periphery, particularly at the neuromuscular junction, and ß-BuTX has been shown to induce the degeneration of cholinergic nerves (Section 1.3.2.2). However, attempts to demonstrate ^{125}I-ß-BuTX binding to endplate regions in rodent diaphragm preparations by biochemical methods (Kato *et al.*, 1977; Newton *et al.*, 1983) or autoradiography (Lee and Tseng, 1966) have not been successful. Similarly, autoradiography of rat thigh muscle cryostat sections labelled with ^{125}I-DTX only revealed a non-specific accumulation of the toxin in some satellite cells,

while nerve and endplate regions (stained for acetylcholinesterase) were unlabelled (A. Pelchen-Matthews, unpublished observations). Likewise, neither ^{125}I-β-BuTX nor ^{125}I-DTX could be localized in mouse diaphragm or chick biventer cervicis nerve muscle preparations, using methods which successfully demonstrated the presynaptic binding and internalization of botulinum neurotoxin (Black and Dolly, 1986b): ^{125}I-β-BuTX and ^{125}I-DTX appeared to become trapped non-specifically in some muscle fibres, while endplate regions remained unlabelled (unpublished observations). However, one early immunocytochemical study with horseradish peroxidase-linked β-BuTX demonstrated toxin binding to frog neuromuscular junction nerve terminal plasma membranes, as well as to some internal membranes (e.g. to the cytoplasmic surface of synaptic vesicles and mitochondria, Strong *et al.*, 1977). Since this study used very high toxin concentrations (μM) and long incubation times (>2 hr), membrane disruption due to phospholipolysis may account for this unexpected labelling pattern.

A high resolution autoradiography study of the binding of β-BuTX to purified cholinergic synaptosomes from *Torpedo* electric organ has revealed a preferential labelling of presynaptic membranes (Esquerda *et al.*, 1982). However, the ^{125}I-β-BuTX preparation used in these studies was not adequately characterized; a sample of β-BuTX iodinated under the same, comparatively harsh, conditions described by these authors yielded a preparation of low specific activity (25 Ci/mmol) which had much reduced toxicity in mice (intraperitoneal toxicity =0.2 μg/g body weight; cf. Section 1.3.2) and bound with low affinity (K_d ≃20 nM) to a very large number of sites (B_{max} ≃1.8 pmol/mg protein; A. Pelchen-Matthews, unpublished observations). The specificity of this toxin in labelling functional acceptors is, therefore, questionable. Furthermore, a very high concentration of ^{125}I-β-BuTX (0.7 μM) was used in the experiments on *Torpedo* synaptosomes (Esquerda *et al.*, 1982); thus the membrane binding observed by autoradiography may have been due to the interaction of the toxin's phospholipase active site with membrane lipids. The presence of toxin acceptors on *Torpedo* synaptosomes has not been demonstrated directly, although it has been reported that high concentrations of β-BuTX can inhibit choline uptake and K^+-stimulated Ca^{2+} influx in this preparation (Dowdall *et al.*, 1979; Marsal *et al.*, 1980).

In the present work, the use of biologically active prepa-

rations of ^{125}I-β-BuTX and ^{125}I-DTX at physiological concentrations has, for the first time, allowed the direct demonstration of the existence of toxin acceptors in neurones.

5.5.2. Electron Microscope Autoradiography of Toxin Acceptors on Brain Slices

Brain slices represent a useful preparation for studies on the distribution of toxin acceptors in the central nervous system. Defined brain areas containing a variety of tissue elements in their normal anatomical arrangement can be dissected, and slices prepared at a controlled thickness. Since brain slices from certain brain regions can also be used in electrophysiology experiments, direct comparison of the morphological distribution of the acceptors with the toxin's effects is possible. Brain slices can be treated with high concentrations of toxin (unlabelled toxin in excess of the physiologically active concentrations must be applied to control samples to assess the level of non-specific binding), which would be lethal if applied *in vivo* (for the intracerebroventricular toxicities of β-BuTX and DTX see Sections 1.3.4 and 1.4.2, respectively). As the blood brain barrier is bypassed, the toxins have direct access to the tissue. However, as detailed in Section 5.4.1, the ability of a toxin to penetrate into the tissue may sometimes be restricted; this appears to be related to toxin size, the number of acceptors present and the amount of intercellular space in the tissue. The diffusion restrictions may be similar to those on cryostat sections (see Section 2.5.1); however, the tissue slices are much thicker (thus toxin penetration over several hundred μm is required) and more compact (there is no disruption by freezing and thawing as in the preparation of cryostat sections). It should be noted that penetration barriers have also been observed with much smaller ligands, for example in electron microscope autoradiography studies using [^{3}H]propylbenzylcholine mustard to label muscarinic cholinergic receptors (Kuhar *et al.*, 1981).

A further disadvantage in the use of brain slices is that some tissue components may be sensitive to the slicing or chopping procedures, and (possibly selectively) damaged. In the experiments described here cell bodies, particularly those of the large Purkinje cells of the cerebellum or of the pyramidal cells of the hippocampus, and glial structures appeared most sensitive. Immature brain tissue from both chick and rat was more resistant to the

treatments; hence, toxin localization studies have been particularly successful on chick cerebellum slices.

Other limitations to the localization studies are inherent in the autoradiography methods used. Scatter of silver grains from the source of the radiation (Section 5.1.1.1) reduces the resolution of autoradiography far below that of the electron microscope. In particular, scatter reduces the number of silver grains observed over small tissue elements like the fine interdigitated processes frequently found in the brain. When the resolution of the present autoradiography system was measured directly (Section 5.4.2) the diameter of a 50% probability circle (2×HR =350 nm) was found to be much greater than that of the parallel fibre axons in the cerebellar molecular layer (≈200 nm). The number of grains over these structures is therefore underestimated, although the use of 50% probability circles partly corrects for such scatter. However, crossfire between small adjacent structures, possibly labelled to different amounts, remains a problem. Thus, in this study, strongly labelled synaptic boutons and unmyelinated axons were frequently found in close apposition. Furthermore, although silver grains were observed over dendrites or glial elements in some experiments, this was always found to be due to crossfire from nearby synaptic boutons. Crossfire from unmyelinated axons has not been analysed in detail. A thorough study of the distribution of toxin acceptors on different tissue elements, taking account of crossfire between all of the structures present, would require computer-aided testing of hypothetical grain distributions, as described by Blackett and Parry (1977) or Salpeter *et al.* (1978).

Another disadvantage of autoradiography is the low efficiency of detection of bound toxin molecules. The specific activities of the radioiodinated toxins used (Section 5.2) indicate that only approximately ⅛ of all the DTX and ½ of the β-BuTX molecules contained an atom of ^{125}I. No more than ¾ of the ^{125}I would have decayed during the exposure time (120 days, 2 half-lives) used in most experiments. Since <50% of decays actually can produce silver grains, only a small proportion of all toxin molecules can be detected. Quantitative analysis of the densities of toxin acceptors has therefore not been attempted.

5.5.3. Ultrastructural Distribution of β-BuTX Acceptors in the Central Nervous System

In the present study, β-BuTX acceptors have been localized to neurones, where they were found to be enriched on unmyelinated axons and, particularly, in the limiting membrane of synaptic boutons. Dendritic and neuronal soma plasma membranes did not appear to contain significant levels of acceptors. Statistical analysis of the silver grain distributions further suggested that glial processes do not bind ^{125}I-β-BuTX. This distribution of the acceptors agrees with the electrophysiological and ultrastructural studies of the action of β-BuTX in the peripheral nervous system (Section 1.3.2), which demonstrated that the toxin specifically damages presynaptic nerve terminals. Electrophysiology studies on brain slices also revealed a presynaptic inhibition of neurotransmitter release by the toxin (Section 1.3.4), while toxin binding studies on synaptosomes directly demonstrated an enrichment of the acceptors on synaptic membranes (Section 1.3.5).

In contrast, previous attempts to localize β-BuTX in brain slices using anti-β-BuTX antibodies linked to horseradish peroxidase showed a deposition of stain within certain cerebellar neurones (particularly in the Purkinje cells, Hirokawa, 1979; Katoh-Semba *et al.*, 1987). Even in the present studies on chick brain slices, a strong labelling of certain poorly preserved Purkinje cells by ^{125}I-β-BuTX was observed on semithin survey section autoradiograms (Figure 5.3), while well preserved cells remained unlabelled; the intense cell labelling was absent from control sections. Electron microscopy revealed accumulations of silver grains only over the burst fragments of degraded Purkinje, cells whose plasma membranes were severely disrupted. ^{125}I-DTX similarly, though less prominently, labelled some poorly preserved Purkinje cells, as well as poorly preserved pyramidal and granule cells in the hippocampal formation. The cell labelling by ^{125}I-DTX was observed on both test and control sections. This suggests that the toxin was trapped non-specifically in certain large neurones which had been damaged during the slice preparation and incubation procedures (cf. Section 5.5.2). ^{125}I-β-BuTX may be trapped similarly in Purkinje cells, the effect being more pronounced due to the larger size of this toxin. The trapping of ^{125}I-β-BuTX, like that of ^{125}I-DTX, is probably non-specific, despite its absence from controls: The phospholipase activity of the excess unlabelled

β-BuTX used on control slices has probably severely disrupted the tissue, allowing more efficient removal of unbound ^{125}I-β-BuTX during the washes of the tissue slices. The cerebellar granule cells never trapped either toxin, possibly because these small interneurones contain less endoplasmic reticulum and other internal membranes than the much larger Purkinje cells.

It is likely that the cell body labelling observed by Hirokawa (1979) and Katoh-Semba *et al.* (1987) in chick and rat cerebellum slices is also due to non-specific trapping of the toxin. These authors used manually cut thick (1 mm) cerebellar slices incubated in a very high concentration (1 μM) of β-BuTX. Under these conditions the Purkinje cells would certainly have suffered severe anoxia, burst, and therefore become able to trap the toxin. Thus, it appears that the cell staining observed by these authors was artifactual. The staining of different cell types of the rat cerebellum with increasing age (Katoh-Semba *et al.*, 1987) suggests that different cell populations may become sensitive to anoxia at different stages during development. The above illustrates the necessity of using physiologically relevant toxin concentrations in localization experiments, and the need for careful interpretation of the resulting labelling patterns.

5.5.4. Distribution of DTX Acceptors in the Central Nervous System

The acceptors for DTX have also been localized to synaptic boutons and parallel fibres in the cerebellum. Inspection of a large number of photographs suggested that the labelling of parallel fibres by ^{125}I-DTX was more prominent than had been noted for ^{125}I-β-BuTX. Thus 58 and 57% of the silver grains over the chick and rat cerebellum molecular layer, respectively, were observed within one HR of parallel fibre membranes, while only 26% of the silver grains on ^{125}I-β-BuTX-labelled chick cerebellum sections were found in a similar position. However, the analysis of random points also revealed that parallel fibres occupied a greater proportion of the tissue sample studied with ^{125}I-DTX (40 and 31% of the random points in chick and rat, respectively) than with ^{125}I-β-BuTX (only16%); this is probably due to the excessive shrinkage suffered by parallel fibres in the tissue slices incubated with ^{125}I-β-BuTX (cf. Figures 5.4 and 5.5). DTX acceptors in rat hippocampus were also found to occur mainly on synaptic boutons and

unmyelinated axons. In addition, ^{125}I-DTX prominently labelled myelinated axons (Figures 5.12 and 5.14, cf. Table 5.3). This saturable binding by ^{125}I-DTX contrasts with the nonspecific trapping of ^{125}I-β-BuTX in similar white matter bundles, but agrees with the Ultrofilm localization studies described in Chapter 4.

The electron microscope localization studies also suggested that some DTX acceptors occur on the cell soma membrane of certain neurones. Thus, silver grains were found near the membrane of granule cells in chick and rat cerebellum (Figures 5.11a and 5.14b) and of pyramidal cells in rat hippocampus (Figures 5.16c and 5.17b). However, the detailed analysis of the silver grain distributions did not reveal any significant enrichment of grains in this location when the inaccessible cell volume was subtracted (Tables 5.4 and 5.7). This is similar to the result obtained with ^{125}I-β-BuTX (Table 5.2). It is noteworthy that half of the silver grains produced by ^{125}I-β-BuTX were shared grains with synaptic bouton structures (9 of 18 silver grains over the granule cell membrane), indicating that the apparent cell membrane labelling was due to crossfire from synapses. In contrast, while similar overall proportions of silver grains (≃15%) were observed over cell membranes in the DTX localization studies, only 1 of 24 grains in the chick cerebellum granule cell layer (Table 5.4) and 1 of 10 over rat hippocampus pyramidal cells (Table 5.7) were shared with synaptic boutons. This suggests that some DTX acceptors may be located on the neuronal plasma membrane, although their density there is not high enough to be statistically significant. The existence of DTX acceptors directly on the plasma membrane of hippocampal pyramidal cells has been demonstrated in the electrophysiology studies of Halliwell *et al.* (1986), where voltage clamp of neuronal cell bodies demonstrated a bockade of the A-current (see also below).

Although variants of DTX acceptors have been identified in binding studies on cryostat sections (Chapter 2, Section 2.5.4) and by Ultrofilm autoradiography (Chapter 4), these acceptor sub-populations have not been distinguished in the electron microscope autoradiography experiments described here. The direct localization of the β-BuTX-resistant DTX acceptors would require pre-incubation and toxin labelling of brain slices in the presence of an excess of unlabelled β-BuTX, which would lead to degradation of the tissue by the phospholipase activity of β-BuTX (cf. the work with ^{125}I-β-BuTX described in Section 5.3.3), making labelled neuronal

structures unidentifiable; such studies may be possible in Sr^{2+} buffer. However, since ^{125}I-DTX prominently labelled myelinated axons, on which no saturable ^{125}I-β-BuTX binding could be observed, it is clear that at least a proportion of the β-BuTX-resistant DTX acceptors are located there. This agrees with the Ultrofilm autoradiography studies, which revealed an enrichment of the resistant acceptors in white matter regions. Some β-BuTX-resistant DTX acceptors may also be found on cell bodies.

5.5.5. Toxin Acceptors and K^+ Channels

The neuronal location and subcellular distribution of the toxin acceptors observed here by electron microscope autoradiography supports the proposal that DTX and β-BuTX act on certain voltage-activated K^+ channels. Thus, axonal K^+ channels would affect the rate of repolarization of action potentials and thereby control neuronal conduction properties, while synaptic K^+ currents determine the duration of synaptic potentials and hence the amount of neurotransmitter released. Furthermore the acceptors appear to be absent from dendrites, which rely on passive potentials initiated by ligand gated channels for their integrating properties, and tend to be devoid of voltage-activated channels (Section 1.2.1). The role of DTX-sensitive K^+ channels on myelinated axons has already been discussed (Section 4.4.4). K^+ channels on the neuronal soma membrane regulate the cell's response to and integration of the graded potentials arriving from the dendrites or from synapses directly onto the soma (Section 1.2.1). It should also be noted that the DTX acceptors in hippocampal slices have here been detected after labelling with ^{125}I-DTX at concentrations shown to attenuate one variant of the K^+ current known as I_A (cf. Halliwell *et al.*, 1986).

The interaction of the toxins with K^+ channels on synapses, axons and cell bodies is also supported by the results from electrophysiology studies. The occurrence of DTX acceptors on synaptic boutons was suggested by the ability of the toxin to facilitate neurotransmitter release at peripheral (Harvey and Karlsson, 1982; Harvey *et al.*, 1984a; Anderson and Harvey, 1985) and central neuromuscular junctions (Docherty *et al.*, 1983). Furthermore the toxin causes a slight depolarization of synaptosomes and promotes the release of [^{3}H]GABA (Weller *et al.*, 1985). Similarly, β-BuTX blocks neurotransmitter release at peripheral

neuromuscular junctions (Section 1.3.2.1) and in the central nervous system (Dolly *et al.*, 1980; Halliwell *et al.*, 1982; Halliwell and Dolly, 1982), and causes a depolarisation of isolated synaptic terminals (Nicholls *et al.*, 1985; Rugolo *et al.*, 1986). The presence of DTX acceptors on axons is suggested by studies on peripheral nerves, which showed that a component of the K^+ current at the frog node of Ranvier was blocked by the toxin (Weller *et al.*, 1985; see also Benoit and Dubois, 1986). The effects of the toxins on cell bodies of hippocampal pyramidal cells and peripheral neurones from various ganglia have been studied by voltage-clamp techniques (Halliwell *et al.*, 1986; Stansfeld *et al.*, 1986; 1987; Penner *et al.*, 1986; Petersen *et al.*, 1986).

CHAPTER 6

General Discussion

6.1. Dendrotoxin and β-Bungarotoxin Bind to Neuronal K^+ Channels

During the last few years, plenty of evidence has accumulated, which shows very clearly that DTX acts by attenuating certain K^+ currents in a variety of neurones (Section 1.4.3; see also Section 4.4.5). All of the physiological effects of the toxin can be explained by such a reduction in neuronal K^+ conductances. Furthermore, patch clamp experiments have recently demonstrated that DTX interacts directly with fast activating, slowly inactivating voltage-sensitive K^+ channels, producing a rapid and reversible blockade of single channel currents when applied to the external surface of detached patches of neuronal membrane (Stansfeld, C.E. and Dolly, J.O., personal communication).

The actions of β-BuTX are less clearly defined than those of DTX because the phospholipase activity masks some of the specific effects of this toxin. Thus, β-BuTX binding is followed by phospholipolysis, resulting in a complex triphasic effect on peripheral neurotransmission (a transient depression is followed by augmentation and finally blockade, Section 1.3.2.1). The effects of β-BuTX in the central nervous system similarly require both specific toxin binding and phospholipase activity (Section 1.3.4). However, recently β-BuTX has also been shown to attenuate K^+ currents on dorsal root ganglion neurones (Petersen *et al.*, 1986) and at peripheral neuromuscular junctions (Anderson *et al.*, 1987),

although the overall inhibition is usually less than that observed with DTX.

The attenuation of K^+ currents by β-BuTX could thus arise either from a direct interaction of the toxin with K^+ channels (as in the case of DTX), or indirectly through lipolysis of essential annular phospholipids of K^+ channels. Other phospholipase-containing presynaptic neurotoxins from snake venoms (e.g. notexin, taipoxin or crotoxin, Howard and Gundersen, 1980; Chang, 1985) also bind specifically to nerve terminals and have similar triphasic effects on neurotransmitter release (Chang *et al.*, 1977b; Chang 1985). However, the mutual facilitation of these presynaptic toxins and β-BuTX (Section 1.3.2.2), and their inability to antagonize the action of DTX in the same way as β-BuTX (Harvey and Karlsson, 1982; Section 1.5) suggest that they bind to different sites. Furthermore, none of the other phospholipase toxins efficiently compete with radiolabelled β-BuTX or DTX binding on synaptosomes (Othman *et al.*, 1982; Rehm and Betz, 1982; Dolly *et al.*, 1984; Black *et al.*, 1986). To date there has been no investigation as to whether any of these toxins also affect K^+ currents, although it has been demonstrated that in the presence of tetraethylammonium ions crotoxin and taipoxin, as well as DTX and β-BuTX, prolong the influx of Ca^{2+} into presynaptic motor nerve terminals during depolarizations (Dreyer and Penner, 1987).

A direct interaction of β-BuTX with specific acceptors distinct from the target site(s) of the other phospholipase toxins is suggested by its unique structure among the presynaptic neurotoxins. Thus, a comparison of the hydropathic indexes of 24 sequenced phospholipase enzymes and toxins (Kini and Iwanaga, 1986) has revealed the existence of a hydrophobic region on the toxic phospholipases (e.g. notexin or the α- and β- subunits of taipoxin); this "neurotoxic site" was absent from non-neurotoxic enzymes (e.g. bovine or porcine pancreatic phospholipase A_2, or non-neurotoxic phospholipase enzymes from various snake venoms). Since this hydrophobic region is exposed on the surface of the phospholipase molecules, close to the catalytic site, it was suggested that it is responsible for the binding of these toxins to nerve terminals (Kini and Iwanaga, 1986). However, despite the potent toxicity of β-BuTX, the neurotoxic site was not found on any of the three A-chains of the β-BuTX isotoxins (cf. Section 1.3.1); β-BuTX therefore depends on the B chain (which is homologous to DTX, Section

1.5 and Figure 1.2) for its ability to bind to nerve terminals. This unique structure of the toxin is believed to be responsible for the exclusively presynaptic specificity of β-BuTX compared to the other phospholipase toxins (Ho *et al.*, 1986). Thus β-BuTX is able to interact with a distinct population of neuronal acceptors which, by analogy with DTX, are likely to be K^+ channels.

6.2. Localization of K^+ Channels by Autoradiography and other Methods

In the present study, the distributions of functional acceptors for β-BuTX and DTX have been mapped in both the rat and chick central nervous systems using various autoradiographic methods. As detailed in Chapters 3 and 4, quantitative Ultrofilm autoradiography has revealed distinct and overlapping distributions of the binding sites for these toxins. These studies have allowed measurements of acceptor densities in many brain areas, some of which are too small or complex in structure to be accessible for electrophysiological studies or dissected and analysed biochemically. Electron microscope autoradiography has furthermore shown that the acceptors are located on the plasma membrane of neurones, being particularly enriched on axons and synaptic boutons. However, due to problems with regard to obtaining well preserved tissue samples and achieving adequate toxin penetration into the brain slices (cf. Chapter 5, Section 5.5.2), it was not clear what proportion of the acceptors was saturated under the conditions used. Thus, while the silver grain distributions were studied statistically, a full quantitative analysis of acceptor densities has not been attempted. Furthermore the different DTX acceptor sub-types have not been distinguished directly in the electron microscope studies.

Because cross-fire effects limit the resolution of electron microscope autoradiography, the question of the existence of DTX-sensitive K^+ channels on cell soma membranes could not be answered unambiguously. Histochemical techniques, which potentially have a much higher resolution than autoradiography, are now required. However, although the preparation of both polyclonal and monoclonal antibodies to β-BuTX (Caratsch *et al.*, 1982; Strong *et al.*, 1984) and DTX (Mehraban *et al.*, 1986) has been described, immunocytochemical localization methods have not yet been successful with either toxin, even though a range of conditions has been

tested (K.A. Awan and A. Pelchen-Matthews, unpublished observations). This may at least partly be due to steric hindrance preventing antibody access to the bound toxins. The monoclonal antibodies raised against DTX are specific for this toxin and do not cross-react with any of its homologues, suggesting that they do not bind directly to the toxin's active site, which is likely to be highly conserved. Nonetheless, the antibodies were able to neutralize the toxicity of DTX on intracerebroventricular injection and prevent ^{125}I-DTX binding to synaptosomes (Mehraban *et al.*, 1986). Hence the epitope recognized by the antibodies may be hidden once DTX is bound to its acceptor. Similarly, monoclonal antibodies to β-BuTX, which recognize an epitope on the phospholipase-containing A-chain of the toxin, can prolong the time to death in mice injected intraperitoneally with β-BuTX (Strong *et al.*, 1984), but are unable to prevent neuromuscular blockade once the toxin has bound to nerve terminals, suggesting again that the epitopes recognized are hidden (cf. Chang, 1985). In addition, it should be noted that the DTX acceptors appear to be very sensitive to the strong fixatives required to preserve tissue for electron microscopy (c.f. Section 2.4.1.1). Methods relying on the localization of bound toxin by immunolabelling or histochemical techniques in conjunction with postembedding staining or cryosectioning will therefore still require the labelling of tissue preparations with DTX or β-BuTX prior to fixation; thus the problems of toxin penetration, achieving adequate preservation and of unbound toxin being trapped in the tissue will remain. As the acceptors for β-BuTX and DTX can now be solubilized in active form (Rehm and Betz, 1984; Mehraban *et al.*, 1985; Black *et al.*, 1988) it should be possible to prepare monoclonal antibodies directly to the acceptor proteins. These antibodies may then be used in light or electron microscope localization studies.

6.3. Heterogeneity of DTX Acceptors and K^+ Channel Variants

The present Ultrofilm autoradiography study has provided the most direct evidence so far of heterogeneity among the DTX acceptors in the rat central nervous system. At least three acceptor populations may be distinguished: The fact that DTX potently inhibits ^{125}I-β-BuTX binding to rat brain cryostat sections (Sections 2.4.2 and 3.4.1) suggests that there must be a population of

acceptors binding both β-BuTX and DTX with high affinity. The lower efficacy of the competition by β-BuTX with most of the ^{125}I-DTX binding identifies a second DTX acceptor variant with reduced affinity for β-BuTX (see also Sections 2.5.4 and 4.4.2). In addition, a population of apparently β-BuTX-resistant ^{125}I-DTX acceptors has been localized in white matter regions. The autoradiography studies have also shown that these acceptor variants have overlapping, but distinctly different, distributions in the brain. Similar distributions of the common β-BuTX/DTX acceptors in synaptic areas and the β-BuTX-resistant DTX acceptors along myelinated tracts were observed in both chick and rat brain. The electron microscopy experiments (Chapter 5) have confirmed these observations and have demonstrated the distribution of both the common and β-BuTX-resistant acceptors on different parts of the neurone.

As noted in Section 1.4.3, DTX and its homologue, toxin I, have also been shown to attenuate a number of K^+ currents on various neurones. These have been listed in Table 6.1 in order of increasing sensitivity to the facilitatory toxins and to 4-AP (which, however, is orders of magnitude less potent). At least three variants of rapidly activating 4-AP sensitive K^+ currents can be distinguished in mammalian neurones. The rapid transient variant of I_A in dorsal root ganglion, superior cervical ganglion or nodose ganglion A cells (I) is apparently insensitive to DTX. In contrast, the more slowly inactivating I_A of hippocampal pyramidal cells (II) shows an intermediate sensitivity to DTX and toxin I, while the non-inactivating K^+ current of nodose ganglion A cells or dorsal root ganglion neurones (III) is blocked by nanomolar concentrations of DTX. The latter mammalian K^+ current may be similar to one of the currents of the frog node of Ranvier, I_{Kf1} (IV), which is inhibited by sub-nanomolar concentrations of toxin I (see also Dubois, 1983). A proportion of the K^+ current of motor nerve terminals is also sensitive to DTX (Anderson *et al.*, 1987), but the detailed characterization of the currents present in this location has not yet been possible.

It is possible that these DTX-sensitive K^+ current variants correspond to the acceptor populations identified here in binding studies and by autoradiography. Some indications of how the acceptor heterogeneity may arise at the molecular level have recently come from studies of *Drosophila Shaker* mutants.

Table 6.1. Variants of rapidly activating voltage dependent K^+ currents and their sensitivity to facilitatory neurotoxins

	Cell type	Current	Time constant of current decay ($t_{1/2}$)	Blockade by diamino-pyridines	Inhibition by DTX (nM)	Inhibition by toxin I (nM)	References
I	Dorsal root ganglion	I_A	ND	Some inhibition by 3,4-DAP	insensitive	ND	(1)
	Superior cervical ganglion	I_A	10 ms	1-5 mM 4-AP	>800	ND	(2,3)
	Nodose ganglion C cell	I_A	18-24 ms	1-5 mM 4-AP	>800	ND	(3,4)
II	Hippocampus CA_1 pyra-midal cells	I_A	50->100 ms	0.1-0.5 mM 4-AP	50-350	10-50	(5,6)
III	Nodose ganglion A cell	slowly inactivating	15-24 s	3-30 μM 4-AP	2.1 (IC_{50})	ND	(3,4)
	Dorsal root ganglion	non-inactivating	ND	0.5 mM 3,4-DAP	0.14-1.4	ND	(1)
IV	Frog node of Ranvier	I_{Kf1}	45 s	10 μM 4-AP	ND	0.4	(7)

References: (1) Penner *et al.* (1986); (2) Stansfeld *et al.* (1987); (3) Dolly *et al.* (1987); (4);Stansfeld *et al.* (1986); (5) Dolly *et al.* (1984); (6) Halliwell *et al.* (1986); (7) Benoit and Dubois (1986).

6.4. Possible Structure of Rapidly Activating Voltage Sensitive K^+ Channels

6.4.1. Sequences of K^+ Channel Subunits in *Drosophila*

Shaker mutants in *Drosophila melanogaster* were first isolated because they shake their legs vigorously under ether anaesthesia. Electrophysiological studies demonstrated that the mutations caused hyperexcitability of larval presynaptic terminals and abnormally long action potentials in the adult giant axon. These effects could be mimicked by the application of 4-AP to wild-type preparations, suggesting that I_A is defective in the *Shaker* mutants (Jan *et al.*, 1977; Tanouye *et al.*, 1981). This has been confirmed by voltage clamp studies of pupal preparations (Salkoff, 1983).

Recently genomic DNA from the *Shaker* locus has been identified by chromosomal walking, and several *Shaker* mutations have been mapped to this region on the genome (Papazian *et al.*, 1987). Furthermore a number of complementary DNA (cDNA) clones, which hybridized with genomic DNA from the *Shaker* region, have been identified and sequenced (Tempel *et al.*, 1987; Schwarz *et al.*, 1988). These cDNA's predict protein sequences with several features common to other characterized integral membrane channels. For example, conceptual translation of the single long open reading frame of one of the cDNAs, ShA, predicts a protein of 616 amino acid residues and M_r 70,200 d (Tempel *et al.*, 1987). The gene product would be an integral membrane protein containing a central core of six hydrophobic, apparently membrane-spanning segments; in addition there is a stretch of 22 mainly hydrophobic amino acids, in which, however, every third residue is either arginine or lysine. A similar, highly homologous positively charged region was first observed on the voltage-dependent Na^+ channel (the S4 region; Noda *et al.*, 1984; 1986), and more recently also on the mammalian dihydropyridine receptor/Ca^{2+} channel (Tanabe *et al.*, 1987), and is believed to be involved in voltage-gating of the channels (cf. Catterall, 1986). Since the predicted ShA protein does not have a signal sequence, the N-terminus is proposed to be cytoplasmic (Tempel *et al.*, 1987). This might result in a trans-membrane topography as shown in Figure 6.1a. Two of three possible N-linked glycosylation sites are thus located extracellularly, as is a possible cyclic AMP-mediated phosphorylation site; obviously if this site were found to be phosphorylated *in vivo*, the model would have to be revised.

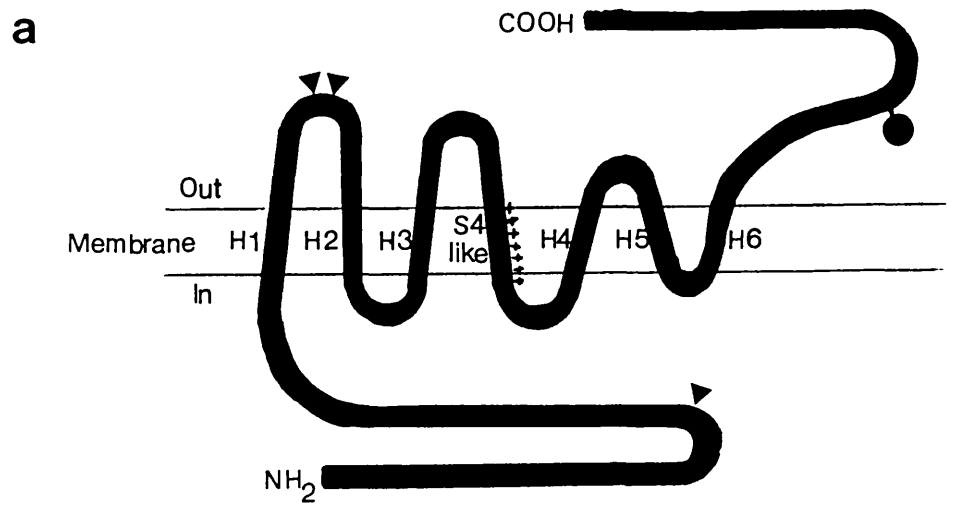
Figure 6.1. Structure of *Drosophila Shaker* K^+ channel protein subunits

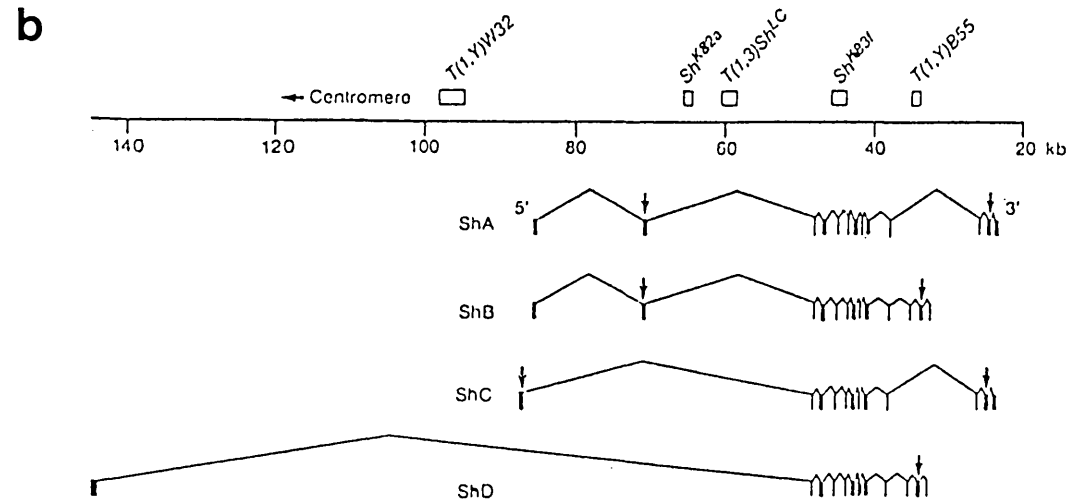
(a) Proposed model for the transmembrane topography of the ShA protein. Potential sites for N-glycosylation (▼) and cyclic AMP-mediated phosphorylation (Ⓟ) are shown. The positions of the hydrophobic transmembrane helices (H1-H6) and the voltage-sensor (S4-like region) are also indicated.

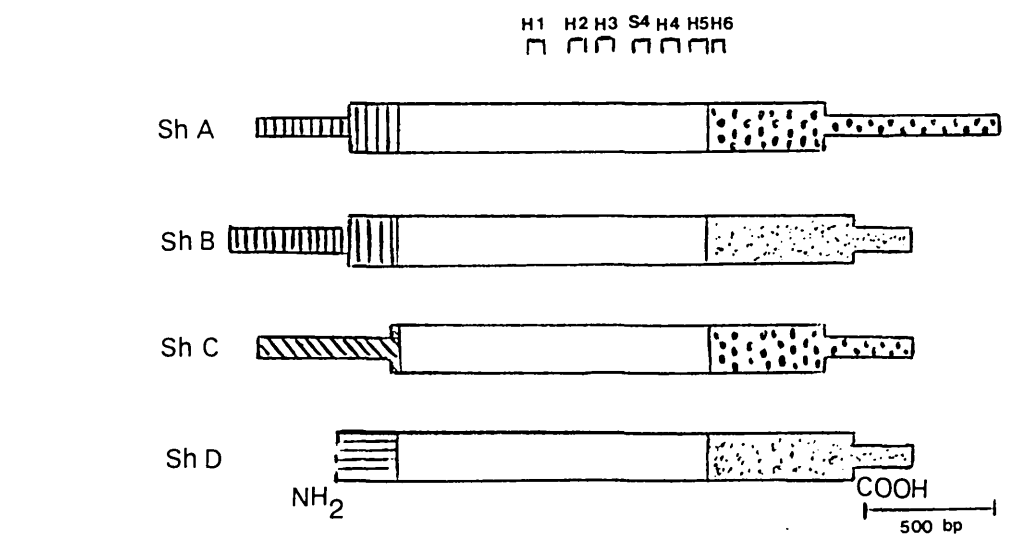
(b) The exon map of cDNA clones from the *Shaker* locus, as determined by sequencing of genomic and cDNA clones. The gene is located on the X chromosome in the region of the polytene bands 16F. The distance along the genome is given relative to the origin of the chromosomal walk used to sequence it, which started with cDNA clone adm135H4 (Papazian *et al.*, 1987). The positions of several *Shaker* mutations are marked (□). The arrows point to the limits of the predicted open reading frames in ShA-ShD.

(c) A diagram of the four classes of cDNA sequenced. Regions shaded identically have identical amino acid sequences and arise from identical exons (cf. b above). The common central region is unshaded. The predicted open reading frames encoding protein are drawn wider. The locations of the putative transmembrane helices H1-H6, and of the S4-like region are indicated above.

(based on Tempel et al., 1987 and Schwarz et al., 1988)


a
COOH
Out
Membrane
In
H1
H2
H3
S4
like
H4
H5
H6
NH2


b
T(1;Y)W32
Sh^KS3a
T(1;3)ShLC
Sh^KS3l
T(1;Y)B55
Centromere
140
120
100
80
60
40
20 kb
ShA
5'
3'
ShB
ShC
ShD


c
H1 H2 H3 S4 H4 H5H6
Sh A
Sh B
Sh C
Sh D
NH2
COOH
500 bp

Shaker is a complex transcription unit, containing multiple exons distributed over at least 65 kilobases of genomic DNA (Papazian *et al.*, 1987). This gene, furthermore, produces several alternatively spliced messenger RNA transcripts, the cDNAs of which predict at least four different proteins (Figure 6.1b). In addition to ShA (above), ShB and ShC encode proteins containing 656, and 554 or 556 amino acid residues, corresponding to M_r of 74,000d and 64,000d, respectively (Schwarz *et al.*, 1988). The N-terminus of a fourth protein, ShD, has not yet been identified, although a sequence similar to ShD has also been reported by Kamb *et al.* (1987). All four classes of protein share a common central region of about 380 amino acid residues, containing four of the six putative trans-membrane helices, as well as the S4 region, but differ from each other in the N- and C-terminal regions, and in some of the untranslated regions which presumably control expression (Figure 6.1c). Of two possible C-terminal regions, which account for about one third of the protein, one is shared by ShA and ShC, the other by ShB and ShD. At the N-terminus, three variants diverge at a single splice site: ShA and ShB are similar, while different N-termini are observed in ShC and in ShD (Figure 6.1c). Another recently sequenced cDNA clone predicts a further N-terminal variant (Baumann *et al.*, 1987).

Evidence that these proposed *Shaker* proteins do encode K^+ channels was recently obtained by transcribing the ShA and ShB cDNA clones *in vitro* and injecting the resulting messenger RNAs into *Xenopus* oocytes. 4-AP-sensitive A-currents could be recorded on the oocytes two days after injection. Interestingly, the detailed characteristics of the currents from the two cDNA clones differed. Thus, while the current from ShB inactivated more quickly than that from ShA, the inactivation of the ShB current was not complete (Timpe *et al.*, 1988).

6.4.2. Structure of K^+ Channels

Although a direct interaction of DTX with *Drosophila* A-current K^+ channels has not yet been demonstrated, it seems likely that the vertebrate K^+ channels affected by this toxin are similar to the *Shaker* gene products described. Channel proteins appear to be widely conserved in evolution. Thus, for example, the acetylcholine receptors from electric fish, chick and rat consist of similar homologous subunits, which furthermore resemble the

glycine and GABA receptor channel subunits in both primary sequence and trans-membrane topology (Grenningloh *et al.*, 1987; Schofield *et al.*, 1987). Likewise, Na^+ channels from electric eel (Noda *et al.*, 1984), rat brain (Noda *et al.*, 1986) and *Drosophila* (Salkoff *et al.*, 1987) have conserved amino acid sequences and trans-membrane structure; in addition, the mammalian T-tubule dihydropyridine receptor/Ca^{2+} channel has been shown to be homologous to the Na^+ channel (Tanabe *et al.*, 1987). It should also be noted that cross-linking studies with ^{125}I-DTX have identified polypeptide components of M_r 65,000-75,000d in synaptic membranes from chick and rat brain (Section 1.4.4), corresponding exactly to the size of the *Shaker* gene products. Thus the studies with DTX may shed some further light on the structure of mammalian voltage-sensitive K^+ channels.

Channels which allow inorganic ions (Na^+, K^+, Ca^{2+} or Cl^-) to diffuse through the hydrophobic plasma membrane must include a pore structure lined with approximately 20 trans-membrane α-helices. The ligand gated ion channels (acetylcholine, GABA and glycine receptors, cf. Dolly and Barnard, 1984, and the references cited above) for instance consist of four or five (different) sub-units, each of which contains 4-5 trans-membrane helices. The voltage-gated Na^+ and Ca^{2+} channels, by contrast, are larger proteins (M_r 200,000-250,000d), consisting of four homologous internal repeats each with six membrane-spanning segments (including the arginine-rich positively charged voltage gating segment, S4, Noda *et al.*, 1984; 1986; Tanabe *et al.*, 1987). A single *Shaker* polypeptide (≃70,000d) is thus obviously not sufficient to form an ion channel. Studies of the DTX acceptors have also indicated that the polypeptides which can be chemically cross-linked to bound ^{125}I-DTX must be part of a larger oligomer: The solubilized DTX acceptors appear to have a molecular weight between 405,000 and 465,000d ($s_{20,w}$ =13.2, Stokes radius =8.6 nm) on gel filtration or sucrose density gradient sedimentation analysis (Mehraban *et al.*, 1985; Black, *et al.*, 1988).

It is clear, therefore, that several *Shaker*-like protein subunits are required to form a K^+ channel. The expression of ShA and ShB in oocytes (Timpe *et al.*, 1988, see above) indicates that homo-oligomeric complexes can act as functional K^+ channels. Since the major part of the hydrophobic core of the *Shaker* gene products is conserved (Figure 6.1c), hetero-oligomeric associations of

different classes of *Shaker* protein subunits should be possible. Such associations might be used *in vivo* to allow fine-tuning of K^+ currents. At least a proportion of the putative K^+ channel/DTX acceptors of vertebrate neurones also appear to have a heterogeneous subunit composition. Thus, cross-linking studies on synaptic membranes from rat and chick brain have revealed that ^{125}I-DTX and ^{125}I-β-BuTX label separate polypeptide subunits with M_r of ≃70,000d (Section 1.4.4) and 95,000d (Rehm and Betz, 1983, cf. Section 1.3.5), respectively. As the labelling with ^{125}I-DTX can be reduced by β-BuTX (Mehraban *et al.*, 1984; Black and Dolly, 1986), and because mutual inhibition of toxin binding is observed with the toxin acceptors solubilized from purified synaptic plasma membranes (Mehraban *et al.*, 1985; Black *et al.*, 1988; Rehm and Betz, 1984), it appears that both polypeptides are common constituents of at least one oligomeric species of the acceptor.

Since alternative splicing of transcripts from the *Drosophila Shaker* gene complex allows the expression of at least four types of K^+ channel subunits (other cDNAs have not yet been sequenced), significant heterogeneity of multimeric K^+ channels with different subunit compositions is theoretically possible. While it is not yet clear whether mammalian K^+ channels are formed in the same way, the cloning of the *Shaker* gene complex has provided a molecular model to explain the heterogeneity of DTX acceptors and the variants of K^+ currents affected by the toxin.

6.5. Conclusions

The distribution of acceptors for DTX and β-BuTX, two potent neurotoxins, have here been mapped in the rat and chick central nervous systems using Ultrofilm and electron microscope autoradiography methods. Furthermore, evidence has been presented for the existence of several sub-types of DTX acceptors. These appear to correspond to variants of DTX-sensitive K^+ currents defined electrophysiologically.

The DTX acceptor sub-populations were shown to have distinct, but overlapping distibutions in the grey and white matter regions of the brain, and to be located on different parts of neurones. It is not clear, however, whether individual neurones express the different acceptor variants, or whether one cell may have more than one acceptor type in different sub-cellular

locations. With the recent sequencing of *Drosophila* K^+ channels, the elucidation of the structure of mammalian K^+ channels should be possible in the near future. In particular, it will be necessary to establish which combinations and stoichiometries of polypeptide subunits create the multiplicity of K^+ channels required physiologically. *In situ* hybridization techniques may complement the present localization studies. Further exciting questions concern the control of expression of the different channel variants, and their sorting to different cellular locations.

APPENDIX A.1

Purification and Radiolabelling of β-Bungarotoxin

A.1.1. Purification of β-BuTX from *Bungarus multicinctus* Venom

Ion exchange fractionation methods allow the separation of *B. multicinctus* venom into between six and 15 peaks (see e.g. Lee *et al.*, 1972; Kelly and Brown, 1974; Dryden *et al.*, 1974; Eterovic *et al.*, 1975; Abe *et al.*, 1977a; Spokes and Dolly, 1980). Usually a weakly acidic cation exchanger like CM-Sephadex C-50 is used. The venom component to elute first under these conditions is guanosine. The largest peak on the elution profile is α-BuTX. This is followed by one or more smaller peaks of postsynaptically active toxins, and then a group of presynaptic toxin peaks, the largest of which (peak V according to Lee *et al.*, 1972; Spokes and Dolly, 1980; fraction 10 according to Eterovic *et al.*, 1975; X according to Kondo *et al.*, 1982a; or 14 according to Wu *et al.*, 1982) contains mainly β-BuTX.

β-BuTX was purified here by the method of Spokes and Dolly (1980), except that the preparative flat bed isoelectric focusing step was replaced by a column chromatofocusing step. *B. multicinctus* venom (0.5g, Miami Serpentarium Laboratories, Florida, U.S.A.) was dissolved in 10 ml of 50 mM ammonium acetate buffer, pH 7, cleared by centrifugation for 15 min at 1000g, and loaded onto an 85 cm (2.5 cm diameter) column of CM-Sephadex C-50 (Pharmacia Fine Chemicals, Hounslow, Middlesex) equilibrated in 50 mM ammonium acetate, pH 7, at 4°C. The column was washed with ≈150 ml of this buffer before elution with a convex gradient of ammonium acetate buffer (prepared with 400 ml of 50 mM ammonium acetate, pH 7, the start buffer, and 0.9 M ammonium acetate, pH 7.4). Fractions (4 ml) were collected, and their protein content determined by measuring A_{280}. The resulting elution profile was similar to that of Spokes and Dolly (1980). Fractions from the β-BuTX-containing peak (V) were pooled, concentrated, desalted on a 40 cm (1 cm diameter) column of Sephadex G-50 equilibrated in and eluted with 50 mM ammonium acetate, pH 7.4 and lyophilized.

The chromatofocusing step used a column of Polybuffer™ exchanger, PBE 118 (Pharmacia), equilibrated in 0.025 M triethylamine hydrochloric acid, pH 11. A pH elution gradient was produced

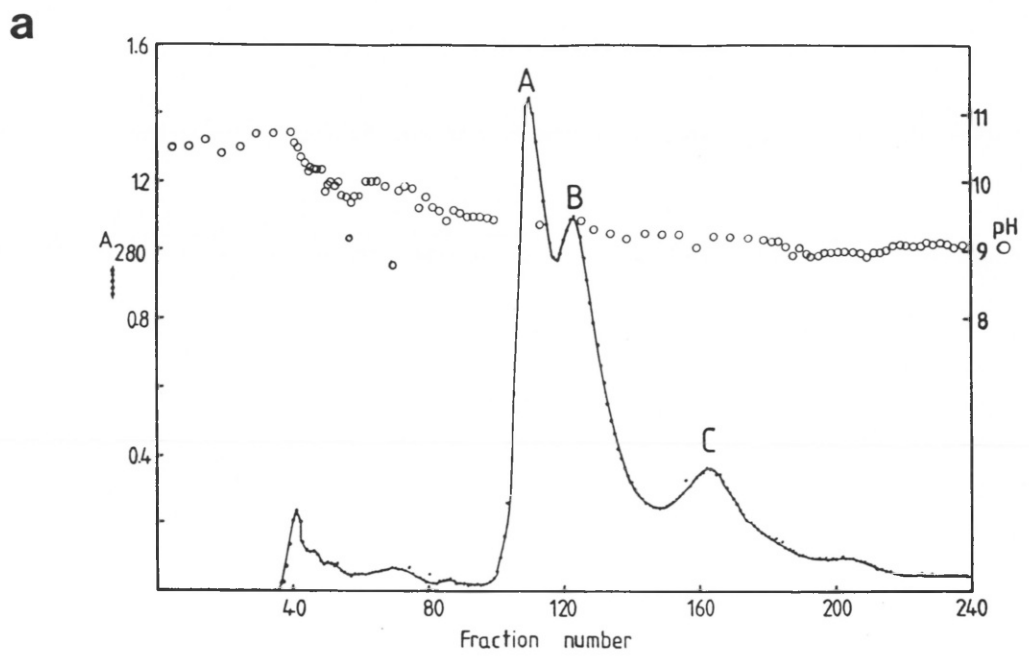
with Pharmalyte™ pH 8-10.5 (Pharmacia), diluted 52.5× (i.e. 3.5 ml Pharmalyte solution in 180 ml of deionized, degassed water) and adjusted to pH 8.5 with HCl (the elution buffer). The lyophilized peak V sample (see above) was dissolved in 3 ml of this elution buffer, loaded onto the polybuffer exchanger column after a bed of 3 ml of elution buffer, and eluted. Fractions (0.6 ml) were collected, their protein content measured as A_{280}, and their pH determined. A typical elution profile is shown in Figure A.1a. The β-BuTX fractions (peak A) were pooled as shown, freeze-dried and separated from the Pharmalytes by gel filtration on a Sephadex G-50 column as above. The resulting β-BuTX had an apparent molecular weight of 20,500d on non-reducing sodium dodecyl sulphate polyacrylamide gel electrophoresis, and consisted of two subumnits of apparent molecular weight 12,000d and 9,000d, close the the values reported by other authors (Abe *et al.*, 1977a; Hanley *et al.*, 1977; Kondo *et al.*, 1978a). When studied on non-denaturing β-alanine polyacrylamide gel electrophoresis (Reisfeld *et al.*, 1962), the toxin appeared essentially free of impurities compared to peak V of *B. multicinctus* venom and the other fractions from the chromatofocusing step (Figure A.1b). All β-BuTX samples prepared in this way were lethal to mice at ≤0.01 μg/g body weight.

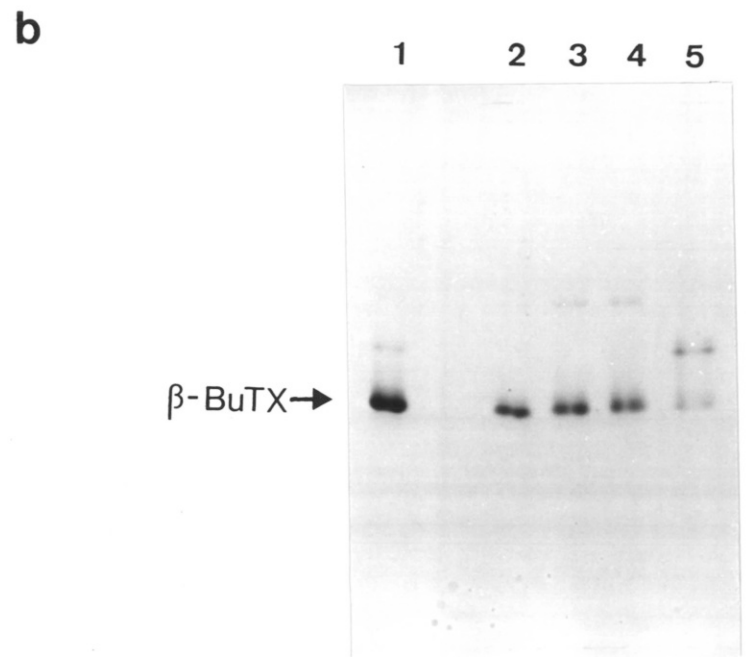
A.1.2. Labelling of β-BuTX with ^{3}H-N-succinimidyl propionate

This was done essentially as described by Othman *et al.*, (1982). Briefly, N-succinimidyl-[2,3-^{3}H]propionate (Amersham International plc, Buckinghamshire; 5 ml containing 100 nmol at 48 Ci/mmol) was transferred to a glass reaction tube and the solvent (toluene) evaporated under a stream of nitrogen gas. β-BuTX (0.63 mg, 30 nmol) was added in 0.2 ml of 0.02 M sodium phosphate buffer, pH 7.4. After incubation at 22°C for 2 hr the reaction mixture was separated by gel filtration on a 40 cm (1 cm diameter) column of Sephadex G-50 equilibrated in and eluted with 50 mM ammonium acetate buffer, pH 7.4.

75% of the ^{3}H-N-succinimidyl propionate reagent was recovered in the reaction mixture, and 60% of the ^{3}H from this was incorporated into the protein, yielding ^{3}H-β-BuTX of a final specific activity of 140 Ci/mmol. The resulting toxin had ≈80% of the phospholipase activity of native β-BuTX, and bound to rat brain synaptosomes with a K_d =0.6 nM.

Figure A.1. Chromatofocusing of fraction V of *B. multicinctus* venom





(a) Absorbance at 280 nm (●-●-●) and pH (ooo) of fractions (0.6 ml) eluted after chromatofocusing 70 mg of peak V from *B. multicinctus* venom as described. β-BuTX elutes as peak A: fractions 100 to 113 were pooled, freeze dried and separated from pharmalytes by gel filtration (see text).

(b) Non-denaturing polyacrylamide gel electrophoresis of the toxin peaks obtained above. Lane 1: Fraction V of *B. multicinctus* venom. Lane 2: Chromatofocusing peak A (pure β-BuTX). Lane 3: Chromatofocusing peak B. Lane 4: Sample of chromatofocusing fraction 150, between peak B and peak C. Lane 5: Chromatofocusing peak C.

A.1.3. Labelling of β-BuTX with Iodine-125

This was done under relatively mild conditions using a modification of the chloramine-T method as described by Williams *et al.* (1983) for botulinum neurotoxin. Briefly, $Na^{125}I$ (50 µl containing 5 mCi, Amersham International) was added to β-BuTX (100 µg) in 20 µl of 0.1 M sodium phosphate buffer, pH 7.4. The reaction was initiated by adding chloramine-T (sodium toluene-p-sulphonochloramine) to a final concentration of 60 µg/ml. After thorough mixing for 30s the reaction was quenched by addition of 50 µl of saturated DL-tyrosine solution. The ^{125}I-β-BuTX was separated from free ^{125}I-iodine by gel filtration on Sephadex G-50 equilibrated and eluted with 0.1 M sodium phosphate buffer, pH 7.4. This yielded a preparation of ^{125}I-β-BuTX with a specific activity ≈540 Ci/mmol, binding to rat cerebrocortical synaptosomes with high affinity (K_d =0.25 nM).

Some of the ^{125}I-β-BuTX samples used in the studies described in this thesis were prepared by Alexander Breeze, using a further modification of the method above, as detailed for ^{125}I-DTX by Black *et al.* (1986).

APPENDIX A.2

Analysis of Ligand-Acceptor Interaction: Formulae and Definitions

The binding of a homogeneous univalent species of ligand to a single non-interacting population of acceptor sites can be described by the second order binding equation:

$$L + A \underset{k_{-1}}{\overset{k_1}{\rightleftharpoons}} LA \qquad (1)$$

At equilibrium

$$K_d = \frac{[L][A]}{[LA]} \qquad (2)$$

where [L] is the concentration of free (unbound) ligand, [A] is the concentration of acceptor sites and [LA] the concentration of ligand-acceptor complex. K_d is the equilibrium dissociation constant, related to k_1 and k_{-1}, the kinetic association and dissociation rate constants (respectively) by the equation:

$$K_d = \frac{k_{-1}}{k_1} \qquad (3)$$

In binding experiments a radiolabelled ligand, L, is used to study the properties of its acceptors.

A.2.1. The Scatchard Equation

The proportion of acceptors occupied by ligand, r, is given by:

$$r = \frac{[LA]}{[A] + [L]} \qquad (4)$$

when [LA] is measured at a series of ligand concentrations, [L], a plot of [LA] against [L], the saturation binding curve, is a rectangular hyperbola, with [LA] tending asymptotically towards $[A]_T$, the total number of acceptors present ($[A]_T = [A] + [LA]$; $[A]_T$ is also known as B_{max}).

The hyperbolic binding curve can be transformed to give a

straight line relationship using the Scatchard equation (Scatchard, 1949)

$$\frac{[LA]}{[L]} = \frac{[A]_T - [LA]}{K_d} \qquad (5a)$$

more commonly represented as

$$\frac{B}{F} = \frac{B_{max} - B}{K_d} \qquad (5b)$$

where B = [LA] and F = [L]. A plot of B/F against B gives a straight line with a slope of $-1/K_d$ and an x-axis intercept = B_{max}.

A.2.2. The Hill Equation

If the concentration of binding sites, $[A]_T$ or B_{max}, is known, it may be used in the Hill equation (Hill, 1910),

$$\log\left(\frac{[LA]}{[A]_T - [LA]}\right) = n_H \log[L] - n_H \log K_{0.5} \qquad (6a)$$

alternatively expressed as

$$\log\left(\frac{B}{B_{max} - B}\right) = n_H \log F - n_H \log K_{0.5} \qquad (6b)$$

where n_H is the Hill coefficient, and $K_{0.5}$ is the concentration of ligand at which half of the binding sites are occupied. Thus a plot of the right hand side of equation (6a) or (6b) against log[L] or log F, respectively, has a slope of n_H and an intercept on the abscissa of $K_{0.5}$. When the reaction follows the principles of mass action, n_H = 1.0 and $K_{0.5}$ is the K_d.

A.2.3. Kinetic Studies

The second order rate equation (1) can be integrated (Weiland and Molinoff, 1981) to give:

$$\ln\left[\frac{[LA]eq\left([L]_T - \frac{[LA]\,[LA]eq}{[A]_T}\right)}{[L]_T\left([LA]_{eq} - [LA]\right)}\right] = k_1 t\left[\frac{[L]_T\,[A]_T}{[LA]_{eq}} - [LA]_{eq}\right] \qquad (7)$$

where $[L]_T$ is the total concentration of ligand ([L] + [LA]), $[LA]_{eq}$ the concentration of ligand-acceptor complex at equilibrium and [LA] the concentration of ligand-acceptor complex at time = t. When the left side of the equation is plotted against t, a straight line is obtained with a slope of $k_1\left(\frac{[L]_T\,[A]_T}{[LA]_{eq}} - [LA]_{eq}\right)$.

Equation (6) makes no assumptions concerning the relative concen-

trations of ligand and binding sites. However, if $[L]_T >> [LA]_{eq}$, equation (6) simplifies to a first order equation;

$$\ln\left(\frac{[LA]_{eq}}{[LA]_{eq} - [LA]}\right) = k_1 t\left(\frac{[L]_T\,[A]_T}{[LA]_{eq}}\right) \qquad (8)$$

from which k_1 can be likewise determined. When k_1 is derived using (6) or (7), $[A]_T$ (= B_{max}) must be determined from a Scatchard plot.

The right side of equation (7) can be rearranged using (2) and (3) (Weiland and Molinoff, 1981) to give

$$\ln\left(\frac{[LA]_{eq}}{[LA]_{eq} - [LA]}\right) = (\,[L]_T\,k_1 - k_{-1}\,)t \qquad (9)$$

This is a popular equation in determinations of k_1 when B_{max} is not known. However it depends on an accurate estimate of k_{-1}. Any errors in k_{-1} will be passed on to k_1 and cumulate in the subsequent determination of the K_d (Equation (3)).

The dissociation of ligand-acceptor complex is measured under conditions where re-binding of dissociated ligand is prevented by dilution or by "chasing" with an excess of unlabelled ligand. The dissociation is described by the first order rate equation:

$$\ln\frac{[LA]}{[LA_o]} = -k_{-1}t \qquad (10)$$

where $[LA_o]$ is the concentration of ligand-acceptor complex just prior to dissociation by dilution or addition of competing ligand. A simple ligand binding situation as in equation (1) will yield a linear plot of $\ln\frac{[LA]}{[LA_o]}$ against t, with a slope of $-k_{-1}$.

A.2.4. Competition Studies Using Unlabelled Ligands

An unlabelled competitive inhibitor, I, competes with a labelled ligand for acceptor sites. This may be shown as:

$$IA \underset{}{\overset{K_I}{\rightleftharpoons}} I + A + L \overset{K_d}{\rightleftharpoons} LA \qquad (11)$$

The concentration of competitive inhibitor which inhibits specific binding by 50% at equilibrium (the IC_{50}) is related to the equilibrium dissociation constant, K_I, of the compound as described by the equation of Cheng and Prussoff (1983):

$$K_I = \frac{IC_{50}}{1 + \frac{[L]}{K_d}} \qquad (12)$$

In a purely competitive situation as shown in (10), the theoretical ratio of the inhibitor concentrations required to inhibit 90% and 10% of ligand binding (IC_{90}/IC_{10}) is 81.

A.2.5. Complex Binding Situations and Multiple Acceptor Sites

Many of the plots described above (Section A.2.1, A.2.2, A.2.3 and A.2.4) deviate from the regular shapes described if more than one acceptor population is present, or if ligand binding is followed, for example, by an interaction of the acceptor with an effector protein (see e.g. Boeynaems and Dumont, 1977). The presence of multiple acceptor sites with significantly different affinities for the ligand (K_d) may yield a concave Scatchard plot if the relative proportions of the acceptor sites are favourable (but see Bürgisser, 1984). Multiple acceptors can also cause concave first order dissociation plots (Section A.2.3) and extended inhibition curves (Section A.2.4). In addition, complex plots are obtained if the acceptors interact on ligand binding. Positive cooperativity of ligand binding leads to sigmoid binding curves and downward curved Scatchard plots (Section A.2.1), while the Hill coefficient, n_H, will be >1.0 (Section A.2.2). Negative cooperativity, on the other hand, shows a concave Scatchard plot similar to the Scatchard plots observed when multiple acceptor sites are present, and a Hill coefficient, n_H, <1.0. These acceptor interactions also give rise to complex association and dissociation kinetics (see e.g. Weiland and Molinoff, 1981).

REFERENCES

Abe, T., Limbrick, A.R. and Miledi, R. (1976) Acute muscle denervation induced by β-bungarotoxin. *Proc. R. Soc. Lond. B* ***194***, 545-553.

Abe, T., Alemà, S. and Miledi, R. (1977)a Isolation and characterization of presynaptically acting neurotoxins from the venom of *Bungarus* snakes. *Eur. J. Biochem.* ***80***, 1-12.

Abe, T., Alemà, S. and Miledi, R. (1977)b Phospholipase activity in β-bungarotoxin action. *J. Physiol. (London)* ***270***, 55-56*P*.

Abe, T. and Miledi, R. (1978) Inhibition of β-bungarotoxin action by bee venom phospholipase A_2. *Proc. R. Soc. Lond. B* ***200***, 225-230.

Alderdice, M.T. and Volle, R.L. (1978) The increase in spontaneous transmitter release produced by β-bungarotoxin and its modification by inorganic ions. *J. Pharmacol. Expt. Ther.* ***205***, 58-68.

Alderdice, M.T. and Volle, R.L. (1981) Multiple actions of β-bungarotoxin on acetylcholine release at amphibian motor nerve terminals. *Naunyn-Schmiedeberg's Arch. Pharmacol.* ***316***, 126-130.

Alexander, G.H., Schwartzmann, R.J., Bell, R.D., Yu, J. and Renthal, A. (1981) Quantitative measurement of local cerebral metabolic rate for glucose utilizing tritiated 2-deoxyglucose. *Brain Res.* ***223***, 59-67.

Altar, C.A., Walter, R.J., Neve, K.A. and Marshall, J.F. (1984) Computer-assisted video analysis of [^{3}H]spiroperidol binding autoradiographs. *J. Neurosci. Methods* ***10***, 173-188.

Altman, J. (1972) Postnatal development of the cerebellar cortex in the rat. II. Phases in the maturation of Purkinje cells and of the molecular layer. *J. Comp. Neurol.* ***145***, 399-464.

Anderson, A.J. (1985) The effects of protease inhibitor homologues from mamba snake venoms on autonomic neurotransmission. *Toxicon* ***23***, 947-954.

Anderson, A.J. and Harvey, A.L. (1985) Electrophysiological actions of facilitatory toxins from mamba venoms on mammalian neuromuscular junctions. *Br. J. Pharmacol.* ***86***, 588P.

Anderson, A.J., Harvey, A.L. and Rowan, E.G. (1987) Facilitation of neurotransmitter release by snake toxins. in: Synaptic Transmitters and Receptors. S.Tucek (Ed.), Wiley, Chichester, and Academia, Prague, pp 392-398.

Anderson, D.C. and Parsons, S.M. (1986) Uncoupling of cholinergic synaptic vesicles by the presynaptic toxin β-bungarotoxin. *J. Neurochem.* ***47***, 1305-1311.

Antonov, S.M., Antonova, N.V. and Magazanik, L.G. (1979) Effect of neurotoxins on transmitter release from motor nerve endings of *Drosophila melanogaster* larvae. *Zh. Evol. Biokhim. Fiziol.* ***15***, 623-625.

Armstrong, D. and Eckert, R. (1987) Voltage-activated calcium channels that must be phosphorylated to respond to membrane depolarization. *Proc. Natl. Acad. Sci USA 84*, 2518-2522.

Arseniev, A.S., Wider, G., Joubert, F.J. and Wüthrich, K. (1982) Assignment of the ^{1}H nuclear magnetic resonance spectrum of the trypsin inhibitor E from *Dendroaspis polylepis polylepis: Two-dimensional nuclear magnetic resonance at 500 MHz. J. Mol. Biol. 159*, 323-351.

Atkins, H.L. (1969) Radionuclides and the endocrine system. in: Handbook of Radioactive Nuclides. Y. Wang (Ed.), The Chemical Rubber Company, Cleveland, pp 395-422.

Augustine, G.J., Charlton, M.P. and Smith, S.J. (1987) Calcium action in synaptic transmitter release. *Ann. Rev. Neurosci. 10*, 633-693.

Baker, M., Bostock, H., Grafe, P. and Martius, P. (1987) Function and distribution of three types of rectifying channel in rat spinal root myelinated axons. *J. Physiol. (London) 383*, 45-67.

Barrett, J.C. and Harvey, A.L. (1979) Effects of the venom of the green mamba, *Dendroaspis angusticeps*, on skeletal muscle and neuromuscular transmission. *Br. J. Pharmacol. 67*, 199-205.

Bartschat, D.K. and Blaustein, M.P. (1986) Phencyclidine in low doses selectively blocks a presynaptic voltage-regulated potassium channel in rat brain. *Proc. Natl. Acad. Sci. USA 83*, 189-192.

Baskin, D.G., Davidson, D., Corp, E.S., Lewellen, T. and Graham, M. (1986) An inexpensive microcomputer digital imaging system for densitometry: Quantitative autoradiography of insulin receptors with ^{125}I and LKB Ultrofilm. *J. Neurosci. Methods 16*, 119-129.

Baumann, A., Krah-Jentgens, I., Müller, R., Müller-Holtkamp, F., Seidel, R., Kecskemethy, N., Casal, J., Ferrus, A. and Pongs, O. (1987) Molecular organization of the maternal effect region of the *Shaker* complex of *Drosophila*: Characterization of an I_A channel transcript with homology to vertebrate Na^+ channel. *EMBO J. 6*, 3419-3429.

Benoit, E. and Dubois, J.-M., (1986) Toxin I from the snake *Dendroaspis polylepis polylepis*: A highly specific blocker of one type of potassium channel in myelinated nerve fibre. *Brain Res. 377*, 374-377.

Black, A.R. (1986) Identification of Functional Neuornal Acceptors for Dendrotoxin. Ph.D. Thesis, University of London.

Black, A.R. and Dolly, J.O. (1986)a Two acceptor sub-types for dendrotoxin in chick synaptic membranes distinguishable by β-bungarotoxin. *Eur. J. Biochem. 156*, 609-617.

Black, A.R., Breeze, A.L., Othman, I.B. and Dolly, J.O. (1986) Involvement of neuronal acceptors for dendrotoxin in its convulsive action in rat brain. *Biochem. J. 237*, 397-404.

Black, A.R., Denny, B.J., Donegan, C.M. and Dolly, J.O. (1988) Solubilisation and physical characterization of dendrotoxin acceptors from synaptic membranes of rat brain. *Submitted.*

Black, J.D. and Dolly, J.O. (1986)b Interaction of ^{125}I-labelled botulinum neurotoxins with nerve terminals. I. Ultrastructural autoradiographic localization and quantitation of distinct membrane acceptors for types A and B on motor nerves. *J. Cell Biol.* ***103***, 521-534.

Blackett, N.M. and Parry, D.M. (1977) A simplified method of "hypothetical grain" analysis of electron microscope autoradiographs. *J. Histochem. Cytochem.* ***25***, 206-214.

Blackett, N.M., Parry, D.M. and Baker, J.R.J. (1980) Isotope decay range distribution curves for use in the analysis of electron microscope autoradiographs. *J. Histochem. Cytochem.* ***28***, 1050-1054.

Boeynaems, J.M. and Dumont, J.E. (1977) The two-step model of ligand-receptor interaction. *Mol. Cell. Endocrinol.* ***7***, 33-47.

Bostock, H., Sears, T.A. and Sherratt, R.M. (1981) The effects of 4-aminopyridine and tetraethylammonium ions on normal and demyelinated mammalian nerve fibres. *J. Physiol (London)* ***313***, 301-315.

Brismar, T. (1980) Potential clamp analysis of membrane currents in rat myelinated nerve fibers. *J. Physiol. (London)* ***298***, 171-184.

Bürgisser, E. (1984) Radioligand-receptor binding studies: What's wrong with the Scatchard analysis? *TIPS* ***5***, 142-144.

Cantley, L. (1986) Ion transport systems sequenced. *TINS* ***9***, 1-3.

Caratsch, C.G., Maranda, B., Miledi, R. and Strong, P.N. (1981) A further study of the phospholipase-independent action of β-bungarotoxin at frog end-plates. *J. Physiol. (London)* ***319***, 179-191.

Caratsch, C.G., Maranda, B., Miledi, R. and Strong, P.N. (1982) Antibodies to β-bungarotoxin and its phospholipase inactive derivative. *Proc. R. Soc. Lond. B,* ***215***, 365-373.

Caratsch, C.G., Miledi, R. and Strong, P.N. (1985) Influence of divalent cations on the phospholipase-independent action of β-bungarotoxin at frog neuromuscular junctions. *J. Physiol. (London)* ***363***, 169-179.

Carbone, E., Wanke, E., Prestipino, G., Possani, L.D. and Maelicke, A. (1982) Selective blockage of voltage-dependent K^+-channels by a novel scorpion toxin. *Nature* ***296***, 90-91.

Carbone, E. and Lux, H.D. (1984) A low voltage-activated, fully inactivating Ca channel in vertebrate sensory neurones. *Nature* ***310***, 501-502.

Catterall, W.A. (1980) Neurotoxins that act on voltage-sensitive sodium channels in excitable membranes. *Ann. Rev. Pharmacol. Toxicol.* ***20***, 15-43.

Catterall, W.A. (1984) The molecular basis of neuronal excitability. *Science* ***223***, 653-661.

Catterall, W.A. (1986) Molecular properties of voltage-sensitive sodium channels. *Ann. Rev. Biochem.* ***55***, 953-985.

Chang, C.C. and Lee, C.Y. (1963) Isolation of neurotoxins from the venom of *Bungarus multicintus* and their modes of neuromuscular blocking action. *Arch. Int. Pharmacodyn.* ***144***, 241-257.

Chang, C.C., Chen, T.F. and Lee, C.Y. (1973) Studies of the presynaptic effect of β-bungarotoxin on neuromuscular transmission. *J. Pharmacol. Expt. Ther.* ***184***, 339-345.

Chang, C.C., Chuang, S.T. and Huang, M.C. (1975) Effects of chronic treatment with various neuromuscular blocking agents on the number and distribution of acetylcholine receptors in the rat diaphragm. *J. Physiol. (London)* ***250***, 161-173.

Chang, C.C., Su, M.J., Lee, J.D. and Eaker, D. (1977)a Effects of Sr^{2+} and Mg^{2+} on the phospholipase A and the presynaptic neuromuscular blocking actions of β-bungarotoxin, crotoxin and taipoxin. *Naunyn-Schmiedeberg's Arch. Pharmacol.* ***299***, 155-161.

Chang, C.C., Lee, J.D., Eaker, D. and Fohlman, J. (1977)b The presynaptic neuromuscular blocking action of taipoxin. A comparison with β-bungarotoxin and crotoxin. *Toxicon* ***15***, 571-576.

Chang, C.C. and Su, M.J. (1980) Mutual potentiation, at nerve terminals, between toxins from snake venoms which contain phospholipase A activity: β-Bungarotoxin, crotoxin, taipoxin. *Toxicon* ***18***, 641-648.

Chang, C.C. and Su, M.J. (1982) Presynaptic toxicity of the histidine-modified, phospholipase A_2-inactive, β-bungarotoxin, crotoxin and notexin. *Toxicon* ***20***, 895-905.

Chang, C.C. (1985) Neurotoxins with phospholipase A_2 activity in snake venoms. *Proc. Natl. Sci. Counc. B ROC* ***9***, 126-142.

Chen, I.L. and Lee, C.Y. (1970) Ultrastructural changes in the motor nerve terminals caused by β-bungarotoxin. *Virchows Arch., Abt. B: Zellpath.* ***6***, 318-325.

Cheng, Y.C. and Prusoff, W.H. (1973) Relationship between the inhibitor constant (K_I) and the concentration of inhibitor which causes 50 per cent inhibition (IC_{50}) of an enzymic reaction. *Biochem. Pharmacol.* ***22***, 3099-3108.

Chiappinelli, V.A., Cohen, J.B. and Zigmond, R.E. (1981) The effects of α- and β-neurotoxins from the venoms of various snakes on transmission in autonomic ganglia. *Brain Res.* ***211***, 107-126.

Chiu, S.Y., Ritchie, J.M., Rogart, R.B. and Stagg, D. (1979) A quantitative description of membrane currents in rabbit myelinated nerve. *J. Physiol. (London)* ***292***, 149-166.

Chiu, S.Y. and Ritchie, J.M. (1980) Potassium channels in nodal and internodal axonal membrane of mammalian myelinated fibres. *Nature* ***284***, 170-171.

Chiu, S.Y. and Ritchie, J.M. (1981) Evidence for the presence of potassium channels in the paranodal region of acutely demyelinated mammalian single nerve fibres. *J. Physiol. (London) 313*, 415-437.

Clark, C.R. and Hall, M.D. (1986) Hormone receptor autoradiography: Recent developments. *TIBS 11*, 195-199.

Clarke, P.B.S., Schwartz, R.D., Paul, S.M., Pert, C.B. and Pert, A. (1985) Nicotinic binding in rat brain: Autoradiographic comparison of [^{3}H]acetylcholine, [^{3}H]nicotine and [^{125}I]-α-bungarotoxin. *J. Neurosci. 5*, 1307-1315.

Contreras, P.C., Quirion, R. and O'Donohue, T.L. (1986) Autoradiographic distribution of phencyclidine receptors in the rat brain using [^{3}H]1-(1-(2-thienyl)cyclohexyl)piperidine ([^{3}H]TCP). *Neurosci. Letters 67*, 101-106.

Cortés, R., Supavilai, P., Karobath, M. and Palacios, J.M. (1984) Calcium antagonist binding sites in the rat brain: Quantitative autoradiographic mapping using the 1,4-dihydropyridines [^{3}H]PN 200-110 and [^{3}H]PY 108-068. *J. Neural Transmission 60*, 169-197.

Costa, M.R.C. and Catterall, W.A. (1984) Cyclic AMP-dependent phosphorylation of the α subunit of the sodium channel in synaptic nerve ending particles. *J. Biol. Chem. 259*, 8210-8218.

Creazzo, T.L. and Sohal, G.S. (1981) Beta-bungarotoxin lacking phospholipase activity is not toxic to developing motor neurons and skeletal muscle. *Dev. Neurosci. 4*, 329-336.

Crill, W.E. and Schwindt, P.C. (1983) Active currents in mammalian central neurons. *TINS 6*, 236-240.

Cull-Candy, S.G., Fohlman, J., Gustavsson, D., Lüllmann-Rauch, R. and Thesleff, S. (1976) The effects of taipoxin and notexin on the function and fine structure of the murine neuromuscular junction. *Neuroscience 1*, 175-180.

de Belleroche, J.S. and Bradford, H.F. (1977) On the site of origin of transmitter amino acids released by depolarization of nerve terminals *in vitro*. *J. Neuorchem. 29*, 335-343.

de Camilli, P., Cameron, R. and Greengard, P. (1983) Synapsin I (Protein I), a nerve terminal-specific phosphoprotein. I. Its general distribution in synapses of the central and peripheral nervous system demonstrated by immunofluorescence in frozen and plastic sections. *J. Cell Biol. 96*, 1337-1354.

del Cerro, M.P., Snider, R.S. and Oster, M.L. (1968) Evolution of the extracellular space in immature nervous tissue. *Experientia 24*, 929-930.

Deisenhofer, J. and Steigemann, W. (1975) Crystallographic refinement of the structure of bovine pancreatic trypsin inhibitor at 1.5 Å resolution. *Acta Cryst. B 31*, 238-250.

Docherty, R.J., Dolly, J.O., Halliwell, J.V. and Othman, I.B. (1983) Excitatory effects of dendrotoxin on the hippocampus *in vitro*. *J. Physiol. (London) 336*, 58P.

Dohanich, G.P., Halpain, S., Lambdin, L.T. and McEwen, B.S. (1986) Features of ligand binding in homogenate and section preparations. *Brain Res.* ***366***, 338-342.

Dolly, J.O., Halliwell, J.V. and Spokes, J.W. (1980) Interaction of β-bungarotoxin with synapses in the mammalian central nervous system. in: Natural Toxins. D. Eaker and T. Wadström (Eds.), Pergamon Press, Oxford and New York, pp 549-559.

Dolly, J.O. and Barnard, E.A (1984) Nicotinic acetylcholine receptors: An overview. *Biochem. Pharmacol.* ***33***, 841-858.

Dolly, J.O., Halliwell, J.V., Black, J.D., Williams, R.S., Pelchen-Matthews, A., Breeze, A.L., Mehraban, F., Othman, I.B. and Black, A.R. (1984) Botulinum neurotoxin and dendrotoxin as probes for studies on transmitter release. *J. Physiol. (Paris)* ***79***, 280-303.

Dolly, J.O., Black, J.D., Black, A.R., Pelchen-Matthews, A. and Halliwell, J.V. (1986) Novel roles of neural acceptors for inhibitory and facilitatory toxins. in: Natural Toxins. Animal, Plant and Microbial. J.B. Harris (Ed.), Clarendon Press, Oxford, pp 237-264.

Dolly, J.O., Stansfeld, C.E., Breeze, A.L., Pelchen-Matthews, A., Marsh., S.J. and Brown, D.A. (1987) Neuronal acceptor sub-types for dendrotoxin and their relation to K^+ channels. in: Neurotoxins and their Pharmacological Implications. P.G. Jenner (Ed.), Raven Press, New York, pp 81-96.

Dowdall, M.J., Fohlman, J.P. and Watts, A. (1979) Presynaptic action of snake venom neurotoxins on cholinergic systems. *Adv. Cytopharmacol.* ***3***, 63-76.

Downs, A.M. and Williams, M.A. (1984) An improved approach to the analysis of autoradiographs containing isolated sources of simple shape: Method, theoretical basis and reference data. *J. Microscopy* ***136***, 1-22.

Dreyer, F. and Penner, R. (1987) The actions of presynaptic snake toxins on membrane currents of mouse motor nerve terminals. *J. Physiol. (London)* ***386***, 455-463.

Dryden, W.F., Harvey, A.L. and Marshall, I.G. (1974) Pharmacological studies on the bungarotoxins: Separation of the fractions and their neuromuscular activity. *Eur. J. Pharmacol.* ***26***, 256-261.

Dubois,.J.M. (1981) Evidence for the existence of three types of potassium channels in the frog Ranvier node membrane. *J. Physiol. (London)* ***318***, 297-316

Dubois, J.M. (1982) Capsaicin blocks one class of K^+ channels in the frog node of Ranvier. *Brain Res.* ***245***, 372-375.

Dubois, J.M. (1983) Potassium currents in the frog node of Ranvier. *Prog. Biophys. Molec. Biol.* ***42***, 1-20.

Dufton, M.J. (1985) Proteinase inhibitors and dendrotoxins. *Eur. J. Biochem.* ***153***, 647-654.

Dunlap, K., Holz, G.G. and Rane, S.G. (1987) G proteins as regulators of ion channel function. *TINS 10*, 241-244.

Edelman, G.M. (1984) Modulation of cell adhesion during induction, histogenesis and perinatal development of the nervous system. *Ann. Rev. Neurosci. 7*, 339-377.

Ehn, E. and Larsson, B. (1979) Properties of an antiscratch-layer-free X-ray film for the autoradiographic registration of tritium. *Science Tools 26*, 24-29.

Esquerda, J.E., Solsona, C. and Marsal, J. (1982) Binding of β-bungarotoxin to *Torpedo* electric synaptosomes. A high resolution autoradiographic study. *Neuroscience 7*, 751-758.

Eterovic, V.A., Hebert, M.S., Hanley, M.R. and Bennet, E.L. (1975) The lethality and spectroscopic properties of toxins from *Bungarus multicinctus* (Blyth) venom. *Toxicon 13*, 37-48.

Ferry, D.R., Goll, A., Gadow, C. and Glossmann, H. (1984) (-)-^{3}H-desmethoxyverapamil labelling of putative calcium channels in brain: Autoradiographic distribution and allosteric coupling to 1,4-dihydropyridine and diltiazem binding sites. *Naunyn-Schmiedeberg's Arch. Pharmacol. 327*, 183-187.

Fertuck, H.C. and Salpeter, M.M. (1976) Quantitation of junctional and extrajunctional acetylcholine receptors by electron microscope autoradiography after ^{125}I-α-bungarotoxin binding at mouse neuromuscular junctions. *J. Cell Biol. 69*, 144-158.

Fletcher, J.E. and Middlebrook, J.L. (1986) Effects of β-bungarotoxin and *Naja naja atra* snake venom phospholipase A_2 on acetylcholine release and choline uptake in synaptosomes. *Toxicon 24*, 91-99.

Foster, A.C., Mena, E.E., Monaghan, D.T. and Cotman, C.W. (1981) Synaptic localization of kainic acid binding sites. *Nature 289*, 73-75.

Fox, A.P., Hirning, L.D., Kongsamut, S., McCleskey, E.W., Miller, R.J., Olivera, B.M., Perney, T.M., Thayer, S.A. and Tsien, R.W. (1987) The interaction of toxins with calcium channels. in: Neurotoxins and their Pharmacological Implications. P.G. Jenner (Ed.), Raven Press, New York, pp 115-131.

Furukawa, S. and Hayashi, K. (1978) Purification and characterization of nerve growth factor from the venom of *Bungarus multicinctus*. *Biochim. Biophys. Acta 533*, 383-395.

Garthwaite, J., Woodhams, P.L., Collins, M.J. and Balázs, R (1979) On the preparation of brain slices: Morphology and cyclic nucleotides. *Brain Res. 173*, 373-377.

Garthwaite, J., Woodhams, P.L., Collins, M.J. and Balázs, R (1980) A morphological study of incubated slices of rat cerebellum in relation to postnatal age. *Dev. Neurosci. 3*, 90-99.

Goochee, C., Rasband, W. and Sokoloff, L. (1980) Computerized densitometry and color coding of [^{14}C]deoxyglucose autoradiography. *Ann. Neurol. 7*, 359-370.

Gopalakrishnakone, P. and Hawgood, B.J. (1984) Morphological changes induced by crotoxin in murine nerve and neuromuscular junction. *Toxicon 22*, 791-804.

Gould, R.J., Murphy, K.M.M. and Snyder, S.H. (1985) Autoradiographic localization of calcium channel antagonist receptors in rat brain with [^{3}H]nitrendipine. *Brain Res. 330*, 217-223.

Gray, E.G. and Whittaker, V.P. (1962) The isolation of nerve endings from brain: An electron-microscopic study of cell fragments derived by homogenization and centrifugation. *J. Anat. 96*, 79-88.

Greenamyre, J.T., Young, A.B. and Penney, J.B. (1984) Quantitative autoradiographic distribution of L-[^{3}H]glutamate-binding sites in rat central nervous system. *J. Neurosci. 4*, 2133-2144.

Grenningloh, G., Rienitz, A., Schmitt, B., Methfessel, C., Zensen, M., Beyreuther, K., Gundelfinger, E.D. and Betz, H. (1987) The strychnine-binding subunit of the glycine receptor shows homology with nicotinic acetylcholine receptors. *Nature 328*, 215-220.

Gulya, K., Budai, D., Kása, P. and Rakonczay, Z. (1984) *In vivo* effects of β-bungarotoxin on the acetylcholine system in different brain areas of the rat. *J. Neurochem. 43*, 112-119.

Gundersen, C.B. (1981) Diminished response to β-bungarotoxin in neonatal rat diaphragm. *J. Physiol. (London) 314*, 151-159.

Gundersen, C.B. and Jenden, D.J. (1981) Alterations of acetylcholine and choline metabolism in mammalian preparations treated with β-bungarotoxin. *J. Neurochem. 36*, 938-948.

Gustafsson, B., Galvan, M., Grafe, P. and Wigström, H. (1982) A transient outward current in a mammalian central neurone blocked by 4-aminopyridine. *Nature 299*, 252-254.

Halliwell, J.V. and Dolly, J.O. (1982) Preferential action of β-bungarotoxin at nerve terminal regions in the hippocampus. *Neurosci. Letters 30*, 321-327.

Halliwell, J.V., Tse, C.K., Spokes, J.W., Othman, I. and Dolly, J.O. (1982) Biochemical and electrophysiological demonstrations of the actions of β-bungarotoxin on synapses in brain. *J. Neurochem. 39*, 543-550.

Halliwell, J.V., Othman, I.B., Pelchen-Matthews, A. and Dolly, J.O. (1986) Central action of dendrotoxin: Selective reduction of a transient K conductance in hippocampus and binding to localized acceptors. *Proc. Natl. Acad. Sci. USA, 83*, 493-497.

Halpain, S., Wieczorek, C.M. and Rainbow, T.C. (1984) Localization of L-glutamate receptors in rat brain by quantitative autoradiography. *J. Neurosci. 4*, 2247-2258.

Hanley, M.R., Eterovic, V.A., Hawkes, S.P., Hebert, A.J. and Bennett, E.L. (1977) Neurotoxins of *Bungarus multicinctus* venom. Purification and partial characterization. *Biochemistry 16*, 5840-5849.

Hanley, M.R. and Emson, P.C. (1979) Neuronal degeneration induced by stereotaxic injection of β-bungarotoxin into rat brain. *Neurosci. Letters* ***11***, 143-148.

Harris, A.J. (1981) Embryonic growth and innervation of rat skeletal muscles. I. Neural regulation of muscle fibre numbers. *Phil. Trans. R. Soc. Lond. B* ***293***, 257-277.

Harris, J.B., Johnson, M.A. and MacDonell, C.A. (1980) Muscle necrosis induced by some presynaptically active neurotoxins. in: Natural Toxins. D. Eaker and T. Wadström (Eds.), Pergamon Press, Oxford and New York, pp 569-578.

Harvey, A.L. and Karlsson, E. (1980) Dendrotoxin from the venom of the green mamba, *Dendroaspis angusticeps*: A neurotoxin that enhances acetylcholine release at neuromuscular junctions. *Naunyn-Schmiedeberg's Arch. Pharmacol.* ***312***, 1-6.

Harvey, A.L. and Gage, P.W. (1981) Increase of evoked release of acetylcholine at the neuromuscular junction by a fraction from the venom of the green mamba snake (*Dendroaspis angusticeps*). *Toxicon* ***19***, 373-381.

Harvey, A.L. (1982) Common site of action of dendrotoxin-like facilitatory neurotoxins and β-bungaratoxin. *Toxicon* ***20***, 117-118.

Harvey, A.L. and Karlsson, E. (1982) Protease inhibitor homologues from mamba venoms: Facilitation of acetylcholine release and interactions with prejunctional blocking toxins. *Br. J. Pharmacol.* ***77***, 153-161.

Harvey, A.L., Anderson, A.J. and Karlsson, E. (1984)a Facilitation of transmitter release by neurotoxins from snake venoms. *J. Physiol. (Paris)* ***79***, 222-227.

Harvey, A.L., Anderson, A.J., Mbugua, P.M. and Karlsson, E. (1984)b Toxins from mamba venoms that facilitate neuromuscular transmission. *J. Toxicol. Toxin Rev.* ***3***, 91-137.

Harvey, A.L. and Anderson, A.J. (1985) Dendrotoxins: Snake toxins that block potassium channels and facilitate neurotransmitter release. *Pharmacology and Therapeutics* ***31***, 33-55.

Hassoni, A.A., Kerkut, G.A. and Walker, R.J. (1985) The action of cholinomimetic and cholinolytic agents, hemicholinium 3 and α- and β-bungarotoxin, on the body wall muscle of the earthworm, *Lumbricus terrestris*. *Comp. Biochem. Physiol. C. Comp. Pharmacol. Toxicol.* ***82***, 179-192.

Hill, A.V. (1913) The combination of haemoglobin with oxygen and with carbon monoxide. *Biochem. J.* ***7***, 470-480.

Hinzen, D.H. and Tauc, L. (1977) Membrane properties of *Aplysia* neurones intracellularly injected with phospholipases A and C. *J. Physiol. (London)* ***268***, 21-34.

Hirokawa, N. (1977) Disappearance of afferent and efferent nerve terminals in the inner ear of the chick embryo after chronic treatment with β-bungarotoxin. *J. Cell Biol.* ***73***, 27-46.

Hirokawa, N. (1978) Characterization of various nervous tissues of the chick embryos through responses to chronic aplication and immunocytochemistry of β-bungarotoxin. *J. Comp. Neurol.* ***180***, 449-466.

Hirokawa, N. (1979) A study of the synaptogenesis in the cerebellar cortex through chronic treatment and immunocytochemistry of β-bungarotoxin. *J. Comp. Neurol.* ***185***, 107-120.

Ho, C.L., Ko, J.L. and Lee, C.Y. (1986) Differences in pharmacological actions between β-bungarotoxin and other neurotoxic phospholipases A_2 purified from snake venoms. *Proc. Natl. Sci. Counc. B, ROC* ***10***, 196-202.

Hofman, W.W. and Thesleff, S. (1972) Studies on the trophic influence of nerve on skeletal muscle. *Eur. J. Pharmacol.* ***20***, 256-260.

Hollecker, M., Creighton, T.E. and Gabriel, M. (1981) Preliminary circular dichroism study of the conformations of intermediates trapped during protein folding. *Biochimie* ***63***, 835-839.

Hollecker, M. and Creighton, T.E. (1983) Evolutionary conservation and variation of protein folding pathways: Two protease inhibitor homologues from black mamba venom. *J. Mol. Biol.* ***168***, 409-437.

Howard, B.D. (1975) Effects of β-bungarotoxin on mitochondrial respiration are caused by associated phospholipase A activity. *Biochem. Biophys. Res. Commun.* ***67***, 58-65.

Howard, B.D. and Truog, R. (1977) Relationship between the neurotoxicity and phospholipase A activity of β-bungarotoxin. *Biochemistry* ***16***, 122-125.

Howard, B.D. and Gundersen, C.B. (1980) Effects and mechanisms of polypeptide neurotoxins that act presynaptically. *Ann. Rev. Pharmacol. Toxicol.* ***20***, 307-336.

Howard, B.D. (1982) Presynaptic polypeptide neurotoxins. *TIPS* ***3***, 167-169.

Huber, R., Kukla, D., Rühlmann, A. and Steigemann, W. (1971) Pancreatic trypsin inhibitor (Kunitz). Part I: Structure and function. *Cold Spring Harbor Symp. Quant. Biol.* ***36***, 141-150.

Hyatt, M.C. and Russell, J.A. (1981) Effects of β-bungarotoxin and taipoxin on contractions of canine airways caused by nerve stimulation. *Life Sci.* ***29***, 1755-1759.

Ikeda, K. and Hayashi, K. (1983) pH-Dependence of the binding constant of Ca^{2+} to β-bungarotoxin from *Bungarus multicinctus* venom. *J. Biochem. (Tokyo)* ***93***, 1343-1351.

Israel, A., Correa, F.M.A., Niwa, M. and Saavedra, J.M. (1984) Quantitative determination of angiotensin II binding sites in rat brain and pituitary gland by autoradiography. *Brain Res.* ***322***, 341-345.

Jan, Y.N., Jan, L.Y. and Dennis, M.J. (1977) Two mutations of synaptic transmission in *Drosophila*. *Proc. R. Soc. Lond. B* ***198***, 87-108.

Joubert, F.J. and Strydom, D.J. (1978) Snake venoms: The amino-acid sequence of trypsin inhibitor E of *Dendroaspis polylepis polylepis* (black mamba) venom. *Eur. J. Biochem.* ***87***, 191-198.

Joubert, F.J. and Taljaard, N. (1980) The amino acid sequences of two proteinase inhibitor homologues from *Dendroaspis angusticeps* venom. *Hoppe-Seyler's Z. Physiol. Chem.* ***361***, 661-674.

Kamb, A., Iverson, L.E. and Tanouye, M.A. (1987) Molecular characterization of *Shaker*, a *Drosophila* gene that encodes a potassium channel. *Cell* ***50***, 405-413.

Kassell, B., Radicevic, M., Ansfield, M.J. and Laskowski, M (1965) The basic trypsin inhibitor of bovine pancreas. IV. The linear sequence of the 58 amino acids. *Biochem. Biophys. Res. Commun.* ***18***, 255-258.

Kato, A.C., Pinto, J.E.B., Glavinovic, M. and Collier, B. (1977) Action of a β-bungarotoxin on autonomic ganglia and adrenergic neurotransmission. *Can. J. Physiol. Pharmacol.* ***55***, 574-584.

Katoh-Semba, R., Semba, R. and Kashiwamata, S. (1987) Age-dependent and selective binding of β-bungarotoxin to GABAergic neurons in the rat cerebellum. *Neurosci. Letters* ***76***, 32-36.

Kelly, R.B. and Brown, F.R. (1974) Biochemical and physiological properties of a purified snake venom neurotoxin which acts presynaptically. *J. Neurobiol.* ***5***, 135-150.

Kelly, R.B., Oberg, S.G., Strong, P.N. and Wagner, G.M. (1975) β-Bungarotoxin, a phospholipase that stimulates transmitter release. *Cold Spring Harbor Symp. Quant. Biol.* ***40***, 117-125.

Kelly, R.B., von Wedel, R.J. and Strong, P.N. (1979) Phospholipase-dependent and phospholipase-independent inhibition of transmitter release by β-bungarotoxin. *Adv. Cytopharmacol.* ***3***, 77-85.

Keller, R.M., Baumann, R., Hunziker-Kwik, E.-H., Joubert, F.J. and Wüthrich, K. (1983) Assignment of the ^{1}H nuclear magnetic resonance spectrum of the trypsin inhibitor homologue K from *Dendroaspis polylepis polylepis*. Two-dimensional nuclear magnetic resonance at 360 and 500 MHz. *J. Mol. Biol.* ***163***, 623-646.

Kini, R.M. and Iwanaga, S. (1986) Structure-function relationships of phospholipases. I: Prediction of presynaptic neurotoxicity. *Toxicon* ***24***, 527-541.

Kocsis, J.D. and Waxman, S.G. (1980) Absence of potassium conductance in central myelinated axons. *Nature* ***287***, 348-349.

Kocsis, J.D., Gordon, T.R. and Waxman, S.G. (1986) Mammalian optic nerve fibers display two pharmacologically distinct potassium channels. *Brain Res.* ***383***, 357-361.

Kocsis, J.D. Eng, D.L., Gordon, T.R. and Waxman, S.G. (1987) Functional differences between 4-aminopyridine and tetraethylammonium-sensitive potassium channels in myelinated axons. *Neurosci. Letters* ***75***, 193-198.

Kondo, K., Narita, K. and Lee, C.-Y. (1978)a Chemical properties and amino acid composition of β_1-bungarotoxin from the venom of *Bungarus multicinctus* (Formosan banded krait). *J. Biochem. (Tokyo) 83*, 91-99.

Kondo, K., Narita, K. and Lee, C.-Y. (1978)b Amino acid sequences of the two polypeptide chains in β_1-bungarotoxin from the venom of *Bungarus multicinctus*. *J. Biochem. (Tokyo) 83*, 101-115.

Kondo, K., Toda, H. and Narita, K. (1978)c Characterization of phospholipase A activity of β_1-bungarotoxin from *Bungarus multicinctus* venom. I. Its enzymatic properties and modification with p-bromophenacyl bromide. *J. Biochem. (Tokyo) 84*, 1291-1300.

Kondo, K., Toda, H. and Narita, K. (1978)d Characterization of phospholipase A activity of β_1-bungarotoxin from *Bungarus multicinctus* venom. II. Identification of the histidine residue of β_1-bungarotoxin modified by p-bromophenacyl bromide. *J. Biochem. (Tokyo) 84*, 1301-1308.

Kondo, K., Toda, H. and Narita, K. (1981) Amino acid sequence of phospholipase A from *Bungarus multicinctus* venom. *J. Biochem. (Tokyo) 89*, 37-47.

Kondo, K., Toda, H., Narita, K. and Lee, C.-Y. (1982)a Amino acid sequence of β_2-bungarotoxin from *Bungarus multicinctus* venom. The amino acid substitutions in the B-chains. *J. Biochem. (Tokyo) 91*, 1519-1530.

Kondo, K., Toda, H., Narita, K. and Lee, C.-Y. (1982)b Amino acid sequences of three β-bungarotoxins (β_3-, β_4- and β_5-bungarotoxins) from *Bungarus multicinctus* venom: Amino acid substitutions in the A-chains. *J. Biochem. (Tokyo) 91*, 1531-1548.

Kuffler, S.W., Nicholls, J.G. and Martin, A.R. (1984) From Neuron to Brain. A Cellular Approach to the Nervous System. Sinauer Associates Inc., Sunderland, Massachusets.

Kuhar, M.J., Taylor, N., Wamsley, J.K., Hulme, E.C. and Birdsall, N.J.M. (1981) Muscarinic cholinergic receptor localization in brain by electron microscope autoradiography. *Brain Res. 216*, 1-9.

Kuhar, M.J. and Unnerstall, J.R. (1985) Quantitative receptor mapping by autoradiography: Some current technical problems. *TINS 8*, 49-53.

Kuhar, M.J., De Souza, E.B. and Unnerstall, J.R. (1986) Neurotransmitter receptor mapping by autoradiography and other methods. *Ann. Rev. Neurosci. 9*, 27-59.

Landon, D.N., Westgaard, R.H., MacDermot, J. and Thompson, E.J. (1980) The morphology of rat soleus neuromuscular junctions treated *in vitro* with purified β-bungarotoxin. *Brain Res. 202*, 1-20.

Lau, Y.H., Chiu, T.H., Caswell, A.H. and Potter, L.T. (1974) Effects of β-bungarotoxin on calcium uptake by sarcoplasmic reticulum from rabbit skeletal muscle. *Biochem. Biophys. Res. Commun. 61*, 510-516.

Lee, C.Y. and Tseng, L.F. (1966) Distribution of *Bungarus multicinctus* venom following envenomation. *Toxicon 3*, 281-290.

Lee, C.Y. and Tseng, L.F. (1969) Species differences in susceptibility to Elapid venoms. *Toxicon 7*, 89-93.

Lee, C.Y. (1972) Chemistry and pharmacology of polypeptide toxins in snake venoms. *Ann. Rev. Pharmacol. 12*, 265-286.

Lee, C.Y., Chang, S.L., Kau, S.T. and Luh, S.H. (1972) Chromatographic separation of the venom of *Bungarus multicinctus* and characterization of its components. *J. Chromatog. 72*, 71-82.

Lee C.Y. and Ho, C.L. (1980) Pharmacology of presynaptic neurotoxins from snake venoms. in: Natural Toxins. D. Eaker and T. Wadström (Eds.), Pergamon Press, Oxford and New York, pp 539-547.

Lee, C.Y., Tsai, M.C., Chen, Y.M., Ritonja, A. and Gubensek, F. (1984) Mode of neuromuscular blocking action of toxic phospholipases A_2 from *Vipera ammodytes* venom. *Arch. Int. Pharmacodyn. 268*, 313-324.

Levi, G. and Lattes, M.G. (1970) Changes with age in water and extracellular space in incubated brain tissue. *J. Neurochem. 17*, 587-596.

Livengood, D.R., Manalis, R.S., Donlon, M.A., Masakuwa, L.M., Tobias, G.S. and Shain, W. (1978) Blockade of neuromuscular transmission by enzymatically active and inactive β-bungarotoxin. *Proc. Natl. Acad. Sci. USA 75*, 1029-1033.

Llados, F., Matteson, D.R. and Kriebel, M.E. (1980) β-Bungarotoxin preferentially blocks one class of miniature endplate potentials. *Brain Res. 192*, 598-602.

Lowry, O.M., Rosebrough, J.T., Farr, A.L. and Randall, R.J., (1951) Protein measurement with the Folin-phenol reagent. *J. Biol. Chem. 193*, 265-275

MacDermot, J., Westgaard, R.H. and Thompson, E.J. (1978) Beta-bungarotoxin: Separation of two discrete proteins with different synaptic actions. *Biochem. J. 175*, 271-279.

McIlwain, H. (1975) Preparing neural tissues for metabolic study in isolation. in: Practical Neurochemistry. H. McIlwain (ed.), Churchill Livingstone, London, pp 105-132.

Mao Chen, C.-J., Chang, P.-L., Lin Shiau, S.-Y. and Lee, C.-Y. (1978) Effect of β-bungarotoxin on acetylcholinesterase activity and ultrastructure of the skeletal muscle isolated from the chick embryo. *Toxicon 16*, 461-471.

Marsal, J., Esquerda, J.E., Fiol, C., Solsona, C. and Tomas, J. (1980) Calcium fluxes in isolated pure cholinergic nerve endings from the electric organ of *Torpedo marmorata*. *J. Physiol. (Paris) 76*, 443-457.

Masukawa, L.M. and Livengood, D.R. (1982) Alterations in spontaneous transmitter release by divalent cations after treatment of the neuromuscular junction with β-bungarotoxin. *Cell. Mol. Neurobiol. 2*, 277-290.

Meech, R.W. (1978) Calcium-dependent potassium activation in nervous tissues. *Ann. Rev. Biophys. Bioeng. 7*, 1-18.

Mehraban, F., Breeze, A.L. and Dolly, J.O. (1984) Identification by cross-linking of a neuronal acceptor protein for dendrotoxin, a convulsant polypeptide. *FEBS Letters 174*, 116-122.

Mehraban, F., Black, A.R., Breeze, A.L., Green, D.G. and Dolly, J.O. (1985) A functional membranous acceptor for dendrotoxin in rat brain: Solubilization of the binding component. *Biochem. Soc. Trans. 13*, 507-508.

Mehraban, F., Haines, A. and Dolly, J.O. (1986) Monoclonal and polyclonal antibodies against dendrotoxin: Their effects on its convulsive activity and interaction with neuronal acceptors. *Neurochem. Int. 9*, 11-22.

Miller, R.J. (1986) Protein kinase C: A key regulator of neuronal excitability? *TINS 9*, 538-541.

Miura, A., Muramatsu, I., Fujiwara, M., Hayashi, K. and Lee, C.Y. (1981) Species and regional differences in cholinergic blocking actions of β-bungarotoxin. *J. Pharmacol. Expt. Ther. 217*, 505-509.

Monaghan, D.T. and Cotman, C.W. (1982) The distribution of [^{3}H]kainic acid binding sites in rat CNS as determined by autoradiography. *Brain Res. 252*, 91-100.

Mourre, C., Lombet, A. and Lazdunski, M. (1984) Autoradiographic localization of tetrodotoxin-sensitive Na^+ channels in rat brain. *Neurosci. Letters 52*, 31-35.

Mourre, C., Hugues, M. and Lazdunski, M. (1986) Quantitative autoradiographic mapping in rat brain of the receptor of apamin, a polypeptide toxin specific for one class of Ca^{2+}-dependent K^+ channels. *Brain Res. 382*, 239-249.

Muramatsu, I., Fujiwara, M., Miura, A., Hayashi, K. and Lee, C.Y. (1980) β-Bungarotoxin and parasympathetic nerve blocking action. *J. Pharmacol. Expt. Ther. 213*, 156-160.

Nauta, W.J.H. and Feirtag, M. (1986) Fundamental neuroatanomy. W.H. Freeman and Company, New York.

Newton, M.W., Gundersen, C.B. and Jenden, D.J. (1983) The effect of β-bungarotoxin on acetylcholine and choline content of vertebrate tissues. *Toxicon 21*, 825-832.

Ng, R.H. and Howard, B.D. (1978) Deenergization of nerve terminals by β-bungarotoxin. *Biochemistry 17*, 4978-4986.

Ng, R.H. and Howard, B.D. (1980) Mitochondria and sarcoplasmic reticulum as model targets for neurotoxic and myotoxic phospholipases A_2. *Proc. Natl. Acad. Sci. USA 77*, 1346-1350.

Nicholls, D.G., Snelling, R. and Dolly, J.O. (1985) Bioenergetic actions of β-bungarotoxin, dendrotoxin and bee-venom phospholipase A_2 on guinea-pig synaptosomes. *Biochem. J.* ***229***, 653-662.

Noda, M., Shimizu, S., Tanabe, T., Takai, T., Kayano, T., Ikeda, T., Takahashi, H., Nakayama, H., Kanaoka, Y., Minamino, N., Kangawa, K., Matsuo, H., Raftery, M.A., Hirose, T., Inayama, S., Hayashida, H., Miyata, T. and Numa, S. (1984) Primary structure of *Electrophorus electricus* sodium channel deduced from cDNA sequence. *Nature* ***312***, 121-127.

Noda, M., Ikeda, T., Kayano, T., Suzuki, H., Takeshima, H., Kurasaki, M., Takahashi, H. and Numa, S. (1986) Existence of distinct sodium channel messenger RNAs in rat brain. *Nature* ***320***, 188-192.

Noël, S.-P. and Strong, P.N. (1982) Lipoproteins as models to study the phospholipase A activity of β-bungarotoxin. *Biochem. Biophys. Res. Commun.* ***109***, 716-722.

Nonaka, R. and Moroji, T. (1984) Quantitative autoradiography of muscarinic cholinergic receptors in the rat brain. *Brain Res.* ***296***, 295-303.

Nonaka, R. and Moroji, T. (1985) Time-dependent changes in the binding parameters of muscarinic cholinergic receptors in the rat brain. *Brain Res.* ***326***, 379-383.

Nowycky, M.C., Fox, A.P. and Tsien, R.W. (1985) Three types of neuronal calcium channel with different calcium agonist sensitivity. *Nature* ***316***, 440-443.

Oberg, S.G. and Kelly, R.B. (1976) The mechanism of β-bungarotoxin action. I. Modification of transmitter release at the neuromuscular junction. *J. Neurobiol.* ***7***, 129-141.

Okamoto, H. (1980) Binding of scorpion toxin to sodium channels *in vitro* and its modification by β-bungarotoxin. *J. Physiol.* ***299***, 507-520.

Olefsky, J.M., Chang, H. and Stanford, M.S. (1978) Insulin binding to adipocytes: Evidence for functionally distinct receptors. *Diabetes* ***27***, 946-958.

Olek, A.J. (1980) Effects of α and β bungarotoxin on motor neuron loss in *Xenopus* larvae. *Neuroscience* ***5***, 1557-1563.

Othman, I.B., Spokes, J.W. and Dolly, J.O. (1982) Preparation of neurotoxic ^{3}H-β-bungaratoxin: Demonstration of saturable binding to brain synapses and its inhibition by toxin I. *Eur. J. Biochem.* ***128***, 267-276.

Othman, I.B. (1983) Interactions of β-bungarotoxin and dendrotoxin with nerve terminals. Ph.D. Thesis, University of London.

Othman, I.B., Wilkin, G.P. and Dolly, J.O. (1983) Synaptic binding sites in brain for [^{3}H]-β-bungarotoxin - a specific probe that perturbs transmitter release. *Neurochem. Internat.* ***5***, 487-496.

Palacios, J.M., Young, W.S. III and Kuhar, M.J. (1980) Autoradiographic localization of γ-aminobutyric acid (GABA) receptors in the rat cerebellum. *Proc. Natl. Acad. Sci. USA 77*, 670-674.

Palacios, J.M., Niehoff, D.L. and Kuhar, M.J. (1981) Receptor autoradiography with tritium-sensitive film: Potential for computerized densitometry. *Neurosci. Letters 25*, 101-105.

Pan, H.S., Frey, K.A., Young, A.B. and Penney, J.B. (1981) Changes in [^{3}H]-muscimol binding in substantia nigra, entopeduncular nucleus, globus pallidus and thalamus after striatal lesions as demonstrated by quantitative receptor autoradiography. *J. Neurosci. 3*, 1189-1198.

Papazian, D.M., Schwarz, T.L., Tempel, B.L., Jan, Y.N. and Jan, L.Y. (1987) Cloning of genomic and complementary DNA from *Shaker*, a putative potassium channel gene from *Drosophila*. *Science 237*, 749-753.

Pardi, A., Wagner, G. and Wüthrich, K. (1983) Protein conformation and proton nuclear-magnetic-resonance chemical shifts. *Eur. J. Biochem. 137*, 445-454.

Parsons, B. and Rainbow, T.C. (1983) Quantitative autoradiography of sodium-dependent [^{3}H]D-aspartate binding sites in rat brain. *Neurosci. Letters 36*, 9-12.

Paxinos, G. and Watson, C. (1982) The Rat Brain in Stereotaxic Coordinates. Academic Press, New York.

Penner, R., Petersen, M., Pierau, F.-K. and Dreyer, F. (1986) Dendrotoxin: A selective blocker of a non-inactivating potassium current in guinea-pig dorsal root ganglion neurones. *Pflüger's Arch. 407*, 365-369.

Penney, J.B., Frey, K. and Young, A.B. (1981)a Quantitative autoradiography of neurotransmitter receptors using tritium-sensitive film. *Eur. J. Pharmacol. 72*, 421-422.

Penney, J.B., Pan, H.S., Young, A.B., Frey, K.A. and Dauth, G.W. (1981)b Quantitative autoradiography of[^{3}H]muscimol binding in rat brain. *Science 214*, 1036-1038.

Peters, A., Palay, S.L. and Webster, H.F. (1976) The Fine Structure of the Nervous System: The Neurons and Supporting Cells. W.B. Saunders Company, Philadelphia, London, Toronto.

Petersen, M., Penner, R., Pierau, F.K. and Dreyer, F. (1986) β-Bungarotoxin inhibits a non-inactivating potassium current in guinea pig dorsal root ganglion neurones. *Neurosci. Letters 68*, 141-145.

Petersen, O.H. and Maruyama, Y. (1984) Calcium-activated potassium channels and their role in secretion. *Nature 307*, 693-696.

Pittman, R., Oppenheim, R.W. and Chu-Wang, I.-W. (1978) Beta-bungarotoxin induced neuronal degeneration in the chick embryo spinal cord. *Brain Res. 153*, 199-204.

Politi, L.E. and Adler, R. (1986) Generation of enriched populations of cultured photoreceptor cells. *Invest. Ophthalmol. Visual Sci.* ***27***, 656-665.

Powell-Jones, C.H.J., Thomas, C.G. and Nayfeh, S.N. (1980) Thyrotropin receptors in normal human thyroid: Nonclassical binding kinetics not explained by the negative cooperativity model. *J. Biol. Chem.* ***255***, 4001-4010.

Quirion, R., Hammer, R.P., Herkenham, M. and Pert, C.B. (1981) Phencyclidine (angel dust)/σ "opiate" receptor: Visualization by tritium-sensitive film. *Proc. Natl. Acad. Sci. USA* ***78***, 5881-5885.

Quirion, R. (1983) Autoradiographic localization of a calcium channel antagonist, [^{3}H]-nitrendipine, binding site in rat brain. *Neurosci. Letters* ***36***, 267-271.

Reed, J.K. (1981) Modification of the tetrodotoxin receptor in *Electrophorus electricus* by phospholipase A_2. *Biochim. Biophyus. Acta* ***646***, 43-50.

Rehm, H. and Betz, H. (1982) Binding of β-bungarotoxin to synaptic membrane fractions of chick brain. *J. Biol. Chem.* ***257***, 10015-10022.

Rehm, H., Schäfer, T. and Betz, H. (1982) β-Bungarotoxin-induced cell-death of neurons in chick retina. *Brain Res.* ***250***, 309-319.

Rehm, H. and Betz, H. (1983) Identification by cross-linking of a β-bungarotoxin binding polypeptide in chick brain membranes. *EMBO J.* ***2***, 1119-1122.

Rehm, H. and Betz, H. (1984) Solubilization and characterization of the β-bungarotoxin-binding protein of chick brain membranes. *J. Biol. Chem.* ***259***, 6865-6869.

Reisfeld, R.A., Lewis, U.J. and Williams, D.E. (1962) Disc electrophoresis of basic proteins and peptides on polyacrylamide gels. *Nature* ***195***, 281-283.

Rogawski, M.A. (1985) The A-current: How ubiquitous a feature of excitable cells is it? *TINS* ***8***, 214-219.

Romey, G., Hugues, M., Schmid-Antomarchi, H. and Lazdunski, M. (1984) Apamin: A specific toxin to study a class of Ca^{2+}-dependent K^+ channels. *J. Physiol. (Paris)* ***79***, 259-264.

Rostène, W. and Mourre, C. (1985) Préparation de standards iodés pour radioautographie quantitative *in vitro* à l'aide d'un film sensible au tritium. *Comptes Rendus Acad. Sci. Paris Serie III* ***301***, 245-250.

Roth, L.J., Diab, I.M., Watanabe, M. and Dinerstein, R.J. (1974) A correlative radioautographic, fluorescent and histochemical technique for cytopharmacology. *Mol. Pharmacol.* ***10***, 986-998.

Rugolo, M., Dolly, J.O. and Nicholls, D.G. (1986) The mechanism of action of β-bungarotoxin at the presynaptic plasma membrane. *Biochem. J.* ***233***, 519-523.

Salkoff, L. (1983) Genetic and voltage-clamp analysis of a *Drosophila* potassium channel. *Cold Spring Harbor Symp. Quant. Biol.* ***48***, 221-231.

Salkoff, L., Butler, A., Wei, A. Scavarda, N., Giffen, K., Ifune, C., Goodman, R. and Mandel, G. (1987) Genomic organization and deduced amino acid sequence of a putative sodium channel gene in *Drosophila*. *Science* ***237***, 744-749.

Salpeter, M.M. and Bachmann, L. (1964) Autoradiography with the electron microscope: A procedure for improving resolution, sensitivity and contrast. *J. Cell Biol.* ***22***, 469-477.

Salpeter, M.M., Bachmann, L. and Salpeter, E.E. (1969) Resolution in electron microscope radioautography. *J. Cell Biol.* ***41***, 1-20.

Salpeter, M.M. and Salpeter, E.E. (1971) Resolution in electron microscope autoradiuography: II Carbon-14. *J. Cell Biol.* ***50***, 324-332.

Salpeter, M.M. and Bachmann, L. (1972) Autoradiography. in: Principles and Techniques of Electron Microscopy: Biological Applications. M.A. Hayat (ed.), Van Nostrand Reinhold, New York, volume II, pp 221-278.

Salpeter, M.M. and McHenry, F.A. (1972) Electron microscope autoradiography: Analyses of autoradiograms. in: Electron Microscope Techniques in Biology. J.H. Koehler (ed.), Springer Verlag, Berlin, pp 113-152.

Salpeter, M.M., Fertuck, H.C. and Salpeter, E.E. (1977) Resolution in electron microscope autoradiography: III: Iodine-125, the effect of heavy metal staining, and a reassessment of critical parameters. *J. Cell Biol.* ***72***, 161-173.

Salpeter, M.M., McHenry, F.A. and Salpeter, E.E. (1978) Resolution in electron microscope autoradiography: IV: Application to analysis of autoradiographs. *J. Cell Biol.* ***76***, 127-145.

Scatchard, G. (1949) The attractions of proteins for small molecules and ions. *Ann. N.Y. Acad. Sci.* ***51***, 660-672.

Schofield, P.R., Darlison, M.G., Fujita, N., Burt, D.R., Stephenson, F.A., Rodriguez, H., Rhee, L.M., Ramachandran, J., Reale, V., Glencorse, T.A., Seeburg, P.H. and Barnard, E.A. (1987) Sequence and functional expression of the $GABA_A$ receptor shows a ligand-gated receptor super-family. *Nature* ***328***, 221-227.

Schwarz, T.L., Tempel, B.L., Papazian, D.M., Jan, Y.N. and Jan, L.Y. (1988) Multiple potassium-channel components are produced by alternative splicing at the *Shaker* locus in *Drosophila*. *Nature* ***331***, 137-142.

Sen, I., Grantham, P.A. and Cooper, J.R. (1976) Mechanism of action of β-bungarotoxin on synaptosomal preparations. *Proc. Natl. Acad. Sci. USA* ***73***, 2664-2668.

Sen, I. and Cooper, J.R. (1978) Similarities of β-bungarotoxin and phospholipase A_2 and their mechanism of action. *J. Neurochem.* ***30***, 1369-1375.

Shepherd, G.M. (1983) Neurobiology. Oxford University Press, New York, Oxford.

Sigworth, F.J. and Neher, E. (1980) Single Na^+ channel currents observed in cultured rat muscle cells. *Nature 287*, 447-449.

Simantov, R., Childers, S.R. and Snyder, S.H. (1978) The opiate receptor binding interactions of [^{3}H]-methionine enkephalin, an opioid peptide. *Eur. J. Pharmacol. 47*, 319-331.

Simonneau, M., Distasi, C., Tauc, L. and Barbin, G. (1987) Potassium channels in mouse neonate dorsal root ganglion cells: A patch-clamp study. *Brain Res. 412*, 224-232.

Skou, J.C. and Nørby, J.G. (1979) Na,K-ATPase: Structure and Kinetics. Academic Press, London, New York, San Francisco.

Small, J.V. (1968) Measurement of section thickness. in: Proceedings of the 4TH European Congress of Electron Microscopy, Volume 1; Tipografica Poliglotta Vaticana, Roma, pp 609-610.

Smith, C.C.T., Bradford, H.F., Thompson, E.J. and MacDermot, J. (1980) Actions of ß-bungarotoxin on amino acid transmitter release. *J. Neurochem. 34*, 487-494.

Spokes, J.W. and Dolly, J.O. (1980) Complete purification of ß-bungarotoxin. Characterization of its action and that of tityustoxin on synaptosomal accumulation and release of acetylcholine. *Biochim. Biophys. Acta 596*, 81-93.

Spurr, A.R. (1969) A low-viscosity epoxy resin embedding medium for electron microscopy. *J. Ultrastruct. Res. 26*, 31-43.

Stansfeld, C.E., Marsh, S.J., Halliwell, J.V. and Brown, D.A. (1986) 4-Aminopyridine and dendrotoxin induce repetitive firing in rat visceral sensory neurones by blocking a slowly inactivating outward current. *Neurosci. Letters 64*, 299-304.

Stansfeld, C.E., Marsh, S.J., Parcej, D.N., Dolly, J.O. and Brown, D.A. (1987) Mast cell degranulating peptide and dendrotoxin selectively inhibit a fast-activating potassium current and bind to common neuronal proteins. *Neuroscience 23*, 893-902.

Strong, P.N., Goerke, J., Oberg, S.G. and Kelly, R.B. (1976) ß-Bungarotoxin, a pre-synaptic toxin with enzymatic activity. *Proc. Natl. Acad. Sci. USA 73*, 178-182.

Strong, P.N. and Kelly, R.B. (1977) Membranes undergoing phase transitions are preferentially hydrolysed by beta-bungarotoxin. *Biochim. Biophys. Acta 469*, 231-235.

Strong, P.N., Heuser, J.E. and Kelly, R.B. (1977) Selective enzymatic hydrolysis of nerve terminal phospholipids by ß-bungarotoxin: Biochemical and morphological studies. in: Cellular Neurobiology. Z. Hall, R.B. Kelly and C.F. Fox (Eds.). A.R. Liss, New York, pp 227-249.

Strong, P.N., Wood, J.N. and Ivanyi, J. (1984) Characterization of monoclonal antibodies against β-bungarotoxin and their use as structural probes for related phospholiapse A_2 enzymes and presynaptic phospholipase neuotoxins. *Eur. J. Biochem.* ***142***, 145-151.

Strydom, D.J. (1973) Protease inhibitors as snake venom toxins. *Nature New Biology* ***243***, 88-89.

Strydom, D.J. (1976) Snake venom toxins: Purification and properties of low-molecular weight polypeptides of *Dendroaspis polylepis polylepis* (black mamba) venom. *Eur. J. Biochem.* ***69***, 169-176.

Strydom, D.J. (1977) Snake venom toxins: The amino acid sequence of toxin Vi2, a homologue of pancreatic trypsin inhibitor from *Dendroaspis polylepis polylepis* (black mamba) venom. *Biochim. Biophys. Acta* ***491***, 361-369.

Strydom, D.J. and Joubert, F.J. (1981) The amino acid sequence of a weak trypsin inhibitor B from *Dendroaspis polylepis polylepis* (black mamba) venom. *Hoppe-Seyler's Z. Physiol. Chem.* ***362***, 1377-1384.

Su, M.J. and Chang, C.C. (1984) Presynaptic effects of snake venom toxins which have phospholipase A_2 activity (β-bungarotoxin, taipoxin, crotoxin). *Toxicon* ***22***, 631-640.

Swanson, P.D. (1977) Effects of beta-bungarotoxin, diphenyl-hydantoin and metabolic inhibitors on calcium uptake and on monovalent cations and high energy phosphate contents of the brain. *J. Neurochem.* ***29***, 767-769.

Tait, J.F., Weinman, S.A. and Bradshaw, R.A. (1981) Dissociation kinetics of ^{125}I-nerve growth factor from cell surface receptors. *J. Biol. Chem.* ***256***, 11086-11092.

Tanabe, T., Takeshima, H., Mikami, A., Flockerzi, V., Takahashi, H., Kangawa, K., Kojima, M., Matsuo, H., Hirose, T. and Numa, S. (1987) Primary structure of the receptor for calcium channel blockers from skeletal muscle. *Nature* ***328***, 313-318.

Tanouye, M.A., Ferrus, A. and Fujita, S.C. (1981) Abnormal action potentials associated with the *Shaker* complex locus of *Drosophila*. *Proc. Natl. Acad. Sci. USA* ***78***, 6548-6552.

Taylor, N.R., Unnerstall, J.R., Mashal, R.D., De Souza, E.B. and Kuhar, M.J. (1984) Receptor autoradiography: Coping with regional differences in autoradiographic efficiency with tritium. *Soc. Neurosci. Abstracts* ***10***, 557.

Tempel, B.L., Papazian, D.M., Schwarz, T.L., Jan, Y.N. and Jan, L.Y. (1987) Sequence of a probable potassium channel component encoded at *Shaker* locus of *Drosophila*. *Science* ***237***, 770-775.

Timpe,L.C., Schwarz, T.L., Tempel. B.L., Papazian, D.M., Jan, Y.N. and Jan, L.Y. (1987) Expression of functional potassium channels from *Shaker* cDNA in *Xenopus* oocytes. *Nature* ***331***, 143-145.

Tobias, G.S., Donlon, M.A., Catravas, G.N. and Shain, W. (1978) Purification and biochemical characterization of an 11 000-dalton β-bungarotoxin. *Biochim. Biophys. Acta 537*, 348-357.

Tse, C.K., Dolly, J.O. and Diniz, C.R. (1980) Effects of β-bungarotoxin and tityustoxin on accumulation of putative amino acid neurotransmitters by rat cortex synaptosomes. *Neuroscience 5*, 135-143.

Tümmers, U., Müller, T.H., Schmidt, R., Seidl, K., Lichtwald, K., Vescei, P., Wagner, H.-J. and Unsicker, K. (1986) Destruction of the preganglionic nerves by β-bungarotoxin does not interfere with normal embryonic development of the rat adrenal medulla. *Dev. Biol. 117*, 619-627.

Ueda, T., Greengard, P., Berzins, K., Cohen, R.S., Blomberg, F., Grab, D.J. and Siekevitz, P. (1979) Subcellular distribution in cerebral cortex of two proteins phosphorylated by a cAMP-dependent protein kinase. *J. Cell Biol. 83*, 308-319.

Unnerstall, J.R., Niehoff, D.L., Kuhar, M.J. and Palacios, J.H. (1982) Quantitative receptor autoradiography using [^{3}H]-Ultrofilm: Application to multiple benzodiazepine receptors. *J. Neurosci. Methods 6*, 59-73.

Van Tienhoven, A. and Juhasz, L.P. (1962) The chicken telencephalon, diencephalon and mesencephalon in stereotaxic coordinates. *J. Comp. Neurol. 118*, 185-197

Wagner, G.M., Mart, P.E. and Kelly, R.B. (1974) β-Bungarotoxin inhibition of calcium accumulation by rat brain mitochondria. *Biochem. Biophys. Res. Commun. 58*, 475-481.

Wainer, B.H., Levey, A.I., Mufson, E.J. and Mesulam, M.-M. (1984) Cholinergic systems in mammalian brain identified with antibodies against choline acetyltransferase. *Neurochem. Int. 6*, 163-182.

Wamsley, J.K., Lewis, M.S., Young, W.S. and Kuhar, M.J. (1981) Autoradiographic localization of muscarinic cholinergic receptors in rat brainstem. *J. Neurosci. 1*, 176-191.

Watkins, J.C. and Evans, R.H. (1981) Excitatory amino acid transmitters. *Ann. Rev. Pharmacol. Toxicol. 21*, 165-204.

Weiland, G.A. and Molinoff, P.B. (1981) Quantitative analysis of drug-receptor interactions: I Determination of kinetic and equilibrium properties. *Life Sci. 29*, 313-330

Weller, U., Bernhardt, U., Siemen, D., Dreyer, F., Vogel, W. and Habermann, E. (1985) Electrophysiological and neurochemical evidence for the blockade of a potassium channel by dendrotoxin. *Naunyn Schmiedeberg's Arch. Pharmacol. 330*, 77-83.

Wernicke, J.F., Oberjat, T. and Howard, B.D. (1974) β-Neurotoxin reduces neurotransmitter storage in brain synapses. *J. Neurochem. 22*, 781-788.

Wernicke, J.F., Vanker, A.D. and Howard, B.D. (1975) The mechanism of action of β-bungarotoxin. *J. Neurochem. 25*, 483-496.

Williams, M.A. (1969) The assessment of electron microscopic autoradiographs. *Adv. Opt. Electr. Microscopy 3*, 219-272.

Williams, R.S., Tse, C.-K., Dolly, J.O., Hambleton, P. and Melling J. (1983) Radioiodination of botulinum neurotoxin type A with retention of biological activity and its binding to brain synaptosomes. *Eur. J. Biochem. 131*, 437-445.

Worley, P.F. and Baraban, J.M. (1987) Site of anticonvulsant action on sodium channels: Autoradiographic and electrophysiological studies in rat brain. *Proc. Natl. Acad. Sci. USA 84*, 3051-3055.

Wu, S.H., Wang, K.T. and Ho, C.L. (1982) Purification and pharmacological characterization of a cardiotoxin-like protein from Formosan banded krait (*Bungarus multicinctus*) venom. *Toxicon 20*, 753-764.

Yamamura, H.I., Kuhar, M.J., Greenberg, D. and Snyder, S.H. (1974) Muscarinic cholinergic recptor binding: Regional distribution in monkey brain. *Brain Res. 66*, 541-546.

Young, W.S. and Kuhar, M.J. (1979) A new method for receptor autoradiography: [^{3}H]Opioid receptors in rat brain. *Brain Res. 179*, 255-270.

Zeman, W. and Innes, J.R.M. (1963) Craigie's Neuranantomy of the Rat. Academic Press, New York.

Zilles, K., Becker, C.-M. and Schleicher, A. (1981) Transmission blockade during neuronal development. Observations on the trochlear nucleus with quantitative histological methods and with ultrastructural and axonal transport studies in the chick embryo. *Anat. Embryol. 163*, 87-123.